Biological materials: Structure and mechanical properties

Marc André Meyers *, Po-Yu Chen, Albert Yu-Min Lin, Yasuaki Seki

Materials Science and Engineering Program, Department of Mechanical and Aerospace Engineering, University of California, San Diego, La Jolla, CA 92093, United States

Abstract

Most natural (or biological) materials are complex composites whose mechanical properties are often outstanding, considering the weak constituents from which they are assembled. These complex structures, which have risen from hundreds of million years of evolution, are inspiring Materials Scientists in the design of novel materials.

Their defining characteristics, hierarchy, multifunctionality, and self-healing capability, are illustrated. Self-organization is also a fundamental feature of many biological materials and the manner by which the structures are assembled from the molecular level up. The basic building blocks are described, starting with the 20 amino acids and proceeding to polypeptides, polysaccharides, and polypeptides–saccharides. These, on their turn, compose the basic proteins, which are the primary constituents of 'soft tissues' and are also present in most biominerals. There are over 1000 proteins, and we describe only the principal ones, with emphasis on collagen, chitin, keratin, and elastin. The 'hard' phases are primarily strengthened by minerals, which nucleate and grow in a biomediated environment that determines the size, shape and distribution of individual crystals. The most important mineral phases are discussed: hydroxyapatite, silica, and aragonite.

Using the classification of Wegst and Ashby, the principal mechanical characteristics and structures of biological ceramics, polymer composites, elastomers, and cellular materials are presented. Selected systems in each class are described with emphasis on the relationship between their structure and mechanical response. A fifth class is added to this: functional biological materials, which have a structure developed for a specific function: adhesion, optical properties, etc.

An outgrowth of this effort is the search for bioinspired materials and structures. Traditional approaches focus on design methodologies of biological materials using conventional synthetic

---

* Corresponding author.
  E-mail address: mameyers@mae.ucsd.edu (M.A. Meyers).

materials. The new frontiers reside in the synthesis of bioinspired materials through processes that are characteristic of biological systems; these involve nanoscale self-assembly of the components and the development of hierarchical structures. Although this approach is still in its infancy, it will eventually lead to a plethora of new materials systems as we elucidate the fundamental mechanisms of growth and the structure of biological systems.

Contents

1. Introduction and basic overview of mechanical properties

The study of biological systems as structures dates back to the early parts of the 20th century. The classic work by D'Arcy W. Thompson [1], first published in 1917, can

be considered the first major work in this field. He looked at biological systems as engineering structures, and obtained relationships that described their form. In the 1970s, Currey investigated a broad variety of mineralized biological materials and authored the well-known book ''Bone'' [2]. Another work of significance is Vincent's ''Structural Biological Materials'' [3]. The field of biology has, of course, existed and evolved during this period, but the engineering and materials approaches have often been shunned by biologists.

Materials Science and Engineering is a young and vibrant discipline that has, since its inception in the 1950s, expanded into three directions: metals, polymers, and ceramics (and their mixtures, composites). Biological materials are being added to its interests, starting in the 1990s, and are indeed its new future.

Many biological systems have mechanical properties that are far beyond those that can be achieved using the same synthetic materials [3,4]. This is a surprising fact, if we consider that the basic polymers and minerals used in natural systems are quite weak. This limited strength is a result of the ambient temperature, aqueous environment processing, as well as of the limited availability of elements (primarily C, N, Ca, H, O, Si, P). Biological organisms produce composites that are organized in terms of composition and structure, containing both inorganic and organic components in complex structures. They are hierarchically organized at the nano, micro, and meso levels. The emerging field of biological materials introduces numerous new opportunities for materials scientists to do what they do best: solve complex multidisciplinary scientific problems. A new definition of Materials Science is emerging, as presented in Fig. 1a; it is situated at the confluence of chemistry, physics, and biology. Biological systems are subjected to complex constraints which exhibit specific characteristics shown in Fig. 1b. The modified pentahedron proposed by Arzt [5] has five components: self assembly, ambient temperature and pressure processing, functionality, hierarchy of structure and evolution/environmental effects. They are specific and unique to biological materials. Biological systems have many distinguishing features, such as being the result of evolution and being multifunctional; however, evolution is not a consideration in synthetic materials and multifunctionality still needs further research. The schematics shown in Fig. 1b are indicative of the complex contributions and interactions necessary to fully understand and exploit (through biomimicking) biological systems.

Some of the main areas of research and activity in this field are

- Biological materials: these are the materials and systems encountered in nature.
- Bioinspired (or biomimicked) materials: approaches to synthesizing materials inspired on biological systems.
- Biomaterials: these are materials (e.g., implants) specifically designed for optimum compatibility with biological systems.
- Functional biomaterials and devices.

This overview will restrict itself primarily to the first two areas. Using a classical 'materials' approach we present the basic structural elements of biological materials (Section 5) and then correlate them to their mechanical properties. These elements are organized hierarchically into complex structures (Section 2). The different structures will be discussed in Sections 6–9. In Section 11, we provide some inroads into biomimetics, since the goal of
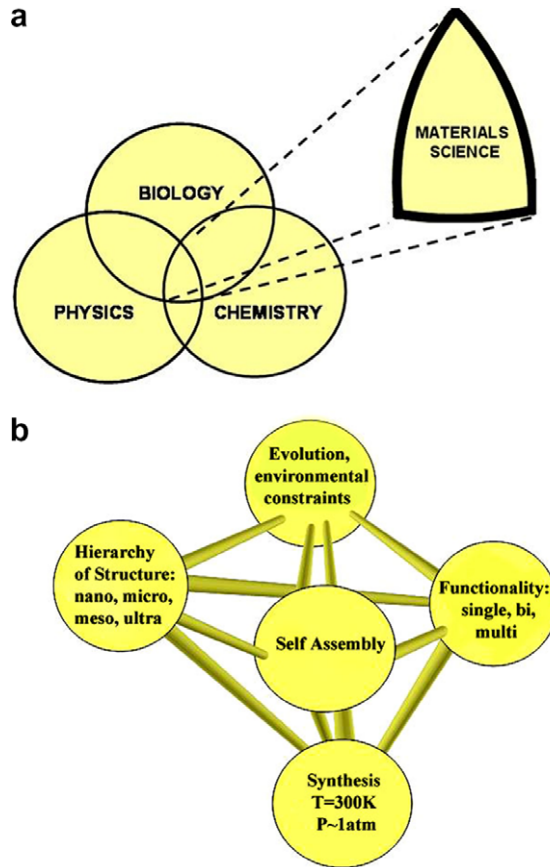
Fig. 1. Schematic representation of (a) contributing scientific fields and (b) constraints/components in the study of biological systems (modified from Arzt [5, p. 1246, Fig. 1]).

materials engineering is to utilize the knowledge base developed in materials science to create new materials with expanded properties and functions.

Although biology is a mature science, the study of *biological materials and systems* by Materials Scientists and Engineers is recent. It is intended, ultimately:

(a) To provide the tools for the development of biologically inspired materials. This field, also called *biomimetics* [6], is attracting increasing attention and is one of the new frontiers in materials research.
(b) To enhance our understanding of the interaction of synthetic materials and biological structures with the goal of enabling the introduction of new and complex systems in the human body, leading eventually to organ supplementation and substitution. These are the so-called *biomaterials*.

The extent and complexity of the subject are daunting and will require many decades of global research effort to be elucidated. Thus, we focus in this overview on a number

Fig. 2. Ashby plots for biological materials showing (a) elastic modulus and (b) strength as a function of density (from Wegst and Ashby [17]).

of systems that have attracted our interest. This is by no means an exhaustive list, and there are many systems that have only been superficially investigated. We are currently investigating: abalone [8,9], conch [10,11], toucan beaks [12,13], and crab exoskeleton [14]. We

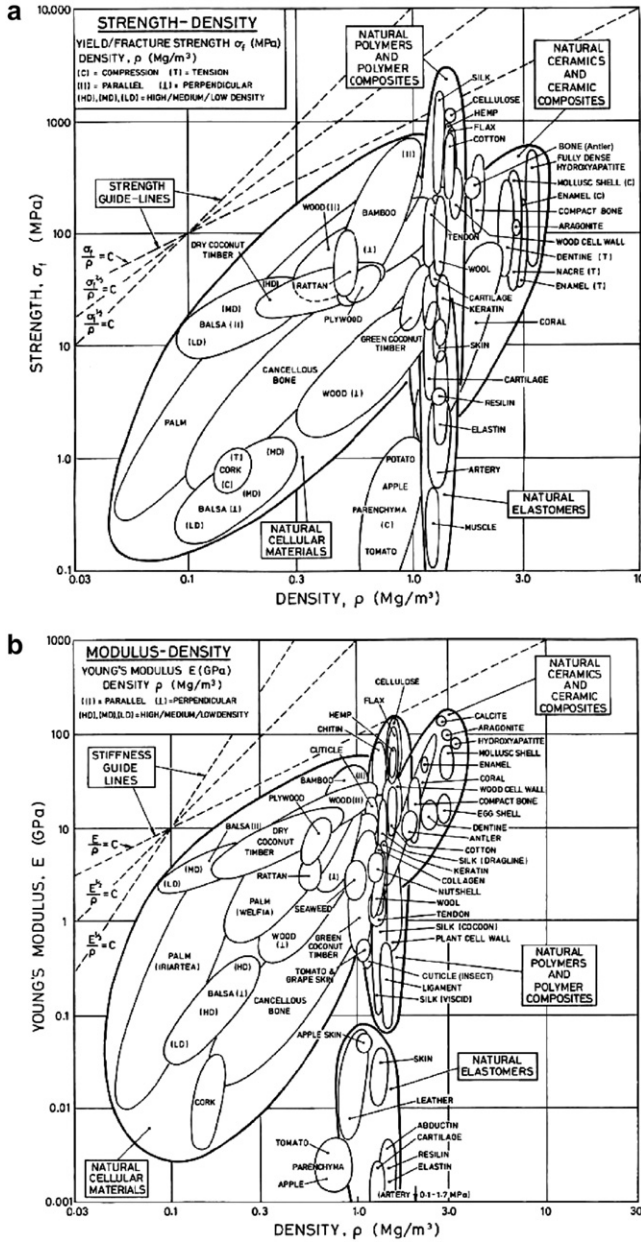add the silica spicules, that have been studied and extensively described by Mayer and coworkers [6,7], as well some other selected systems.

Mechanical property maps [15], more commonly known as Ashby maps, have become a convenient manner of concentrating a large amount of information into one simple diagram. The first such map was proposed, for metals, by Weertman [16], and therefore the name Weertman–Ashby is sometimes used. They constitute a valuable design tool and have been extended to biological materials by Wegst and Ashby [17]. Thus, they are a good starting point for this overview. Two maps are presented in Fig. 2; they present the Young moduli and strength as a function of density. There are several striking and defining features:

(a) The density of natural (biological) systems is low. It rarely exceeds 3, whereas synthetic structural materials often have densities in the 4–10 range.
(b) There is a broad range in Young moduli all the way from 0.001 to 100 GPa. This represents five orders of magnitude.
(c) The range of strengths is almost as broad as the Young moduli, varying over four orders of magnitude: 0.1–1000 MPa.
(d) There is an absence of metals, which require for the most part either high temperature or high electric current processing. Nature does not have at its disposal these variables.

Wegst and Ashby [17] classify biological (natural) materials into four groups, indicated by ellipses in Fig. 2:

Ceramics and ceramic composites: these are biological materials where the mineral component is prevalent, such as in shells, teeth, bones, diatoms, and spicules of sponges.

Polymer and polymer composites: examples of these are the hooves of mammals, ligaments and tendons, silk, and arthropod exoskeletons.

Elastomers: these are characteristically biological materials that can undergo large stretches (or strains). The skin, muscle, blood vessels, soft tissues in body, and the individual cells fall under this category.

Cellular materials: typical are the light weight materials which are prevalent in feathers, beak interior, cancellous bone, and wood.

In this overview we will follow this classification since it enables a logical and tractable description of very broad classes of biological materials. A considerable number of books and review articles have been written on biological materials and they constitute the foundation necessary to embark in this field. Some of the best known are given in Tables 1 and 2, respectively.

2. Hierarchical organization of structure

It could be argued that all materials are hierarchically structured, since the changes in dimensional scale bring about different mechanisms of deformation and damage. However, in biological materials this hierarchical organization is inherent to the design. The design of the structure and material are intimately connected in biological systems, whereas in synthetic materials there is often a disciplinary separation, based largely on tradition, between materials (materials engineers) and structures (mechanical engineers). We

Table 1
Principal books on biological materials and biomimetism [only first author listed]

Author	Year	Title
Thompson [1]	1917	On Growth and Form
Fraser [18]	1972	Keratins: Their Composition, Structure, and Biosynthesis
Brown [19]	1975	Structural Materials in Animals
Wainwright [20]	1976	Mechanical Design in Organisms
Vincent [21]	1980	The Mechanical Properties of Biological Materials
Vincent [3]	1982	Structural Biomaterials
Currey [32]	1984	The Mechanical Adaptations of Bone
Simkiss [22]	1989	Biomineralization: Cell Biology and Mineral Deposition
Lowenstam [31]	1989	On Biomineralization
Byrom [23]	1991	Biomaterials: Novel Materials from Biological Sources
Fung [24]	1993	Biomechanics: Mechanical Properties of Living Tissues
Fung [25]	1990	Biomechanics: Motion, Flow, Stress, and Growth
Fung [26]	1997	Biomechanics: Circulation 2nd edition
Feughelman [27]	1997	Mechanical Properties and Structure of Alpha-keratin Fibers
Gibson [28]	1997	Cellular Solids: Structure and Properties
McGrath [29]	1997	Protein-based Materials
Elices [30]	2000	Structural Biological Materials
Mann [7]	2001	Biomineralization: Principles and Concepts in Bioinorganic Materials Chemistry
Currey [2]	2002	Bones: Structure and Mechanics
Ratner [33]	2004	Biomaterials Science: An Introduction to Materials in Medicine
Forbes [34]	2005	The Gecko's Foot

Table 2
Principal review articles on biological materials and biomimetism [only first author listed]

Author	Year	Title
Srinivasan [4]	1991	Biomimetics: Advancing man-made materials through guidance from nature
Mann [35]	1993	Crystallization at inorganic–organic interfaces: Biominerals and biomimetic synthesis
Kamat [36]	2000	Structural basis for the fracture toughness of the shell of the conch *Strombus gigas*
Whitesides [37]	2002	Organic materials science
Mayer [38]	2002	Rigid biological composite materials: Structural examples for biomimetic design
Altman [39]	2003	Silk-based biomaterials
Wegst [17]	2004	The mechanical efficiency of natural materials
Mayer [40]	2005	Rigid biological systems as models for synthetic composites
Sanchez [41]	2005	Biomimetism and bioinspiration as tools for the design of innovative materials and systems
Wilt [42]	2005	Developmental biology meets materials science: Morphogenesis of biomineralized structures
Meyers [43]	2006	Structural biological composites: An overview
Mayer [44]	2006	New classes of tough composite materials – Lessons from nature rigid biological systems
Lee [45]	2007	Nanobiomechanics Approaches to Study Human Diseases

illustrate this by three examples in Figs. 3 (bone), 4 (abalone shell), and 5 (crab exoskeleton).

In bone (Fig. 3), the building block of the organic component is the collagen, which is a triple helix with diameter of approximately 1.5 nm. These tropocollagen molecules are intercalated with the mineral phase (hydroxyapatite, a calcium phosphate) forming fibrils
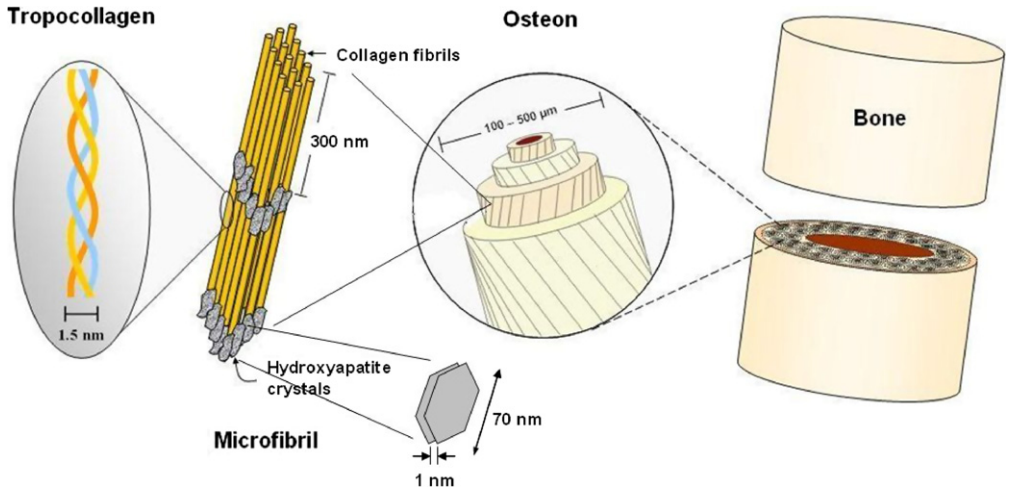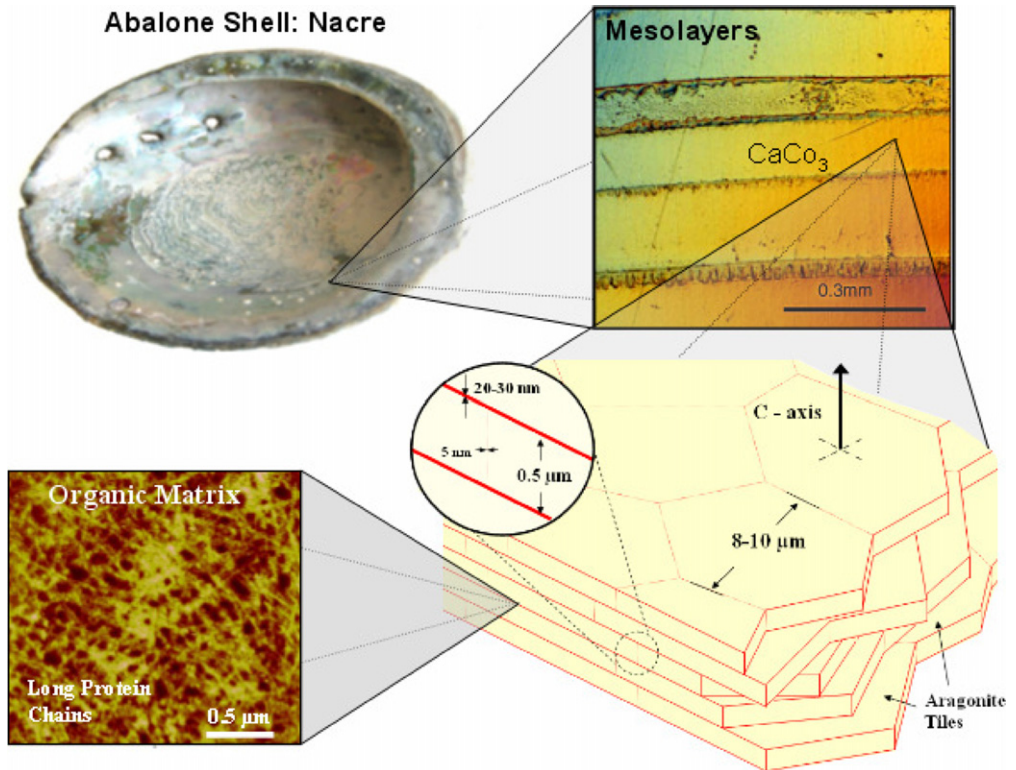
Fig. 3. Hierarchical organization of bone.

Fig. 4. Hierarchy of abalone structure. Clockwise from top left: entire shell; mesostructure with mesolayers; microstructure with aragonite tiles; nanostructure showing organic interlayer comprising 5 wt% of overall shell.
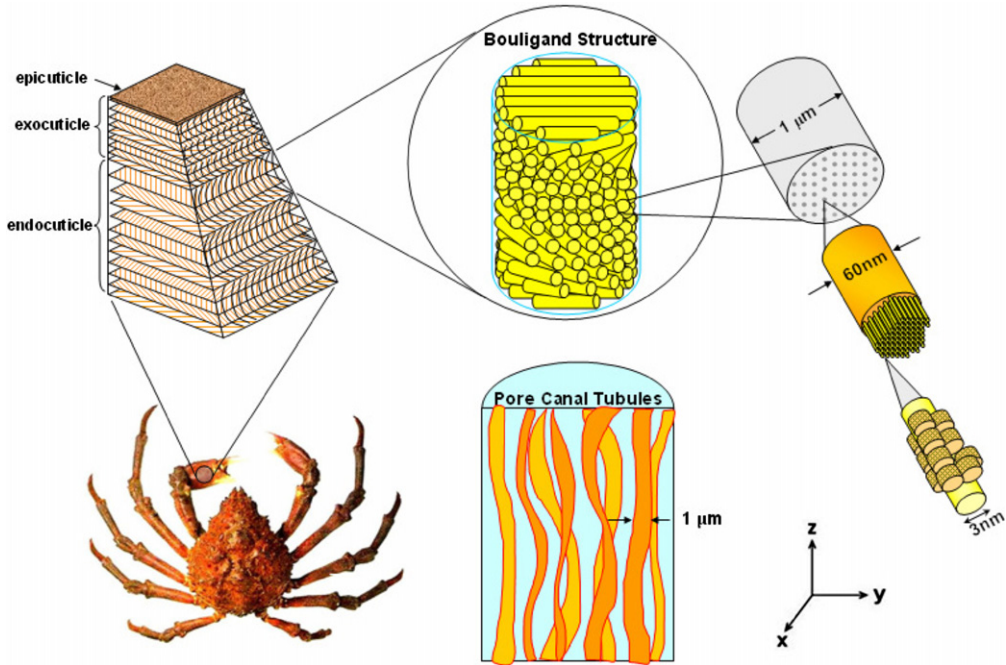
Fig. 5. Hierarchy of crab exoskeleton.

that, on their turn, curl into helicoids of alternating directions. These, the osteons, are the basic building blocks of bones. The volume fraction distribution between organic and mineral phase is approximately 60/40, making bone unquestionably a complex hierarchically structured biological composite. There is another level of complexity. The hydroxyapatite crystals are platelets that have a diameter of approximately 70–100 nm and thickness of ~1 nm. They originally nucleate at the gaps between collagen fibrils. Not shown is the Haversian system that contains the vascularity which brings nutrients and enables forming, remodeling, and healing of the bone.

Similarly, the abalone shell (Fig. 4) owes its extraordinary mechanical properties (much superior to monolithic $CaCO_3$) to a hierarchically organized structure, starting, at the nanolevel, with an organic layer having a thickness of 20–30 nm, proceeding with single crystals of the aragonite polymorph of $CaCO_3$, consisting of "bricks" with dimensions of 0.5 vs. 10 μm (microstructure), and finishing with layers approximately 0.3 mm (mesostructure).

Crabs are arthropods whose carapace is comprised of a mineralized hard component, which exhibits brittle fracture, and a softer organic component, which is primarily chitin. These two components are shown in the Fig. 5. The brittle component is arranged in a helical pattern called Bouligand structure [46,47]. Each of these mineral 'rods' (~1 μm diameter) contains chitin–protein fibrils with approximately 60 nm diameter. These, on their turn, are comprised of 3 nm diameter segments. There are canals linking the inside to the outside of the shell; they are bound by tubules (0.5–1 μm) shown in the micrograph and in schematic fashion. The cross-section of hard mineralized component has darker spots seen in the SEM.

3. Multifunctionality and self-healing

Most biological materials are *multifunctional* [4], i.e., they accumulate functions such as

(a) Bone: structural support for body plus blood cell formation.
(b) Chitin-based exoskeleton in arthropods: attachment for muscles, environmental protection, water barrier.
(c) Sea spicules: light transmission plus structural.
(d) Tree trunks and roots: structural support and anchoring plus nutrient transport.
(e) Mammalian skin: temperature regulation plus environmental protection.
(f) Insect antennas: they are mechanically strong and can self-repair. They also detect chemical and thermal information from the environment. They can change their shape and orientation.

Another defining characteristic of biological systems, in contrast with current synthetic systems, is their *self-healing ability*. This is nearly universal in nature. Most structures can repair themselves, after undergoing trauma or injury. Exceptions are teeth and cartilage, that do not possess any significant vascularity. It is also true that brains cannot self-repair; however, other parts of the brain take up the lost functions.

4. Self-organization and self-assembly

In the traditional study of thermodynamics, we, Materials Scientists, restrict ourselves, for the most part, to isolated and closed systems. We know, from the second law of thermodynamics, that in an isolated system equilibrium is reached at maximum entropy. If t is defined as time, a system will approach equilibrium as

$$dS/dt > 0 \tag{1}$$

Thus, we learn that the entire universe marches inexorably toward entropy maximization. This translates into disorder because disordered states have a greater number of possible configurations, W (recall that $S = k \ln W$).

For closed systems, equilibrium is reached when the free energy is minimized. If pressure and temperature are constant, the Gibbs free energy is used; for systems at constant volume and temperature, the Helmholtz free energy criterion holds. However, we know that temporal evolution in nature starts from simpler to more complex structures and leads to ever greater order and self-organization. This is clear around us: subatomic particles aggregate to form atoms, atoms combine to form compounds, organic compounds form complex molecules which eventually lead to life, life progresses from the simplest to the more complex forms, biological units combine in ever increasing complex arrays, civilizations form and evolve. How can all this be reconciled with thermodynamics? The seminal work of Prigogine [48,49], 1977 Nobel Laureate in Chemistry, is essential to our understanding. He developed the thermodynamics of irreversible systems and provided a link between thermodynamics and evolution. This was actually preceded by Teilhard de Chardin, a French paleontologist and philosopher that advanced the law of complexity-conscience. In his classic work, 'Le Phenomène Humain' [50], he proposed boldly that complexity inexorably increases in the universe at the expense of a quantity

which he named 'physical energy.' This increase in complexity results in an increase in conscience.

Most complex systems are indeed open and off equilibrium. Prigogine demonstrated that non-isolated (open) systems can evolve, by self-organization and self-assembly, toward greater order [48,49]. Open systems exhibit fluxes of energy, matter, and exchanges in mechanical, electrical, and magnetic energy with the environment. The entropy variation can be expressed as having two components: one internal, i, and one due to the exchanges, e:

$$dS/dt = d_iS/dt + d_eS/dt \qquad (2)$$

If the system were isolated, we would have $d_eS/dt = 0$. For an open system, this term is not necessarily zero. There is no law dictating the sign of d_eS/dt and it can be either positive or negative. The second law still applies to the internal components, i. Thus

$$d_iS/dt > 0 \qquad (3)$$

Thus, it is possible to have a temporal decrease in S, if the flux component contributes with a sufficiently negative d_eS/dt term: $dS/dt < 0$ if $d_eS/dt > -d_i\,S/dt$.

The physical interpretation of Eq. (2) is that order can increase with time. This is a simple and incomplete explanation for the origin of complex phenomena. Irreversible thermodynamics of complex systems involves other concepts such as perturbation and symmetry breaking. Nicholas and Progogine [49] showed that non-linearities combined with non-equilibrium constraints can generate multiple solutions through bifurcation and thus allow for more complex behavior in a system. The biosphere is an example of an open system, since it receives radiative energy from the sun and exchanges energy with the earth.

Self-organization is a strategy by which biological systems construct their structures. There are current efforts at this design strategy duplicating in order to manufacture synthetic structures. Among the first were Nuzzo and Allara [51] who fabricated self-assembled monolayers (SAMs). This work and other work by Whitesides [37,52] and Sarikaya [53] (GEPIs) will be reviewed in Section 11. (Biomimetics) is laying the groundwork for biologically inspired self-assembly processes which have considerable technological potential.

As an example of a self-assembled structure, Fig. 6a shows a schematic rendition of a diatom. The end surface is shown in Fig. 6b. This elaborate architecture is developed by self-assembly of the enzymes forming a scaffold upon which biomineralization takes place [54,55]. These orifices are each at the intersections of three lines: two spiral lines with opposite chirality and radiating lines. The rows of orifices radiating from the center exhibit 'dislocations' since the number of spokes has to increase with the radius. These dislocations are marked with circles in Fig. 6c. The orifices have a striking regularity and spacing, as shown in Fig. 7. Their diameter is approximately 2 μm and they each have a ridge that serves, most probably, as reinforcement, such as in cast iron components.

5. Basic building blocks (nano and microstructure of biological materials)

Biological materials are more complex than synthetic materials. As seen in the previous sections, they form complex arrays, hierarchical structures and are often multifunctional, i.e., one material has more than one function. We classify biological materials, from the mechanical property viewpoint, into soft and hard. Hard materials provide the skeleton,
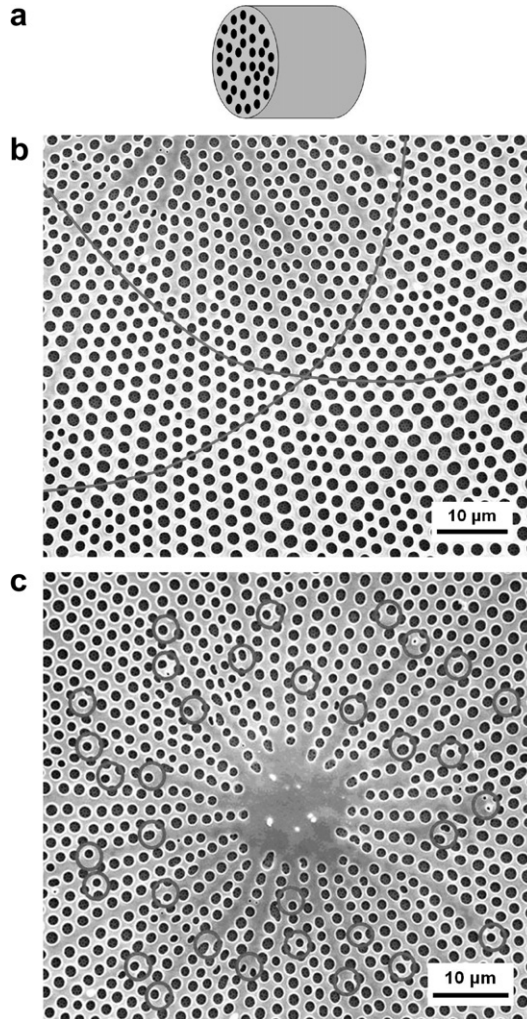
Fig. 6. (a) A cylindrical silica diatom; (b) end surface of cylindrical silica diatom showing self-organized pattern of orifices. Notice spiral patterns (both chiralities); (c) center of cylinder with radiating spokes; extremities of 'dislocations' marked by circles (courtesy of E. York, Scripps Institute of Oceanography, UC San Diego).

teeth, and nails in vertebrates and the exoskeleton in arthropods. Soft biological materials build skin, muscle, internal organs, etc. Table 3 provides the distribution (on a weight percentage) of different constituents of the human body.

Here are some examples of "hard" biological materials:

Calcium phosphate (hydroxyapatite-$Ca_{10}(PO_4)_6(OH)_2$): teeth, bone, antlers.
Calcium carbonate (aragonite): mollusk shells, some reptile eggs.
   (calcite): bird eggs, crustaceans, mollusks.
Amorphous silica ($SiO_2(H_2O)_n$): spicules in sponges, diatoms.
Iron oxide (Magnetite-Fe_3O_4): teeth in chitons (a weird looking marine worm), bacteria.
Collagen: organic component of bone and dentine, tendons, muscle, blood vessels.
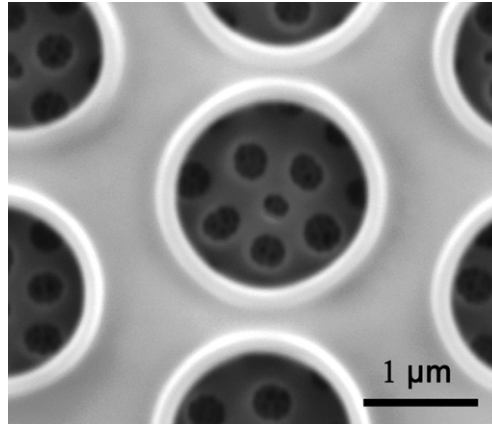
Fig. 7. Detailed view of orifice; back surface of diatom with hexagonal pattern can be seen in central orifice (Courtesy of E. York, Scripps Institute of Oceanography, UC San Diego).

Table 3
Occurrences of different biological materials in body

Biological material	Weight percentage in human body
Proteins	17
Lipids	15
Carbohydrates	1
Minerals	7
DNA, RNA	2
Water	58

Chitin: arthropod and insect exoskeletons.
Cellulose: plant cell walls.
Keratin: bird beaks, horn, hair.
Elastin: skin, lungs, artery walls.

Of the above, iron oxide, carbon phosphate, calcium carbonate, silica, and iron oxide are minerals. Chitin and cellulose are polysaccharides. Collagen, keratin and elastin are proteins (polypeptides).

5.1. Molecular units

In order to fully understand proteins, we have to start at the atomic/molecular level, as we did for polymers. Actually, proteins can be conceived of as polymers with a greater level of complexity. We start with amino acids, which are compounds containing both an amine ($-NH_2$) and a carboxyl ($-COOH$) group. Most of them have the structure:
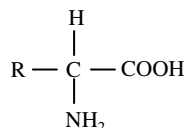
$$R - \underset{\underset{NH_2}{|}}{\overset{\overset{H}{|}}{C}} - COOH$$

Table 4
Eight of the 20 amino acids found in proteins

Name	Chemical formula
Alanine (Ala)	$^{+}NH_3 - CH - C - O^{-}$, with $C=O$ and side chain CH_3
Leucine (Leu)	$^{+}NH_3 - CH - C - O^{-}$, with $C=O$ and side chain $CH_2 - CH - (CH_3\ CH_3)$
Phenylalanine (Phe)	$^{+}NH_3 - CH - C - O^{-}$, with $C=O$ and side chain CH_2 — benzene ring
Proline (Pro)	$NH - CH - C - O^{-}$, with $C=O$; ring $CH_2\ CH_2\ CH_2$
Serine (Ser)	$^{+}NH_3 - CH - C - O^{-}$, with $C=O$ and side chain $CH_2 - OH$
Cysteine (Cys)	$^{+}NH_3 - CH - C - O^{-}$, with $C=O$ and side chain $CH_2 - SH$
Glutamate (Glu)	$^{+}NH_3 - CH - C - O^{-}$, with $C=O$ and side chain $CH_2 - CH_2 - C=O - O^{-}$

Table 4 (*continued*)

Name	Chemical formula
Lysine (Lys)	$$^+NH_3 - CH - \overset{\overset{\displaystyle O}{\|\|}}{C} - O^-$$ $$\|$$ $$CH_2$$ $$\|$$ $$CH_2$$ $$\|$$ $$CH_2$$ $$\|$$ $$CH_2$$ $$\|$$ $$NH_3^+$$

R stands for a radical. Table 4 shows eight main amino acids. There are 20 different amino acids in proteins. In addition to these eight, we have the following: Arginine (Arg), Asparagine (Asn), Aspartate (Asp), Glutamine (Gln), Glycine (Gly), Histidine (His), Isoleucine (Ile), Methionine (Met), Threonine (Thr), Tryptophan (Trp), Tyrosine (Tyr), and Valine (Val).

Deoxyribonucleic (DNA) and ribonucleic acid (RNA) are the molecular repositories of genetic information. The structure of protein is a product of information programmed into the nucleotide sequence of a nucleic acid. Nucleotides are the building blocks of nucleic acids. In DNA, the four nucleotides present are designated by the letters ACTG: Adenine, Cytosine, Thymine, and Guanine. A links to T and G links to C trough hydrogen-bonding, as shown in Fig. 8.

The amino acids form linear chains similar to polymer chains; these are called polypeptide chains. These polypeptide chains acquire special configurations because of the formation of bonds (hydrogen, van der Waals, and covalent bonds) between amino acids on the same or different chains. The two most common configurations are the alpha helix and the beta sheet. Fig. 9 shows how an alpha helix is formed. The NH and CO groups form hydrogen bonds between them in a regular pattern, and this creates the particular conformation of the chain that is of helical shape. The backbone of the chain is shown as dark rods and is comprised of a repeating segment of two carbon and one nitrogen atoms. In
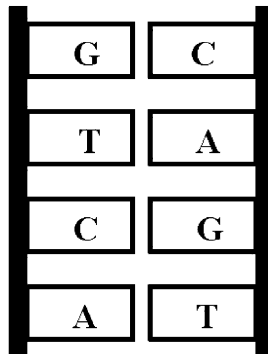
Fig. 8. Arrangement of four nucleosides (Adenine, Cytosine, Thymine, Guanine) and the hydrogen-bonding (A to T, C to G) across chain in DNA.
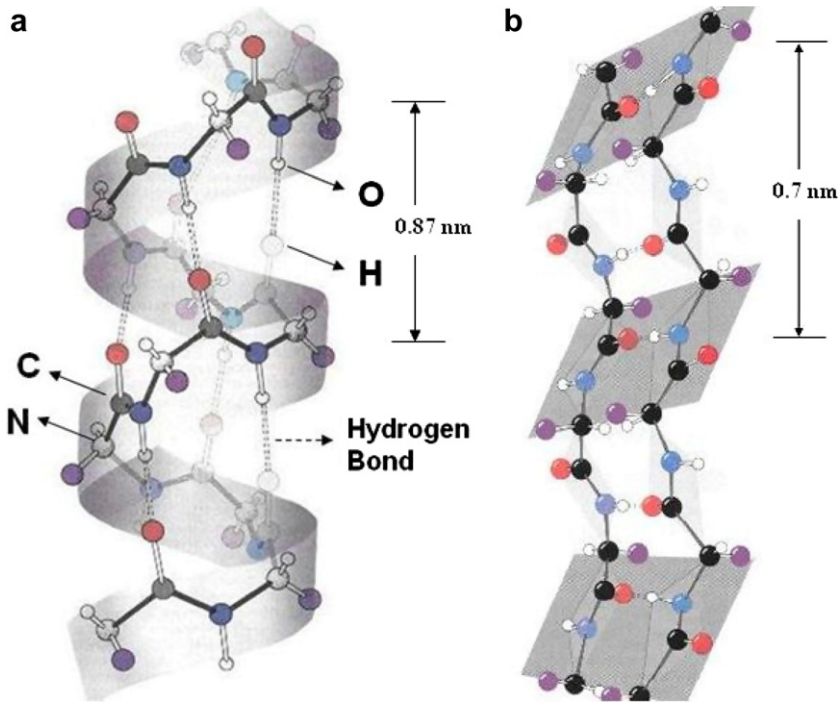
Fig. 9. (a) Structure of alpha helix; dotted double lines indicate hydrogen bonds; (b) structure of beta sheet with two anti-parallel polypeptide chains connected by hydrogen bonds (double dotted lines) (from Lodish et al. [56]).
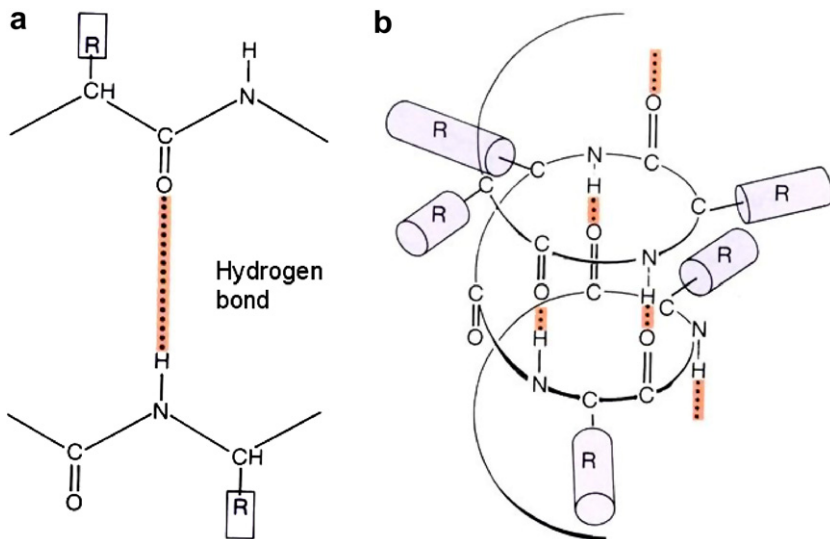
Fig. 10. (a) Hydrogen bond connecting a CO to a NH group in a polypeptide; (b) successive hydrogen bonds on same polypeptide chain leading to formation of a helical arrangement (From Human Physiology 8th edition by Vander et al. [57, Fig. 2.18, p. 29]).

Fig. 9b several hydrogen bonds are shown, causing the polypeptide chain to fold. The radicals stick out. Another common conformation of polypeptide chains is the beta sheet. In this conformation, separate chains are bonded. Fig. 9 shows two anti-parallel chains that are connected by hydrogen bonds (shown, again, by double dashed lines). We can see that the radicals (large grey balls) of two adjacent chains stick out of the sheet plane on opposite sides. Successive chains can bond in such a fashion, creating pleated sheets. Fig. 10 shows the hydrogen bond and the α helix in greater detail. It is the hydrogen bonds that give the helical conformation to the chain, as well as the connection between the adjacent chains in the β sheet. This is shown in a clear fashion in Fig. 10a. The hydrogen bonds are indicated by double dashed lines.

The three main fiber-forming polymers in the nature are

- Polypeptide chains, which are the building blocks for collagen, elastin, silks, and keratins.
- Polysaccharides, the building blocks for cellulose and hemicellulose.
- Hybrid polypeptide–polysaccharide chains, the building blocks for chitin.

Polysaccharides will be discussed in Section 5.4.

5.2. Biominerals

One of the defining features of the rigid biological systems that comprise a significant fraction of the structural biological materials is the existence of two components: a mineral
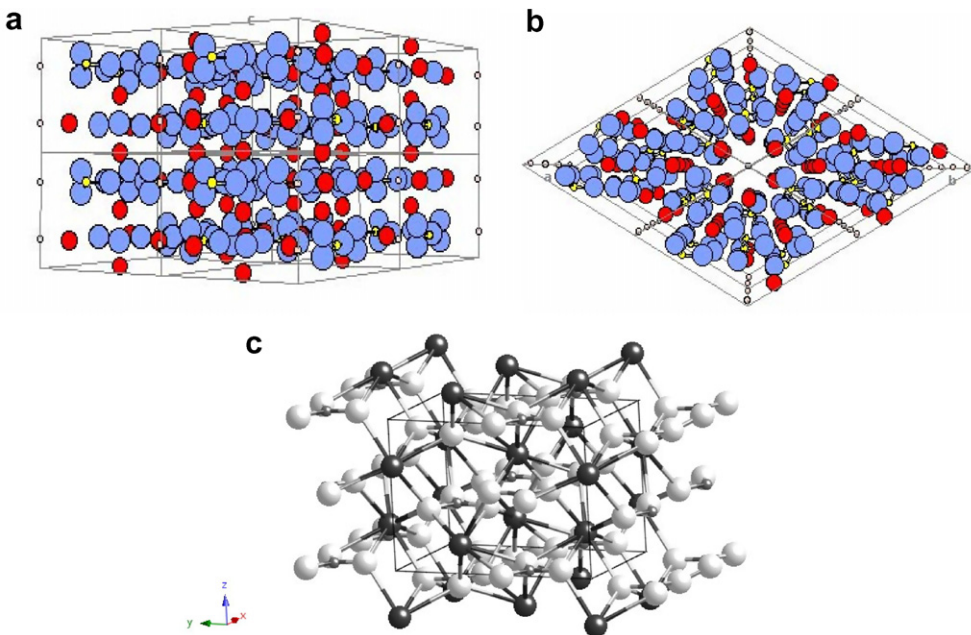
Fig. 11. (a) Atomic structure of hydroxyapatite; smallest white atoms: P; largest gray atoms: O; medium black atoms: Ca (b) atomic structure of aragonite; large dark atoms: Ca; small gray atoms: C; large white atoms: O.

Table 5
Principal components of common structural biological composites

Biological composite	Mineral					Organic				
	Calcium carbonate	Calcium phosphate	Silica	Hydroxyapatite	Other	Keratin	Collagen	Chitin	Cellulose	Other
Shells	X									X
Horns		X				X				
Bones				X			X			
Teeth				X						X
Bird Beaks		X				X				
Crustacean Exoskeleton	X							X		X
Insect Cuticle								X		X
Woods									X	
Spicules			X							X

and an organic component. The intercalation of these components occurs at the nano, micro, or mesoscale and often takes place at more than one-dimensional scale. Table 5 exemplifies this, for a number of systems. The mineral component provides the strength whereas the organic component contributes to the ductility. This combination of strength and ductility leads to high energy absorption prior to failure. The most common mineral components are calcium carbonate, calcium phosphate (hydroxyapatite), and amorphous silica, although over 20 minerals (with principal elements being Ca, Mg, Si, Fe, Mn, P, S, C, and the light elements H and O) have been identified. These minerals are embedded in complex assemblages of organic macromolecules which are on their turn, hierarchically organized. The best known are keratin, collagen, and chitin.

Table 6 shows the minerals that have been identified in biological systems [58]. The number of minerals is continuously increasing.

Table 6
Principal minerals found in biological systems (from Weiner and Addadi [58])

Carbonates	Calcite	Amorphous calcium carbonate family
	Aragonite	Hydrocerrusote
	Vaterite	Protodolomite
	Monohydrocalcite	
Phosphates	Carbonated apatite (dahllite)	Brushite
	Francolite	Amorphous calcium phosphate family
	Octacalcium phosphate	Vivianite
	Whitlockite	Amorphous pyrophosphate
	Struvite	
Halides	Fluorite	Amorphous fluorite
	Hieratite	Atacamite
Sulfates	Gypsum	Jarosite
	Celestite	Calcium sulfate hemihydrate
	Barite	
Silicates	Silica (opal)	
Oxides and hydroxides	Magnetite	Amorphous manganese oxide
	Goethite	Amorphous ilmenite
	Lepidocrocite	Todotokite
	Ferrihydrite	Birnessite
	Amorphous iron oxide	
Sulfides	Pyrite	Galena
	Amorphous pyrrhotite	Greigite
	Hydrotroilite	Mackinawite
	Shalerite	Wurtzite
Native element	Sulfur	
"Organic Minerals"	Whewellite	Uric acid
	Weddelite	Paraffin hydrocarbon
	Manganese oxalate	Wax
	Calcium tartrate	Magnesium oxalate (glushinskite)
	Calcium malate	Copper oxalate (moolooite)
	Earlandite	Ferric oxalate anhydrous
	Guanine	Sodium urate

Fig. 11a shows the atomic arrangement of the calcium, phosphorus, and oxygen atoms in hydroxyapatite. The unit cell is quite complex and consists of four primitive hexagonal cells juxtaposed (top view). We should remember that the hexagonal cell is composed of three primitive cells, brought together at their 120^0 angles ($3 \times 120° = 360°$). In the case of the hydroxyapatite unit cell, there are four unit cells: two at the 60° angle and two at the 120° ($2 \times 60° + 2 \times 120° = 360°$).

Fig. 11b shows the aragonitic form of calcium carbonate. Aragonite has the orthorhombic structure. However, it is important to recognize that the minerals do not occur in isolation in living organisms. They are invariably intimately connected with organic materials, forming complex hierarchically structured composites. The resulting composite has mechanical properties that far surpass those of the monolithic minerals. Although we think of bone as a cellular mineral, it is actually composed of 60% collagen and 30–40% hydroxyapatite (on a volume basis). If the mineral is dissolved away, the entire collagen framework is retained.

5.2.1. Biomineralization

Organic molecules in solution can influence the morphology and orientation of inorganic crystals if there is molecular complementarity at the crystal-additive interface. Phase transformations are believed to occur by surface dissolution of precursors which mediate the free energies of activation of interconversions. Yet these principles are yet to be well developed. Understanding the process in which living organisms control the growth and structure of inorganic materials could lead to significant advances in Materials Science, opening the door to novel synthesis techniques for nano scale composites. Mann [31] states that in order to address the question of nanoscale biologically-induced phase transformations and crystallographic control we must study the bonding and reactivity of extended organized structures under the mediation of organic chemistry. We examine two important processes: nucleation and morphology.

5.2.2. Nucleation

The control of nucleation of inorganic materials in nature is achieved by the effect of activation energy dependency on organic substrate composition. Inorganic precipitation is controlled by the kinetic constraints of nucleation. Mann [31] states that this activation energy may also depend on the two-dimensional structure of different crystal faces, indicating that there is a variation in complementarity of various crystal faces and the organic substrate. Weissbuch et al. [59] describe the auxiliary molecules which promote or inhibit crystal nucleation depending on their composition.

5.2.3. Morphology

The morphology of the inorganic material created in nucleation is controlled through the interaction with the organic matrix. Activation energies can be influenced in the presence of an organic matrix in three possible ways. Fig. 12 describes the possibilities of polymorphic nucleation [31]. The activation energies of two non-specific polymorphs, "A" and "B", are shown in the presence (state 2) and absence (state 1) of the organic matrix. If "A" is more kinetically favored in the absence of the organic matrix then it is possible to examine the possibilities of organic effect on the activation free energy ($\Delta G^{\#}$) of various polymorphs with respect to each other. In the first case both polymorphs are affected equally,
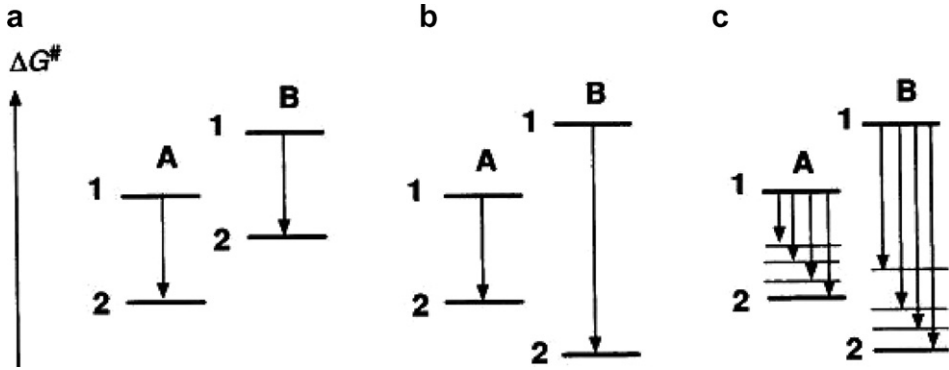
Fig. 12. Structural control by organic matrix-mediated nucleation. (a) Promotion of non-specific nucleation in which both polymorphs have the activation energies reduced by the same amount; (b) promotion of structure-specific nucleation of polymorph B due to more favorable crystallographic recognition at the matrix surface; (c) promotion of a sequence of structurally non-specific to highly specific nucleation (from Mann [7, p. 110, Fig. 6.29]).

thus "A" remains kinetically favorable. In the second case the effect on the "B" polymorph is much larger than for "A" and thus, when in the presence of the organic matrix,
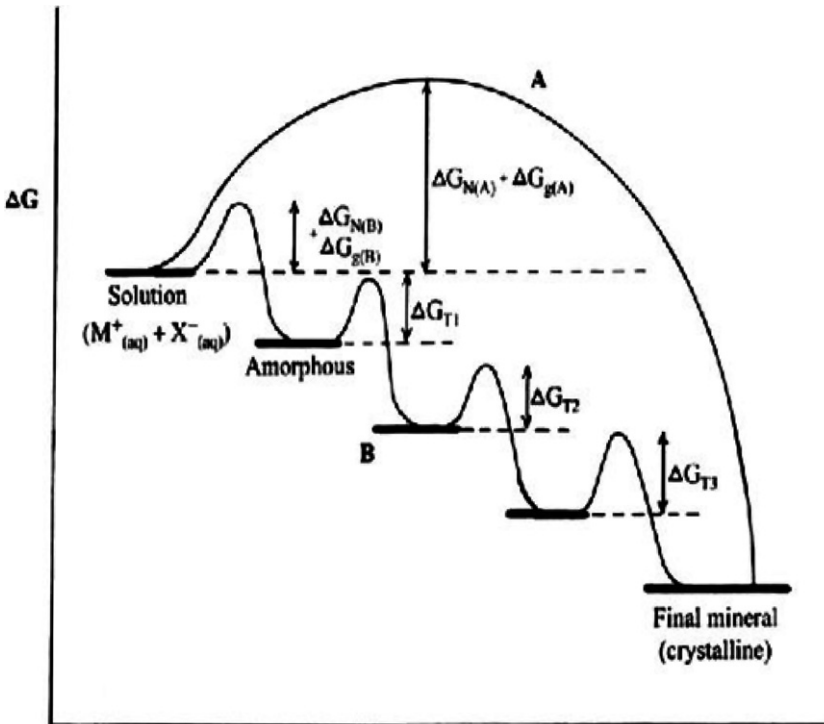

Fig. 13. Representation of activation energies of nucleation in the presence and absence of an organic matrix for two non-specific polymorphs (from Mann [7, p. 60, Fig. 4.25]).

"B" is kinetically favorable. In the last case we see a combination of the two earlier cases, in which the kinetic favorability of the two polymorphs is influenced by genetic, metabolic, and environmental processes.

The selection of the polymorph will also be determined by the transformation sequence. This starts, in Fig. 13, with an amorphous mineral and continues through a series of intermediate structures that have the same composition but decreasing free energy (increasing thermodynamic stability [31,60]). This cascade is shown in Fig. 13. The system will either follow the one step route (A) or travel along a sequential transformation route (B) depending on the activation energies of nucleation, growth, and transformation. Addadi et al. [61–63] proposed that the role of the solid-state amorphous precursor phase could be fundamental in the biomineralization process.

The composition of the complex structure in nacre and other biocomposites is mediated by the phase transformations which occur by surface dissolution of the precursor. The phase transformation is dictated by the solubility of amorphous precursor into the crystalline intermediates, and the effect of these precursors on the free energies of activation of these interconversions. Thus an animal which is able to control its emission of molecular precursor (organic matrix, or soluble protein) will be able to control the growth and structure of its inorganic biocomposite. Addadi and Weiner [61] and Addadi et al. [62,63] demonstrated the stereoselective adsorption of proteins in the growth of calcite crystals resulting in a slowing down of growth in the *c* direction and altering the final shape of the crystal. This evidence of the influence of organics on inorganic crystal growth led them to examine the influence of proteins on the morphology of crystal growth.

Belcher et al. [64] showed that a controlled phase transition between aragonite and calcite in nacre could be obtained in the laboratory with the use of soluble polyanionic proteins. They showed that biological phase transformation did not require the deposition of an intervening protein sheet, but simply the presence of soluble proteins. This was directly observed by Hansma et al. [65] through atomic force microscopy. Mann et al. [60] explained the role of soluble proteins as effective agents to the reduction of interfacial energies on the surface of the inorganic. An increase in hydrophobicity of the additive reduces its ability to control morphology and phase transition during crystallization. The effectiveness of the soluble proteins in the process of morphology control depends on their interaction with crystal surfaces in a way which is identical to that of an organic matrix (protein sheet). Thus, the effect of the protein sheet is the control of crystal orientation with respect to bonding energies of specific crystal phases.
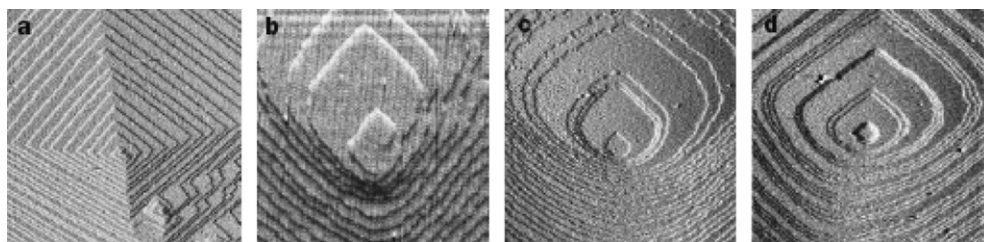

Fig. 14. AFM images showing; (a) pure calcite growth hillock. (b–d) Growth hillocks after the addition of supersaturated solutions of (b) glycine, an achiral amino acid, (c and d) aspartic acid enantiomers (from Orme et al. [66, p. 776, Fig. 1]).

Orme et al. [66,67] reported a dependency of calcite growth morphology on the selective binding of amino acids on the crystal step-edges. Through in situ atomic force microscopy they were able to show that in solution amino acids bind to geometric and chemically favored step-edges, changing the free energy of the step-edge. Fig. 14a shows the AFM image of pure calcite growth hillocks. When a supersaturated solution of glycine is introduced into the growth solution, it can be observed in Fig. 14b that the two acute steps become curved. By modifying the free energy of step-edges, preferential attachment of calcium ions onto specific locations can be controlled, thus resulting in macroscopic crystal shape manipulation. Similar results were obtained following the addition of aspartic acid enantiomers, Fig. 14c and d. The importance of this observation is the verification of such theories as those proposed by Mann et al. [60], proving that the addition of various organic growth modifiers can change the rate and location in which calcite attaches onto surfaces. In essence, this is an in situ observation of nature's hand laying the bricks of self-organization and biomineralization.

5.3. Proteins (polypeptides)

The principal organic building blocks in living organisms are the proteins. The word comes from Greek (Proteios) which means ''of first rank'' and indeed proteins play a key role in most physiological processes. The soft tissues in the mammalian body are made of proteins. They are also an important component of biominerals.

5.3.1. Collagen

Collagen is a rather stiff and hard protein. It is a basic structural material for soft and hard bodies. It is present in different organs and tissues and provides structural integrity. Fung [24] compares it to steel in structures, not because of its strength, but because it is a basic structural component in our body. Steel is the principal load carrying component in structures. In living organisms, collagen plays the same role: it is the main load carrying component of blood vessels, tendons, bone, muscle, etc. In rats, 20% of the proteins are collagen. Humans are similar to rats in physiology and behavior, and the same proportion should apply. Approximately 20 types of amino acid compositions of collagen have been identified and their number is continuously increasing. In humans (and rats) the collagen is the same, called Type I collagen. Other collagens are named II, X, etc. The amino acid composition of different collagens differs slightly. This composition gives rise to the different types. Table 7 [68] provides a few illustrative examples.

Fig. 15 shows the structure of collagen. It is a triple helix, each strand being made up of sequences of amino acids. Each strand is itself a left-handed α helix with approximately 0.87 nm per turn. The triple helix has a right-handed twist with a period of 8.6 nm. The dots shown in a strand in Fig. 15 represent glycine and different amino acids. Fiber forming collagens organize themselves into fibrils. Fig. 16 is a transmission electron micrograph of tendon fibrils [69]. Each fibril has transverse striations, which are spaced approximately 67 nm apart. These striations are due to the staggering of the individual collagen molecules. The length of each collagen molecule is approximately 300 nm, which is about 4.4 times the distance of stagger, 67 nm. The gap between adjacent chains is about 35 nm ($67 \times 5 - 300 = 35$) and the overlap is about 32 nm ($300 - 67 \times 4 = 32$). Thus, there is a periodicity in the structure, shown on the right hand side in Fig. 17b. Each repeating unit is comprised of five segments and this periodicity produces a characteristic interference

Table 7
Amino acid composition from several collagens (Adapted from Ehrlich and Worch [68])

| Collagen sources	Amino acid (%)																	
	Asp	Thr	Ser	Glx	Pro	HyPr	Gly	Ala	Val	Met	Ile	Leu	Tyr	Phe	His	HyLys	Lys	Arg
Sturgeon swim-bladder	6.9	3.8	5.8	11.4	12.8	11.8	27.7	11.6	2.3	1.4	1.7	2.6	0.5	2.5	0.8	1.9	3.5	10.0
Shark	6.4	2.4	3.3	11.0	13.3	8.8	25.4	11.4	2.7	1.8	2.7	2.6	7.2	2.1	1.7	0.9	3.7	8.6
Femur of ox	4.3	1.9	3.5	6.5	11.8	10.3	31.7	10.8	2.4	0.5	1.3	3.0	0.7	1.9	0.6	0.8	3.0	5.0
Porcine skin	5.1	1.7	3.5	11.4	13.3	12.6	22.1	8.7	2.1	0.5	1.1	2.9	0.5	1.9	0.7	–	3.5	8.4
Human tendon	3.9	1.5	3.0	9.5	10.3	7.5	26.4	9.0	2.1	0.5	0.9	2.1	0.3	1.2	1.4	1.5	3.5	16.0
Human bone	3.8	1.5	2.9	9.0	10.1	8.2	26.2	9.3	1.9	0.4	1.1	2.1	0.4	1.2	1.4	0.6	4.6	15.4
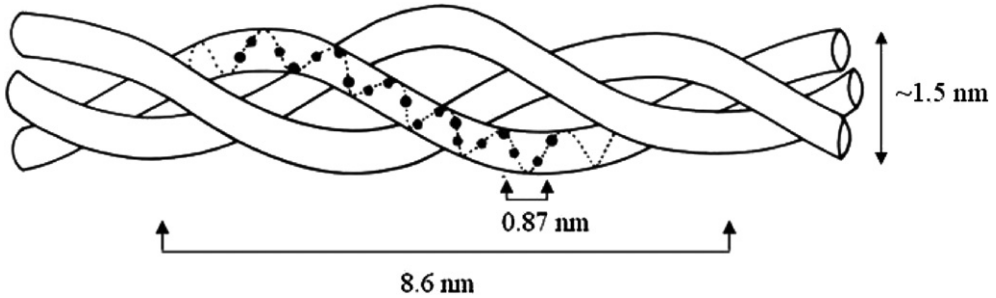
Fig. 15. Triple helix structure of collagen (adapted from Fung [24, p. 248, Fig. 7.3.1]).
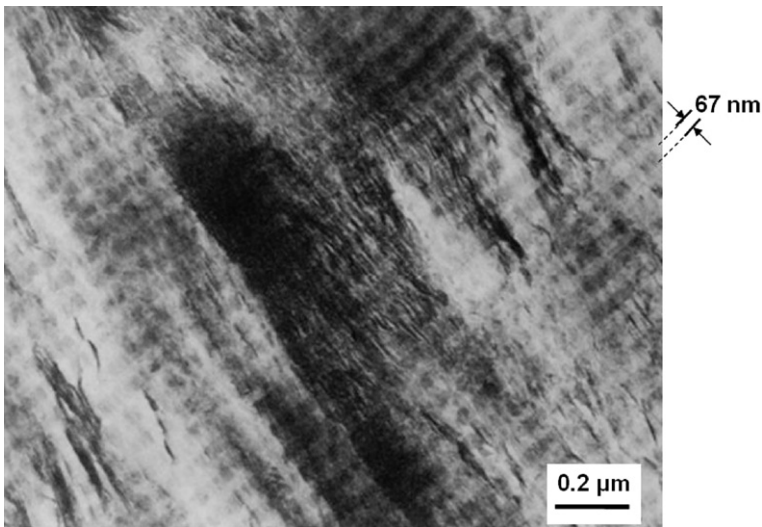

Fig. 16. Transmission electron micrograph of tendon fibrils (from Traub et al. [69, p. 9819, Fig. 4]).

pattern that is observed as bands in electron microscopy, and is shown in Fig. 17c. The collagen chains are directional, i.e., they have a "head" and a "tail", and the staggered arrangement allows for bonding between the "head" of one chain and the "tail" of the adjacent one, as shown in Fig. 17b.

The collagen molecules, with a diameter of ∼1.5 nm, form fibrils with diameter of ∼50 nm. The molecules attach to the adjacent molecules by intrafibrillar bonding. These fibrils form fibers, with diameter of ∼1 μm. This is mediated by proteoglycans. Microfibrils, in turn, arrange themselves into fibrils, which are organized into fibers. Fibers are bundles of fibrils with diameters between 0.2 and 12 μm. In tendon, these fibers can be as long as the entire tendon. In tendons and ligaments, the collagen fibers form primarily one-dimensional networks. In skin, blood vessels, intestinal mucosa and the female vaginal tract, the fibers organize themselves into more complex patterns leading to two- and three-dimensional networks.
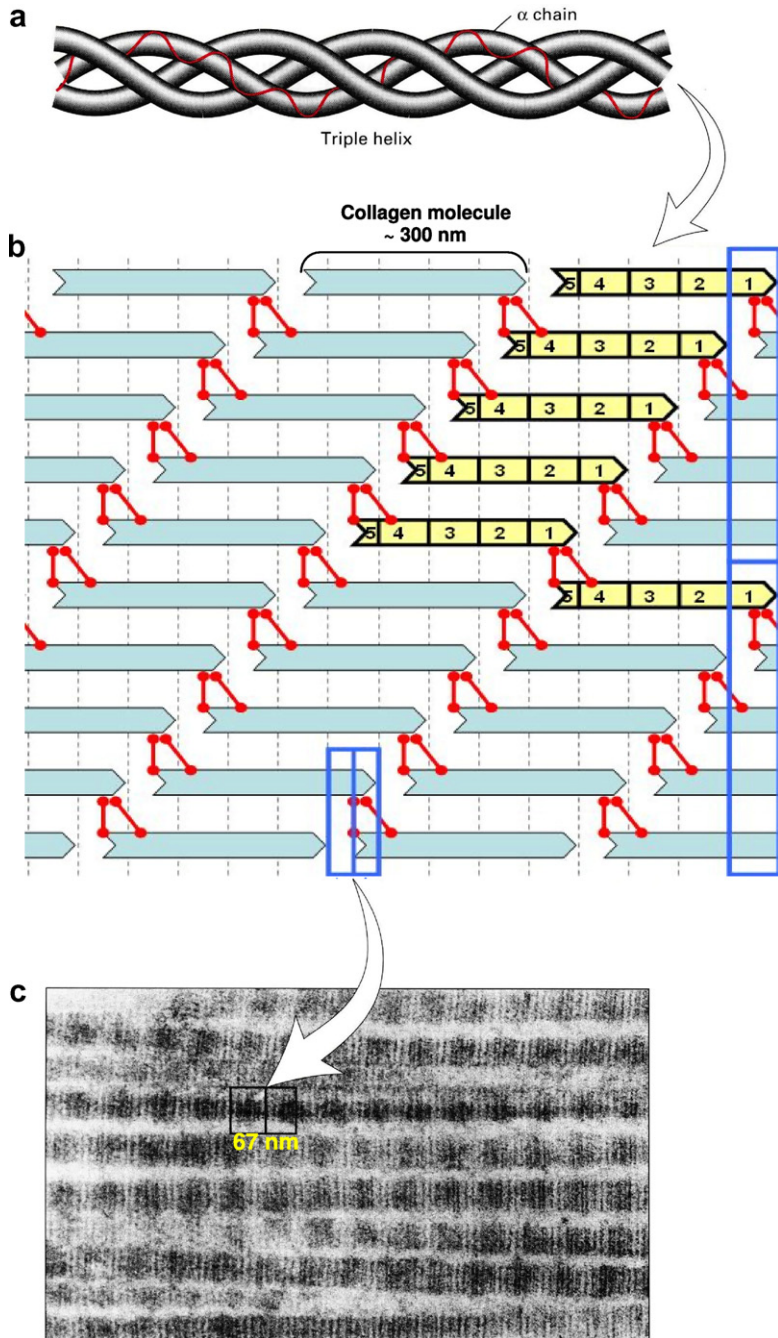
Fig. 17. Collagen-composed triple helix, forming microfibrils which have 67 nm gaps; (a) general scheme; (b) representation of 300 nm segments with gaps and overlaps (c) electron micrograph (from Lodish et al. [56, Fig. 22-11]).
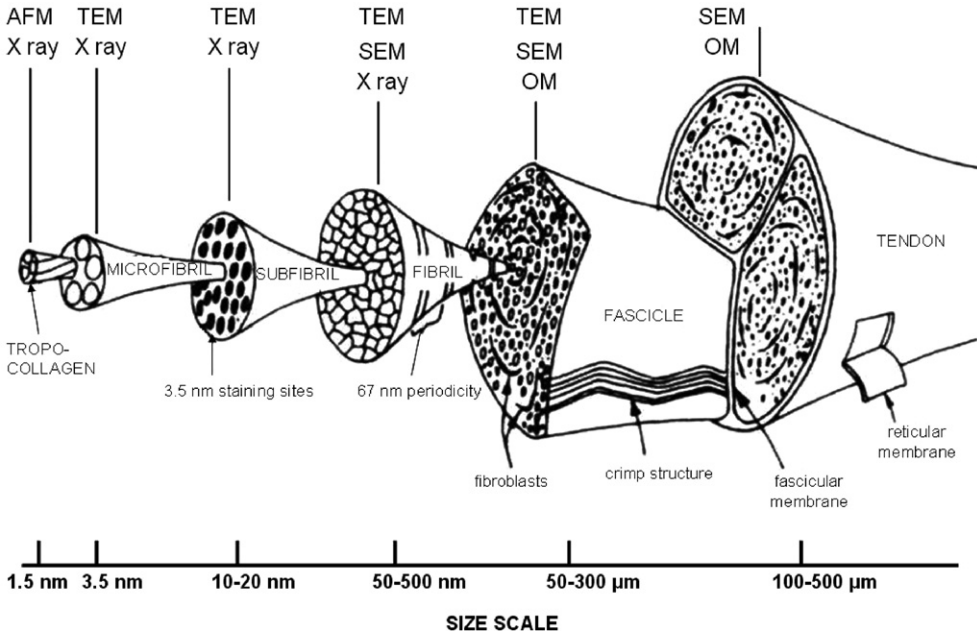
Fig. 18. Hierarchical structure of tendon starting with collagen molecules and techniques used to identify it (from Baer et al. [70, p. 60]).

Fig. 18 [70] shows the hierarchical organization of a tendon, starting with tropocollagen (a form of collagen), and moving up, in length scale, to fascicles. There is a crimped or wavy structure shown in the fascicles that has an important bearing on the mechanical properties. Fig. 19 shows an idealized representation of a wavy fiber. Two parameters define it: the wavelength $2l_0$ and the angle θ_0. Typical values for the Achilles tendon of a mature human are $l_0 = 20$–$50\ \mu m$ and $\theta_0 = 6$–$8°$. These bent collagen fibers stretch out in tension. When the load is removed, the waviness returns. When the tendon is stretched beyond the straightening of the waviness, damage starts to occur. Fig. 20a shows a schematic stress–strain curve for tendon. The tendon was stretched until rupture. There are essentially three stages:
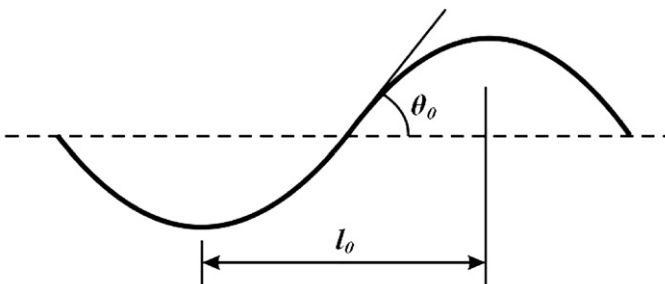

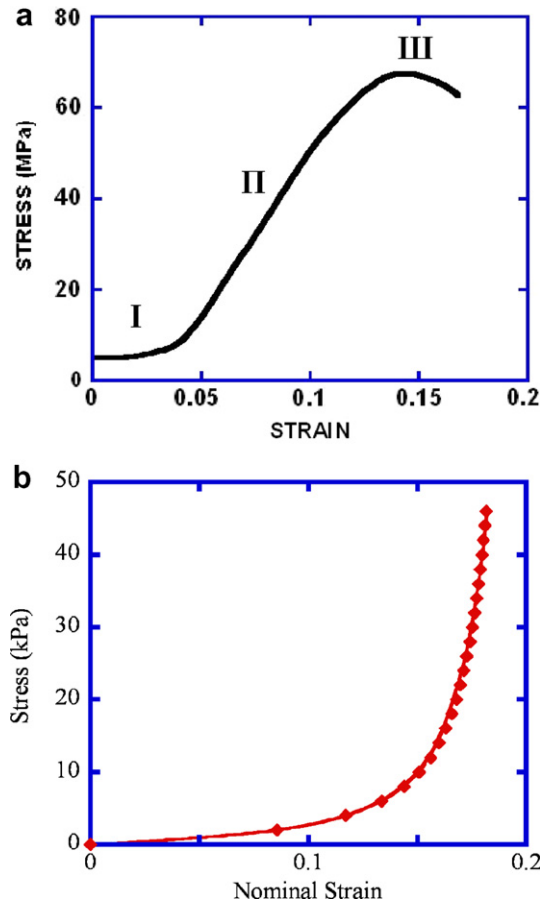Fig. 19. Idealized configuration of a wavy collagen fiber.

Fig. 20. (a) Stress–strain curve of collagen with three characteristic stages; I: Toe; II: linear elastic; III: failure. (b) Stress–strain curve for ventricular papillary muscle, composed of titin and collagen (courtesy of A. Jukiel, Dept. of Bioengineering, UCSD [99]).

Region I: toe part, in which the slope rises rapidly. This is the physiological range in which the tendon operates under normal conditions.

Region II: linear part, with a constant slope.

Region III: slope decreases with strain and leads to failure.

The elastic modulus of collagen is approximately 1–1.5 GPa and the maximum strain is in the 10–20% range. The maximum strength is approximately 70–150 MPa. Cross-linking increases with age, and collagen becomes less flexible. Collagen often exists in combination with other proteins. An example is the ventricular papillary muscle. Fig. 20b shows the stress–strain curve. The passive tension in the cardiac muscle is governed by two-load bearing elements in the heart, collagen and titin. Titin has a spring-like region within the I-band of the sarcomere units (seen Section 5.3.3). As the sarcomere units are extended, passive tension increases. At lower strains titin determines most of the passive tension in the heart. At higher strains, collagen begins to straighten and align with the axis

of force and hence it contributes increasingly to the passive tension. Fig. 20b shows the characteristic toe region followed by a linear response.

It is possible to determine the maximum strain that the collagen fibers can experience without damage if their shape is as given in Fig. 19 with a ratio between amplitude and wavelength of r. We can assume a sine function of the form:

$$y = k \sin 2\pi x/\lambda \tag{4}$$

The maximum of y is reached when $x = \lambda/4$.

The relationship between θ_0, l_0, and the amplitude of the sine function is:

$$\frac{dy}{dx} = \frac{2k\pi}{\lambda} \cos \frac{2\pi x}{\lambda} \tag{5}$$

For $x = 0$

$$\tan \theta_0 = \left.\frac{dy}{dx}\right|_{x=0} = \frac{2k\pi}{\lambda} \tag{6}$$

Hence

$$y_{\max} = \frac{l_0}{\pi} \tan \theta_0 \tag{7}$$

We can integrate over the length of the sine wave from 0 to 2π. However, this will lead to an elliptical integral of difficult solution. A simple approximation is to consider the shape of the wavy protein as an ellipse with major axis $2a$ and minor axis $2b$. The circumference is given by the approximate expression:

$$L \approx \pi \left[\frac{3}{2}(a + b) - (ab)^{1/2} \right] \tag{8}$$

In the sine function, we have two arms, one positive and one negative. Their sum corresponds, in an approximate manner, to the circumference of the ellipse.

The strain is equal to

$$\varepsilon = \frac{L - 4a}{4a} = \frac{\pi \left[\frac{3}{2}(a + b) - (ab)^{1/2} \right] - 4a}{4a} \tag{9}$$

Thus

$$\varepsilon = \frac{\pi}{4} \left[\frac{3}{2}\left(1 + \frac{b}{a}\right) - \left(\frac{b}{a}\right)^{1/2} \right] - 1 \tag{10}$$

The following ratio is defined: $\frac{b}{a} = 2r$.

The corresponding strain is

$$\varepsilon = \frac{\pi}{4} \left[\frac{3}{2}(1 + 2r) - (2r)^{1/2} \right] - 1 \tag{11}$$

Beyond this strain, the collagen will undergo bond stretching and eventually break.

The mechanical properties of collagen connective tissue are dictated, to a large extent, by the structure of the constituent collagen, which can form networks that are one-, two-, or three-dimensional. In the case of planar soft tissues, the deformation is complex. An

example of this is the pericardium, which is a double-walled sac that contains the heart. It has a crimped collagen structure shown in Fig. 21a. The crimp period of $\sim$30 μm and the amplitude of $\sim$15 μm were estimated by Liao et al. [71]. Synchroton small angle X-ray scattering (SAXS) was used to follow the molecular D spacing (the 67 nm periodicity) of the collagen as a function of imposed stretching. The results are shown in Fig. 21b. Using Eq. (11) one can estimate the total nominal strain required to completely uncrimp and straighten the collagen structure shown in Fig. 21a. The ratio $2r$ is

$$2r = \frac{b}{a} = \frac{15}{30} = 0.5 \tag{12}$$

The corresponding maximum nominal strain is

$$\varepsilon = 0.22$$

This is slightly higher than the strain at which molecular bond stretching is initiated in Fig. 21b. Up to 0.2, the strains in the fibrils are negligible. Beyond this strain, the molecules stretch. However, not all external strain is accommodated by molecular bond
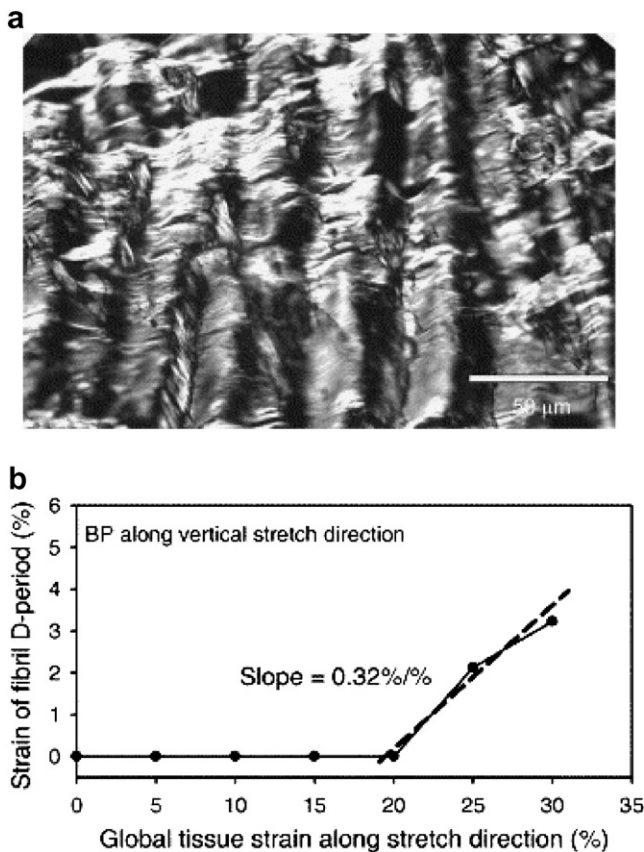

Fig. 21. (a) Crimped collagen structure in bovine pericardium crimp period $\sim$30 μm and amplitude $\sim$15 μm; (b) molecular strain (as determined from change in D period) as a function of externally applied extension for bovine pericardium collagen (from Liao et al. [71, Figs. 9 and 4(a), pp. 51, 49]).
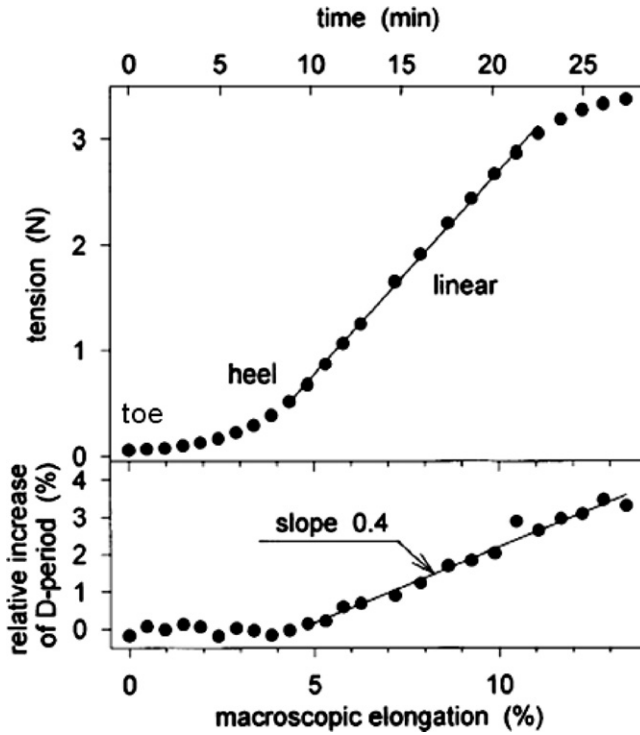
Fig. 22. Top: tension; and bottom: molecular strain (as determined from change in D period) as a function of externally applied extension for rat tail collagen (from Fratzl et al. [72, Fig. 3, p. 122]).

stretching (the increase from 67 nm). Otherwise, the slope in the second stage would be equal to 1. One can speculate that part of the strain is accommodated by residual uncrimping of the structure (the last 0.02) and part by interfibril shear.

Another example illustrating the power of synchrotron X-ray scattering are the results by Fratzl et al. [72] on rat tail tendon. They are shown in Fig. 22. The mechanical tensile force is also plotted. The toe and linear portions of the collagen response are clearly seen. In the bottom portion of the figure, the change in length in the molecular repeat length is shown. The D repeat unit length is constant until a strain of 0.05. This indicates that the rat tendon is stiffer than the bovine pericardium. This is consistent with the parameters in the sine function reported by Fung [25] for the rat tail tendon:

$$l_0 = 100 \ \mu m$$
$$\theta_0 = 12°$$

The corresponding parameters in Eq. (10) are $a = 100 \ \mu m$ and $b = 6.75 \ \mu m$. The maximum nominal strain calculated from Eq. (11) is 0.13. In Fig. 22, the molecular stretching of bonds starts for a strain of 0.05. The slope of the linear portion of the curve is equal to 0.4, indicating that one has concomitant molecular bond stretching, uncrimping of the structure, and possibly shear between fibrils or fibers beyond this point. These results corroborate the bovine pericardium results in Fig. 21b.

The stress–strain response of collagen can be represented mathematically and indeed Fung [24] proposed the following expression for the toe region:

$$\sigma = C\left(e^{\alpha\lambda} - e^{\alpha}\right) = C(e^{\alpha\varepsilon} - 1) \tag{13}$$

where C and α are parameters and λ is the stretch ratio ($=\varepsilon + 1$). This equation was also used by Sacks [73]. Another expression is the Mooney–Rivlin [74,75] equation for rubbers, both the toe and linear regions can be described by

$$\sigma = C_1\left(1 + \mu\frac{1}{\lambda}\right)\left(\lambda^2 + \frac{1}{\lambda}\right)\frac{1}{\lambda} \tag{14}$$

where the parameter μ has one value for the toe region and is equal to zero in the linear region. Collagen is also viscoelastic and therefore a relaxation function has to be added to the constitutive description.

5.3.2. Keratin

Keratin is a structural protein that is found in most vertebrate animals. It is a fibrous protein that is produced in the integument (outer covering) of organisms and is typified by sulfur content. The integument provides the protective layer of animals and consists of two structural entities: the dermis and epidermis. The dermis lies underneath the epidermis and is made of mainly elastin and collagen. The epidermis is the outer layer, produced by the dermis, and is made from epidermal cells. Keratin is produced by the keratinization process where epidermal cells die and build up at the outermost layer. It is usually classified as soft and hard originating from different mechanisms of biosynthesis. It is further classified into α- and β-keratin, depending on its molecular structure. α-keratin, commonly known as mammalian keratin, is found in skin, wool, hoof, whale baleen; β-keratin, also known
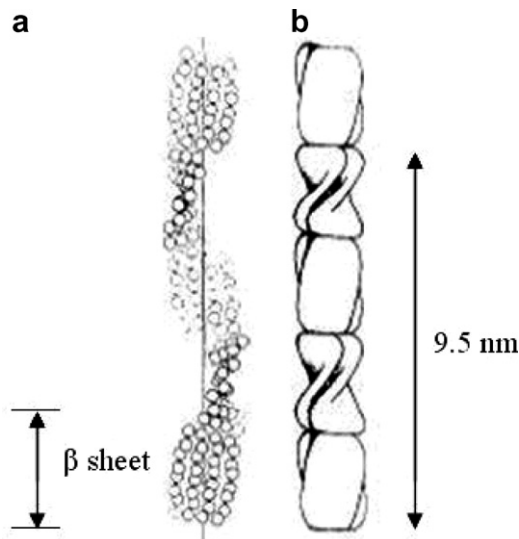

Fig. 23. (a) One of the pair of symmetry-related strands of β-sheets that make up the central framework of the filament. (b) Model for the arrangement of the β-sheet portions of the protein molecules in the filaments of avian keratin (from Fraser and Parry [77, p. 208, Fig. 1]).

as avian and reptilian keratin, is found in claw, scale, feather, and beaks [18,76]. The shell of the toucan beak presented in Section 9.2 is made of β-keratin. A major difference between α-keratin and β-keratin is intermediate filament (IF). The IF of the α-keratin structure is based on α-helix folding pattern. This is a coiled structure similar to collagen (three interwoven helices). These helices combine themselves to form microfibrils with a diameter of 8 nm. Fig. 23 shows the microfibril of β-sheet. The folding pattern of β-keratin is β-sheet [77] and the diameter of β-keratin is 4 nm. The IF of β-keratin has a smaller diameter and the filament has a helical structure with a pitch of 9.5 nm and four turns
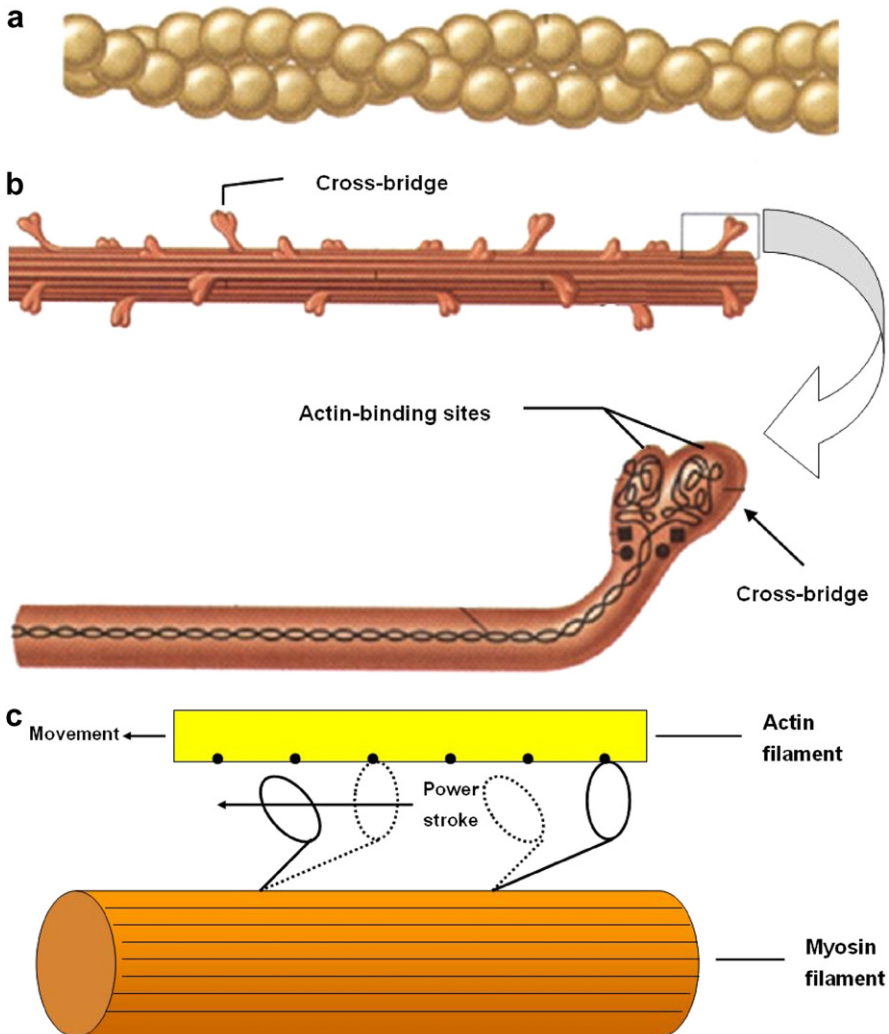

Fig. 24. Molecular structure of (a) actin and (b) myosin; (c) action of cross-bridges when actin filament is moved to left with respect to myosin filament; notice how cross-bridges detach themselves, then reattach themselves to actin.

per unit [77]. Interestingly, it undergoes a phase transformation (α–β transition) under tensile load, which increases its elongation [78].

Keratin is considered as a biological fiber-reinforced composite consisting of a high modulus fiber and a lower modulus viscoelastic matrix. The matrix plays a role as a medium to transfer the applied load to the fiber, thus preventing crack propagation from local imperfections or points of rupture [79]. Mineralization with calcium and other salts contributes to the hardness of keratin [80]. In mammalian keratin, the α-helix is aligned almost parallel to the filament. α-keratin is mechanically linear elastic. While β-keratin is quite different from α-keratin in molecular structure, the β-sheet also behaves linearly elastically and the mechanical behavior is similar. α-keratin changes the structure into the β-keratin during stretching [78]. This change can be observed through X-ray diffraction. Generally, the stiffness of the β-sheet is higher than that of the α-helix. The mechanical behavior of both α-keratin and β-keratin depends on moisture content. Increasing hydration content decreases the stiffness and modulus [77] because the matrix of keratin absorbs moisture. The mechanical properties of keratinous materials and bird feather will be presented in Sections 7.4 and 9.4, respectively.
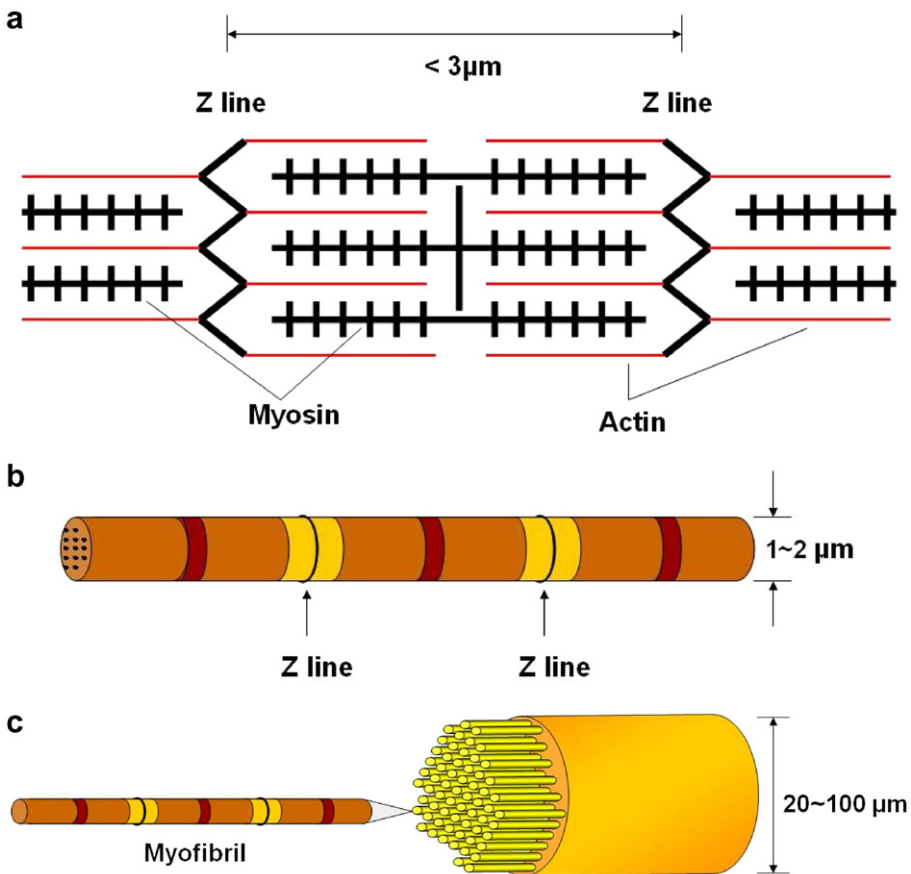

Fig. 25. Structure of muscle, from the (a) sarcomere units, to (b) myofibril, and finally to (c) fibers.

5.3.3. Actin and myosin

These are the principal proteins of muscles, leukocytes, and endothelial cells. Muscles contract and stretch through the controlled gliding/grabbing of the myosin with respect to the actin fibers. Fig. 24a shows an actin fiber. It is composed of two polypeptides in a helical arrangement. Fig. 24b shows the myosin protein. It has little heart-shaped ''grapplers'' called cross-bridges. The tips of the cross-bridges bind and unbind to the actin filaments. Fig. 24c shows the myosin and actin filaments, and the cross-bridges at different positions. The cross-bridges are hinged to the myosin and can attach themselves to different positions along the actin filaments, as the actin is displaced to the left. Thus, the muscles operate by a micro-telescoping action of these two proteins. They form sarcomere units which are actin–myosin arrays in the pattern shown in Fig. 25a.

Fig. 25 shows how the filaments organize themselves into myofibrils. Bundles of myofibrils form a muscle fiber. The Z line represents the periodicity in the myosin–actin units (that are called sarcomeres) and is approximately equal to 3 μm in the stretched configuration (Fig. 25b). It shortens when the muscle is contracted. This gives the muscle a striated pattern when observed at high magnification. They resemble a coral snake in the microscope. Myofibrils have a diameter of approximately 1–2 μm (Fig. 25b). They arrange themselves in bundles with 20–100 μm in diameter, as shown in Fig. 25c.

5.3.4. Elastin

Elastin is one of the most stable and insoluble proteins in the body. The structure of elastin is shown in Fig. 26 [81]. Each fibrous monomer is linked to many others and forms a three-dimensional network. Elastin is found in skin, walls of arteries and veins, and lung tissue. A prominent place is in the *Ligamentum Nuchae*, a long rope that runs along the top
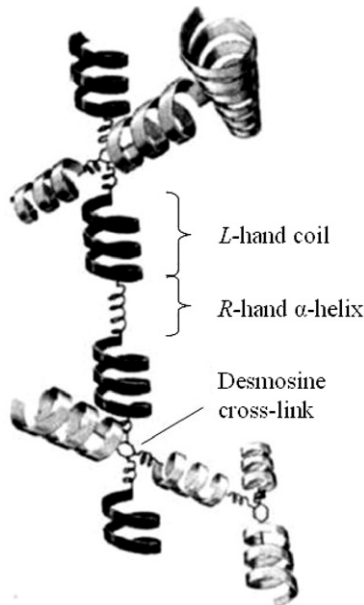

Fig. 26. Molecular model for elastin (from Gray et al. [81, p. 465, Fig. 2]).

of the neck in horses and is constantly under tension. Other vertebrates have it too, but it is less pronounced. In this manner, similar to a cable in a crane, the horse can keep the head up without using muscles. This *Ligamentum Nuchae* plays a role similar to the cables in a suspension bridge. It is a rather robust cylinder, ideally suited for mechanical property measurement. We will present the mechanical properties in Section 7.1.

5.3.5. Resilin and abductin

Resilin is found in arthropods. It has similar properties to elastin, but occurs in a total different animal and has a different structure. When it is dry, it is hard, but can exhibit a strain of up to 3 before failure. This basic resilience is the source of its name. Its elastic modulus in the range of stretch ratio (λ) from 1 to 2 is approximately 1.8 MPa. Insects use resilin as elastic joints for their wings. Fleas and locusts use resilin at the base of their hind legs as catapults in their jumping.

Abductin is the protein found in bivalve (scallop) hinges. Scallops use it to open the valves. Abductin has about the same elastic modulus as resilin.

5.3.6. Other proteins

Proteins are the most abundant biological macromolecules occurring in all cells. Thousands of proteins of different functionality can be found in a single cell. There is a great variety of proteins in biological systems that will not be covered here. Examples of relevance for us are lustrins [82], identified with abalone shell organic layer, and silicatein [83], found in sponge silica spicules.
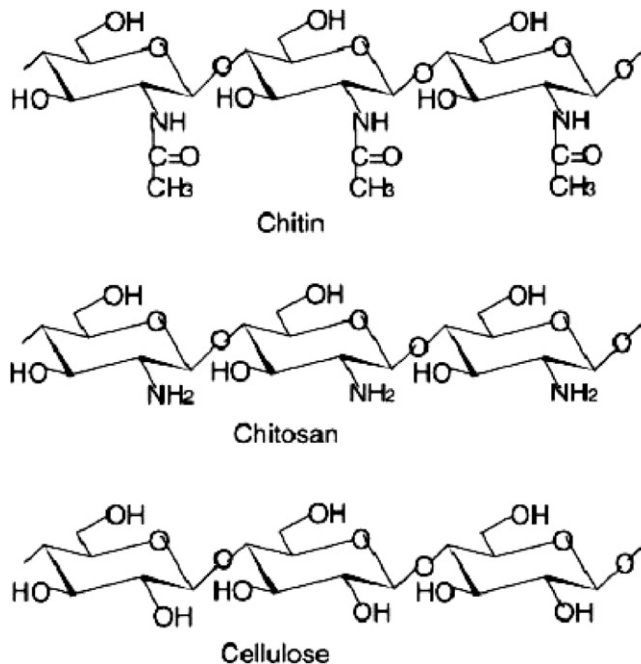

Fig. 27. Chemical structures of chitin, chitosan, and cellulose (from Krajewska [88, Fig. 1]).

5.4. Polysaccharides

5.4.1. Chitin

Chitin is the second most abundant natural polymer (after cellulose) on earth. It is a linear polysaccharide of β-(1-4)-2-acetamido-2-deoxy-D-glucose. The chemical structure of chitin is very similar to that of cellulose with a hydroxyl group replaced by an acetamido group. Pure chitin with 100% acetylation does not exist in nature. Chitin tends to form a co-polymer with its *N*-deacetylated derivative, chitosan. Chitosan is a polymer of β-(1-4)-2-amino-2-deoxy-D-glucose. The chemical structures of cellulose, chitin and chitosan are shown in Fig. 27 [84]. When the fraction of acetamido groups is more than 50% (more commonly 70–90%), the co-polymer is termed chitin. The co-polymer consists of chitin and chitosan units randomly or block distributed through out the polymer chain, as shown in Fig. 28 [85].

Three polymorphic forms of chitin (α-, β-, and γ-chitins) have been differentiated due to their crystal structure as shown in Fig. 29. α-Chitin is arranged in an anti-parallel configuration while β-chitin is organized in a parallel configuration. γ-Chitin is a mixture of α- and β-chitin. α-chitin is the most abundant form found in nature. The anti-parallel
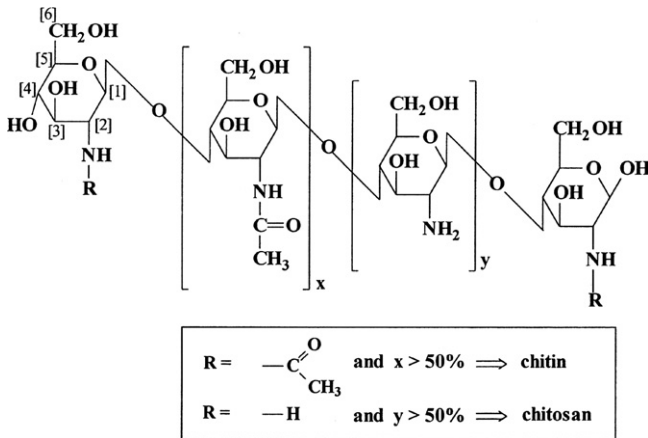

Fig. 28. Chemical structural representation of chitin and chitosan co-polymer (from Kohr [84, p. 3, Fig. 1.2]).
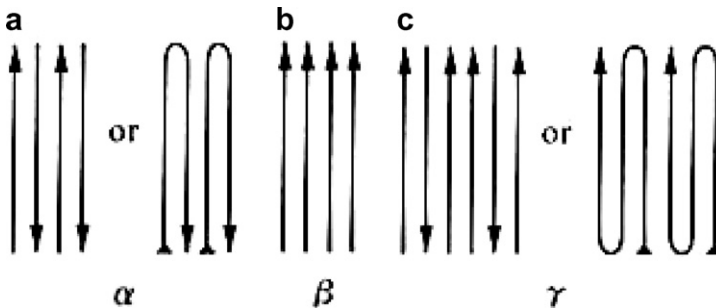

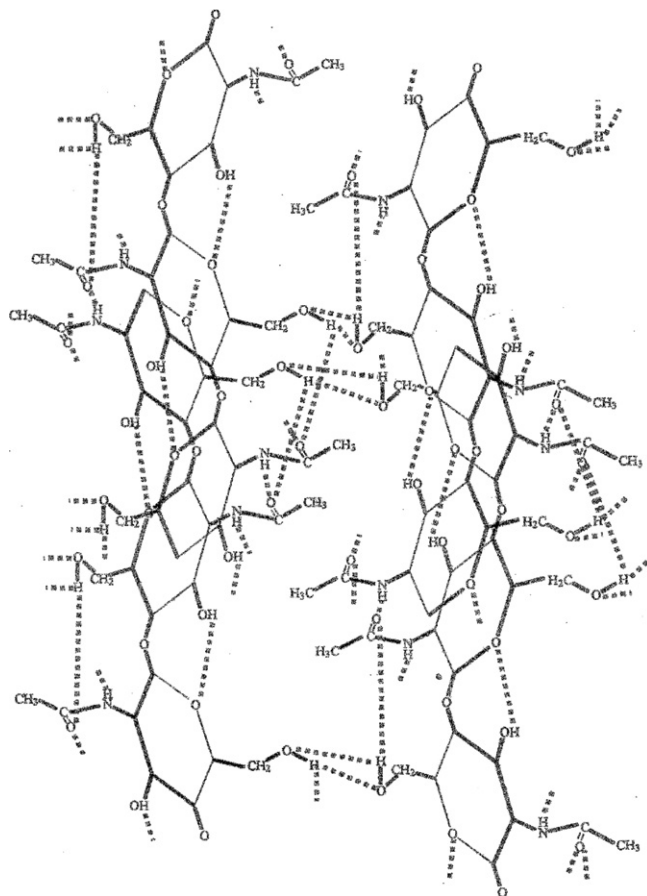Fig. 29. Three polymorphic configurations of chitin. (a) α-chitin (b) β-chitin (c) γ-chitin.

Fig. 30. The extensive hydrogen bonding between α-chitin chains (from Kohr [84, p. 74, Fig. 6.1]).

configuration gives α-chitin a highly ordered crystalline structure with strong hydrogen bonding between chitin chains (Fig. 30). The strong hydrogen bonding leads to the rigid and insoluble properties of α-chitin. Both α-chitin and β-chitin are crystalline. The lattice parameter along the *b*-axis of α-chitin (1.886 nm) is approximately two times that of β-chitin (0.926 nm); while that along the *c*-axis is approximately the same. This can be seen in the electron diffraction patterns (*bc* projection) shown in Fig. 31 [89].

Chitin is widely distributed in fungal and yeast cell walls, mollusk shells, arthropod exoskeletons and other invertebrates. It plays an important role as the structural component that provides support and protection to the organisms.

The cell walls of fungi are made mostly of chitin. Fungal chitin forms randomly oriented microfibrils typically 10–25 nm in diameter and 2–3 μm long. Chitin microfibrils are covalently linked to other polysaccharides, such as glucans, and form a chitin–glucan complex which is the main structural component of fungal cell walls. The chitin content in fungi varies from 0.45% in yeast to 10–40% in some filamentous fungi species.

The presence of chitin has been reported in shells of the mollusk species. Despite the relatively small amount of chitin compared to the inorganic mineral (typically $CaCO_3$),
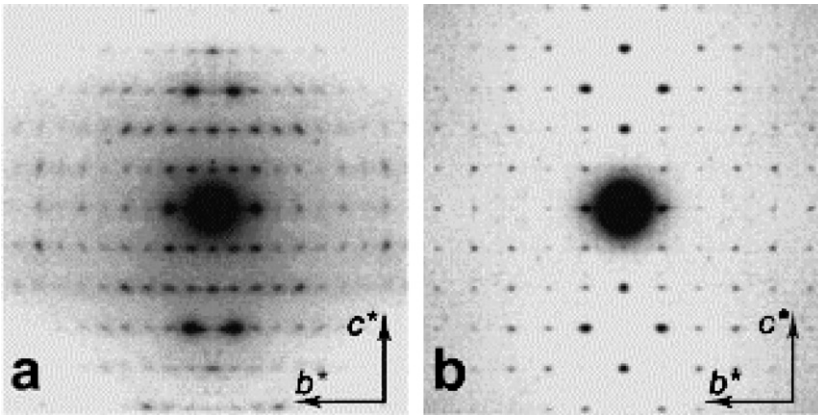
Fig. 31. Electron diffraction patterns of highly crystalline chitin: (a) α-chitin; (b) β-chitin (from Rinaudo [89, p. 605, Fig. 3]).

chitin plays an important role not only in the mechanical support but in the hierarchical control of the biomineralization processes. Studies on the organic matrix in the shell [87,88] revealed that the interlamellar sheets are composed of thin layers of β-chitin sandwiched between two thick layers of silk-like protein gel. The β-chitin is highly ordered at the molecular level and responsible for the overall shell formation. Weiss et al. [87] studied the distribution of chitin in shells of mollusk using chitin-binding green fluorescent protein and confocal laser scanning microscopy. The results showed that bivalve mollusks deposit and orient the chitin in a well defined manner. Chitin distributes mainly in the hinge and edges of the shell and integrates the flexible region connecting two valves.

Chitin is also the main component in the exoskeletons of arthropods. The exoskeleton materials of arthropods are complex composites that are hierarchically structured and multifunctional, as shown in Fig. 5. The linear chitin chains align anti-parallel and form α-chitin crystals at the molecular level. Several of α-chitin crystals which are wrapped by proteins form nanofibrils of about 2–5 nm in diameter and 300 nm in length. A bundle of chitin–protein nanofibrils then form chitin–protein fibers of about 50–100 nm in diameter. These chitin–protein fibers align together forming planar layers which stack up helicoidally. This structure is called a twisted plywood or Bouligand structure [46,47]. In crustaceans, such as crabs and lobsters, there is a high degree of mineralization. The mineral is mostly calcium carbonate, which deposits onto the space of chitin–protein network and gives rigidity to the exoskeleton. The multi-functionality and mechanical properties of arthropod exoskeletons as well as the Bouligand structure are further discussed in Section 7.3.

5.4.2. Cellulose

Cellulose is the most abundant natural polymer, and is the structural component of plant cell walls. It is a linear polysaccharide consisting D-anhydroglucopyranose units (often abbreviated as anhydroglucose units or as glucose units for convenience) linked together by β-(1 → 4)-glycosidic bonds, as shown in Fig. 32 [90].

Like amylase and amylopectin, the polysaccharides of starch, molecular cellulose is a homopolysaccharide consisting of 10,000 to 15,000 D-glucose units. The main difference between cellulose and other D-glucose based polysaccharides is that the glucose residues
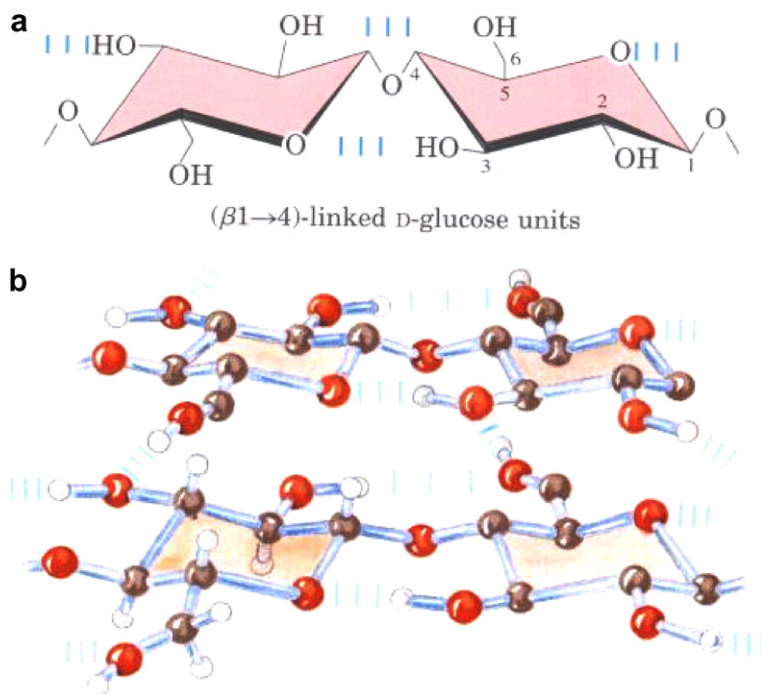
Fig. 32. The structure of cellulose. (a) Two units of a cellulose chain; the D-glucose residues are in β-(1 → 4) linkages. The rigid chair structures can rotate relative to one another. (b) Schematic drawing shows the inter- and intra-molecular hydrogen bonds between two parallel cellulose chains (from Nelson et al. [90, p. 249, Fig. 7–16]).

in cellulose is in β configuration while that in amylase, amylopectin, and glycogen is in α configuration. This difference gives cellulose very unique physical and chemical properties. Most animals cannot digest cellulose, because they lack an enzyme to hydrolyze the β-(1 → 4) linkages. Some animals, particularly ruminants and termites, can digest cellulose with the help of a symbiotic microorganism which hydrolyzes the β-(1 → 4) linkages.

For cellulose, the most stable conformation is that each unit chair is turned 180° relative to its neighbors, yielding a straight, extended chain. When the cellulose is fully extended, all hydroxyl groups are capable of forming both inter-molecular and intra-molecular hydrogen bonds (Fig. 32b). The extensive hydrogen bonds produce stable supramolecular fibers with excellent mechanical properties. This property has made cellulose a useful material in civilization for millennia.

Cellulose forms a structure with regions of high order, i.e. crystalline regions, and regions of low order, i.e. amorphous regions. Naturally occurring cellulose (cellulose I) crystallizes in the monoclinic sphenodic structures. The unit cell of cellulose is shown in Fig. 33 [91]; the lattice parameter are $a = 0.835$ nm; $b = 1.03$ nm; $c = 0.79$ nm.

Pure cellulose is never found in nature. The cotton fiber is the purest natural source, containing more than 95% of cellulose and about 5% of other substances. More commonly, cellulose is associated with lignin and other substances so-called hemicelluloses in considerable quantities. The hemicelluloses are not forms of cellulose at all. They comprise a group of polysaccharides that remains associated with the cellulose after lignin
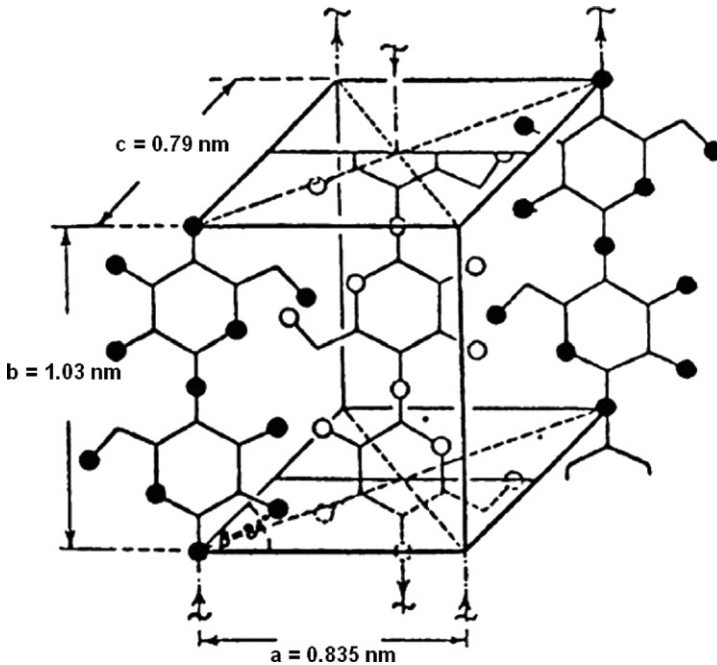
Fig. 33. The unit cell of crystalline cellulose (from Bledzki and Gassan [91, p. 231]).

has been removed. Depending on the species, wood contains on a dry basis about 40–55% cellulose, 15–35% lignin, and 25–40% hemicelluloses [92]. The plant cell wall is a composite of cellulose, lignin, and hemicelluloses which provides strength, rigidity, and prevents the swelling of the cell. The plant cell wall is discussed in Section 9.2.

6. Biological ceramics and ceramic composites

We follow the Wegst–Ashby classification in Sections 6–9, and present four classes of biological materials given in Fig. 1. For each class, we provide illustrative examples.

6.1. Sponge spicules

Sea sponges have often long rods (spicules) that protrude out. Their outstanding flexural toughness was first discovered by Levi et al. [93] who were able to bend a 1 m rod, having a diameter similar to a pencil, into a full circle. This deformation was fully reversible. Additionally, these rods are multifunctional and carry light. The optical properties were studied by Aizenberg et al. [94]. The structural hierarchy of the hexactinellid sponge spicule is a remarkable example of nature's ability to create sophisticated composites from relatively weak constituent materials. These spicules, which are found at the base of the silica basket (seen in Fig. 34), highly resemble the fragile fibers which are used in modern fiber optics [95]. They will be discussed in Section 11. As seen in Fig. 35a, the microcomposite design of this natural rod creates remarkable toughness especially in comparison to its industrial counterpart [94]. Fig. 35b shows a fractured Hexactinellid spicule (much
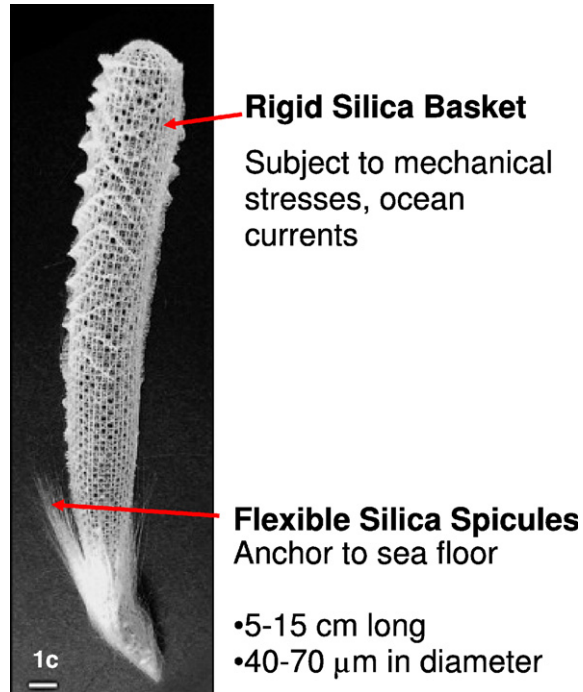
Fig. 34. Glass sponge, showing the basket cage and the spicules (from Sundar et al. [95]).

smaller than the one studied by Levi et al. [93]) that reveals its structure. This spicule, which has been studied by Mayer and Sarikaya [38], is a cylindrical amorphous silica rod and has an 'onion skin' type structure which effectively arrests cracks and provides an increased flexural strength. Fig. 35a shows the flexural stress as a function of strain. The spicule response is compared with that of a synthetic monolithic silica rod. The breaking stress of the spicule is four times higher than the monolithic silica. Additionally, an important difference exists between the two: whereas the monolithic silica breaks in a single catastrophic event, the spicule breaks 'gracefully' with progressive load drops. This is the direct result of the arrest of the fracture at the 'onion' layers. These intersilica layers contain an organic component which has been identified by Cha and coworkers [83] as silicatein (meaning a silica-based protein).

Each silica rod is composed of a central pure silica core of approximately 2 μm in diameter surrounded by concentric striated shells of decreasing thickness [95]. The individual shells are separated by the thin organic layer (silicatein) which is marked by an arrow in Fig. 36b. The mechanical toughness of the material is highly dependent on the striated layers as they offer crack deflection and energy absorption at their interfaces [93,94,96]. The gradual reduction in the thickness of the layers as the radius is increased is clearly evident in Fig. 36c.

Another fascinating spicule from a sea sponge is the *Hyalonema sieboldi*. This is also called glass rope sponge and it contains anchoring spicules that are remarkable for their size (up to 1 m), durability, flexibility, and optical properties. Fig. 37a shows a basal spicule in *H. sieboldi*. It can be seen how it can be into a circle. Ehrlich and Worch [68]
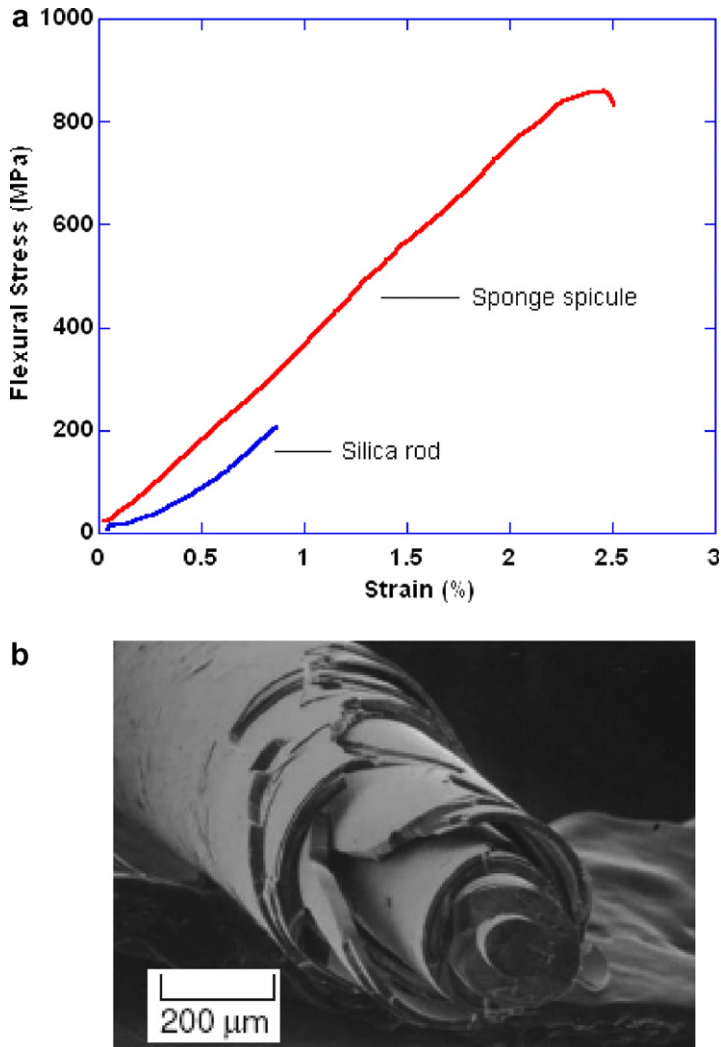
Fig. 35. (a) Flexural stress vs. strain for monolithic (synthetic) and for sea spicule; (b) Fractured spicule on sea sponge (courtesy of G. Mayer, U. Washington [38]).

describe their structure with emphasis on the elaborate collagenous network, which has a twisted plywood structure quite different from the one exhibited by the *Hexactinellida* sponge. This can be seen in Fig. 37b, this collagen acts as mediation for the nucleation and growth of the amorphous silica. Ehrlich and Worch [68] comment on the evolutionary aspects. Silicon is thought to have been a first stage in the inorganic to organic evolutionary process, leading finally to carbon based organisms. Silicon is the most common of the elements on the surface of the earth after oxygen and the ocean floors are covered with amorphous silica sediment, most of which results form living organisms. Ehrlich and coworkers [97,98] indicate that chitin is a component of the skeletal fibers of marine sponges, which have intricate elaborate structures.
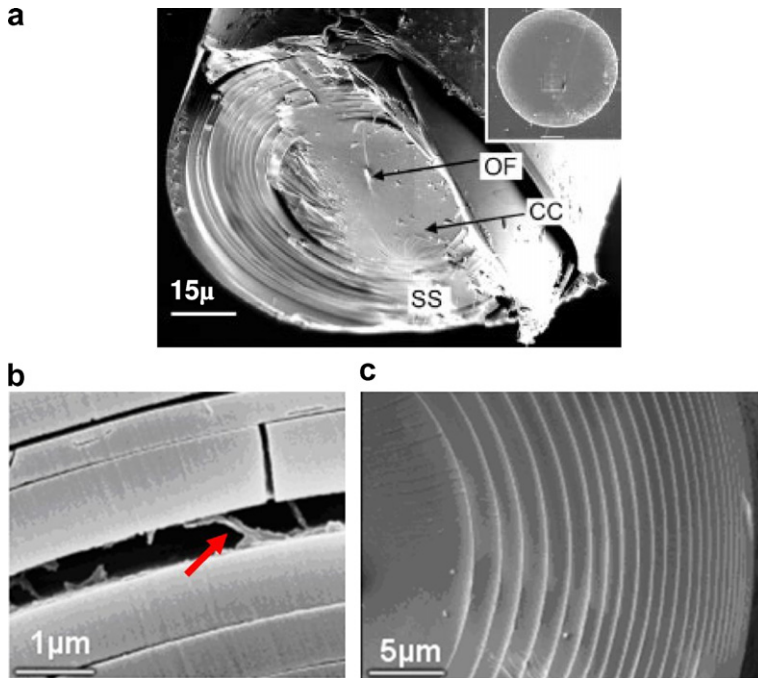
Fig. 36. Microstructure of a sponge spicule (from Aizenberg et al. [94]).

6.2. Shells

Shells have fascinated mankind since prehistory. They have been found in Neanderthal burial sites, evidencing the attraction they have exerted. Indeed, Aristotle and Pliny the Elder were among the first to write about shells; it seems that it was Aristotle who coined the name "Mollusca," meaning soft-bodied. Two aspects of seashells are of esthetic significance:

- The mother-of-pearl coloration, which results from the interference of visible light with the tiles that comprise nacre (~0.5 μm thickness, approximately equal to the wavelength).
- Their multiple and intricate shapes.

D'Arcy Thompson showed that this shape is, for many shells, a derivative of the logarithmic spiral [1]. Fig. 38a shows the top of an abalone shell. There are two spiral lines indicated; one follows the pattern of perforations which circulate the water and are closed as the shell grows. The second represents the markings of successive growth surfaces. The logarithmic spiral which exists in many shells is shown in Fig. 38b. It can be understood as formed by the aggregation of mineral, composed of two vectors: one with the radial direction ($d\vec{r}$), and one in the tangential direction ($d\vec{s}$). If the ratio of the magnitude of these two vectors is constant throughout the growth process, the angle α is unchanged:
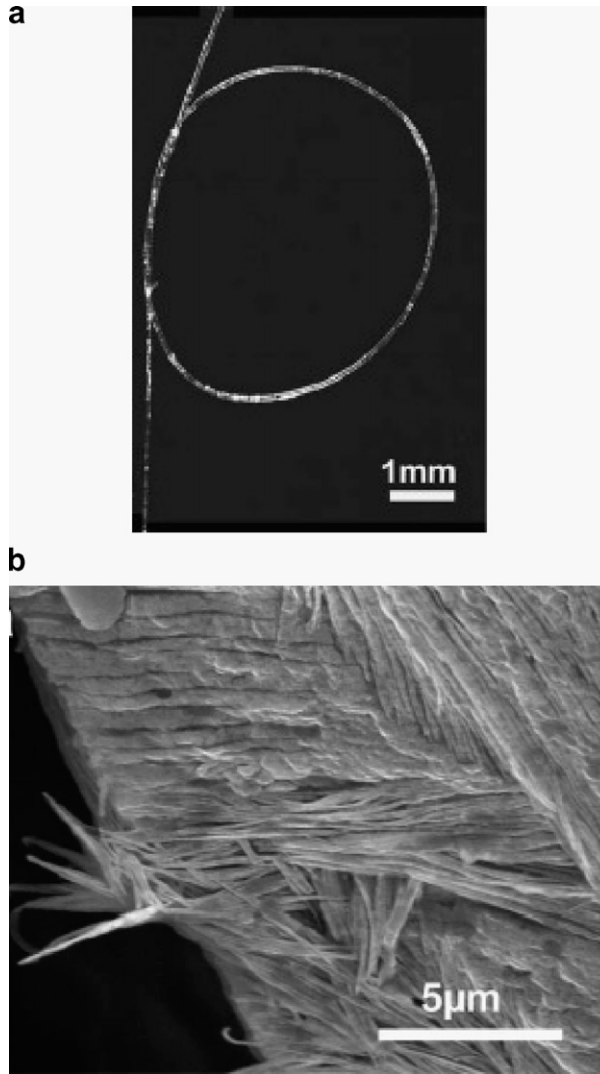
Fig. 37. (a) Unique flexibility of basal spicules of *H. sieboldi*. (b) SEM micrograph showing the twisted plywood orientation of collagen microfibrils (from Ehrlich and Worch [68]).

$$\tan \alpha = \frac{\mathrm{d}r}{\mathrm{d}s} \tag{15}$$

But, we have

$$\mathrm{d}s \cong r\mathrm{d}\theta \tag{16}$$

where r is the radial coordinate of a point along the curve and θ its angular coordinate. Substituting Eq. (15) into (16)

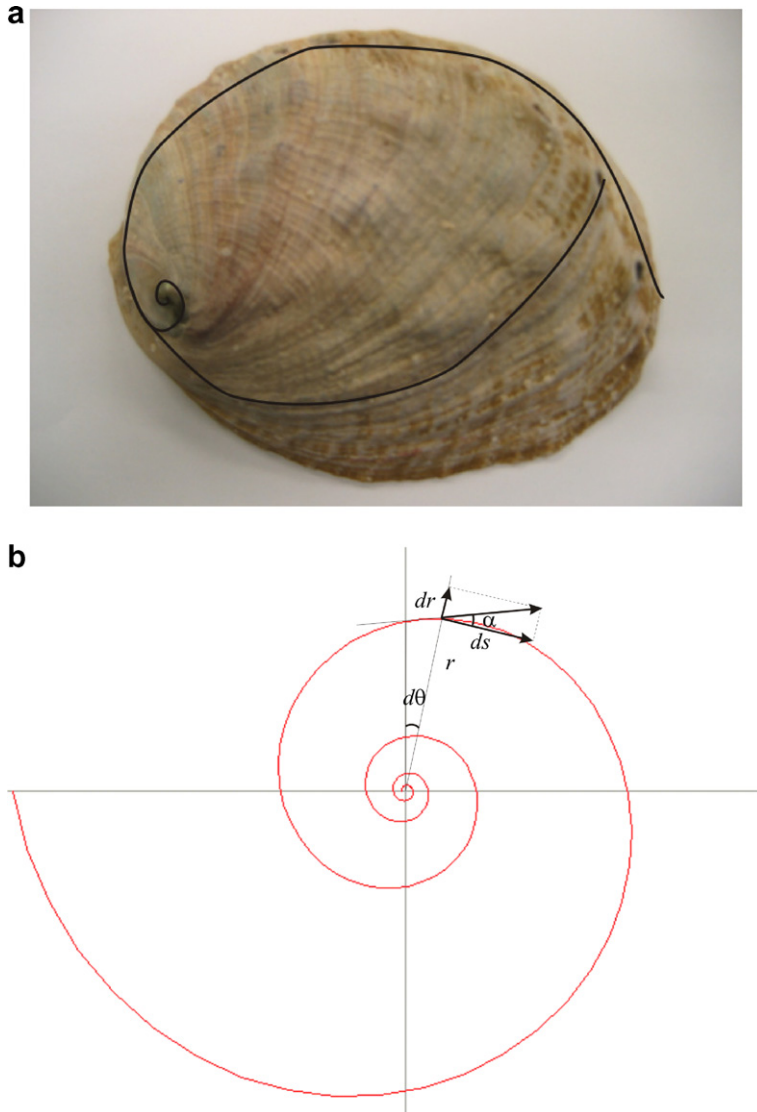$$\frac{\mathrm{d}r}{r} = \mathrm{d}\theta \tan \alpha \tag{17}$$

Fig. 38. (a) A photograph of abalone shell. There are two lines indicating the logarithmic spiral fashion of growth. (b) The growth vector of a logarithmic spiral consists of two vectors, one in tangential direction, the other in the radial direction. The ratio of the magnitude of these two vectors is constant throughout the growth process, and the angle α remains unchanged.

Integrating

$$\ln r = \theta \tan \alpha + C \qquad (18)$$

Or

$$r = e^C e^{\theta \tan \alpha} \qquad (19)$$

Eq. (19) expresses the logarithmic spiral curve. Skalak et al. [100] present a detailed analysis.

Other than their esthetic attributes, these shells provide the primary means of protection for the soft bodies of the animals they house. They are permanent encasements of body armor, which must be strong enough to withstand the impact and compression capabilities of a sea of predators. Mollusk shells consist of one or more ceramic phases and small fraction (0.1–5%) proteins. These ceramic phases alone, i.e. calcium carbonate ($CaCO_3$), are not suitable as structural materials because of their inherent brittleness. However, when combined into these intricate natural structures a resulting biocomposite with outstanding mechanical properties is created. This is true for many biological materials [38]. The micro-structure and macro-structure of these shells plays a significant role in increasing the toughness of an otherwise brittle ceramic base. Five main types of mollusk shell structures have been identified. They are nacreous (flat tablets), crossed lamellar (plywood-like), prismatic (polygonal columns), foliated (long thin crystals in overlapping layers) and homogeneous (fine-scale rubble), which can, in some cases, occur alongside each other. In the following sections, we discuss the growth and formation of some of these structures, and the mechanisms through which they achieve their amazing mechanical properties.

6.2.1. Nacreous shells

The schematic of the longitudinal cross-section (Fig. 39) of the abalone shell (Haliotis) shows two types of microstructure: an outer prismatic layer (calcite) and an inner nacreous layer (aragonite) as observed by Nakahara et al. [101]. The two forms of $CaCO_3$ have the structures; calcite (rhombohedral) and aragonite (orthorhombic). The structure of nacre (the inside portion of the shell, shown in Fig. 39) within the shells of abalone consists of a tiled structure of crystalline aragonite; moreover there is a very high degree of crystallographic texture characterized by a nearly perfect "*c*-axis" alignment normal to the plane of the tiles. Fig. 40a shows schematically the brick and mortar microstructure found in abalone nacre [102], and Fig. 40b shows the layered structure in a TEM micrograph [103]. In Fig. 40c the "*c*-axis" orientation is shown. The staggering of tiles in adjacent layers is also clearly visible.

Periodic growth arrests create mesolayers that also play a critical role in the mechanical properties and are powerful crack deflectors. Fig. 41 shows this structures. Layers of viscoplastic material separate the thicker layers (mesolayers) which are approximately 300 μm thick and an inorganic layer with a thickness of about 20 μm. These layers were identified by Menig et al. [8] but are not often mentioned in other reports dealing with the
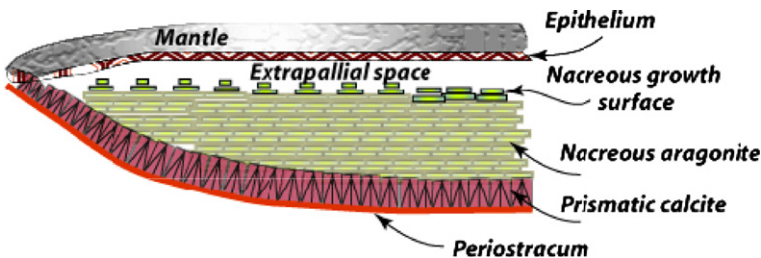

Fig. 39. Structure of typical abalone shell (adapted from Zaremba et al. [108]).
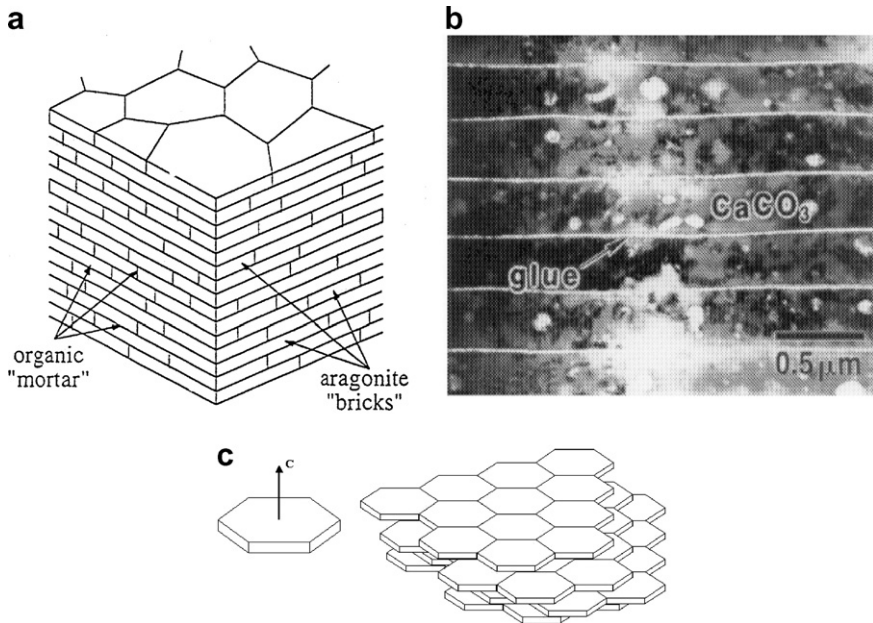
Fig. 40. (a) Brick and mortar microstructure of nacre (schematically) (from Sarikaya [102]). (b) TEM micrograph of layered structure of abalone (courtesy of K.S. Vecchio, University of California, San Diego [103]). (c) Microstructure of abalone nacre showing tiles layers staggered one on top of the other with the same c-axis orientation.
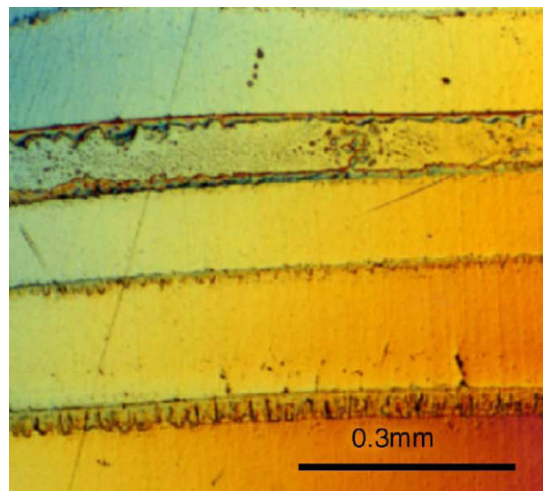

Fig. 41. Mesostructure of abalone shell, showing growth bands (from Menig et al. [8]).

mechanical properties of abalone. It is thought that these thick organic layers form in abalone grown in the sea during periods in which there is little calcification.

In the case of the abalone nacre, the mineral phase corresponds to approximately 95 wt% of the total composite. The deposition of a protein layer of approximately
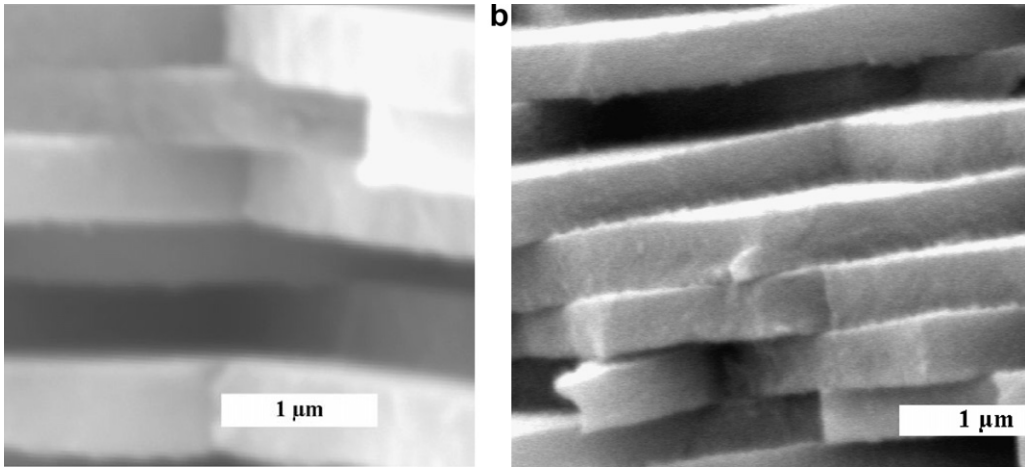
Fig. 42. Nacreous tile structures; (a) Abalone (*H. rufescens*) from Southern California; (b) Bivalve shell from Araguaia River, Brazil.

20–30 nm is intercalated aragonite platelets, which are remarkably consistent in dimension for each animal regardless of age [9]. However, there are differences when examining varying species of nacre forming animals: the thickness of the tiles in the abalone shells is approximately 0.5 μm, as seen in Fig. 42a, while it is around 0.3 μm for a bivalve shell found in the Araguaia River (Brazil), thousands of miles from the ocean (Fig. 42b).
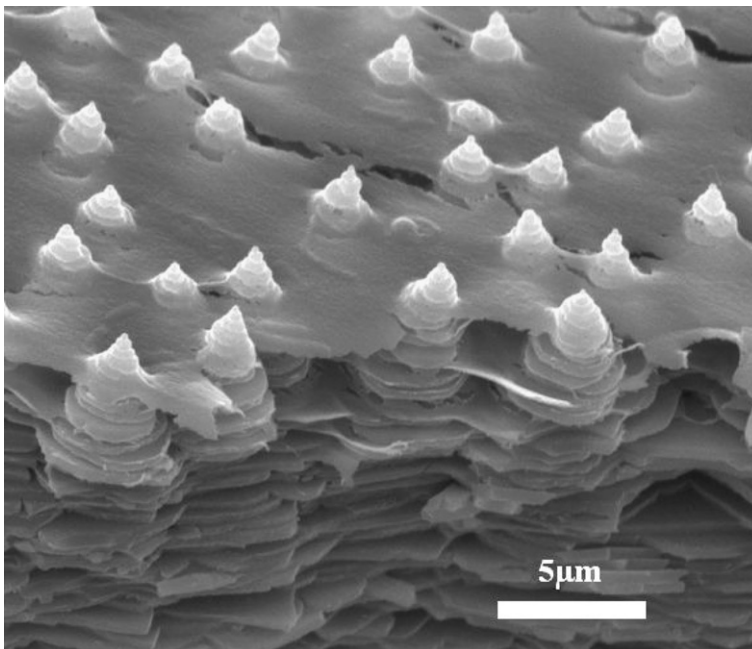

Fig. 43. ''Christmas tree'' pattern observed on the growth surface of steady state tiled aragonite nacre.

6.2.1.1. Growth of abalone (Haliotis rufescens) nacre. The growth of the red abalone shell has been the subject of considerable study starting in as early as the 1950s with Wada [104,105], continuing with Watabe and Wilbur [106], Bevelander and Nakahara [107] and followed by many others. The work by the UC Santa Barbara group [64,82,108–114] represents one of the most comprehensive efforts. Shell growth begins with the
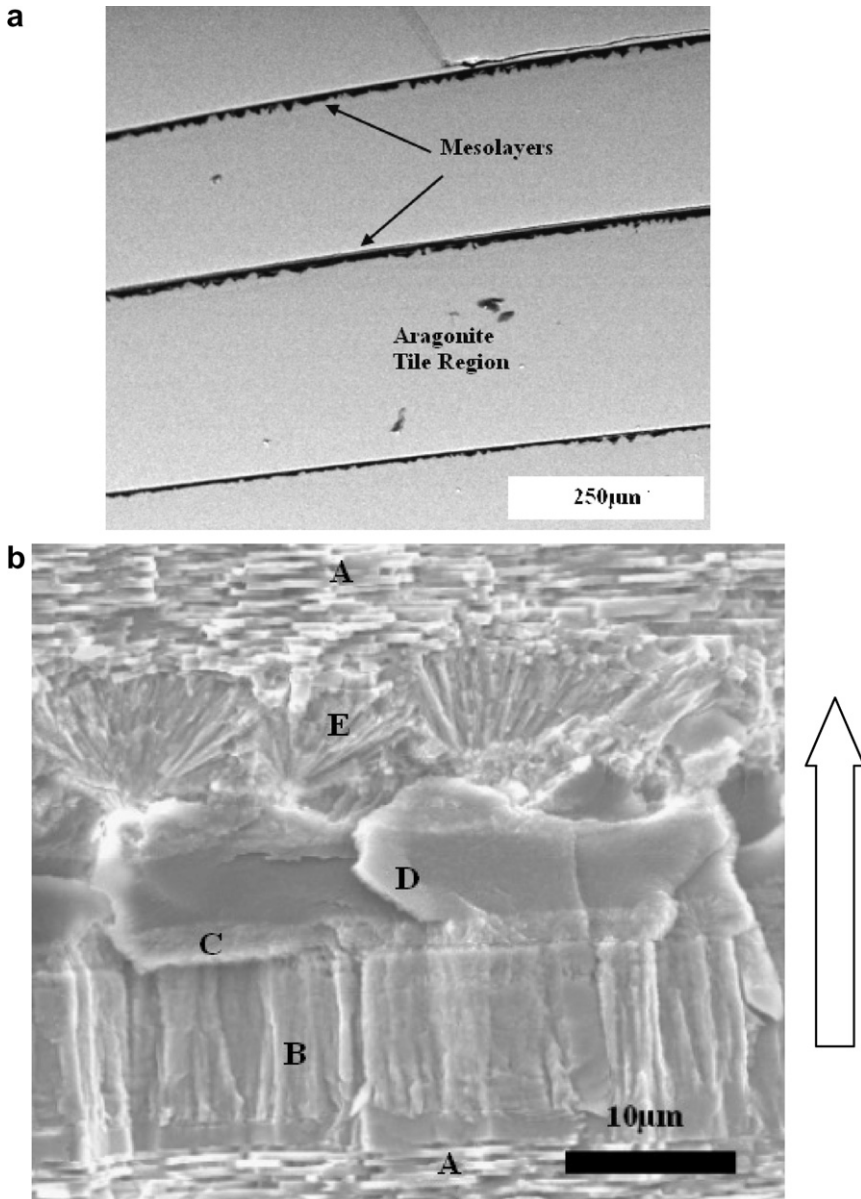
Fig. 44. (a) Macrostructural view of a cross-section of the *H. rufescens* shell. Growth bands are observed separating larger regions of nacre, (b) SEM micrograph of fracture surface; direction of growth marked with arrow.

secretion of proteins that mediate the initial precipitation of calcite, followed by a phase transition from calcite to aragonite. There are at least seven proteins involved in the process. As steady state tiled aragonite growth is reached, nacre deposition occurs through the successive arrest of mineral deposition by means of a protein-mediated mechanism; this is followed by the subsequent re-initiation of mineral growth on the new surface layer. This takes place in the "Christmas-tree pattern" as seen in Fig. 43.

Additional macro-scale structure was identified as the periodic interruption of aragonitic tile growth in the form of mesolayers, possibly being attributed to sporadic interruptions in the animal's diet [8,9]. In nacre there is a synergy of structural hierarchy pertaining to many different length scales. The following discussion begins with the formation of macro-scaled elements, followed by micro-structural formation, and finally the growth of nanoscale component of the shell. Fig. 44a provides a macrostructural view of a cross-section of the inner nacreous layer. Organic bands approximately 8 μm thick can be seen separating larger, 300 μm thick, regions of nacre. These "mesolayers" mark interruptions in nacre growth,
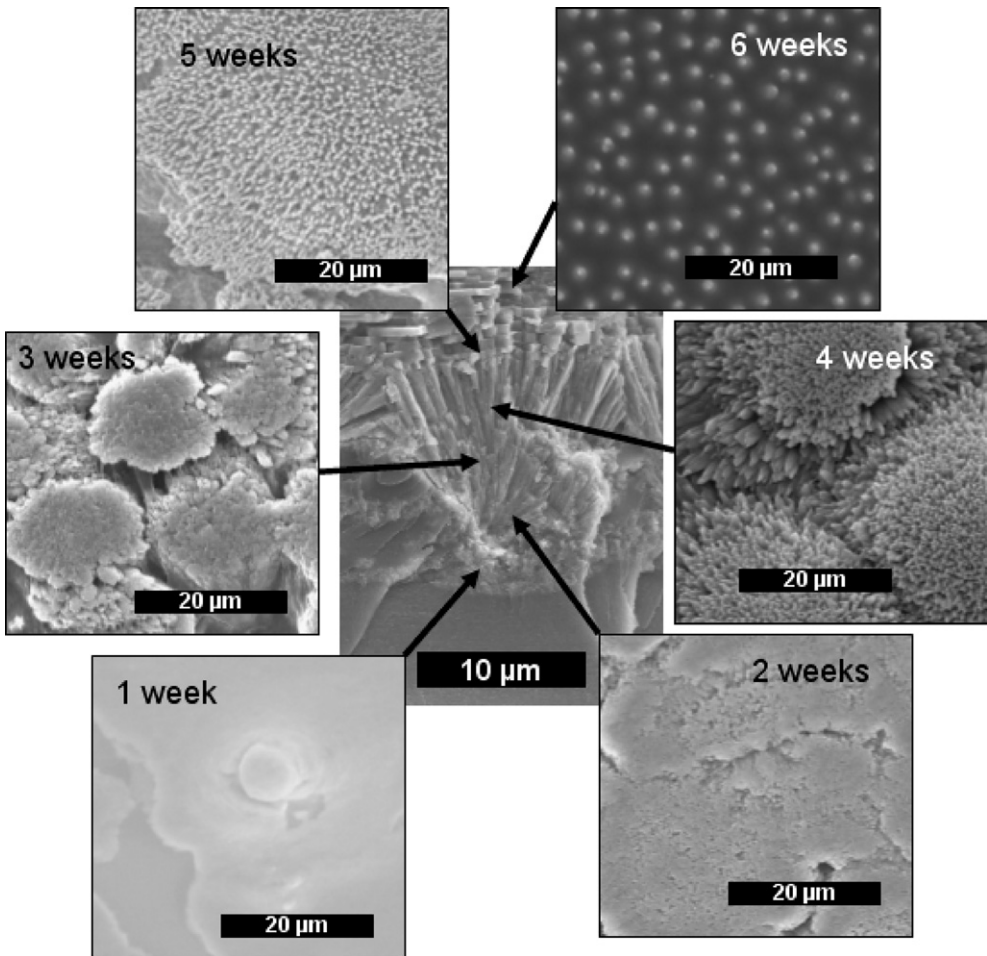

Fig. 45. Summary of sequential growth from flat pearl and trepanning experiments (from Lin et al. [115]).

and thus are therefore also called growth bands. The inorganic $CaCO_3$ undergoes morphological changes before and after the interrupting growth bands [115]. As seen in Fig. 44b, five regions can be identified (direction of growth marked by arrow): tiled (A); block-like aragonite (B); organic/inorganic mix (C); organic (D); and spherulitic (E). The growth sequence is described in greater detail by Lin and Meyers [9]. In Fig. 44b, the growth occurs from bottom to top. Prior to arrest of growth, the characteristic tiles are replaced by a block-like structure (B). This is followed by the massive deposition of the organic layer, which is initially intermediated with mineralized regions. At the end of the mesolayer, when mineralization starts again, a layer comprised of a spherulitic structure is observed. Both the "flat pearl" technique, first introduced by Wada et al. [116,117] then further developed by the UC Santa Barbara group [113], and the "trepanning" technique in which foreign sections of nacre are introduced into the growth surface were used by Lin et al. [115] to observe the various formations following steady state growth interruption. The results of the sequential growth study are presented in Fig. 45.

Two weeks after implantation, the precursor aragonite has spread across the entire substrate. None of the original implantation is left exposed. As seen in the lower half of Fig. 45, the morphology of deposited mineral transitions to spherulitic aragonite between the second and third week. It was earlier thought that the spherulitic layer was calcitic [108], but Su et al. [112] incontrovertibly identified it as aragonitic; this was also later reconfirmed by Lin et al. [115].

After three weeks of implantation the tops of each spherulitic bundle appear flattened. This is thought to be the result of a constant pressure or a rubbing force exerted by the mantle of the animal itself. Indeed, it is proposed that the animal forms the structure of the shell through a mechanical-chemical action. The self-assembly of aragonite in nacre does not translate into the overall architecture of the shell; the animal continuously molds it. The animal has the ability to apply a significant amount of binding force to keep itself attached to virtually any surface. This force translates to an approximately equal and opposite force applied normal to the growth surface of the shell. The epithelial layer of the mantle sits directly over the growth surface. As the animal moves along a rock or a wall it twists itself in a rotating manner. The epithelial skin slides back and forth along the shell producing a sanding effect over the growing mineral structures. This mechanical flattening of the growing surface occurs throughout the nacre deposition region.

After four weeks of implantation, the spherulites are fully formed as a result of the divergent growth of aragonite columns along the fast growing *c*-axis direction. The cross-sectional view of a growth band, shown in Fig. 44, shows the divergent growth of these columns. They spread apart into a lower density as growth continues after five weeks of implantation. Between five and six weeks of implantation the aragonite morphology transitions towards the regular tiled aragonite microstructure as shown at the top of Fig. 45. It is hypothesized that this transition may occur as the ends of each spherulitic needle become nucleation sites for aragonite tiles. The intermittent deposition of the organic matrix which is believed to inhibit crystal growth [118] molds the spherulitic aragonite needles into an increasingly laminate structure, eventually reaching the steady-state aragonite tile formation. The "Christmas tree" like growth fields are associated with tiled aragonite growth [82,108,113,114] and can be seen in Fig. 46.

Fig. 46a shows a low magnification view, and it is seen that the ceramic phase nucleates randomly over the proteinaceous layer. Closer observation, shown in Fig. 46b reveals the "Christmas tree" pattern described earlier by Shen et al. [82] and Fritz and Morse [114].
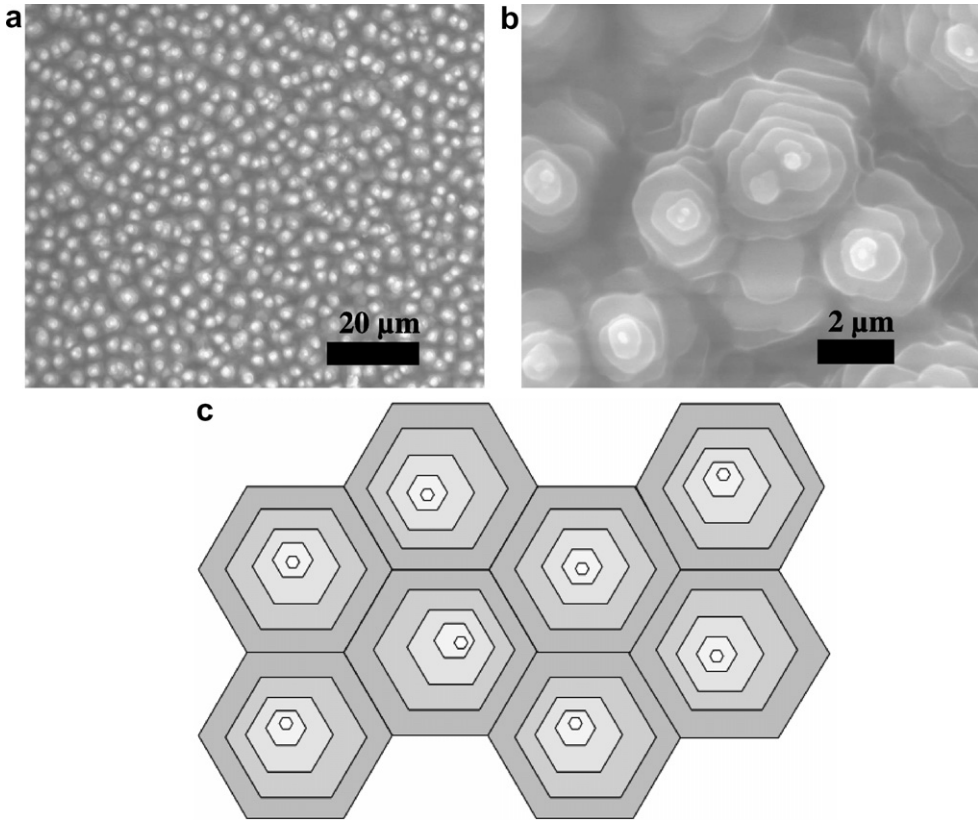
Fig. 46. Growth on 15 mm slide after 24 days; (a) low-magnification SEM; (b) high-magnification SEM; (c) schematic drawing showing the same crystallographic orientation.

However, it should be noticed that the center-to-center distance is less than the tile size in natural abalone, which is 10 μm. It is possible that the glass from the implants provides greater areal density of nucleation sites; however, similar spacing was observed with the trepanning method [115]. A schematic drawing of adjacent "Christmas trees" is shown in Fig. 46 (c). Each tile is smaller than the one below it.

Fig. 47 shows a hypothetical description of the sequence of tile growth, as it has been thought to occur during steady state deposition. First, a proteinaceous layer (possibly, the beta conformation of Addadi et al. [62]) is deposited. The aragonite crystals nucleate and grow on it, with a characteristic spacing. They have the orthorhombic structure with the "*c*" direction is perpendicular to the protein plane [3]. In the absence of proteins, this is the rapid growth direction. Addadi and Weiner [61] and Addadi et al. [62] demonstrated that there is stereoselective adsorption of proteins in the growth of calcite crystals; this results in a slowing down of growth in the "*c*" direction and completely alters the final shape of the crystals. Addadi et al. [62] also showed that the (001) plane of calcite is the one that forms on the protein layer. The similarity between the two polymorphs (calcite and aragonite) of calcium carbonate is a strong indication that a similar mechanism might be operating. It is speculated that the host animals produce the proteins that arrest growth in the
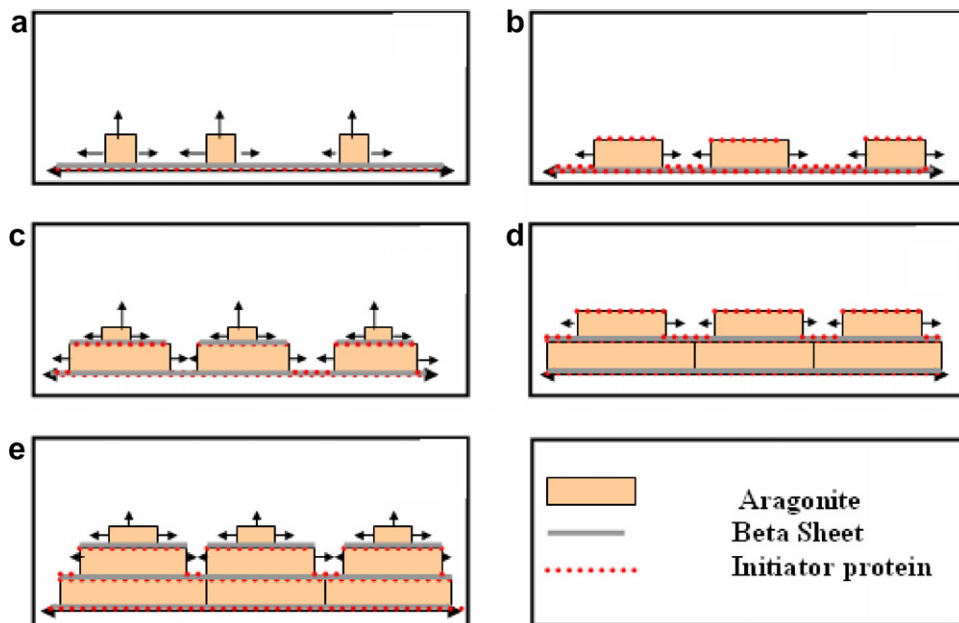
Fig. 47. Hypothetical growth mechanism with periodic injection of proteins arresting growth in "*c*" direction. (a,b) Protein deposition causing the arrest of crystallographic growth in the "*c*" direction; (c) second growth spurt after deposition of beta sheet and nucleation; (d) first aragonite plates are butted together while growth of second layer continues in "*a, b*" direction; (e) nucleation of third layer as second layer growth continues in "*a*" direction (from Lin and Meyers [9]).

"*c*" direction in a periodic manner. Thus, the (0 0 1) growth is periodically arrested. It was earlier thought that new aragonite tiles nucleate at the growth surfaces, on the beta conformation layer. This occurs in parallel with lateral growth. More recent advances show that aragonite does not nucleate on the beta layer, rather mineral growth continues through pores in the organic membrane, allowing sites on which new tiles can form. In this fashion, successive "terraces" are formed and propagate. The resulting configuration is the "Christmas tree" morphology reported by Simkiss and Wilbur [119] and in greater detail by Belcher [109] and Fritz et al. [113].

The organic layers covering each tile layer may play an important role by providing the scaffolding for formation. First observed and described by Nakahara et al. [120,121], they exist and are in place before the growth of aragonite tile is complete. Fig. 48a represents the possible environment surrounding aragonite tiles with the presence of the organic scaffolding. The calcium and carbonate ions can penetrate through the organic layer deposited by the epithelium. Electron microscopy of the resulting growth surfaces shows columns of sequential aragonite tiles (Fig. 48b).

The mechanism of arresting and initiating growth of subsequent layers of aragonite has led to some debate pertaining to the interface between tile layers. The apparent crystallographic alignment along the *c*-axis indicated a mineral connection between tiles. Initially, Sarikaya [122] reported a central core along the "Christmas tree" trunk. This central core would be responsible for triggering lateral growth. Song et al. [123,124], on the other hand, report a large number of bridges in each tile. The bridges traverse the organic layers, which
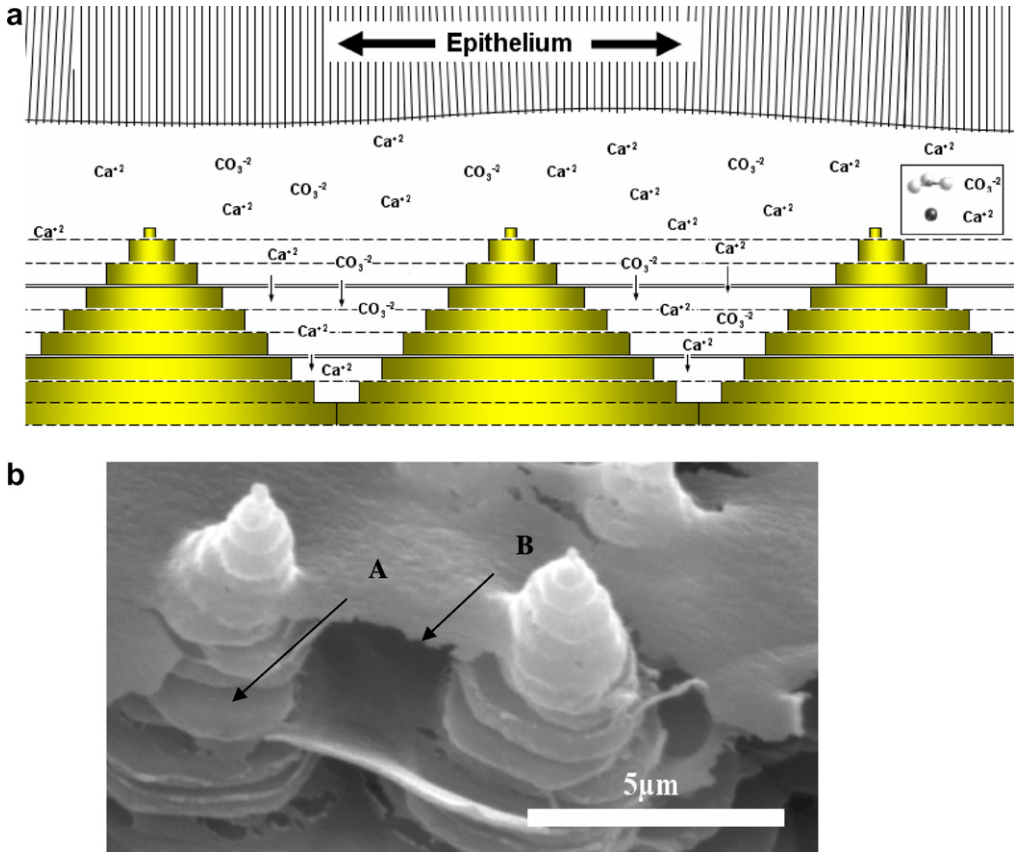
Fig. 48. Growth of nacreous tiles by terraced cone mechanism; (a) Schematic of growth mechanism showing intercalation of mineral and organic layers; (b) SEM of arrested growth showing partially grown tiles (arrow A) and organic layer (arrow B).
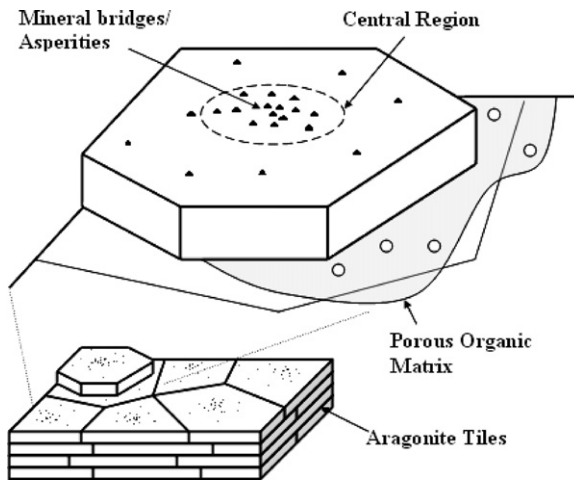

Fig. 49. Schematic representation of mineral bridges connecting sequential aragonite tiles layers.

are porous. They observed a higher concentration of bridges in the central region of the tiles; this is shown schematically in Fig. 49. Having been first described by Schäffer et al. [125], they are responsible for transmitting the crystallographic orientation from layer to layer. Atomic force microscopy [125], transmission electron microscopy [124,115], and scanning electron microscopy [115] have been used to observe the existence of mineral bridges in abalone nacre; the results are presented in Fig. 50(a–d). Fig. 50a shows a TEM of a tile with the lighter regions marked by arrows being identified by Song et al. [124] as bridges. Fig. 50b shows the tiles (boundaries dark). The small white spots are supposedly remnants of bridges. Fig. 50c and d show cross-sectional regions (SEM and TEM, respectively). The bridges are marked by arrows.

Fig. 51a represents the sequence in which growth occurs through mineral bridges. The growth sequence is as follows; (i) organic scaffolding forms as interlamellar membranes between the layers of tiles arresting *c*-direction growth, (ii) a new tile begins growth
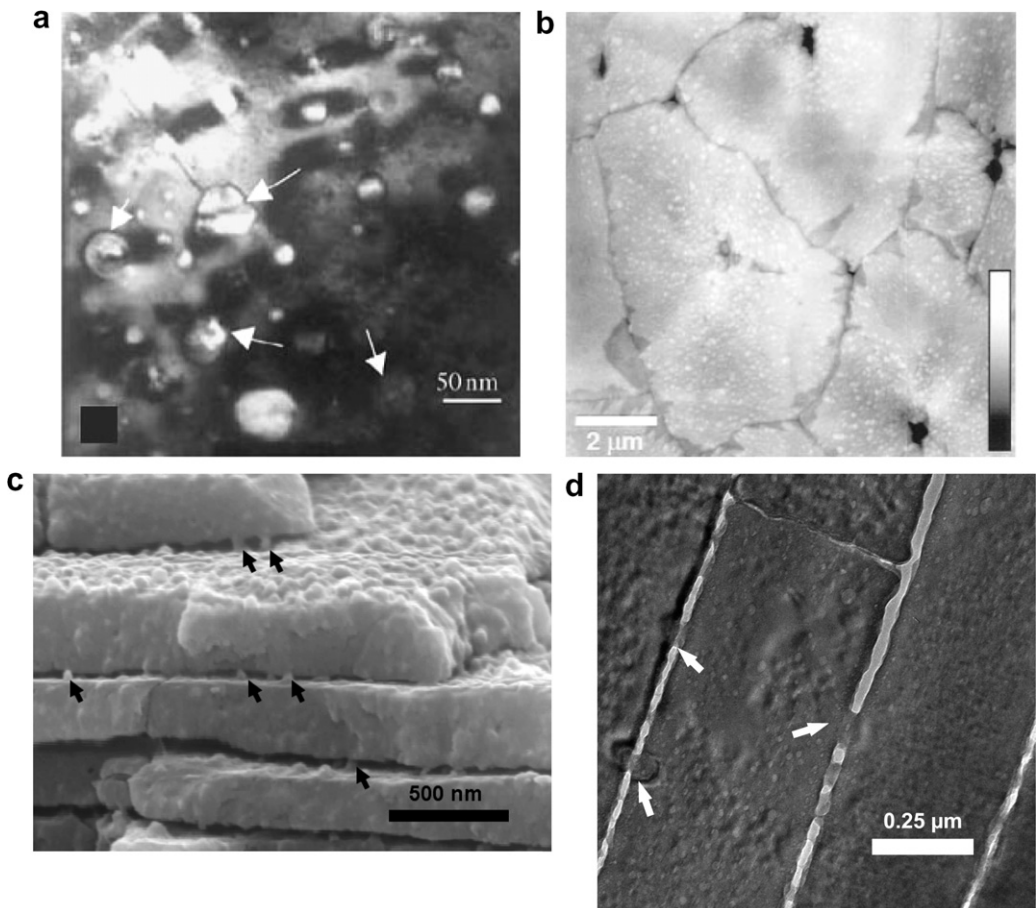

Fig. 50. (a) TEM view of mineral bridges on tile surfaces (from Song et al. [123,124]), (b) AFM image of mineral bridge reminents on tile surface (from Schäffer et al. [125]), (c) SEM micrograph showing mineral bridges between tiles after deproteination (from Lin et al. [115]), (d) TEM micrograph of nacre cross-section showing mineral bridges (from Lin et al. [115]).
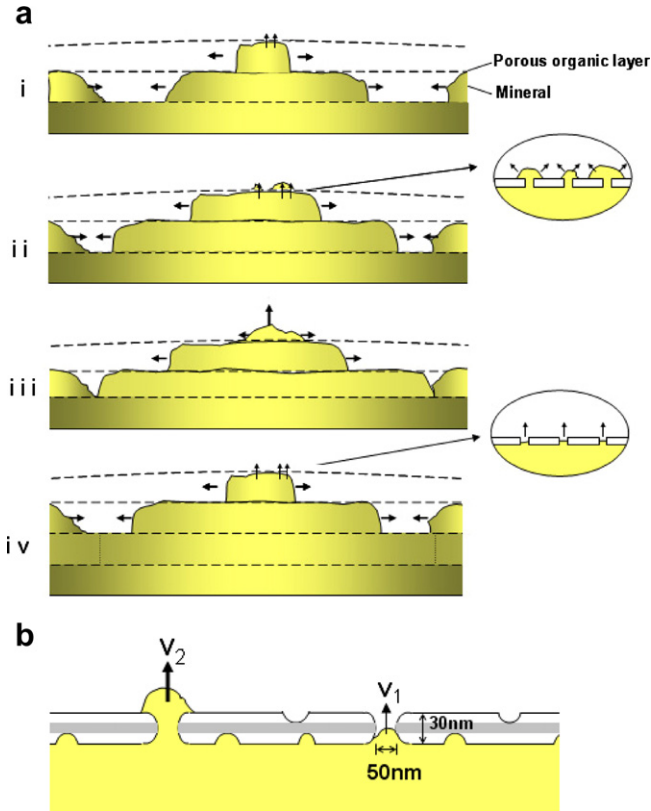
Fig. 51. (a) Growth sequence through mineral bridges (b) Detailed view of mineral bridges forming through holes in organic membranes.

through the porous membrane, (iii) the new tile grows in every direction, but faster along the c-axis, (iv) a new porous organic membrane is deposited, arresting c-axis growth of the new tile while allowing continued a and b-axis; growth, mineral bridges begin to protrude through the second organic membrane while sub-membrane tiles continue to grow along the a and b-axis, sub-membrane tiles abut against each other; a third tile begins to grow above the membrane. As shown, the bridges are believed to be the continuation of mineral growth in the c-axis from a previous layer of tiles. They protrude through the growth arresting layers of proteins, creating a site on the covering organic layer where mineralization can continue. These mineral bridges are the seed upon which the next tile forms.

A detailed view of mineral bridges enabling growth through a permeable organic membrane is shown in Fig. 51b. Holes in the organic nanolayer, which have been identified by Schäffer et al. [125], are thought to be the channels through which growth continues. Mineral growth above the membrane is faster than growth in the membrane holes because of the increase in contact area with surrounding calcium and carbonate ions. Since these holes are small (30–50 nm diameter) the flow of ions is more difficult, resulting in a reduction of growth velocity to $V_1 \ll V_2$ (Fig. 51b). V_2 is the unimpeded growth velocity in the c

direction. The supply of Ca^{2+} and CO$_3^{2-}$ ions to the growth front is enabled by their flow through the holes in the membranes. This explains why the tiles have a width to thickness ratio of approximately 20 whereas the growth velocity in the orthorhombic c direction is much higher than in the a and b direction.

While in gastropods the nucleation of aragonite tiles occurs in the Christmas tree pattern described above, bivalve mineralization takes place with tablets offset with respect to layers above and below them. Fig. 52 from Wang et al. [126] compares the two nacre structures as tile separation occurs: (a) in gastropod (abalone) shell where columns of white markings (identified with white arrows) indicate separation, and (b) in bivalves (pearl oyster) shell where tile location is offset from preceding layers and separation is more random.

Cartwright et al. [127] compare differences in microstructures between gastropods and bivalves and attribute them to variations in growth dynamics. In gastropods there are a large number of holes that enable the growth, therefore a ''Christmas tree'' or terraced cone stacking of tiles is possible. In bivalves a smaller number of holes exist, most of which are filled with proteins and not mineral. There appears to be no direct evidence of mineral bridges. However heteroepitaxy is required for the tiles to retain the same orientation. Cartwright et al. [127] suggest that there are more widely spaced bridges in bivalves, as shown in Fig. 53. There are two bridges per tile, causing the heteroepitaxial growth to dictate a random stacking of subsequent tiles.

6.2.1.2. Mechanical properties of abalone nacre. As a result of the highly ordered hierarchical structure [3,4,70,99,128–131], biocomposites generally exhibit excellent mechanical properties. We shall describe the mechanical characteristics of the shell, then examine each scale of structural design and how they contribute to the strength and toughness of nacre described above, beginning with the mesolayers, followed by the aragonite tiles, and finally ending with the interface between tile layers.

Currey [132] was the first to perform measurements of mechanical properties of nacre from a variety of bivalves, gastropods and cephalopods. He obtained a fracture strength in bending varying between 56 and 116 MPa. This was followed by Jackson et al. [133] who used nacre from the shell of a bivalve mollusk, *Pinctada*. They report a Young's modulus of approximately 70 GPa for dry and 60 GPa for wet samples; the tensile strength of nacre was found to be 170 MPa for dry and 140 MPa for wet samples. The work of fracture varied from 350 to 1240 J/m^2, depending on the span-to-depth ratio and the degree of hydration, wet nacre showing superior toughness by associated introduction of plastic work. In contrast, monolithic CaCO$_3$ showed a work of fracture that was about 3000 times less
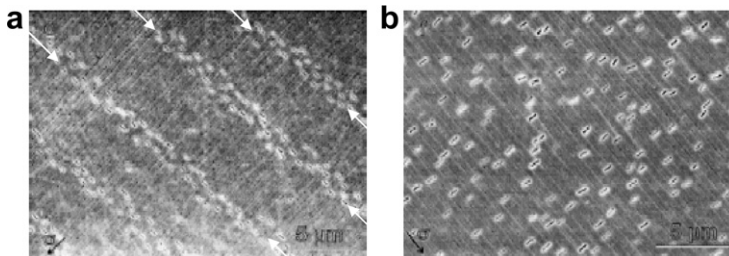

Fig. 52. Tile separation occurs; (a) in a gastropod (abalone) shells where tiles are formed in columns, and (b) in a bivalves (pearl oyster) shells where tile location is offset from preceding layers (from Wang et al. [126]).
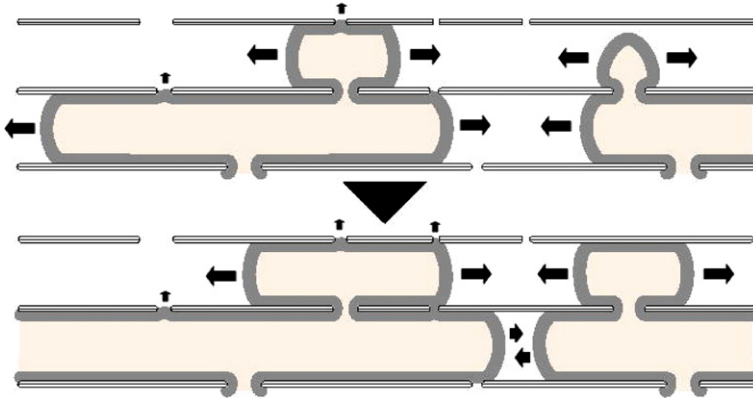
Fig. 53. Growth sequence in bivalve nacre (from Cartwright and Checa [127]).

than that of the composite nacre material. It should be noted that this work of fracture is not identical to the toughness measured by Sarikaya et al. [134]. The work-of-fracture is the area under the stress–strain curve and is deeply affected by gradual, graceful fracture, whereas the fracture toughness does not incorporate this entire process. Thus, one should be careful when considering this number. Early studies show indications of the low span-to-depth ratios of tiles contributing to fracture toughness [129]. Jackson et al. [133] concluded that water affects the Young's modulus and tensile strength by reducing the shear modulus and shear strength of the organic matrix which comprises less than 5 wt% of the total composite. The toughness is enhanced by water, which plasticizes the organic matrix, resulting in greater crack blunting and deflection abilities. In contrast with more traditional brittle ceramics, such as Al_2O_3, or high toughness ceramics, such as ZrO_2, the crack propagation behavior in nacre reveals that there is a high degree of tortuosity.

Sarikaya et al. [134] conducted mechanical tests on *H. rufescens* (red abalone) with square cross-sections. They performed fracture strength σ_f (tension) and fracture toughness K_{IC} tests on single straight notched samples in 4-point and 3-point bending modes, respectively, in transverse direction, i.e. perpendicular to the shell plane. A fracture strength of 185 ± 20 MPa and a fracture toughness of 8 ± 3 MPa m$^{1/2}$ was found. This is an eightfold increase in toughness over monolithic $CaCO_3$. The scatter is explained with the natural defects in the nacre and the somewhat curved shape of the layers. The K_{IC} and σ_f value of synthetically produced monolithic $CaCO_3$ is 20–30 times less than the average value of nacre. The specific flexural strength of $CaCO_3$ is 10 MPa/g cm^{-3}.

Menig et al. [8] measured the compressive strength of red abalone and found considerable variation. Weibull statistics [135] were successfully applied. This is within the range for synthetic ceramics. Presented in Fig. 54 are the results for tests on abalone nacre (a) in quasi-static compression, with failure probabilities of 50% being reached at 235 MPa and 540 MPa with loading parallel and perpendicular to layered structure, respectively, and (b) dynamic compression with 50% failure probabilities for the abalone shell found at 548 MPa and 735 MPa with the layered structure parallel and perpendicular to loading, respectively. Fig. 55 shows the Weibull analysis of nacre in tension with load perpendicular to layers. Here a 50% failure probability was determined at only 5 MPa. The Weibull moduli in tension and compression are similar: 2 and 1.8–2.47, respectively. However,
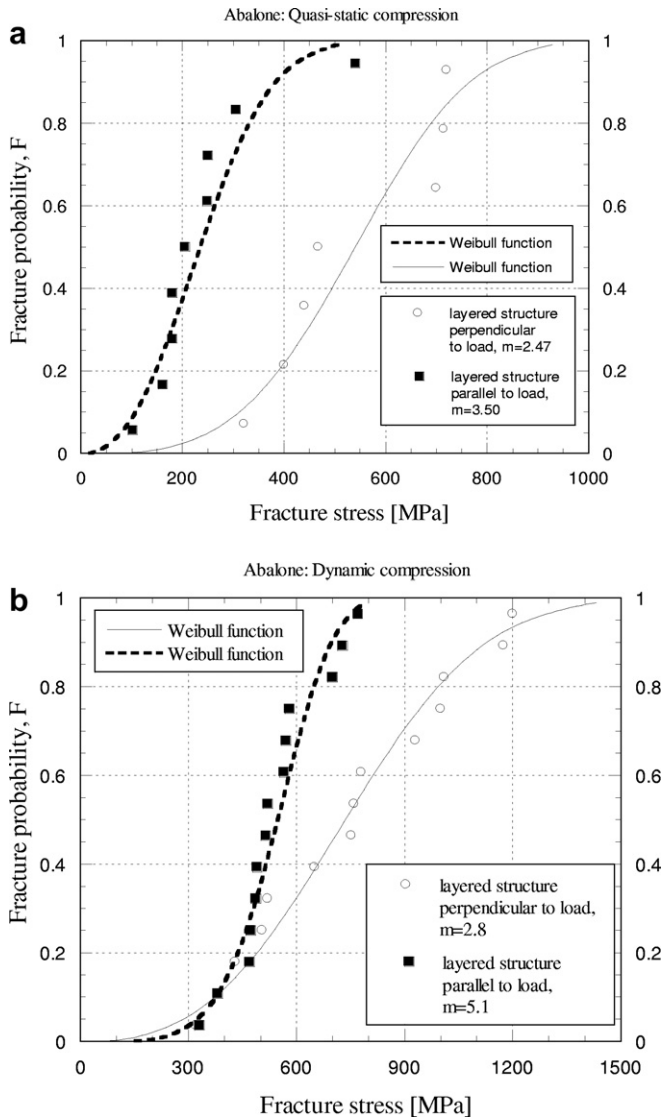
Fig. 54. Weibull plots of abalone nacre in; (a) quasi-static, and (b) dynamic compressive loading (from Menig et al. [8]).

the difference in strength is dramatic and much higher than in conventional brittle materials. The ratio between compressive and tensile strength is on the order of 100, whereas in brittle materials it varies between 8 and 12. This difference is indeed striking, especially if one considers the tensile strength parallel to the layer plane, on the order of 140–170 MPa [133], which is approximately two-thirds the compressive strength. Other work by Barthelat et al. [152] found the tensile strength of nacre to be closer to 100 MPa, which is still just below half the compressive strength. It can be concluded that the shell sacrifices tensile strength in the perpendicular direction to the tiles to use it in the parallel direction. Fig. 56 summarizes the strength of nacre with respect to various loading directions. The unique
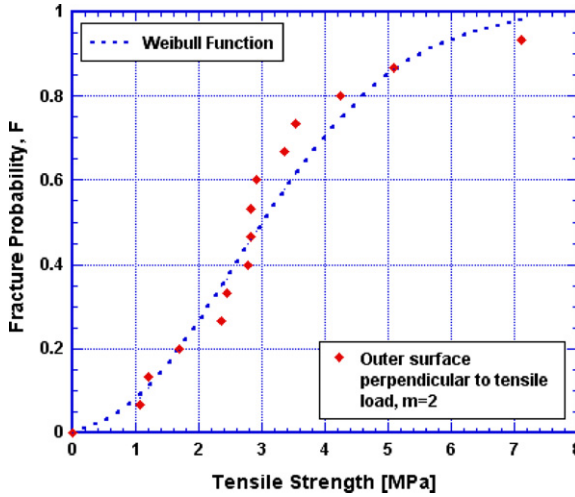
Fig. 55. Weibull distribution of tensile with force direction perpendicular to layered structure (from Meyers et al. [141]).
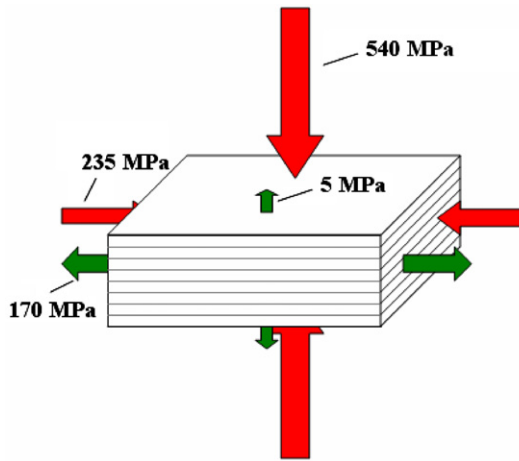

Fig. 56. Strength of nacre with respect to loading direction.

strength anisotropy perpendicular to the layers (5 MPa vs. 540 MPa) is remarkable and will be discussed later. Another marked characteristic is the greater compressive strength when loading is applied perpendicular rather then parallel to the tiles. This is due to the phenomena of axial splitting and microbuckling (kinking) when loading is applied parallel to the tiles. The relatively small difference in tensile and compressive strength (170 MPa vs. 230 MPa) in this direction of loading is directly related to the high toughness. Both these aspects are discussed below.

The abalone exhibits orientation dependence of strength as well as significant strain-rate sensitivity; the failure strength at loading rates of 10^4 GPa/s was approximately 50% higher than the quasi-static strength. Compressive strength when loaded perpendicular to the shell

surface was approximately 50% higher than parallel to the shell surface. Quasi-static compressive failure in both shells occurred gradually, in "graceful failure". The shear strength of the organic/ceramic interfaces of *H. rufescens* was determined by means of a shear test and was found to be approximately 30 MPa. Considerable inelastic deformation of these layers (up to a shear strain of 0.4) preceded failure.

Upon compression parallel to the plane of the tiles, an interesting phenomenon observed previously in synthetic composites was seen along the mesolayers (previously described): plastic microbuckling. This mode of damage involves the formation of a region of sliding and of a knee. Fig. 57 shows a plastic microbuckling event. Plastic microbuckling, which is a mechanism to decrease the overall strain energy, was observed in a significant fraction of the specimens. Plastic microbuckling is a common occurrence in the compressive failure of fiber-reinforced composites when loading is parallel to the reinforcement. The coordinated sliding of layer segments of the same approximate length by a shear strain γ produces an overall rotation of the specimen in the region with a decrease in length. Fig. 57 shows a characteristic microbuckling region. The angle α was measured and found to be approximately 35°. The ideal angle, which facilitates microbuckling according to Argon, is 45° [136].

The angle θ (Fig. 57) varies between approximately 25° and 15° and is determined by the interlamellar sliding. This angle is consistent with the shear strain of 0.45 between lamellae observed in Fig. 58. The shear strain associated with the rotation θ in Fig. 57 is $\tan \theta = \gamma = 0.47$. Hence, the rotation θ in kinking is limited by the maximum shear strain, equal to 0.45. If this kinking rotation were to exceed 0.45, fracture along the sliding interfaces would occur. It is estimated the shear strain undergone by the organic layers prior to failure. The shear strain γ_0 is

$$\gamma_0 = \frac{\gamma}{f} \tag{20}$$

where f is the fraction of organic layer, which has an approximate value of 0.05, providing $\gamma_0 \cong 9$. The results by Menig et al. [8] are of the same order of magnitude as the ones reported by Sarikaya [134]. These results were applied to existing kinking theories [136,137].
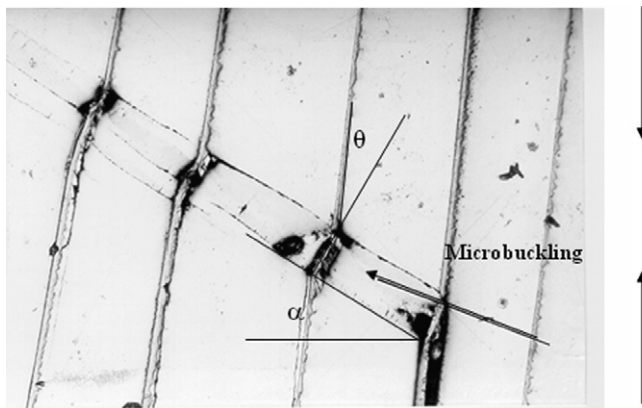

Fig. 57. Mechanisms of damage accumulation in nacreous region of abalone through plastic microbuckling.
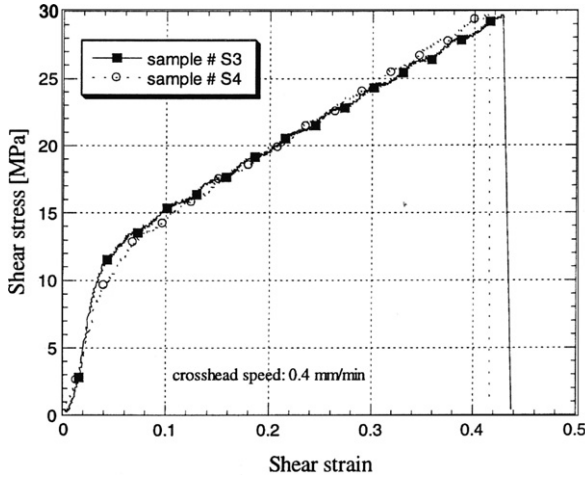
Fig. 58. Experimental shear stress-shear strain curve for nacre (from Menig et al. [8]).

The Argon [136] formalism for kinking based on an energetic analysis, was applied. The plastic work done inside the band (W) is equated to the elastic energy stored at the extremities (ΔE_1) of the band and the energy outside the band (ΔE_2) that opposes its expansion:

$$\Delta E_1 + \Delta E_2 - W = 0 \tag{21}$$

This leads to

$$\sigma \cong \frac{\tau}{\theta_0} \left[1 + \frac{bG_c\Delta\theta}{2\pi a\tau(1-v)} \ln\left(\frac{2\pi a\tau(1-v)}{bG_c\Delta\theta}\right) + \frac{E_r\Delta\theta}{48\tau}\left(\frac{t_r}{b}\right)^2 \right] \tag{22}$$

where τ is the shear strength of the matrix, θ_0 is the angle between the reinforcement and the loading axis, E_r is Young's modulus of the reinforcement, t_r is the lamella thickness, G_c is the shear modulus of the composite, v is Poisson's ratio, and a and b are the kink nucleus dimensions. Fleck et al. [138] and Jelf and Fleck [139] further developed this treatment.

Budiansky [137], using a perturbation analysis, developed the following expression for the ratio between the thicknesses of kink bands and the spacing between reinforcement units (w/d):

$$\frac{w}{d} = \frac{\pi}{4}\left(\frac{2\tau_y}{CE}\right)^{-1/3} \tag{23}$$

where E is the Young's modulus of the fibers and C is their volume fraction. It is interesting to note that Eq. (23) predicts a decrease in w/d with increasing τ_y.

These formalisms for microbuckling were applied to the results of Menig et al. [8] and enable some conclusions to be drawn regarding the kink stress and spacing of the slip units. Fig. 59a shows the predicted compressive kinking stress for abalone as a function of misalignment angle. It can be seen that the strength is highly sensitive to the angle α. Fig. 59b using the Budiansky equation adapted to the abalone geometry shows the kink band thickness (w) as a function of strain rate. The results by Menig et al. [8], carried out at different strain rates, confirmed the Budiansky prediction. Two parameters were used: the mesolayer and microlayer thicknesses. The experimental results shown in
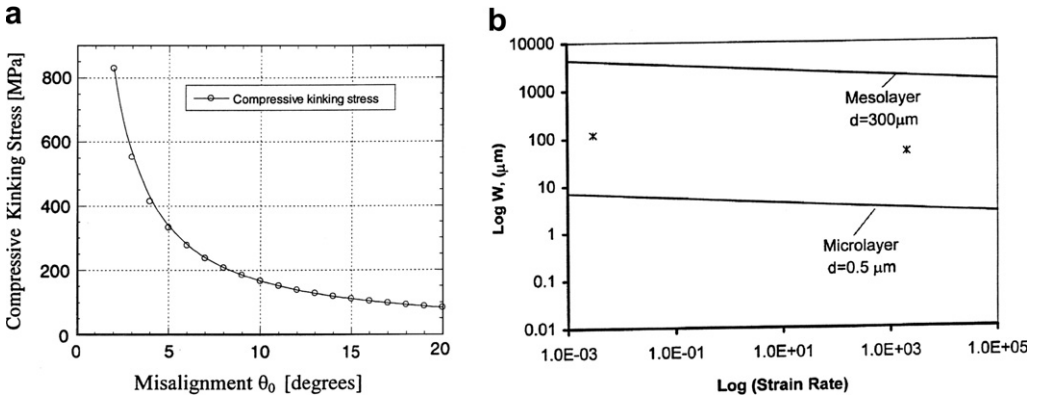
Fig. 59. Application to shell microbuckling (from Menig et al. [8]) of (a) Argon [136] analysis for kink stress formation and (b) Budiansky [137] formalism for the kink-band thickness prediction.

Fig. 59b fall in the middle, showing that both the mesolayers and platelets (microlayers) take part in kinking.

Another significant mechanism of toughening is crack deflection at both the meso- and micro-scale. The effect of the viscoelastic organic interruptions between mesolayers or even individual aragonite tiles is to provide a crack deflection layer so that it becomes more difficult for the cracks to propagate through the composite. Therefore the composite is superior to the monolithic material, in which a propagating crack has no barriers. Jackson
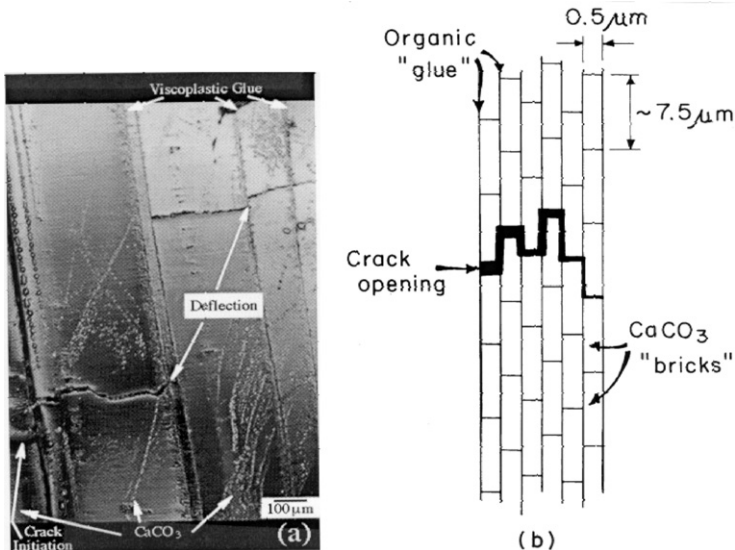

Fig. 60. (a) Cross-section of abalone shell showing how a crack, starting at the left is deflected by viscoplastic layer between calcium carbonate lamellae. (b) Schematic drawing showing arrangement of calcium carbonate in nacre, forming a miniature "brick and mortar" structure (from Meyers and Chawla [161]).

et al. [133] correctly recognized that the increase in path length, created through deflection of cracks, is responsible for enhanced work of fracture. The two levels of the structure presented in Fig. 60 can be seen engaging in this mechanism: (a) mesolayers provide crack deflection, (b) at a smaller scale the tile layers force cracks in a tortuous path. This and several other toughening mechanisms have been proposed [134] including: (a) crack blunting/branching, (b) microcrack formation, (c) plate pull out, (d) crack bridging (ligament formation), and (e) sliding of $CaCO_3$ layers. The high degree of crack tortuosity in these shells may be due mainly to crack blunting and branching. However, it is reported that the many orders of magnitude increase in toughness cannot only be caused by tortuosity. Therefore, it is possible that the major toughening mechanisms are sliding and ligament formation [140]. Fig. 61 shows tensile failure along the direction of the tiles. The tensile strength of the tiles is such that they do not in general break, but slide along their interfaces. The tile sliding is represented in Fig. 61b. This is accomplished by the viscoplastic deformation of the organic layer and/or by the shearing of the mineral ligaments traversing the organic phase.

The organic phase, is not a monolithic material but possesses a structure. The center region is structurally more rigid with high chitin content, as mentioned in Section 5.
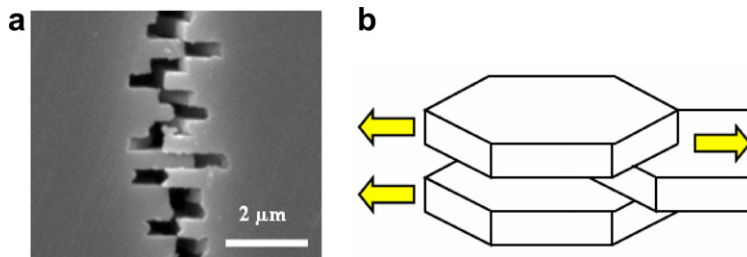

Fig. 61. Mechanisms of damage accumulation in nacreous region of abalone through tile pullout.
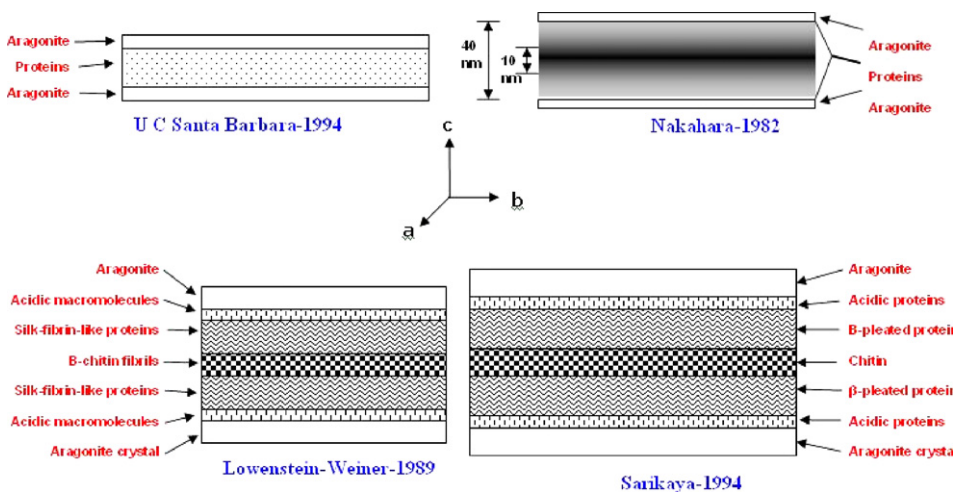

Fig. 62. Various models for the proteinaceous layer.

Aspartic acid is a major constituent of the acid soluble components. Other constituents are glutamic acid, serine, glycine, alamine. Shen et al. [82] reported the characterization of the cDNA coding for ''Lustrin A'' which is a protein they have identified within the nacreous layer of red abalone. Fig. 62 is a representation of the different structures proposed for the organic layer. Early models indicate the presence of a thin protein sheet (10–40 nm thick) sandwiched between the aragonite tiles. More complex models attempt to represent the composition of the organic matrix with a central β-chitin sheet sandwiched between β-pleated proteins which are in turn covered in acidic proteins which act as the interface
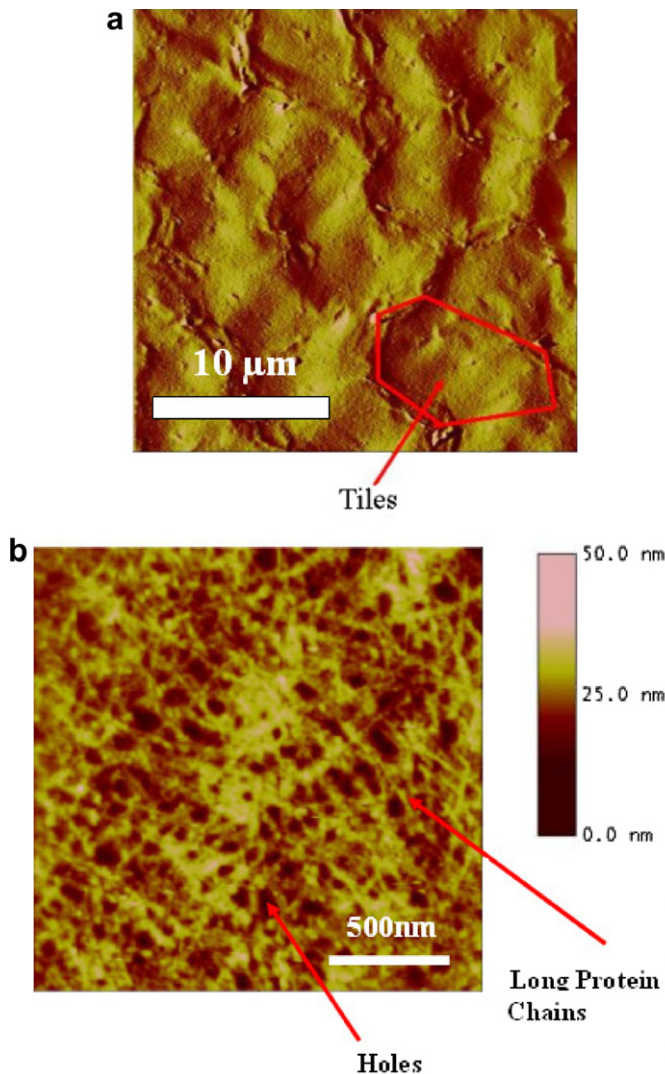

Fig. 63. Atomic force microscopy of organic layer; (a) overall view at low magnification showing outline of hexagonal tiles; (b) high magnification showing linear chains and holes with ∼30 nm diameter (from Meyers et al. [141]).

between the organic and inorganic. Atomic force microscopy of nacre following EDTA demineralization exposes the structure of the organic matrix, Fig. 63. Meyers et al. [141] obtained a biaxial elastic modulus of 100 Pa, by measuring the sagging of the membrane between a tile spacing of 10 μm. This is indeed a very low value. This low value can only be explained if the random network of protein chains in Fig. 63b can slide when tension is applied to the membrane. The value of 100 Pa is an upper bound, and the range of elastic moduli is comparable to that for living cells [142]. This value is also consistent with the high maximum tensile strains that the organic layer can undergo in tension. Belcher and Gooch (Fig. 15.9) [143] quote a value of $\varepsilon_{max} = 3$ (equivalent to a maximum stretch $\lambda = \varepsilon + 1 = 4$). The calculations confirm that the organic layer material has a very small stiffness and is highly stretchable.

The interface between the organic phase and the aragonite may be critical in the shear strength of the laminate components. Fig. 64 shows the unit cell. The (0 0 1) plane is the top surface. The calcium atoms are black; the carbon atoms are black and smaller; the oxygen atoms are gray. As described by Weiner and coworkers [144–146] Fig. 64 shows the aspartic acid-rich protein (Asp-$Y)_n$, where Y is an amino acid bonding to the Ca^{2+} ions of the aragonite structure. These proteins, in their turn, bond to the more rigid beta sheets. Addadi and Weiner [61] describe the phenomenon of stereoselectivity in considerable detail and provide three possible explanations for it. They suggest that the aspartic acid-rich protein binds to calcium atoms preferentially. Indeed the (0 0 1) plane of aragonite is characterized by protruding calcium atoms.

Additional toughening mechanisms such as sliding of $CaCO_3$ layers and organic ligament formation were thought to operate and were analyzed by Lin and Meyers [9]. Fig. 65 shows the tensile strength of the aragonite phase as a function of crack size. The fracture toughness was taken as 1 MPa m$^{1/2}$. It can be seen that, if one considers the strength limited by flaw size, that it increases from values of 50 MPa for large flaws to 250 MPa for a flaw the size of a tile (10 μm). The strength of tiles increases with decreas-
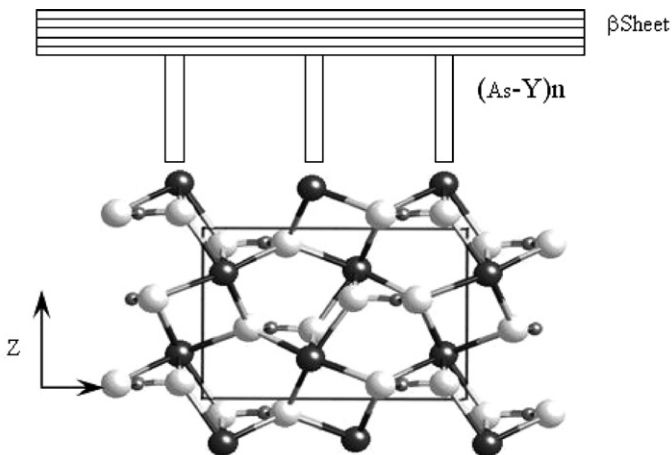

Fig. 64. Unit cell of aragonite showing schematic position of (Asp-$Y)_n$ and β sheet. Notice protruding calcium ions on (0 0 1) face; black atoms: Ca; small black: carbon; gray atoms: oxygen (courtesy of K.S. Vecchio, UCSD [103]).
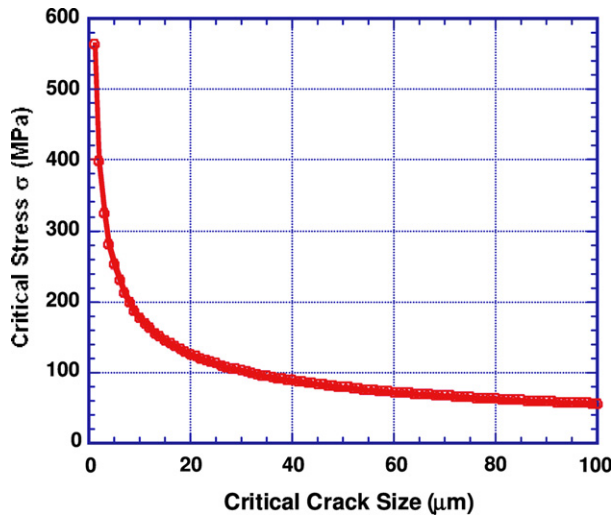
Fig. 65. Critical stress as a function of flaw size for aragonite [$K_{Ic} = 1$ MPa m$^{1/2}$] (from Lin and Meyers [9]).

ing size, and one can safely assume that it is higher than 250 MPa, for the given size. Thus, the values of tensile strength obtained by Menig et al. [8] (180 MPa from flexure tests) and Wang et al. [126] (110 MPa) may be explained by viscoplastic flow of organic matrix or plastic failure of mineral bridges at the tile interface, starting at 10 MPa and proceeding through gradual increase, until separation occurs.

Evans et al. [147] and Wang et al. [126] proposed an alternative toughening mechanism: that nano-asperities on the aragonite tiles are responsible for the mechanical strength. These nano-asperities create frictional resistance to sliding, in a manner analogous to rough fibers in composite material. They developed a mechanism that predicts the tensile mechanical strength based on these irregularities. These nano-asperities were modeled by Barthelat et al. [152], who carried out nanoindentation and FEM analysis of the aragonite crystals. Bruet et al. [148] obtained, through nanoindentation and atomic force microscopy, local measurements of the mechanical properties of the aragonite tiles: $E = 79$ and 92 GPa and compressive strengths of 11 and 9 GPa for dry and seawater soaked tiles, respectively. This strength is much higher than that observed by Menig et al. [8] in compression tests (540 MPa). The Young modulus is consistent with values reported in literature [9,133]. The source of inter-tile shear resistance is still a subject of significant debate.

Meyers et al. [141] made observations indicating that the organic layer, while playing a pivotal role in the growth of the aragonite crystals in the c direction (perpendicular to tile surface), may have a minor role in the mechanical strength. The tensile strength in the direction perpendicular to the layered structure can be explained by the presence of the mineral bridges. These bridges, having a diameter of approximately 50 nm, have a tensile strength no longer determined by the critical crack size, but by the theoretical strength. Their number is such that the tensile strength of the tiles (parallel to the tile/shell surface plane) is optimized for the tile thickness of 0.5 μm, as shown by Lin and Meyers [9]. A higher number of bridges would result in tensile fracture of the tiles with loss of the crack

deflection mechanism. This is a viable explanation for the small fraction of asperities that are bridges.

Meyers et al. [141] estimate the tensile strength of the individual mineral bridges by applying the fracture mechanics equation to aragonite. Consistent with recent analyses by Gao et al. [149], Ji and Gao [150], and Ji et al. [151], the mineral bridges have sizes in the nanometer range. The maximum stress, σ_{fr}, as a function of flaw size, $2a$, can be estimated, to a first approximation, to be

$$\sigma_{fr} = \frac{K_{Ic}}{\sqrt{\pi a}} \tag{24}$$

where K_{Ic} is the fracture toughness. However, the strength is also limited by the theoretical tensile strength, which can be approximated as [149]:

$$\sigma_{th} = \frac{E}{30} \tag{25}$$

We assume that $K_{Ic} = 1$ MPa m$^{1/2}$, $E = 100$ GPa, and that $2a = D$, where D is the specimen diameter. Eqs. (24) and (25) intersect for $a = 28$ nm ($D = 56$ nm). This is indeed surprising, and shows that specimens of this and lower diameter can reach the theoretical strength. This is in agreement with the experimental results: the holes in the organic layer and asperities/bridge diameters are around 50 nm. Recent analyses [123,124,149] also arrive at similar values.

It is possible to calculate the fraction of the tile surface consisting of mineral bridges, f. Knowing that the tensile strength is σ_t and assuming that the bridges fail at σ_{th}, we have

$$f = \frac{\sigma_t}{\sigma_{th}} \tag{26}$$

The number of bridges per tile, n, can be calculated from
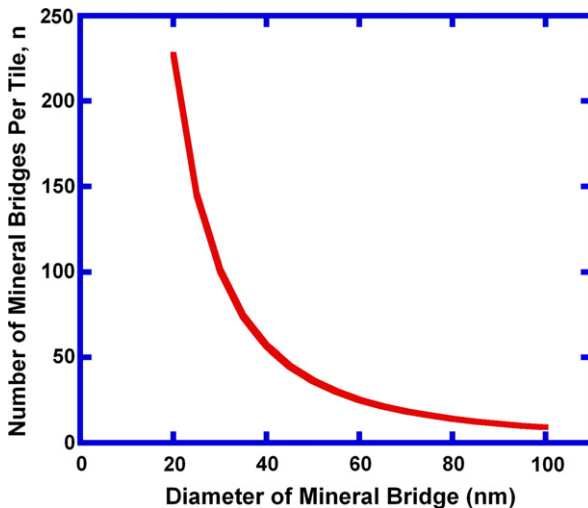
$$f = \frac{nA_B}{A_T} \tag{27}$$

Fig. 66. Calculated number of mineral bridges per tile as a function of bridge diameter.

where A_B is the cross-sectional area of each bridge and A_T is the area of a tile. Thus

$$n = \frac{\sigma_t A_T}{\sigma_{th} A_B} \tag{28}$$

Assuming that the tiles have a diameter of 10 μm and that the bridges have a diameter of 50 nm (the approximate observed value), one obtains, for $\sigma_t = 3$ MPa (the value found by Meyers et al. [141]) and $\sigma_{th} = 3.3$ GPa, $n = 36$. Fig. 66 shows the relationship between mineral bridge diameter and the number of mineral bridges through Eq. (28). The number of bridges calculated above is surprisingly close to the measurements by Song et al. [123,124]: $35 \leqslant n \leqslant 45$. However, the interpretation of the results reported by Song et al. [123,124] is not clear. This result strongly suggests that mineral bridges can, by themselves, provide the bonding between adjacent tiles.

The number of asperities seen in Fig. 67 exceeds considerably the values for bridges calculated herein and measured by Song et al. [123,124]. The estimated density is $60/\mu m^2$ (5000/tile). One conclusion that can be drawn is that a large number of asperities are indeed incomplete bridges and that these bridges are a small but important fraction of the protuberances.
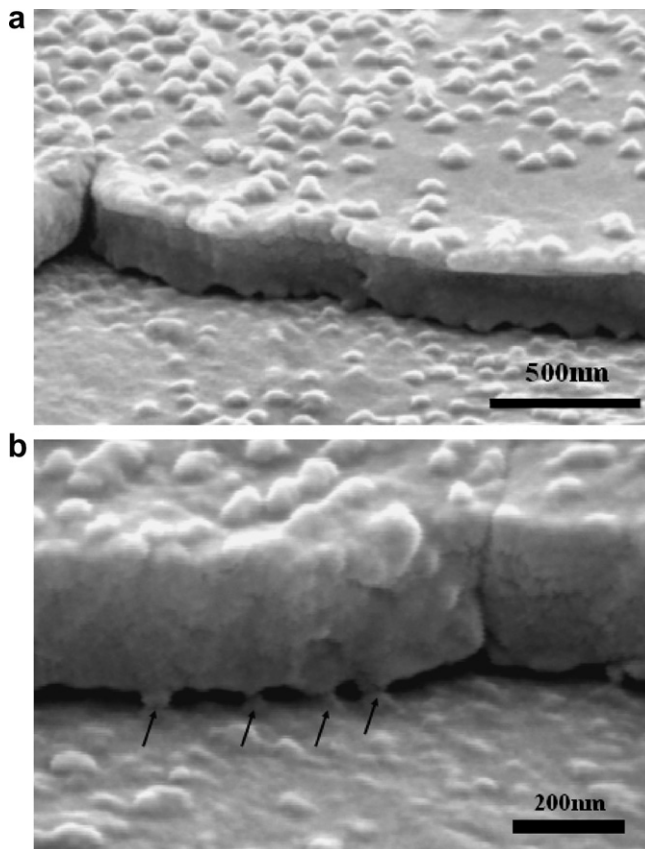

Fig. 67. (a) Asperities (a fraction of which are remnants of mineral bridges) and (b) mineral bridges (marked by arrows) between tile layers.
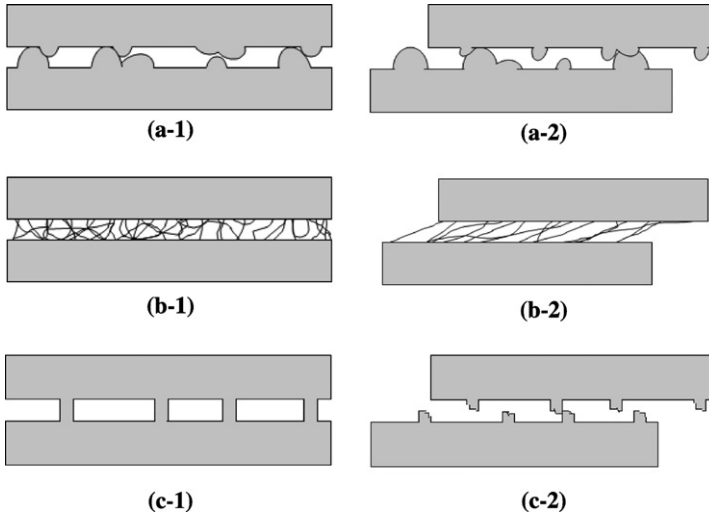
Fig. 68. Different models for sliding between tiles; inter-tile layer formed by (a) asperities; (b) organic layer acting as viscoelastic glue; (c) mineral bridges.

The three models for the inter-tile region are shown in Fig. 68. The asperity model by Evans et al. [147] and Wang et al. [126] is represented in Fig. 68a. Fig. 68b shows the viscoelastic glue model according to which the tensile strength is the result of stretching of molecular chains whose ends are attached to surfaces of adjacent tiles. Fig. 68c shows the mineral bridge model, consistent with our observations. The sliding of adjacent tiles requires the breaking of bridges and the subsequent frictional resistance, in a mode akin to the Wang–Evans [126,147] mechanism. It is possible that all three mechanisms act in a synergetic fashion in which broken bridges act as asperities which are further reinforced by the viscoelastic organic glue [112,141].

6.2.2. Conch (Strombus gigas) shell

The conch shells, with a spiral configuration, have a structure that is quite different from the abalone nacre. Fig. 69a shows the overall picture of the well known *S. gigas* (pink conch) shell. In contrast with the abalone shell, which is characterized by parallel layers of tiles, the structure of the conch consists of three macrolayers which are themselves organized into first-order lamellae, which are in their turn, comprised of second-order lamellae. These are made up of tiles named, in Fig. 69a, third-order lamellae in such a manner that successive layers are arranged in a tessellated ('tweed') pattern. Ballarini et al. [194] described nanoscale components in this structure beyond the third order lamella. The three-tiered structure is shown in Fig. 69b. This pattern, called *cross-lamellar*, is reminiscent of plywood or crossed-ply composites and has been studied extensively by Heuer and coworkers [131]. The crossed lamellar microstructure consists of lath-like aragonite crystals (99,9% of weight) and a tenuous organic layer (0.1 wt%). The "plywood" structure shown in Fig. 69b [11] consists of three macroscopic layers; the inner (closest to the organism), middle and outer layer, which are of relatively uniform thickness within the last whorl. This was further characterized by Hou et al. [153]. Kamat et al. [154] showed that the result of this structure is a fracture toughness exceeding that of single crystals of the
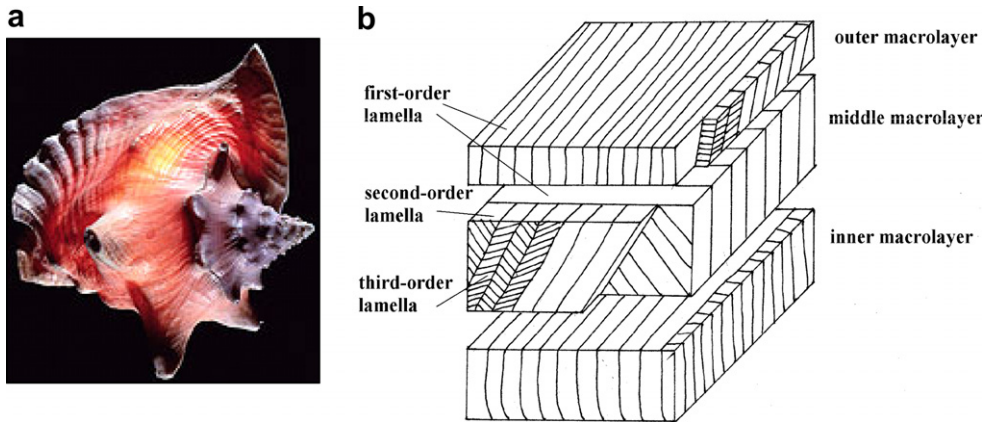
Fig. 69. Conch shell; (a) overall view; (b) schematic drawing of the crossed-lamellar structure. Each macroscopic layer is composed of first-, second- and third-order lamellae (from Menig et al. [11]).

pure mineral by two to three orders of magnitude. An interesting analogy with a large dome structure is shown in Fig. 70. The Florence dome, built by the architect Bruneleschi, uses a tessellated array of long bricks which have a dimensional proportion similar to the
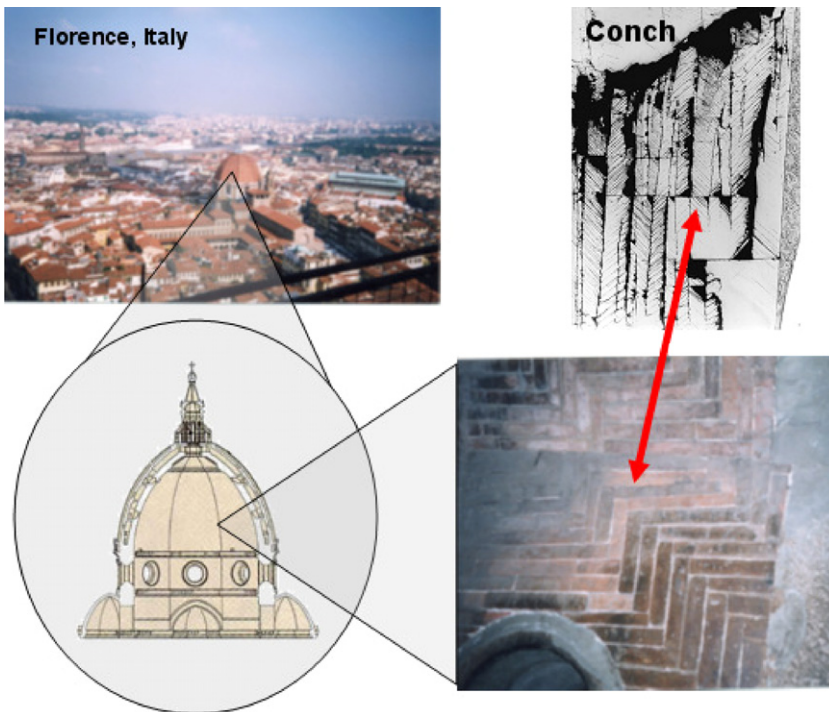

Fig. 70. Tesselated bricks on Brunelleschi's Duomo (Florence, Italy) and equivalent structure of conch shell.

tiles in conch. This arrangement provides the dome with structural integrity not possible before that time.

These three layers are arranged in a 0°/90°/0° direction. So-called first-order lamellae compose each macroscopic layer and are oriented ±35–45° relative to each other. In each first-order lamella are long thin laths stacked in parallel known as second-order lamellae. These second-order lamellae in turn consist of single crystal third-order lamellae. Fine growth twins at an atomic scale layer each third-order lamella [155]. The organic matrix with its 0.1 wt% has only been observed by TEM as an electron dense layer that envelops each of the third order lamellae [144]. Kuhn-Spearing et al. [155] measured flexural strength, crack-density evolution and work of fracture for wet and dry specimens of the *S. gigas* conch shell. Four-point-bending tests in two different orientations were conducted parallel and perpendicular to the shell axis. They report that the tensile strengths of crossed-lamellar shells are 50% lower than the strongest shell microstructure (nacre). Average apparent flexural strengths for dry and wet crossed-lamellar samples in the parallel orientation were found as 156 ± 22 MPa and 84 ± 49 MPa, respectively. The average apparent flexural strength of the perpendicular wet and dry samples was 107 ± 38 MPa. The results of Kuhn-Spearing et al. [155] on the fracture of these shell structures suggest that the mechanical advantage is an increased fracture resistance, in addition to a previously observed increased hardness. The tests revealed a work of fracture of 4 ± 2 J/m^2 for dry and 13 ± 7 J/m^2 for wet samples tested in parallel orientation. These values are much higher than those reported for nacre (0.4 J/m^2 for dry and 1.8 J/m^2 for wet samples [133]). The increased fracture resistance for wet samples is correlated to a decreased interfacial strength that results in more extensive cracking pattern. Menig et al. [11] also performed a series of mechanical tests on the conch shell. Fig. 71 presents the Weibull statistical analysis of conch in (a) quasi-static compression and (b) dynamic compression. In quasi-static compression the conch shell exhibited a failure probability of 50% [$F(V) = 0.5$] at 166 MPa and 218 MPa for the perpendicular and parallel direction of loading, respectively. In dynamic loading the 50% failure probabilities of the conch shell are found at 249 MPa and 361 MPa perpendicular and parallel to layered structure, respectively.

The fraction of organic material in conch is lower than in abalone: ∼1 wt%, vs. 5 wt%. The strategy of toughening that has been identified in the conch shell is the delocalization of crack by distribution of damage [11]. An example of how a crack is deflected by the alternative layers is shown in Fig. 72a. The fracture surface viewed by SEM shows the cross-lamellar structure (Fig. 72b) in a clear fashion. The lines seen in the damaged surface of conch shown in Fig. 70 indicate sliding of the individual, tiles. The absence of a clear crack leads to a significant increase in the fracture energy in comparison with monolithic calcium carbonate.

However, as with the abalone nacre, the structural hierarchies ranging from nano to macro are all responsible for the over all mechanical response of the shell. The crack deflection within the microstructure of tessellated tiles is only part of a larger crack delocalization mechanism. When the crack reaches the inner macrolayer it can again orient itself into an 'axial splitting' configuration (seen in Fig. 72a). The 0°/90°/0° architecture arrests the easy-to-form channel cracks and leads to additional channel cracking. Due to 45° second-order lamellar interfaces the channel cracks (between first-order interfaces), which eventually penetrate the middle macroscopic layer, are deflected and failure is non-catastrophic. It is this complex layered architecture that is responsible for improved toughness over that of nacreous structures [144].
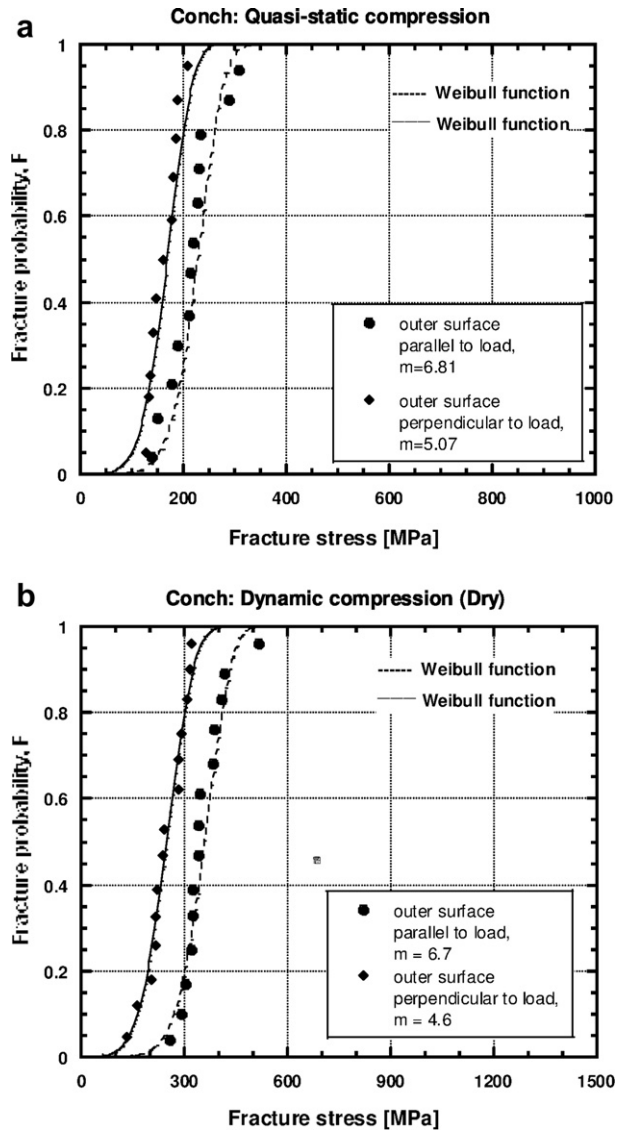
Fig. 71. Weibull plots of conch shell in (a) quasi-static compression, and (b) dynamic compression (from Menig et al. [11]).

Fractographic observations identify delocalized damage in the form of multiple channel cracks, crack bridging, crack branching, and delamination cracking. This increases the total crack area and frictional dissipation. Fig. 73 shows schematically channel- and delamination cracks in a bend specimen-loading configuration used by Kuhn-Spearing et al. [155]. The many interfaces between aragonite grains in the crossed-lamellar structure provide a multitude of places for energy dissipation.

Laraia and Heuer [128] performed four-point bending tests with S. gigas shells while the shell interior and exterior surfaces were the loading surfaces and were not machined out.
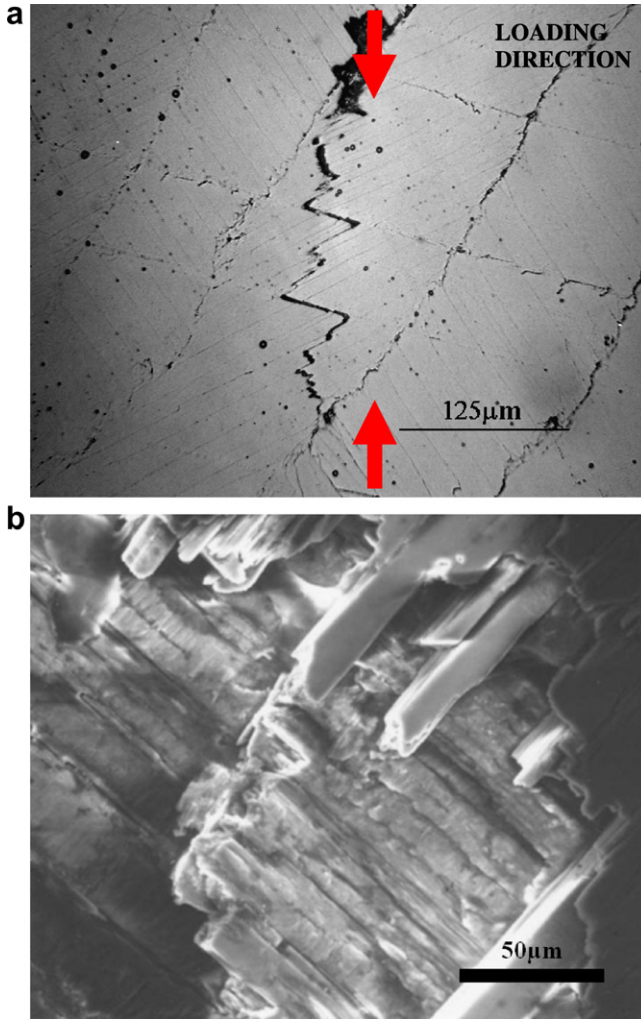
Fig. 72. Fracture patterns in conch shell; (a) crack delocalization shown in polished section; (b) scanning electron micrograph of fracture surface showing cross lamellar structure (from Lin et al. [10]).

They found flexural strengths of about 100 MPa. With the exterior surface loaded in tension, the failure occurred catastrophically; however, when loaded with the interior surface in tension this kind of failure did not occur. This confirms the anisotropy of shells with crossed-lamellar microstructure, which leads to "graceful failure" in some orientations. Another indication for the anisotropy mechanical behavior of crossed-lamellar shells can be found in Curry and Kohn [156]. They found flexural strength (in three-point bending) of shells of *Conus striatus* in the range of 70–200 MPa depending on the orientation.

Laraia and Heuer [144] found that the resistance to crack propagation is due to several toughening mechanisms simultaneously. These are crack branching (i.e. the microstructure forces the cracks to follow a tortuous path), fiber pullout, microcracking (microcracks follow interlamellar boundaries), crack bridging and microstructurally induced crack arrest.
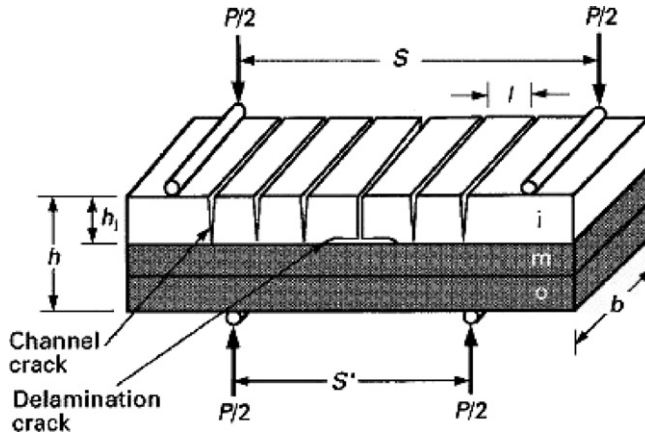
Fig. 73. Bend specimen loading configuration, shown relative to the material architecture, with a typical pre-failure cracking pattern (channel and delamination cracks) (from Kuhn-Spearing et al. [155]).

Kamat et al. [157] found that the synergy between tunneling cracks and crack bridging was the source of a additional factor of 300 in fracture energy. They also carried out microindentation experiments. However, for applied loads from 0.1 to more than 10 kgf the indentations failed to produce radial cracks when applied to polished interior shell surfaces. The damaged zones were elongated and the crack followed first-order lamellae.

The fracture surfaces are shown in Fig. 74. It seems that the conch is designed for maximization of energy dissipation regardless of the cost in terms of crack formation. This allows the mollusk to survive the attack of a crab or another impact event. The mollusk can hide while repairing its damaged material. This designing strategy is also desirable for armor, however, not necessarily appropriate for structural composites where lifetime and maintenance are also issues [154].

6.2.3. Giant clam (Tridacna gigas)

The giant clam (*T. gigas*) can grow its shell to widths greater than 1 m, with weights of over 340 kg [158]. The large amount of shell material produced has made the giant clam of interest in both contemporary, as well as historical context. Moir [159] documented the use of this shell as the raw material for applications such as blades for wood cutting tools in ancient and present day Takuu Atoll dwellers of Papua New Guinea. The structure of the shell has a low level of organization in comparison to other shells, yet its sheer mass results in a strong overall system. The protective shell consists of two distinct regions, an outer white region and an inner translucent region.

A detailed study of the structure of the giant clam shell and the role of that structure on the mechanical strength of the shell was carried out by Lin et al. [10]. The outer region acts as the animal's first line of defense against the harsh environment. This region appears to comprise approximately one third of the shell thickness and is formed from dense structured layers of aragonite needles approximately 1–5 μm in length [159]. Growth bands, which extend perpendicular to the direction of shell growth, are thought to contain a thin organic matrix, partially separating layers of the crossed lamellar aragonite needles [160]. The structure of the outer region of the shell, presented in Fig. 75, somewhat resembles the
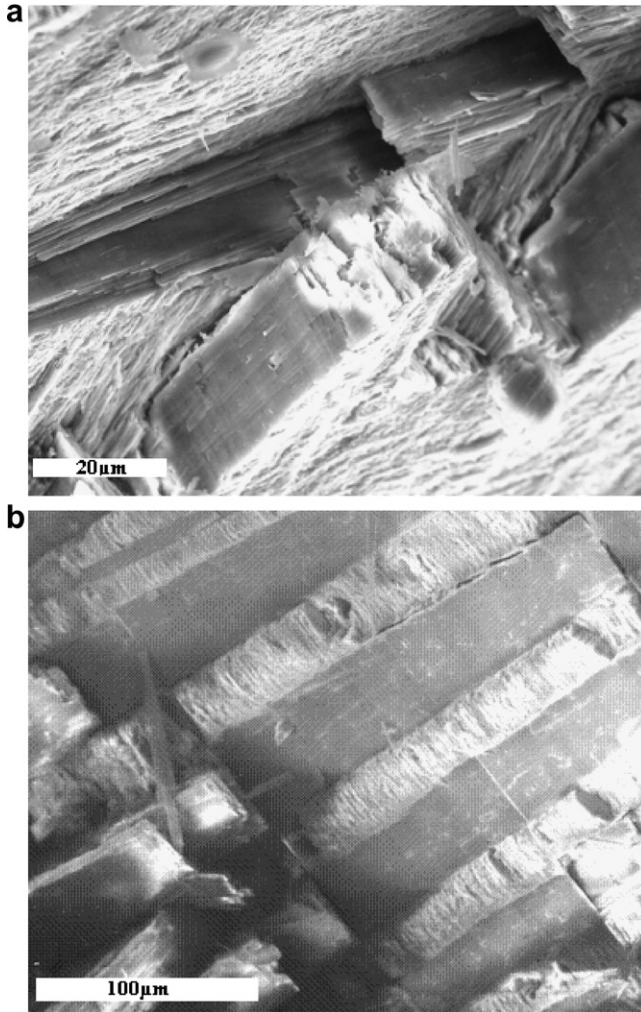
Fig. 74. Fracture surface of *S. gigas* (a) parallel to growth direction, (b) perpendicular growth direction (from Lin et al. [10]).

microstructure of the middle macro-layer of conch shell, yet a considerable decrease in organization is observed. Growth bands form first-order lamellae, separating layers of second and third-order lamellae perpendicular to the direction of growth. The second-order lamella is composed of planes, parallel to the growth direction, which separate planes of needles (third-order lamella) with alternating orientation. The directions of needles alternate between $+60°$ and $-60°$ to the direction of growth for each second-order lamella.

Within the inner region of the shell, the microlayered structure is also observed as continuous planes of growth bands. These layers separate approximately 3–7 μm of inorganic material and span normal to the direction of shell growth. Long single crystals of aragonite travel along the direction of growth and are not interrupted by growth bands. This inner region appears more transparent than the outer region and contains a high concentration of flaws traveling along the single columnar crystal interfaces. These flaws, in the
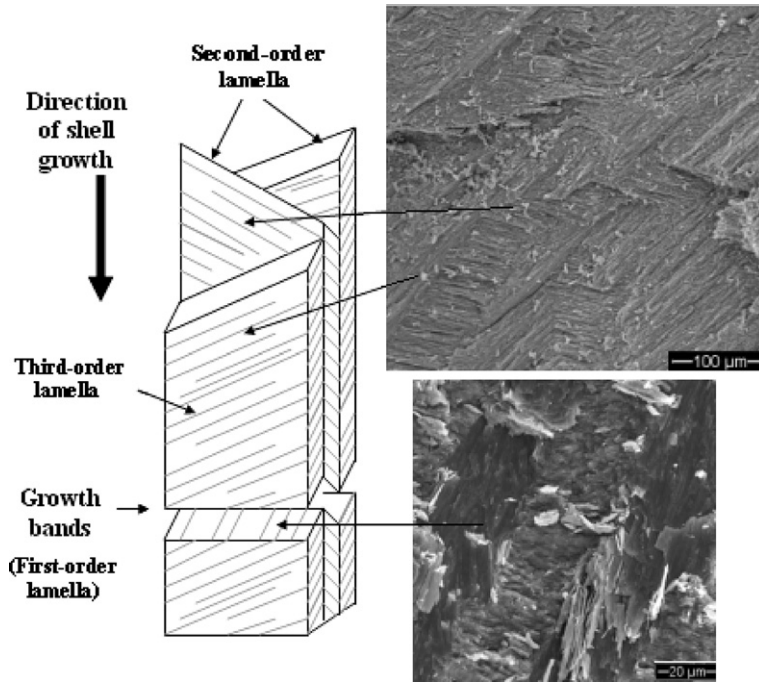
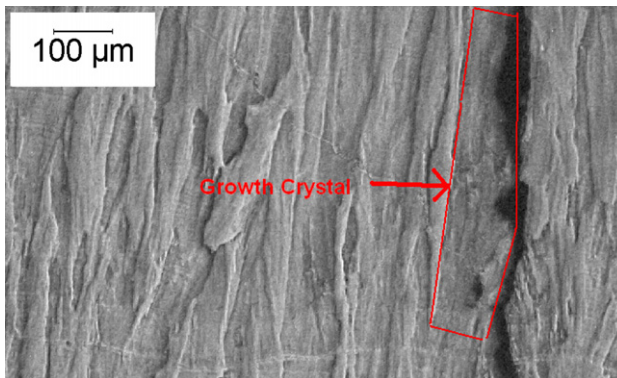Fig. 75. Schematic representation and SEM image of *T. gigas* shell outer region (from Lin et al. [10]).

Fig. 76. Optical micrograph of polished cross-sectional specimen of *T. gigas* shell (inner region), with continuous single crystal facilitating crack propagation (from Lin et al. [10]).

form of microcracks, travel along the direction of growth facilitating crack propagation along abutting interfaces of neighboring crystals. Fig. 76 shows an optical micrograph of the microcracks along columnar crystal interfaces. The observed growth bands in the microstructure do not interrupt the growth of single crystals from one band to the next, and thus have a minimal effect on crack deflection.

Fig. 77a presents the Weibull statistical distribution of giant clam in quasi-static compression. Where the conch shell from Section 6.2.2 had a failure probability of 50% [$F(V) = 0.5$] at 166 MPa and 218 MPa for the perpendicular and parallel direction of loading, respectively, the giant clam shell showed 50% failure probability at 87 MPa and 123 MPa for loading parallel and perpendicular to layered structure, respectively. The abalone shell from Section 6.2.1 outperformed both the conch and the giant clam shells by over twice the compressive strength in quasi-static loading. With failure probabilities of 50% being reached at 235 MPa and 540 MPa with loading parallel and perpendicular
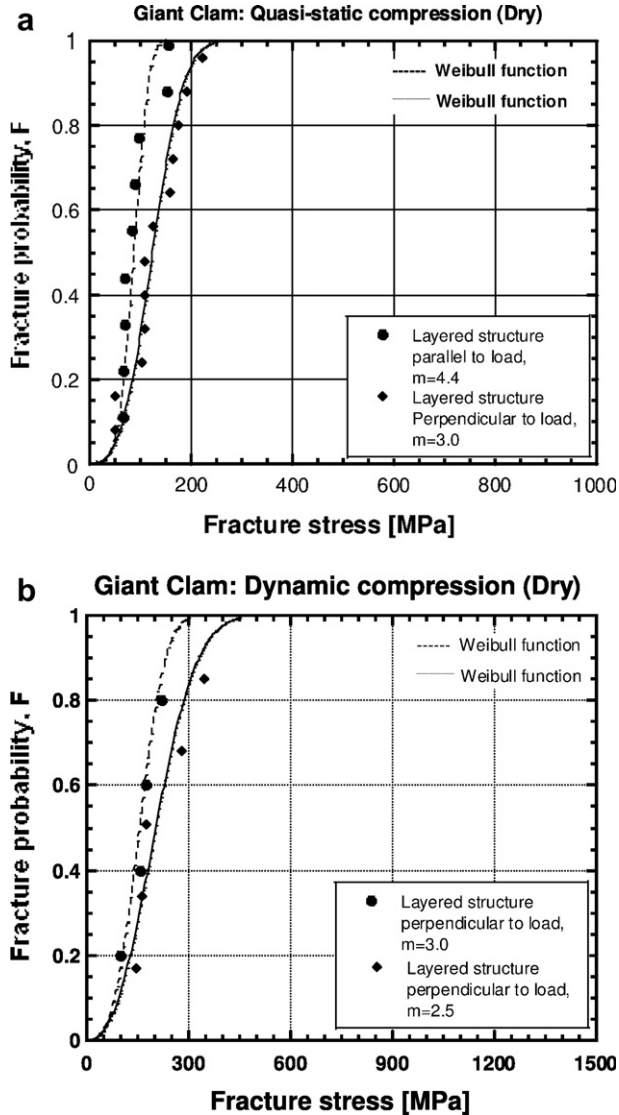

Fig. 77. Weibull plots of *T. gigas* shells in: (a) quasi-static compressive loading, (b) dynamic compressive loading (from Lin et al. [10]).

Table 8
Comparison of compressive strengths at 50% failure probability for various shells

Species	50% Failure probability stress (quasi-static loading)		50% Failure probability stress (dynamic loading)	
	Perpendicular	Parallel	Perpendicular	Parallel
Conch	166 MPa	218 MPa	249 MPa	361 MPa
Giant Clam	123 MPa	87 MPa	202 MPa	154 MPa
Red Abalone	540 MPa	235 MPa	735 MPa	548 MPa

to layered structure, respectively, the abalone also exhibits the highest difference in strength between loading directions, consistent with the level of microstructure anisotropy.

A similar trend in dynamic compression strength is observed with the compressive strength of abalone approximately twice that of the conch shell, and the conch shell having approximately twice the compressive strength of the giant clam shell. Shown in Fig. 77b the 50% failure probabilities of giant glam in dynamic compression are found at 154 MPa and 202 MPa for parallel and perpendicular loading directions, respectively. This is far less than both the conch and the abalone shells. It is clear that all three materials experience greater compressive strengths in dynamic loading than in quasi-static loading; these results have been listed in Table 8.

The microstructure of the giant clam shell consists of both an inner, translucent brittle region, with relatively low organization, and an outer white, tougher region, which resembles the shell of the S. gigas (conch). The inner region fails at the crystal interfaces seen in Fig. 75 through a mechanism of axial splitting. Initial microcracks within this region extend and coalesce under applied stress, resulting in the failure of the shell samples.

It is important to note that the mechanical strength of the outer solid white region of the clam shell is over 10 times that of the inner translucent region. Fig. 78 shows scanning electron microscopy of the fracture surfaces of the shell in bending (a) perpendicular to growth bands, and (b) parallel to growth bands; this directional dependency has been further clarified in Table 9. A cross lamellar structure can be seen in Fig. 78a, in which the horizontal line marked with an arrow is a growth band extending perpendicular to the fracture surface. The alternating planes of fibrous crystals travel at 30° angles to the planes of the growth bands. Separation of material at the growth band interfaces occurred in shear during bending loading perpendicular to planes of growth interruption. Fig. 78b shows the fracture surface of a sample under tension in bending. Separation occurred across a single growth band, and second-order lamellae are observed as planes of fibers traveling perpendicular to the fracture surface and alternating in fiber angles. The surface separated cleanly at a single growth band across the entire sample. These observations indicate that separation occurs at the growth band interfaces in both loading directions, parallel and perpendicular to the growth direction.

6.3. Shrimp hammer

The mantid shrimps are predatory on hard-shelled animals such as clams, abalones, and crabs using their limbs as hammers. Although the smashing shrimp makes thousands of energetic strikes over months, the hammer is rarely damaged. The composition and structural features of the smashing limbs have been studied by Currey and his co-workers [167].
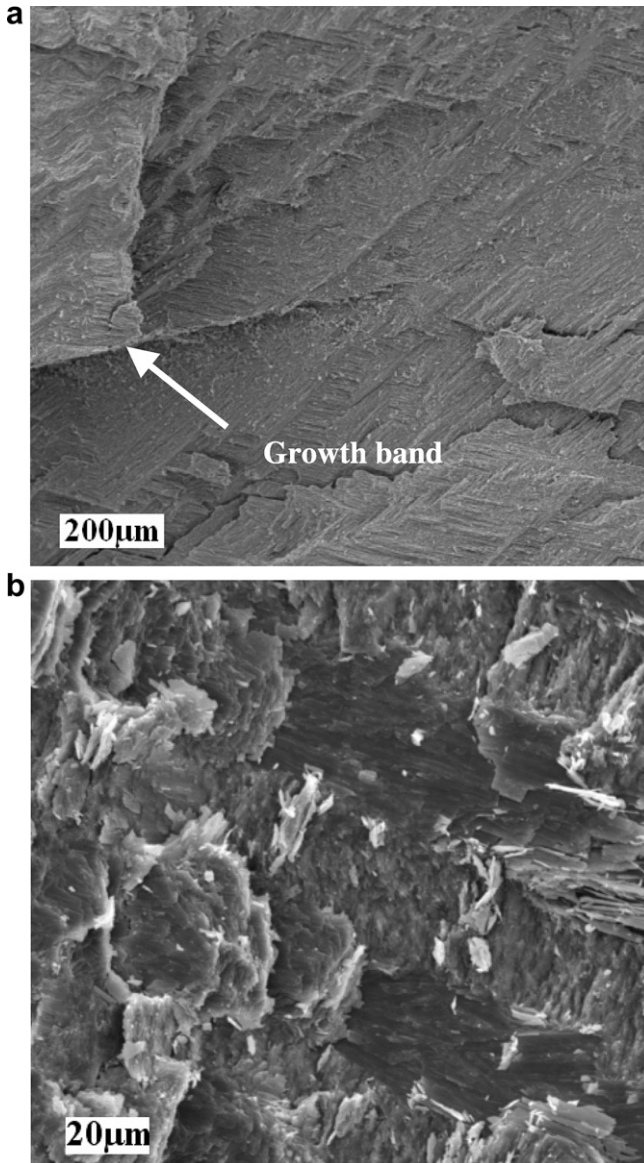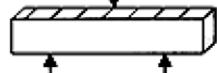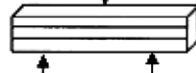
Fig. 78. Fracture surface of *T. gigas* under bending (a) perpendicular to growth bands, (b) parallel to growth bands (from Lin et al. [10]).

Fig. 79a shows a typical mantid shrimp and its smashing action. The smashing limb consists of the merus, the propodite, and the dactyl. The dactyl is the part used to strike the prey and is highly mineralized. Fig. 79b is a schematic presentation showing the cross-section of propodite and dactyl. Both propodite and dactyl show three regions: soft tissue in the central, a layer of fibrous chitin cuticle in between, and a layer of heavily calcified region on the outside. The dactyl used to smash hard-shelled prey has a thick, heavily

Table 9
Flexure strength for various shells [10]

Species	parallel direction, outer surface perpendicular to loading direction Average Bending Stress	layered structure perpendicular to loading direction Average Bending Stress	layered structure parallel to loading direction Average Bending Stress
Conch	74 MPa	29 MPa	–
Giant Clam (outer region)	39.9 MPa	79.6 MPa	–
Giant Clam (inner region)	–	7.86 MPa	–
Red Abalone	–	197 MPa	177 MPa

calcified layer, while the propodite has much thinner heavily calcified layer. The microhardness measurements (Fig. 79c) indicate that the dactyl becomes much harder toward outer surface. The increase in hardness is associated with the increased mineralization of the cuticle as well as the replacement of calcium carbonate by calcium phosphate. Fig. 79d shows the relationship between the microhardness and the ratio of phosphorus
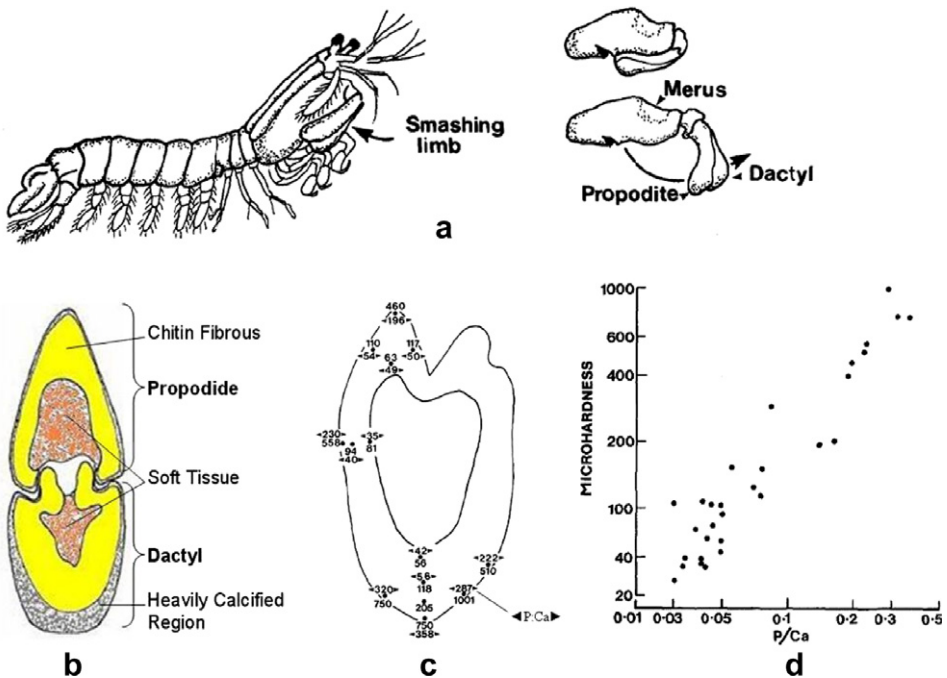

Fig. 79. (a) The smashing limb and typical smashing action of mantid shrimp, *Gonodactylus chiragra*. (b) The cross-section of the propodite and dactyl shows three regions: heavily calcified outer layer, fibrous region, and inner soft tissue. (c) Values for microhardness and values for P:Ca (multiplied by 1000). (d) Relationship between microhardness and the P:Ca ratio (from currey et al. [167]).

to calcium. There is a strong and linear relationship between the hardness and the P:Ca ratio. The smashing limb, or dactyl, of the mantid shrimp is a natural composite which is composed of hard, brittle, highly-calcified outer layer and relatively soft, ductile, fibrous inner layer. The fibrous region between the hard outer layer and soft tissue not only absorbs the kinetic energy but prevents cracks from propagating through the cuticle. The outer layer has a sufficient thickness of heavily calcified cuticle with a significant amount of calcium carbonate replaced by calcium phosphate. The hammer of the mantid shrimp is well designed to break hard objects and is an optimized biological ceramic composite.

6.4. Marine worm teeth

It was discovered in 1962 by Lowenstam [168] that the teeth in chitons (mollusk worms) contained iron oxide in the magnetite structure (Fe_3O_4). This discovery was followed by another one, by Lichtenegger et al. [169]: the carnivorous marine worm *Glycera* has teeth that contain a copper mineral atacamite [$Cu_2(OH)_3Cl$]. These minerals are contained in mineralized fibrils, as shown in the schematic picture of a tooth (Fig. 80a). These mineralized fibrils are similar to the ones forming in dentin and bone. Again, we have a composite structure with hard fibers embedded in a softer protein matrix. The degree of mineralization varies along the tooth and the hardness and the elastic modulus are directly related to the mineralization. Lichtenegger et al. [169] used the Halpin–Tsai equation well known in the composites field to calculate the hardness and Young's modulus upper and
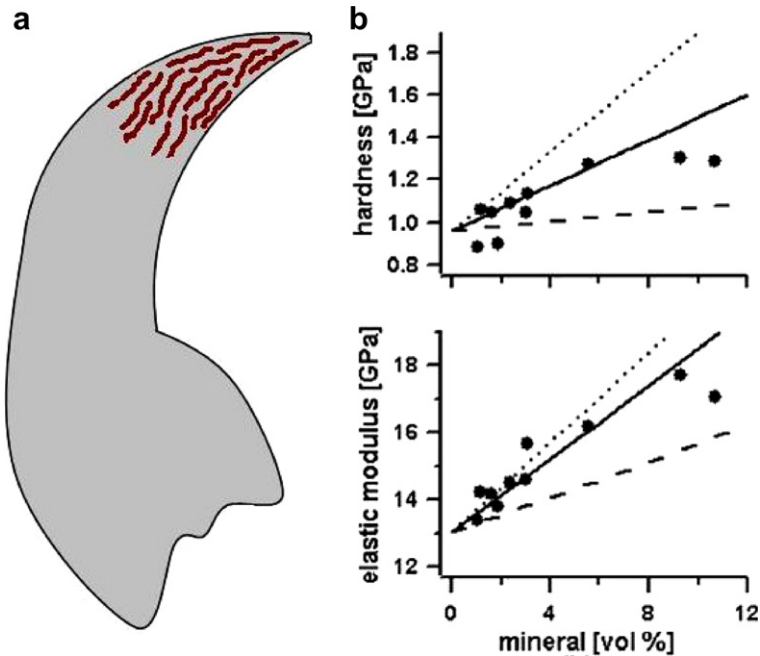

Fig. 80. (a) Schematic model of mineralized fibers in *Glycera* jaws. (b) Hardness and elastic modulus versus mineral content. Dashed and dotted lines: Halpin–Tsai boundaries (from Lichtenegger et al. [169]).

lower bounds. The upper bound corresponds to loading parallel to fiber direction; the lower bound corresponds to loading perpendicular to it. The calculations as well as experimental results are shown in Fig. 80b. The Halpin–Tsai upper and lower bounds are indicated by dotted and dashed lines in Fig. 80b.

6.5. Bone

Bone is a ceramic (calcium phosphate, or hydroxyapatite)-polymer (collagen) composite. Bone is the structural component of our body. It also has other functions, but we will concentrate on the mechanical performance here. There are two principal types of bone:
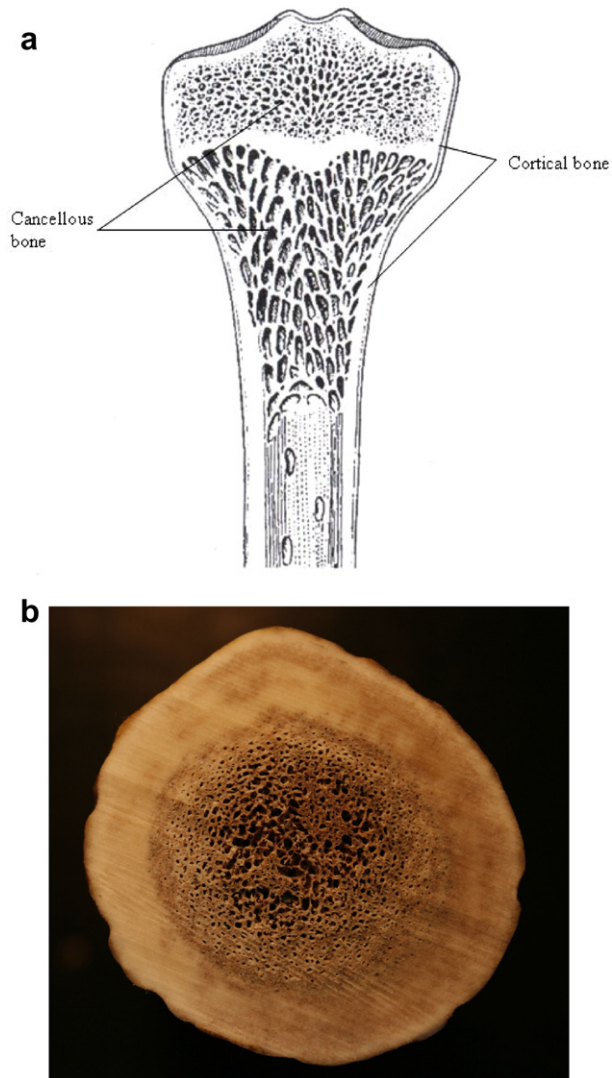

Fig. 81. (a) Longitudinal section of a femur (from Mann [7, Fig. 2.9, p. 11]). (b) Photograph showing a cross-section of elk antler.

cortical (or compact) and cancellous (or trabecular, or porous). Cortical bone is found in long bones (femur, tibia, fibula, etc.). Cancellous bone is found in the core of bones and in flat bones.

6.5.1. Structure

Fig. 81a shows the structure of a long bone. The surface regions consist of cortical bone; the inside is porous and is called cancellous bone. Fig. 81b is a cross-sectional picture of deer antler. The porosity reduces the strength of the bone and antler, but also reduces their weight. They are shaped in such a manner that strength is provided only where it is needed. The porosity of cancellous bone provides interesting mechanical properties. The mechanical strength is determined by the porosity and the manner in which this porosity is structured. The pores also perform other physiological functions and contain the marrow. Thus, bone is a true multifunctional material.

6.5.2. Elastic properties

Bone is a composite of collagen, hydroxyapatite, and water. Hydroxyapatite is a calcium phosphate with the following composition:

$$Ca_{10}(PO_4)_6(OH)_2$$
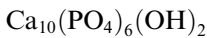
Water corresponds to 15–25 vol% of the bone in mammals. The structure of bone is only partially understood and is, as shown in Fig. 3 hierarchical. The Young's modulus of cortical bone varies from 8 to 24 GPa. This is much lower than that of hydroxyapatite, which has a Young's modulus of approximately 130 GPa and a strength of 100 MPa. Although collagen is not linearly elastic, we can define a tangent modulus; it is approximately 1.25 GPa. The broad variation mentioned earlier is seen clearly. There have been several attempts to model the elastic modulus of bone. They are based on our knowledge of composites. We have two limiting conditions: when the loading is carried out along the reinforcement direction:

Voigt model:

$$E_b = V_{ha}E_{ha} + V_cE_c \tag{29}$$

When it is carried out perpendicular to the reinforcement direction:

Reuss model:

$$1/E_b = V_{ha}/E_{ha} + V_c/E_c \tag{30}$$

The indices b, ha, and c refer to bone, hydroxyapatite, and collagen, respectively. In bone, the orientation of the collagen fibers and mineral is difficult to establish. They are not all aligned, which adds to the complexity. Taking the values given above and applying the Voigt and Reuss equations leads to, for 50 vol% collagen:

$$E_b \text{ (Voigt)} = 50 \text{ GPa}$$
$$E_b \text{ (Reuss)} = 4 \text{ GPa}$$

This is an unacceptably broad range and more elaborate models, discussed below, are needed. Fig. 82 shows the Young moduli for a number of bones with mineral fractions varying from 0.28 to 0.56. The experimental results are compared with the Voigt and Reuss averages. Experimental values [2] (Fig. 82) fall between the two limits set by the Reuss and Voigt averages. The hydroxyapatite content of bone varies from animal to ani-
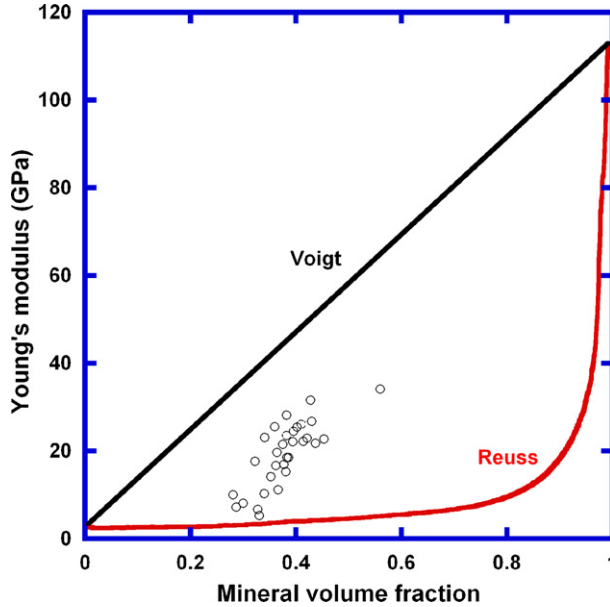
Fig. 82. Effect of mineral volume fraction on Young's modulus of bones from many animals (reproduced from Currey [2, Table 4.3, p. 130]).

mal, depending on function. Antlers have a low mineral content (∼0.3). For instance, an agile animal like a gazelle has bones that have to be highly elastic. Thus, the hydroxyapatite level is fairly low (around 50% by weight). Collagen provides the elasticity. On the other hand a whale has bones with a much higher mineral content (∼80% by weight). An aged professor is somewhere in between. Note that the density of hydroxyapatite is approximately twice that of collagen (∼1 g/cm^3).

A more realistic model was proposed by Katz [170]. It takes into account the misorientation between the external loading axis and the collagen fibrils. He considered different orientations of collagen fibrils, each one with a fraction f_i and angle φ_i with the loading axis. The Young's modulus is

$$E_b = \frac{E_c V_c (1 - v_c v_b)}{1 - v_c^2} + \sum E_{ha} V_{ha} f_i \left(\cos^4 \varphi_i - v_b \cos^2 \varphi_i \sin^2 \varphi_i \right) \tag{31}$$

The Katz equation is essentially a Voigt model that ascribes a contribution to E_b decreasing rapidly with misorientation φ_i because of the fourth power dependence of the cosine of φ_i.

This was the basis of Jäger and Fratzl's [171] model for the elastic modulus, that considers that minerals and collagen can overlap. The mineralized turkey leg tendon is a fascinating material; we have all encountered these long and stiff rods at Thanksgiving dinners and a few of us have wondered why they are so different from chicken bones. These mineralized tendons (connecting bone to muscles) are ideal specimens for the investigation of the strength of partially mineralized bone and for the establishment of their structures. The collagen fibrils are arranged in a parallel fashion and the degree of mineralization increases with the age of the turkey. The minimum degree of mineralization of the turkey leg tendon

is 0.15, which is substantially less than bone. The mineralized turkey tendons enable the understanding of how the hydroxyapatite and collagen interact.

The physical model applied by Jäger and Fratzl [171] is shown in Fig. 83. The collagen fibrils are arranged in concentric layers. Embedded into them are the bone platelets. These mineral crystals have nanoscale size, the thickness being typically on the order of 1 nm, the length being approximately 60–100 nm. This agrees with the picture shown in Fig. 3. The partially mineralized bone can be modeled as a composite in which the reinforcement (hydroxyapatite crystals) is essentially rigid and the continuous collagen matrix carries the load. The degree of mineralization, Φ, is defined as

$$\Phi = \frac{ld}{(l+a)(b+d)} \tag{32}$$

where a is the overlap between the crystals, b is the lateral distance between them, and l and d are the dimensions of the mineral platelets. All parameters are given in Fig. 83b.
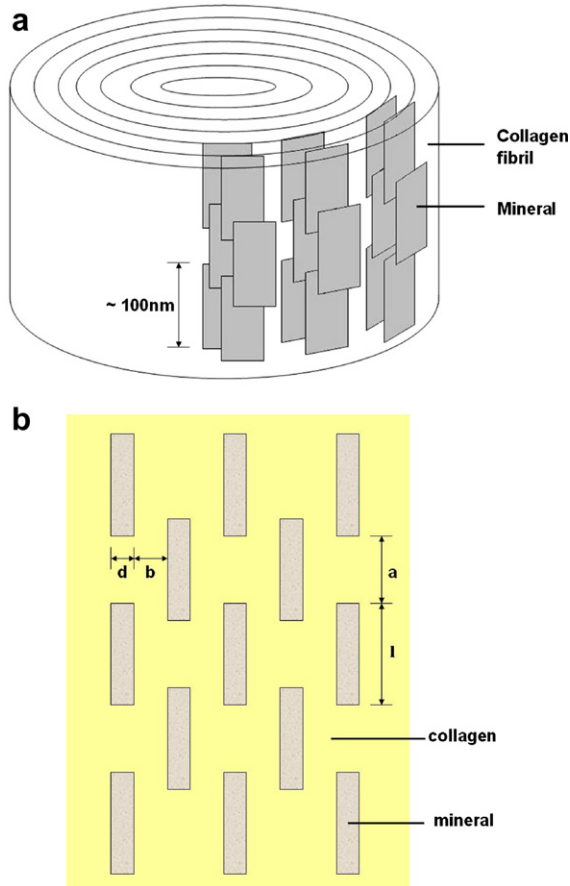

Fig. 83. (a) Schematic drawing showing the 3D arrangement of mineral platelets in a collagen matrix. (b) The staggered arrangement of mineral platelets. The dimensions of the mineral l and d, the distances between them a and b, are indicated (reproduced from Jäger and Fratzl [171, p. 1739, Fig. 3]).
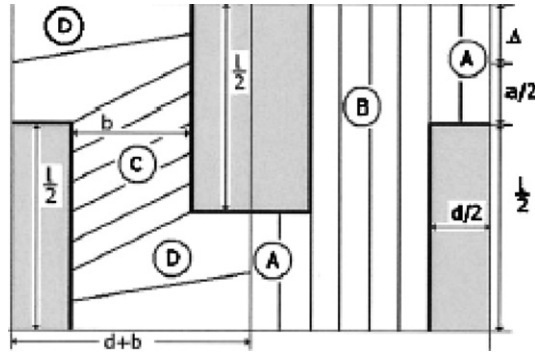
Fig. 84. Two adjacent elementary cells in the staggered model showing the regions of tensile (A and B), and shear stresses (C and D) respectively (from Jäger and Fratzl [171, p. 1740, Fig. 4]).

The elastic modulus is considered as comprised of contributions from four regions: (a) the tensile regions A and B and (b) the shear regions C and D as shown in Fig. 84. The Young's modulus, considering these four contributions, was found to be

$$E' = E/E_C = E_1 + E_2 + E_3 + E_4 \tag{33}$$

where E_C is the Young's modulus of collagen and E_1 to E_4 are the contributions from regions A to D, respectively.

Thus,

$$\frac{E}{E_c} = \frac{d(l+a)}{ab} + \left(1 + \frac{l}{2a}\right) + \frac{\gamma(l-a)(l+a)}{4b^2} + \frac{\gamma a(l+a)}{2b(2b+a)} \tag{34}$$
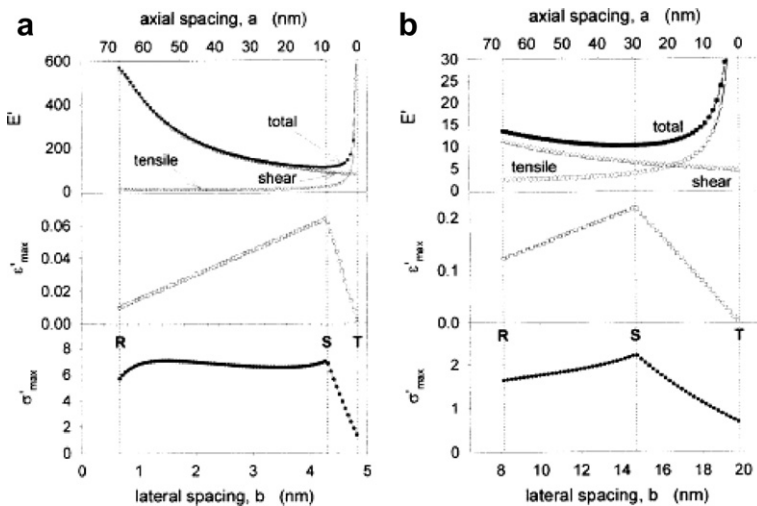

Fig. 85. Results for the elastic modulus, E', the maximum strain, ε'_{max}, and the maximum stress, σ'_{max}. (a) $\Phi = 0.42$, (b) $\Phi = 0.15$ (from Jäger and Fratzl [171, p. 1742, Figs. 5 and 6]).

The predictions of the Jäger–Fratzl crystal model for two values of Φ (= 0.15, typical of mineralized turkey tendon, and = 0.42, typical of bone) are shown in Fig. 85b and a, respectively. A typical value of crystal thickness $d = 3.5$ nm was taken. The line marked s corresponds to the maximum in σ'_{max}, the maximum elastic normalized to the maximum collagen stress, $(\sigma_{max}/(\sigma_{max})_c)$. The spacing between platelets was varied. It can be seen that the optimal spacing corresponds to $b = 4$ nm for bone and $b = 14$ nm for mineralized turkey tendon. The predicted values of the normalized Young's modulus E' (= 15 for $\Phi = 0.15$ and = 150 for $\Phi = 0.42$) correspond to the experimentally obtained values: 8–15 and 200–400, respectively. Thus, one concludes that the stitching and spacing of mineral platelets is very important in determining the mechanical properties.
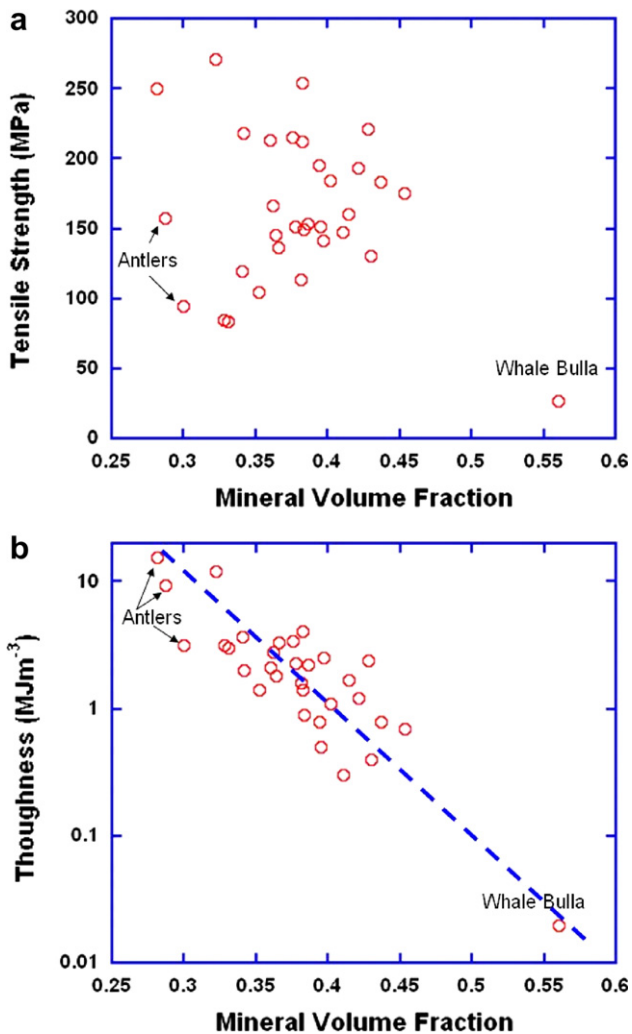

Fig. 86. Effect of mineral volume fraction on (a) tensile strength and (b) toughness (as measured by area under stress–strain curve) of different bones (reproduced from Currey [2, Fig. 4.3, p.132 and Fig. 4.5, p. 135]).

6.5.3. Strength

Both the strength of bone and its toughness, roughly measured by the area of the stress–strain curve to failure, are dependent on the degree of mineralization, as evident in Fig. 86. The correlation between toughness and degree of mineralization, which was developed by Currey [2] from a wide variety of animals, is much better than the one of tensile (3-point
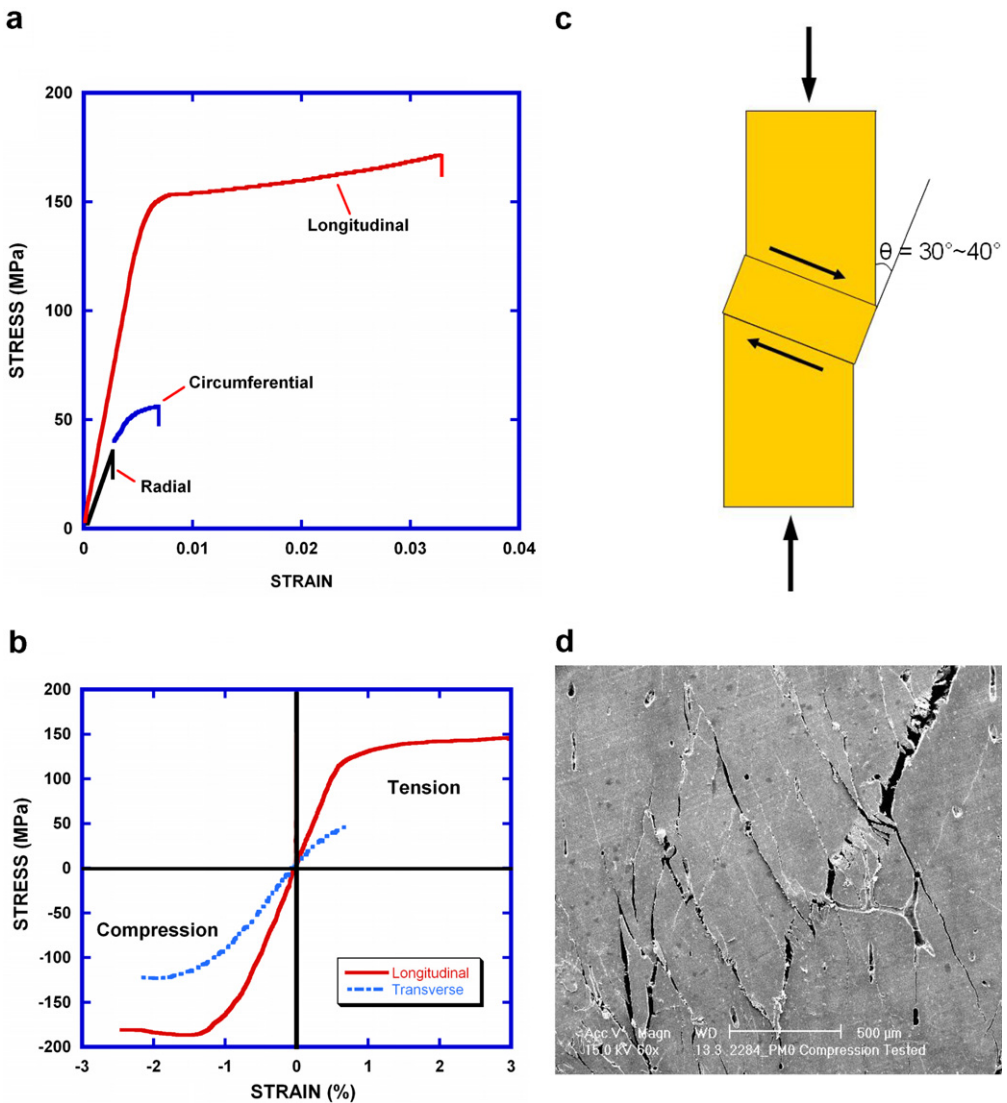
Fig. 87. Effect of orientation on tensile stress–strain curve of bovine fibrolamellar bone (reproduced from Currey [2, Fig. 3.8, p. 89]); (b) tensile and compressive stress–strain curves for cortical bone in longitudinal and transverse directions (reproduced from Lucas et al. [172, Fig. 17.7, p. 268]); (c) schematic drawing showing plastic microbuckling; (d) scanning electron micrograph of horse femur bone after compression test showing buckling (courtesy of R. Kulin and K.S. Vecchio, UC San Diego).

bending) strength, because the latter is also affected by orientation and other factors, as shown below. The point on the right-hand side is the whale bulla. Antlers have a low degree of mineralization and are on the left-hand side.

The longitudinal mechanical properties (strength and stiffness) are higher than the transverse ones. Cortical bone can be considered as orthotropic.

The tensile properties of fibrolamellar bone (compact bone without the Haversian canals) are different along the three directions as is seen in Fig. 87a. The strength achieved
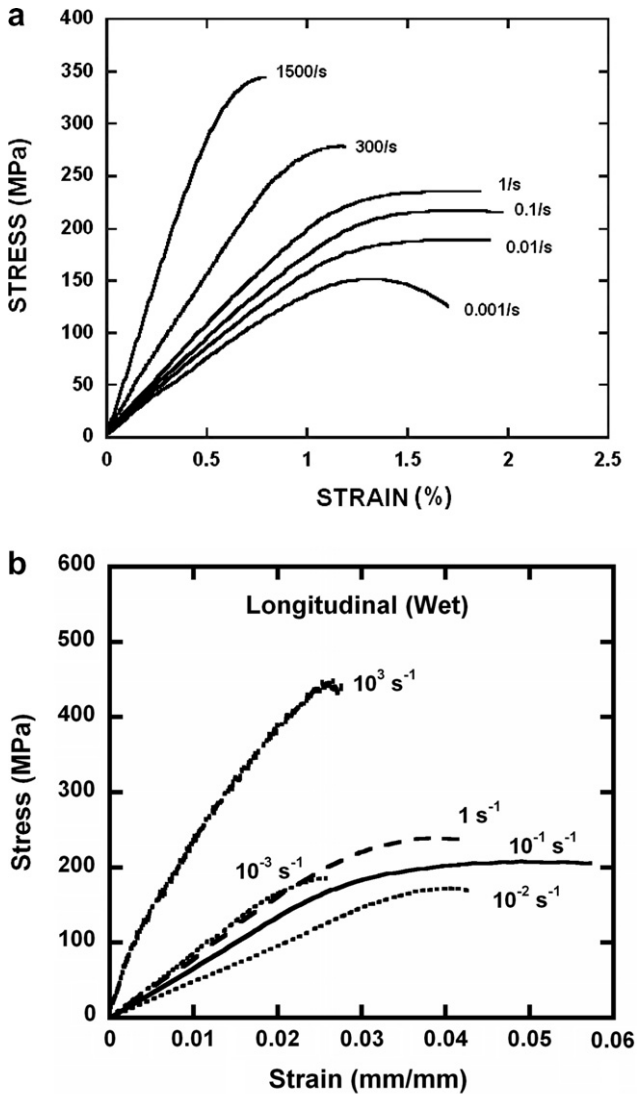

Fig. 88. Strain-rate dependence of tensile response of cortical bone (a) reproduced from McElhaney [174, Fig. 5, p. 1228]; (b) adapted from Adharapurapu et al. [175, p. 1324].

in bone is therefore higher than both hydroxyapatite (100 MPa) and collagen ($\sim$50 MPa), demonstrating the synergistic effect of a successful composite. The tensile strength along the longitudinal direction is three times as high as the one in the circumferential direction. This is the result of the alignment of the collagen fibrils, mineral component, and blood vessel cavities along the longitudinal axis. The strength (30 MPa) and fracture strain are lowest in the radial direction. The energy absorbed to fracture (area under the stress strain curve) in the longitudinal direction is approximately 100 times the one in the radial direction. The bone is, in real life, not loaded radially in a significant way and therefore strength is not needed in that direction.

Fig. 87b provides the tensile and compressive stress–strain curves for cortical bone in longitudinal and transverse directions [172]. The anisotropy is clearly visible. The bone is stronger in the longitudinal direction. It is also considerable stronger in compression than in tension. The compressive response of bone is characterized by a plateau with some softening after the elastic limit is reached (lower curves in Fig. 87b). This plateau is produced, at the structural level, by the formation of shear zones which are the result of localized buckling of the fibrils. Plastic microbuckling is a well-known phenomenon when composites are loaded along the fiber axis and was first described by Evans et al. [173]. This is shown in Fig. 87c. The angle of these buckling regions with the compression axis varies between 30° and 40°. The equivalent process for bone is shown in Fig. 87d. The buckling parameters, applied to abalone nacre as shown in Section 6.5, can also be applied as well to bone. The angles as well as shear strain can be obtained from the Argon and Budiansky–Wu equations (Eqs. (22) and (23)).

The mechanical response of bone is also quite strain-rate sensitive. As the velocity of loading increases, both the elastic modulus and the fracture stress increase. Hence, the stiffness increases with strain rate. The stress–strain curves for human bone at different strain-rate are shown in Fig. 88a [174]. Recent results, by Adharapurapu et al. [175] also confirm that the strain rate dependency of cortical bone as shown in Fig. 88b. The Ramberg–Osgood equation is commonly used to describe this strain-rate dependence of the elastic modulus

$$E = \frac{\sigma}{\varepsilon} = C(\dot{\varepsilon})^d \tag{35}$$

where σ is the stress, ε is the strain, $\dot{\varepsilon}$ is the strain rate, and C and d are experimental parameters. The following are typical values:

Human cranium: $C = 15$ GPa; $d = 0.057$.
Bovine cortical bone (longitudinal): $C = 12$ GPa; $d = 0.018$.

The strain-rate sensitivity of bone is primarily due to the collagen. Polymers have a high strain-rate sensitivity and thermal softening that are well represented by equations developed by Mooney and Rivlin [74,75], Treloar [176], and Arruda and Boyce [177]. Arruda and Boyce used the following formulation to describe the strain-rate sensitivity of strength:

$$\tau_{AP} = \tau \left(\frac{\dot{\gamma}}{\dot{\gamma}_0}\right)^m \tag{36}$$

where $\dot{\gamma}$ is the strain rate, m is the strain-rate sensitivity, τ_{AP} is the applied stress, and the other two terms are material parameters. This is of the same nature power law as the Ramberg–Osgood equation.
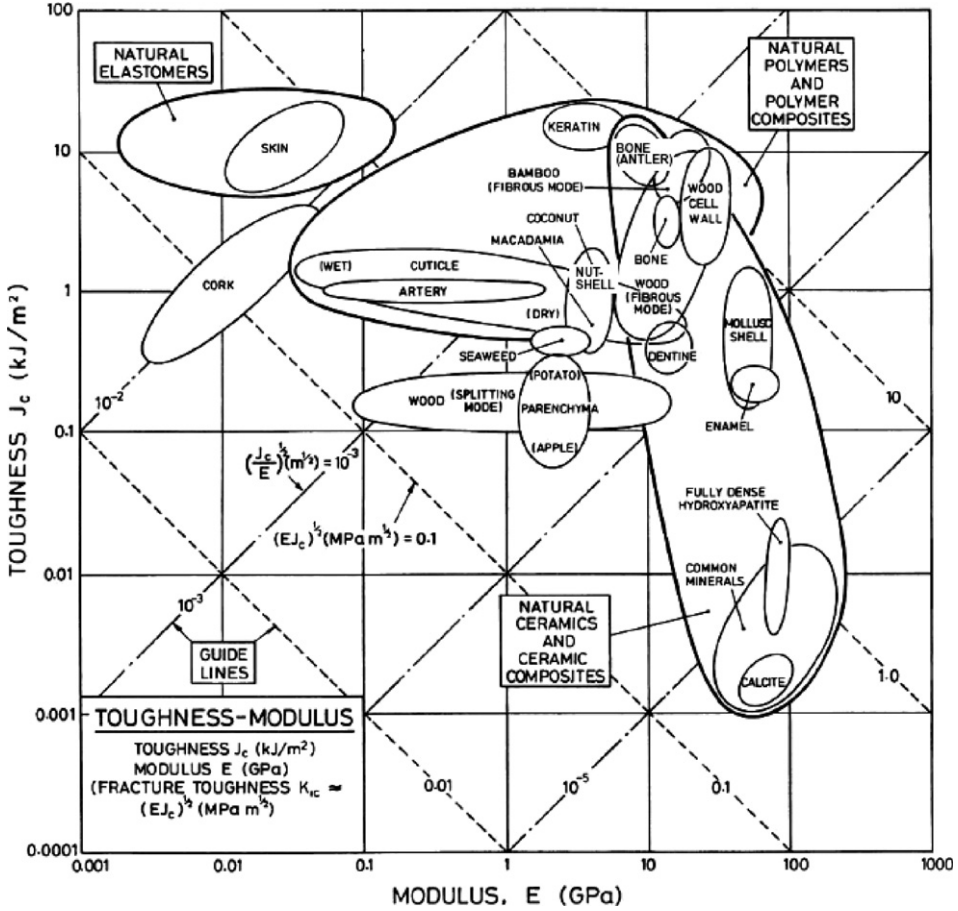
Fig. 89. A material property chart for natural materials, plotting toughness against Young's modulus. Guidelines identify materials best able to resist fracture under various loading conditions (from Wegst and Ashby [17, p. 2171, Fig. 6]).

6.5.4. Fracture and fracture toughness of bone

Fig. 89 gives the *J*-integral (J_c) for a number of biological materials as a function of elastic modulus [17]. The square of fracture toughness (K_c) can be obtained by multiplying J_c by the Young modulus ($K_c = (E \cdot J_c)^{1/2}$). The plot shows lines of equal fracture toughness, drawn as diagonals. As we move toward the right, the toughness increases. Fig. 89 provides a valuable insight into the toughness of biological materials. As seen in Section 6.2, shells have toughness much superior to calcite, although the composition is similar. Similarly, bone has a toughness significantly higher than fully dense hydroxyapatite, and antler is slightly tougher than bone.

Table 10 shows the fracture toughness of bovine bone tested by different research groups [178,179]. Bone owes part of its toughness to the formation of microcracks ahead of the main crack. These microcracks form a process zone which decreases the stress concentration ahead of the crack tip. These microcracks tend to initiate in highly mineralized regions and do not grow to become macrocracks. Rather, they are arrested at internal

Table 10
Fracture toughness of bone

Type bone	Direction	K_{Ic} (MPa m$^{1/2}$)	Source
Bovine femur	Long.[a] (slow)	3.21	Melvin and Evans [178]
	Long. (fast)	5.05	
	Tansv. (slow)	5.6	
	Transv. (fast)	7.7	
Bovine tibia	Long. (very slow)	3.2	Behiri and Bonfield [179]
	Long. (slow)	2.8	
	Long. (fast)	6.3	

[a] Direction of crack propagation.

obstacles, such as Haversian canals. Hard biological materials fracture and the knowledge that we have gained in synthetic materials can be extended to them. The quasi-static fracture toughness of human cortical bone was investigated by Ritchie and co-workers [180]. The key findings are the identification of the principal contributing mechanisms that will be seen later in this section. The fracture toughness, K_{Ic}, varied in the range:

A *greenstick* fracture is incomplete, and the break occurs on the convex surface of the bend in the bone.

A *fissured* fracture involves an incomplete longitudinal break.

A *comminuted* fracture is complete and fragments the bone.

A *transverse* fracture is complete, and the break occurs at a right angle to the axis of the bone.

An *oblique* fracture occurs at an angle other than a right angle to the axis of the bone.

A *spiral* fracture is caused by twisting a bone excessively.
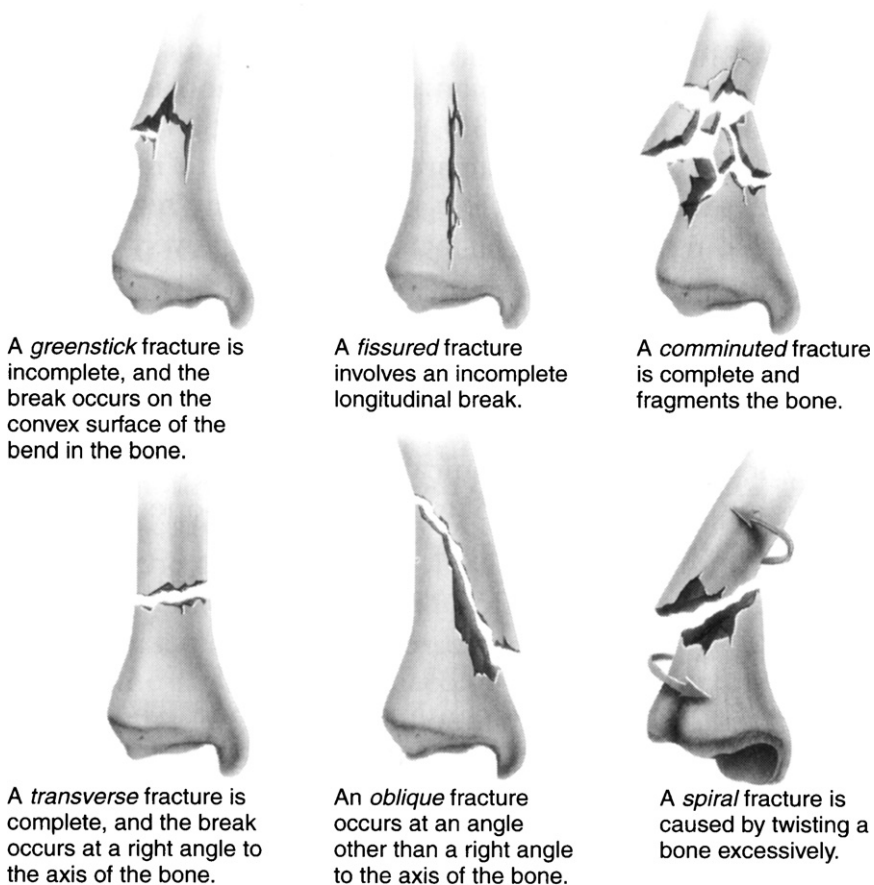
Fig. 90. Six modes of fracture in bone (adapted from Hall [181, Figs. 4–6, p. 102]).

$$2 \text{ MPa m}^{1/2} < K_{Ic} < 5 \text{ MPa m}^{1/2}$$

The fracture and fracture prevention in bone are of extreme importance. We know that bone strength decreases as porosity increases. This is one of the changes undergone by bone with aging. There are many fracture morphologies in bone, depending on the loading stresses, rate of loading, and condition of bone. Fig. 90 presents some of these modalities [181].

Greenstick fracture: This occurs in young bone, which has a large volume fraction of collagen; it can break like a green twig. This zig-zag fracture indicates a high toughness.

Fissured fracture: This corresponds to a longitudinal crack in bone.

Comminuted fracture: many fragments are formed. This is typical of a fracture caused by impact at high velocities. Two factors play key a role. As the velocity of projectile is increased, its kinetic energy increases. This energy is transferred to the bone. The second factor is that at high rates, many cracks are produced simultaneously; they can grow independently until their surfaces intersect. This is the reason why a glass, when thrown on the ground violently, shatters into many small fragments. An additional reason is that the bone becomes stiffer and more brittle as the strain rate is increased. This type of fracture is characteristic of bullet and shrapnel impact.

Transverse fracture: This is a complete fracture approximately normal to the axis of the bone.

Oblique fracture: Complete fracture oblique to the bone axis.

Helical fracture: This fracture is caused by torsional stresses. This type of fracture is known, in the medical community, as spiral. However, this name is not correct, and a helix describes the crack trajectory better than a spiral. Tensile stresses are highest along surfaces making a 45° angle with the torsional stresses.

Gibeling and coworkers [182] studied the fracture toughness in the leg bones (third metacarpal bone) in horses and found that fracture toughness increases with crack length. This behavior is similar to ceramic matrix composites. This increase in fracture toughness with crack growth in ceramic matrix composites is indicative of mechanisms of toughening in the material that are due to the existence of the reinforcing and matrix component. Microcracks in the ceramic phase and crack bridging can produce a decrease in overall stress concentration (crack-tip shielding).
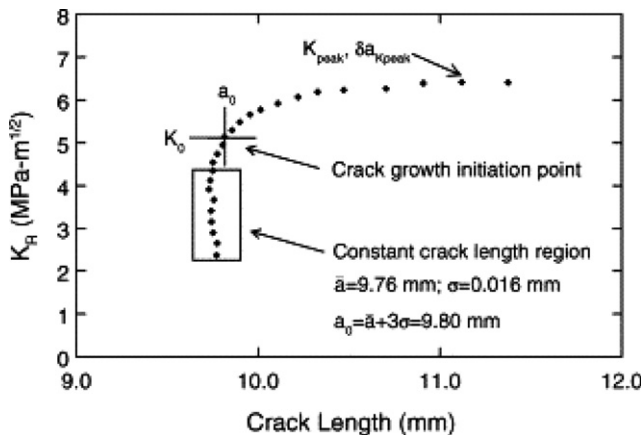

Fig. 91. Crack resistance curve as a function of length for horse bone (from Malik et al. [182, Fig. 3, p. 190]).

When the fracture toughness is dependent of crack size, linear elastic fracture mechanics cannot be applied and one has to apply other testing methods, such as the R curve. In the case of horse leg bone, it was found that there is debonding along macroscopic lamellar structures ahead of the crack, leading to crack deflection, crack energy absorption, and toughening as the crack grows. Fig. 91 shows the increase in K_R with crack length. For an initial crack length of 9.76 mm, the initial value of the toughness is 5 MPa m$^{1/2}$. The toughness increases to 6 MPa m$^{1/2}$. Therefore, the resistance to fracture has to be evaluated according to the R-curve method.

Ritchie and co-workers [180] evaluated the contributions of several mechanisms to the fracture toughness of bone. A couple of mechanisms are shown in Fig. 92 [183]. Fig. 92a shows a crack, ahead of which there is a zone of damaged material consisting of cracks that are not connected. As bridges form between these cracks, the crack front advances. The bridging by collagen fibers in the wake of the crack is another mechanism. This is shown in Fig. 92b.

Table 11 shows the contribution of these mechanisms. For bone, the most important mechanism is crack deflection, which contributes over 50% to the toughness. The second most important one is the formation of bridges between uncracked ligaments, which contributes 1–1.5 MPa m$^{1/2}$.

Fig. 93 shows the critical stress intensity factor for human bone with different ages as a function of the crack size [184]. For young subjects (34–41 years), K increases considerably with crack length, a. This is clear R-curve behavior in bones, i.e., increase in toughness as the crack length is increased and is analogous to the behavior observed by Gibeling et al. [182] and shown in Fig. 91. Fig. 93 also shows that the initial fracture toughness decreased with age. However, and more importantly, the increase in toughness with increasing crack length decreases with age, evidencing that the principal extrinsic toughening mechanisms cease to operate in old bone. Hence, a crack, once initiated, is more likely to stop in a young bone than in an old one.

Longitudinal toughness is lower than transverse toughness. This occurs because the crack propagates more readily along the fibrils. The results in Table 10 also show that the toughness increases as the strain rate is increased. This increase in toughness with strain rate is a desirable property, because bones often break by impact loading. There is no significant difference between the femur and the tibia.

In determining the fracture toughness, the minimum dimensions of the specimen are critical. For plane-strain conditions under which K_{Ic} tests are valid, the minimum thickness is

$$B \geqslant 2.5\left(\frac{K_{Ic}}{\sigma_y}\right) \tag{37}$$

For bone, this value is on the order of a few millimeters. Hence, specimens can be rather thin. However, the increase in K with crack length, a, requires that a G_{Ic} analysis be used.

Bone fatigue is well documented. This phenomenon is commonly – and incorrectly – known in the medical community as 'stress fracture.' Repetitive loading above a threshold often generates this type of damage in athletes. It is attributed to the formation of microcracks which develop throughout the bone. These microcracks do not grow because of the internal barriers posed by the Haversian system. Fig. 94 shows the S–N curves for a number of bones [2]. This is very similar to metal fatigue.
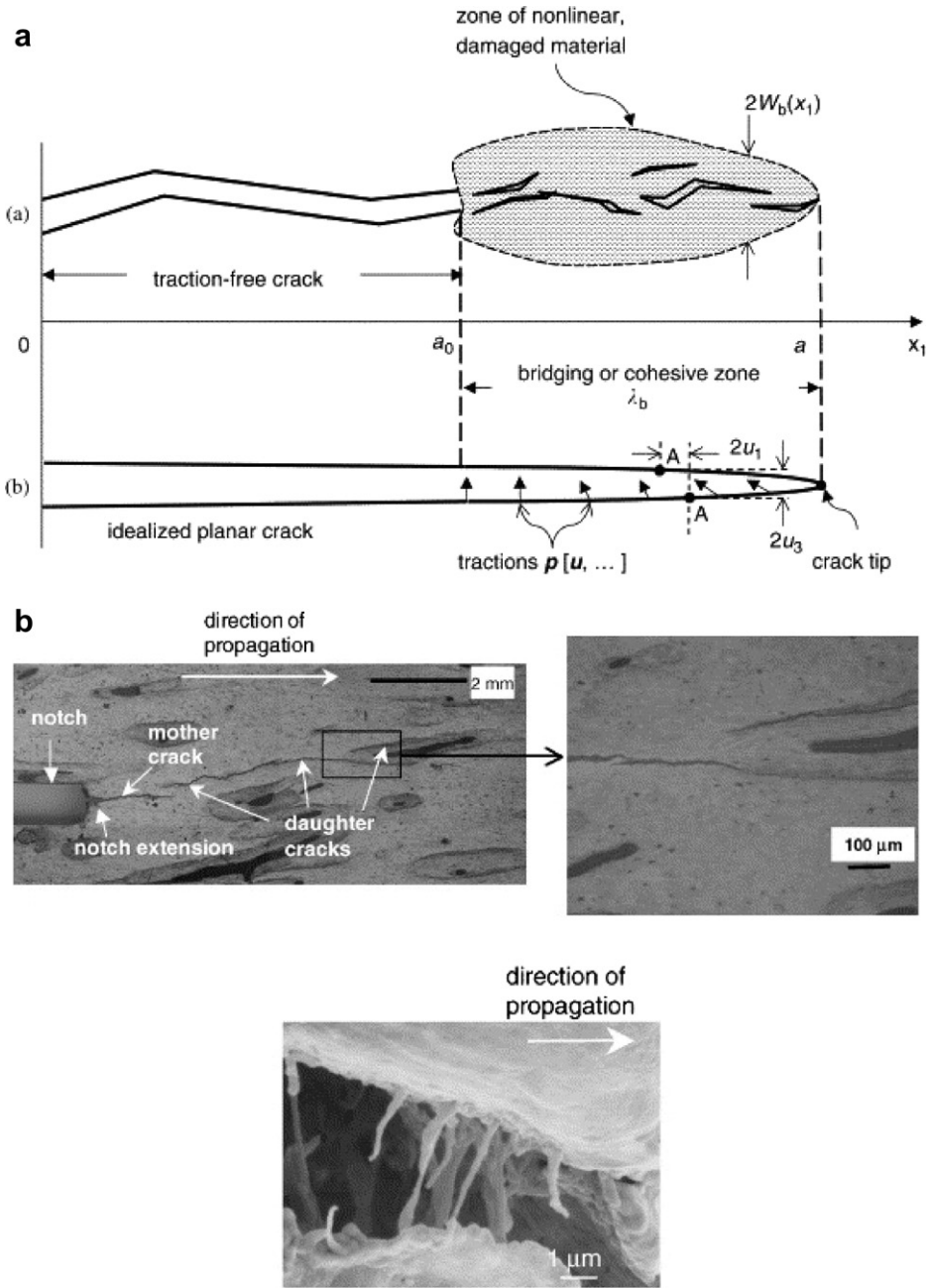
Fig. 92. (a) Schematic of discrete damage that has evolved into a single dominant crack tip damage zone. (b) An optical micrograph of a crack in human cortical bone. Note the formation of daughter cracks and corresponding uncracked ligaments. Bridging by collagen fibrils in the wake of a crack in human cortical bone (from Yang et al. [183]).

Table 11
Contributions to fracture toughness of bone from different mechanisms (from Nalla et al. [180])

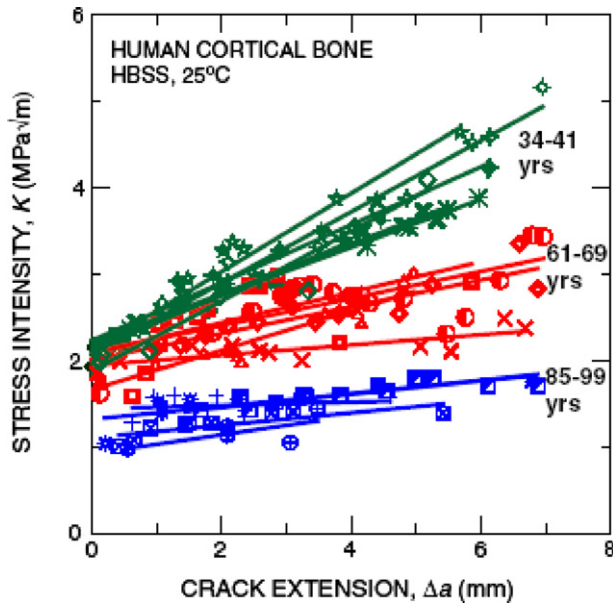| Mechanism	Contribution to fracture toughness, K_{Ic} (MPa m$^{1/2}$)
Uncracked ligament bridging	1–1.5
Crack deflection	3
Collagen-fibril bridging	0.1
Constrained microcracking	0.05
Total	2–5

Fig. 93. Resistance-curves for stable ex vivo crack extension in human cortical bone. Note the linearrly rising R-curve behavior (from Nalla et al. [184, Fig. 4]).

6.6. Teeth

6.6.1. Structure and properties

Teeth are comprised of an internal region called dentin and an external enamel layer as shown in Fig. 95a. The structure of the tooth is designed to provide an external layer that is hard and an internal core (dentin) that is tougher. The hardness of the enamel layer is due to a high degree of mineralization. Enamel does not contain collagen. It is comprised of hydroxyapatite rods woven into a fabric-like composite. These rods have a diameter of approximately 5 μm, as shown in Fig. 95b [185]. Dentine, on the other hand, is more akin to bone. It contains 30 vol% collagen and 25 vol% water, the remainder being hydroxyapatite. One of the major features of dentin is the tubules, which have a diameter of about 1 μm. They are surrounded by hydroxyapatite crystals ($\sim$0.5–1 μm diameter) arranged in a random fashion. These tubular units are, on their turn, embedded in a composite consisting of a collagen matrix reinforced with HAP. This is called the intertubular region. These features are shown in Fig. 95c [186].
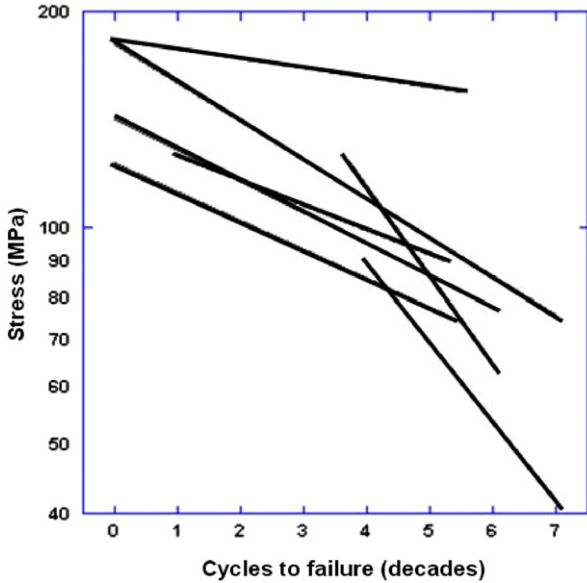
Fig. 94. Stress–number of cycles (SN) curves for a number of bones loaded under different conditions (reproduced from Currey [2, Fig. 2.15, p. 52]).
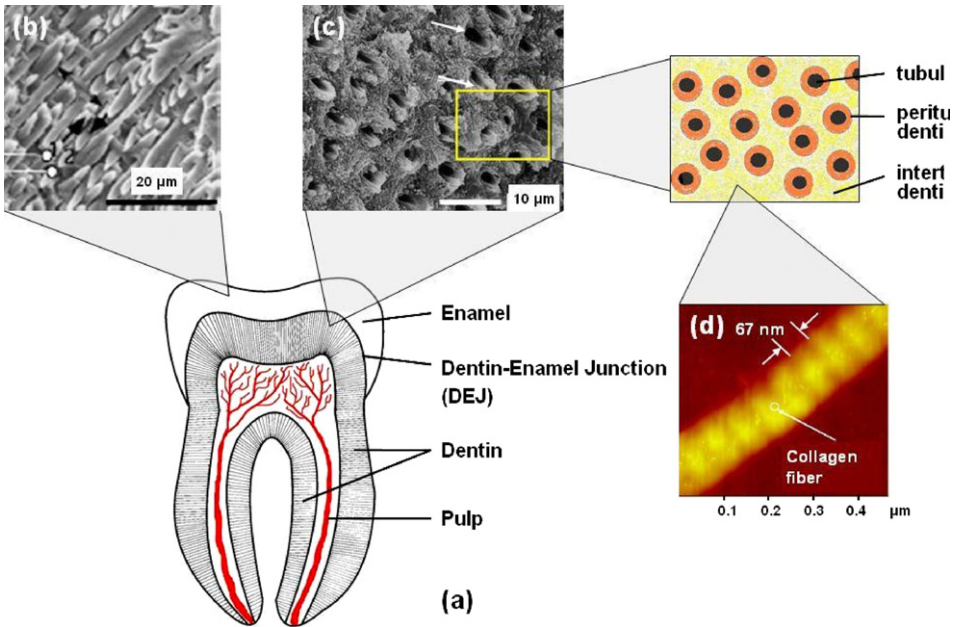

Fig. 95. Hierarchical structure of tooth. (a) Schematic drawing showing enamel, dentin–enamel junction, dentin, and pulp; (b) scanning electron micrograph of mouse tooth shows an etched image of mature enamel where the enamel rods weave past one another (from Snead et al. [185, p. 1292 Fig. 2b]); (c) scanning electron micrograph of dentin (from Imbeni et al. [186, p. 6, Fig. 6b]); (d) AFM image of a collagen fiber (from Nalla et al. [184, p. 1252, Fig. 10a]).

Table 12
Mechanical properties of teeth (from Imbeni et al. [187] and Nalla et al. [188])

	Enamel	Dentin
Fracture toughness, K_{Ic} (MPa m$^{1/2}$)	0.7–1.3	1–2
Hardness (GPa)	4	0.5
σ_{UTS} (MPa)		70–80
Young's modulus, E (GPa)	60	Perpendicular to tubules: 5–6
		Parallel to tubules: 13–17

Table 12 shows the hardness and fracture toughness of tooth [187,188] (the latter obtained from cracks at the extremities of indentation through the Evans–Charles [173] technique). The toughness of enamel is lower than that of the dentin whereas the converse
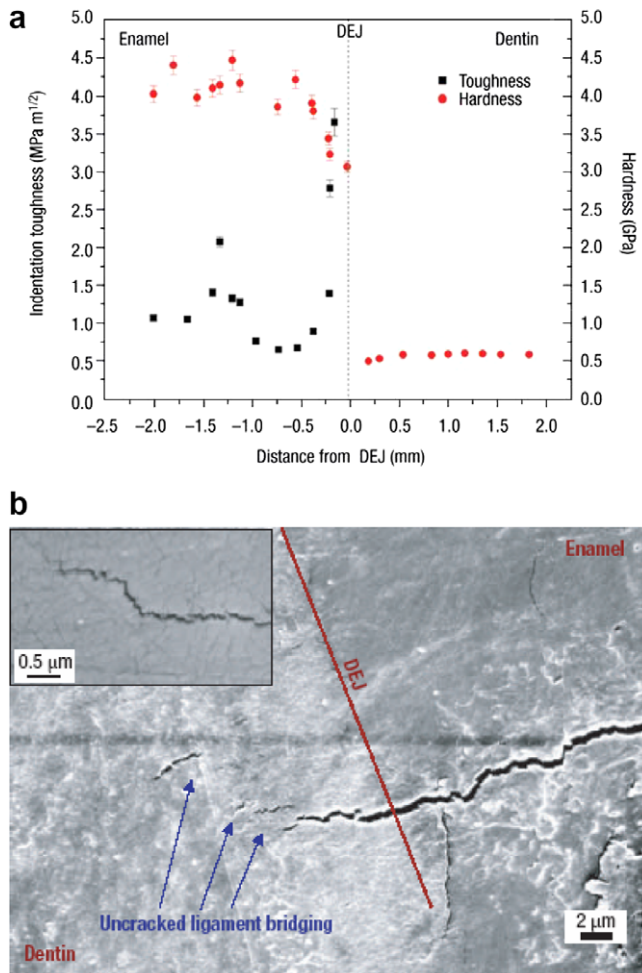

Fig. 96. (a) Typical profiles of the Vickers hardness and indentation toughness across the dentin–enamel junction (DEJ) (from Imbeni et al. [187, p. 229, Fig. 1]), (b) scanning electron micrograph showing that cracks from the enamel are arrested after propagating into the dentin (from Imbeni et al. [187, p. 231, Fig. 4a]).

is the case for the hardness. The high hardness of enamel is indeed significant: it is the hardest material in vertebrates. However, in contrast with bone, which has a vascular structure and can undergo self-repair and remodeling, both enamel and dentin are static, never repair, and cannot remodel. The changes in toughness and in hardness across the dentine–enamel junction (DEJ) are shown in Fig. 96a.

Fig. 96b shows a crack initiated in enamel and with a trajectory perpendicular to the dentin-to-enamel junction (DEJ). Imbeni et al. [187] observed that the interface never debonds. Rather, the crack penetrates it, travels a short distance (~10 μm) into dentin, and subsequently stops. Fig. 96b shows how uncracked ligaments arrest the crack.
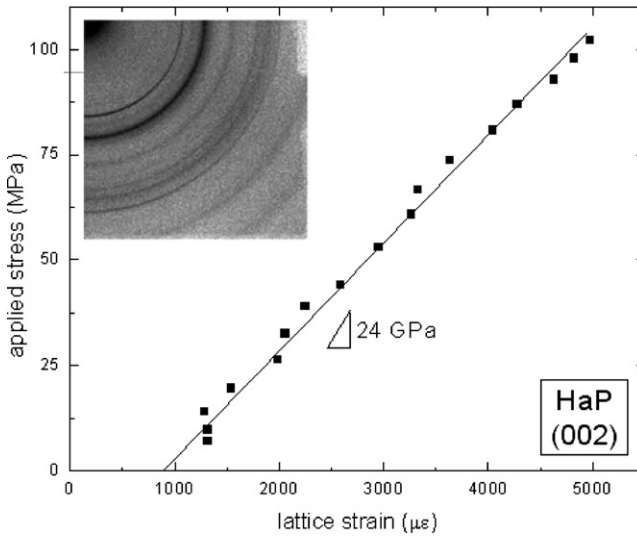

Fig. 97. Macroscopic applied compressive stress versus strain for deciduous bovine dentin. Synchrotron X-ray diffraction rings shown in top left corner (from Deymier et al. [190]).
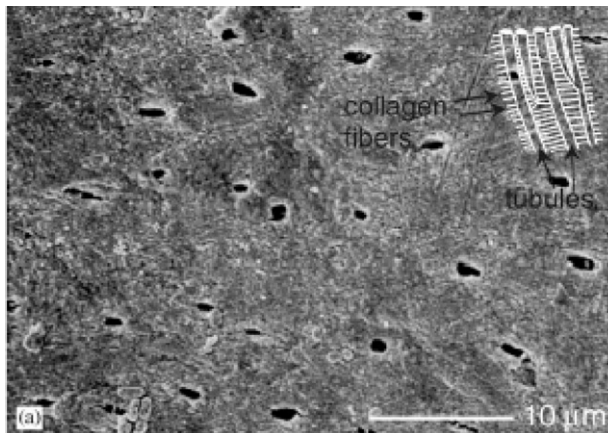

Fig. 98. Scanning electron micrograph of the typical microstructure of elephant tusk dentin (from Nalla et al. [188, p. 3953, Fig. 1a]).

Fig. 97 is an in situ synchrotron transmission diffraction measurement of deciduous bovine dentin done under an external load [190]. The applied stress on the specimen produces an elastic strain in the HaP which is determined by measuring deformation of diffraction rings (shown in insert). The slope is 24 GPa, much less than the modulus of 120 GPa for pure HaP, as expected since the porosity and collagen also present in the tooth but are not load-bearing. Thus, a considerable fraction of the deformation is taken up by the collagen.

6.6.2. Growth and hierarchical structure of elephant tusk

The structure of dentin of elephant tusk is shown in Fig. 98. The tubules are seen as oval features. The insert in the figure shows the tubules and collagen fibers radiating away from them. There is a difference between elephant tusk and human tooth dentin. In the elephant tusk, the tubules are more elliptical and there is an almost absence of peritubular
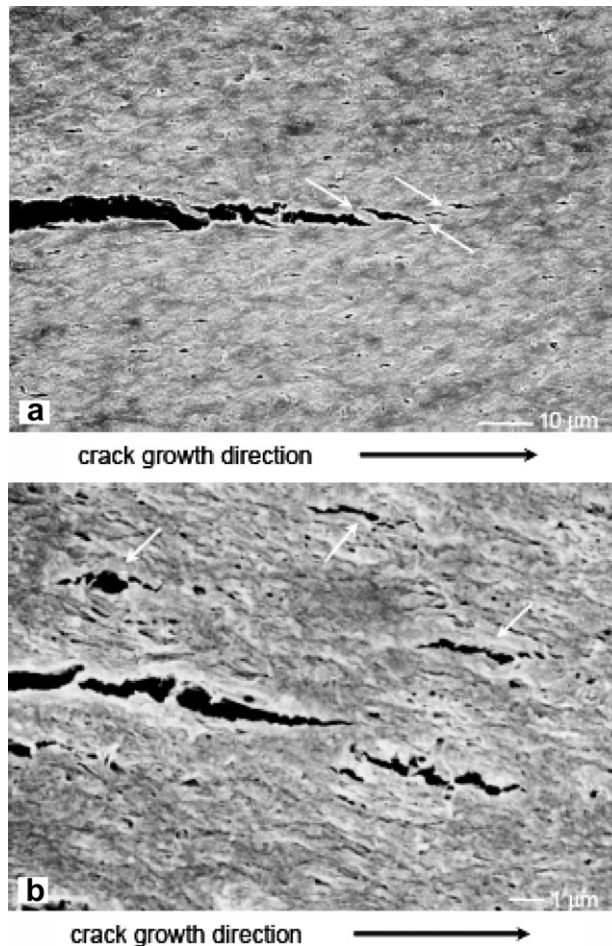

Fig. 99. Scanning electron micrographs of typical crack paths for the nominally "anti-plane parallel" orientation in the context of crack-microstructure interactions. The white arrows indicate in (a) uncracked ligament bridging, and in (b) microcracks in the vicinity of the crack (from Nalla et al. [188, p. 3957, Fig. 9]).
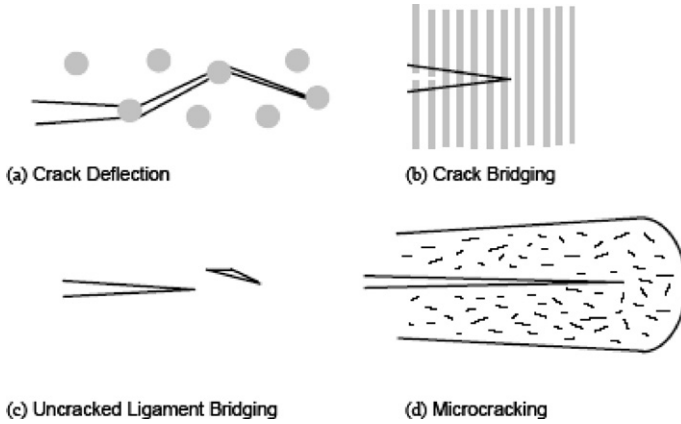
Fig. 100. Schematic illustrations of some possible toughening mechanisms in dentin: (a) crack deflection, (b) crack bridging (by collagen fibers), (c) uncracked ligament bridging, and (d) microcracking (from Nalla et al. [188, p. 3959, Fig. 12]).

dentin. The presence of tubules confers a considerable degree of anisotropy to the structure. Fig. 99 shows two mechanisms of toughening operating when the crack is running in the "anti-parallel" direction to the tubules. Uncracked ligaments are seen and marked by arrows in Fig. 99a; microcracks in the vicinity of the cracks are seen in Fig. 99b.

Fig. 100 shows in schematic fashion the four principal toughening mechanisms operating in dentin. The structure is fairly similar to bone, except that dentin is simpler. The mechanical properties in general and toughness in particular are quite anisotropic due to the presence of the tubules. The Young's modulus parallel to the tubules is ~13 GPa, whereas it is ~5–6 GPa perpendicular to the tubules. Similarly, the fracture toughness is ~2.5 MPa m$^{1/2}$ parallel to the tubules and ~1.6 MPa m$^{1/2}$ perpendicular to the tubules.

The four principal toughening mechanisms are seen schematically in Fig. 100. These mechanisms are akin to the ones in complex materials. Deflection (Fig. 100a) is caused by barriers which change the path of the crack. Deflection increases toughness by providing the initial barriers and by changing the crack angle from the applied stress from the optimum 90° condition. Crack bridging can be provided by the collagen fibers, which provides crack-tip shielding (Fig. 100b). It can also be provided by the linkage of the principal cracks with microcracks ahead of the tip, providing uncracked ligaments (Fig. 100c). Microcracking is the damage that is initiated ahead of the crack and forms a process zone with dilatation which tends to "close" the crack (Fig. 100d). This mechanism has also been identified in bone. Contributions of four different toughening mechanisms to K_{Ic} in dentin are concluded in Table 13.

Table 13
Contributions of different toughening mechanisms to K_{Ic} in dentin (from Nalla et al. [192])

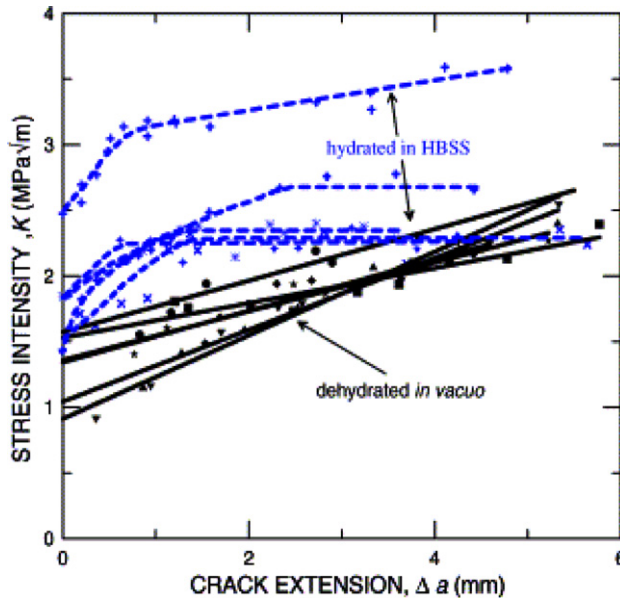| Mechanism	Parallel to tubules	Perpendicular to tubules
Crack deflection	~1.5	~1
Microcracking	0.3	0.25
Uncracked Ligament bridging	0.4	0.1
Collagen bridging	0.1	
Total	~2.5	~1.6

Fig. 101. K_R resistance-curves for hydrated and dehydrated dentin. Note the significantly higher initial increase in toughness with crack extension for hydrated dentin (from Kruzic et al. [191, p. 5207, Fig. 1b]).

The increase in K with crack extension, seen in Section 6.5 for bone, is also observed in dentin. This is a direct consequence of the extrinsic toughening due to the formation of a process zone behind the crack front (crack wake). Fig. 101 shows this response [191]. The different curves apply to specimens with different age, but the trend is clear. Another observation is that dentin hydrated in a standardized saline solution (HBSS) has a higher toughness. Nalla et al. [192] also discovered that dentin toughness increased in alcohol, an auspicious news for hard drinkers.

6.7. Nano-scale effects in biological materials

The spatial frontier of Materials Science has for a long time resided at the nanometer scale. The atomic/molecular interactions dictate the structure and properties. This effect manifests itself significantly, as the scale is reduced, for the three classes of synthetic materials:

(a) Metals: The grain size has a significant effect on strength, and the Hall–Petch equation is widely accepted to determine this dependency. However, it predicts an infinite strength at infinitely small grain sizes, and therefore it breaks down in the nanometer regime. Indeed, the strength reaches a plateau (and may dip lightly) at grain sizes below 50 nm.
(b) Polymers: Polymeric fibers with outstanding mechanical strength can be produced. This strength, which cannot be even approached for bulk materials, is achieved if all molecular chains are aligned, well cross-linked, and long.
(c) Ceramics: Brittle materials have the strength limited by the critical stress at which cracks propagate. To a first approximation, this is
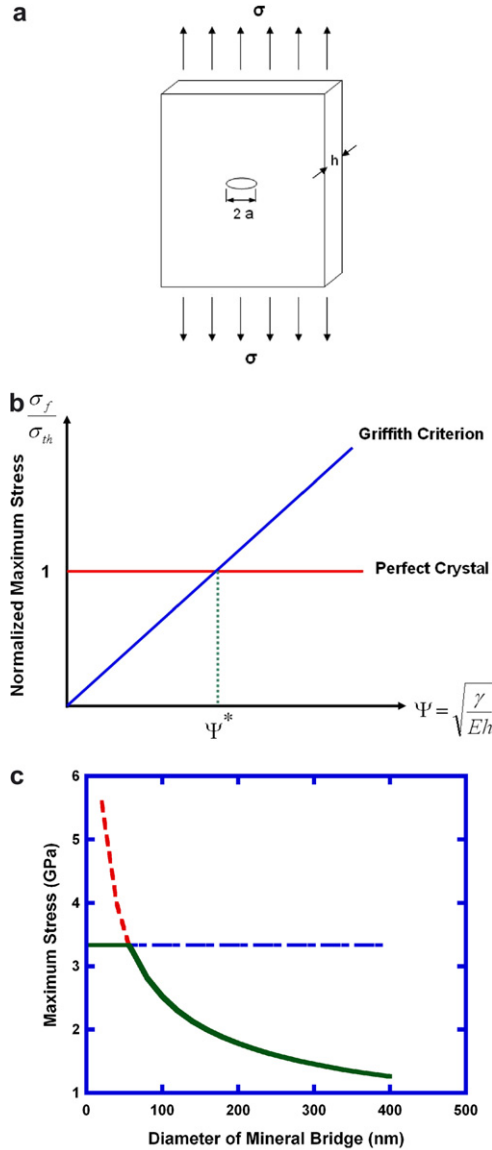
Fig. 102. (a) Schematic of mineral platelet with a surface crack (Griffith analysis); (b) comparison of the fracture strength of a cracked mineral platelet calculated from the Griffith criterion with that of a perfect crystal (from Gao et al. [193]). (c) Fracture stress as a function of crack length, 2a (from Meyers et al. [141]).

$$\sigma_M = \frac{K_{Ic}}{\sqrt{\pi a}} \tag{38}$$

As the particle size is reduced, so is the maximum flaw size. Thus, there is a minimum flaw size at which the stress required to make it grow is higher than the theoretical tensile strength.

Gao et al. [193] and Gao and Ji [149] proposed a conceptual framework that explains the lowest scale of the structural elements in hard biological materials (bone, teeth, and

shells). They applied Griffith's criterion to the mineral components of hard biological materials:

$$\sigma_f = \alpha \left(\frac{E\gamma}{h} \right)^{1/2} \tag{39}$$

where γ is the surface energy, α is a proportionality constant, and h is the thickness of the mineral. They defined a parameter ψ

$$\psi = \sqrt{\frac{\gamma}{Eh}} \tag{40}$$

For the thumbnail crack shown in Fig. 102a, the value of α is $\sqrt{\pi}$. The theoretical stress, σ_{th}, has been defined, according to the Orowan criterion, for crystalline materials, as

$$\sigma_{th} \cong \frac{E}{n}$$
$$2\pi < n < 30 \tag{41}$$

The analysis predicts a limiting value of h (or a) for which the strength is no longer size-dependent

$$h^* \cong \alpha^2 \frac{\gamma E}{\sigma_{th}^2} = \frac{\alpha^2 n \gamma}{E} \tag{42}$$

This critical value was calculated for bone. A value of about 30 nm was obtained. This is the approximate size of the ceramic tablets. The critical value of Ψ, Ψ^*, is marked in Fig. 102b.

Meyers et al. [141] used a similar approach (Section 6.2.1) and obtained, for abalone, the result shown in Fig. 102c. This is quite different from the plate thickness, 500 nm = 0.5 μm. The abalone shell has nanoscale components, and they are the mineral bridges connecting layers of tiles. Fig. 67 shows an SEM and Fig. 103 is a schematic illustration of these bridges, which have a diameter of ~50 nm, in agreement with the analysis presented here.
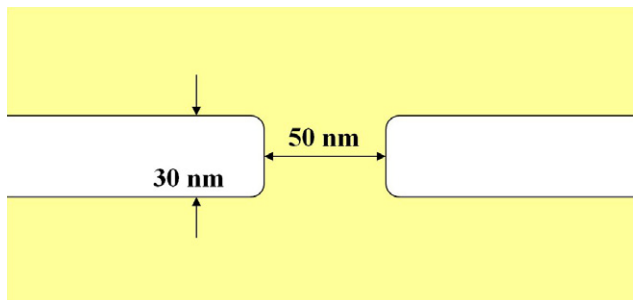

Fig. 103. Schematic drawing showing the nano-sized mineral bridges connecting layers of aragonite tiles.

(d) Soft biological materials

The long polymeric chains that comprise polypeptides are akin to the synthetic polymers. In biological systems, they exist in an aqueous environment. Proteins are comprised, at the elemental level, of –C–C–N– chains. These bonds are covalent and of a high order. The configurations of molecules (e.g. folding) and bonding between neighboring molecules are often accomplished by hydrogen bonding, which is much weaker. Thus, one would expect a high strength, at the individual molecule level, for proteins. Experiments with AFM are enabling the establishment of the mechanical response of individual molecules, as discussed in Section 8.5. Fig. 104 shows a force–displacement curve obtained by AFM from the extension of an individual protein. The sequence of peaks followed by load drops is indicative of the sequential unfolding of the protein chain. It is possible to convert the load into a stress by assigning a cross-sectional diameter to the molecule. This is taken very conservatively as 1.5 nm (the diameter of a collagen molecule), to a first approximation. The last peak corresponds to the extension of the fully unfolded protein and leads to failure. The stress is given by

$$\sigma = \frac{800 \times 10^{-12}}{1.76 \times 10^{-18}} = 454 \text{ MPa}$$

Thus, at the nanolevel the protein chains are very strong. The much lower tensile strengths obtained at the meso level are due to weak links that are introduced between molecular chains, microfibrils, fibrils, and fibers. There are a few exceptions, such as the strength in fibers from plant, which is 300–400 MPa (e.g., the curaua fibers from Brazil, that are used in composites and have a tensile strength of ~500 MPa [189]) and silk, with a strength on the order of 1 GPa.
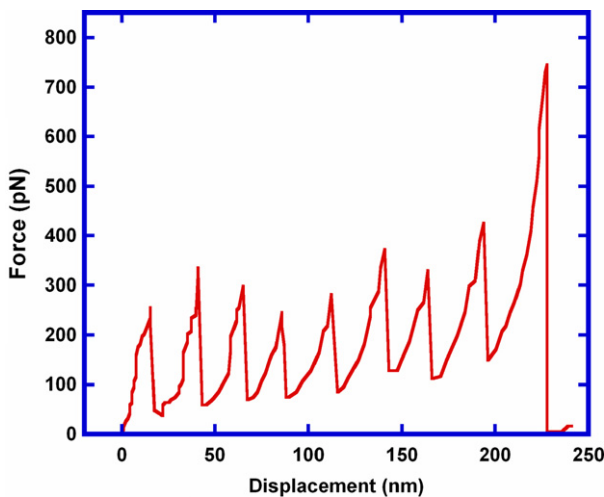

Fig. 104. Force vs. displacement curve for protein by AFM for protein. Successive load drops correspond to unfolding of molecular chains by breaking secondary bonds (reproduced from Fisher et al. [274, Fig. 1c]).

6.8. Multi-scale effects

Although nanoscale effects definitely play a role in the strength of shells, bone, and other biological materials, they by no way determine their toughness, which is established by a hierarchy of mechanisms. Hence, the estimate of collagen strength based on a single molecule (AFM) gives an ultimate strength around 450 MPa, while the strength in the toe region of tendon varies between 10 and 20 MPa. The breaking stress after considerable non-recoverable deformation is ~50 MPa. Cross-linking of the collagen molecules by artificial means can increase the strength to ~80 MPa.

Failure in larger specimens occurs by a cascade of effects that is better understood if we look at the schematic of Fig. 18. There exist permanent deformation/partial failure events at the different hierarchical levels: nano, micro, meso, and structural. Separation of the microfibrils, fibrils, fibers, and fascicles, can produce permanent stretching, and this indeed occurs in the linear portion of the stress–strain curve, beyond the toe portion. Similarly,
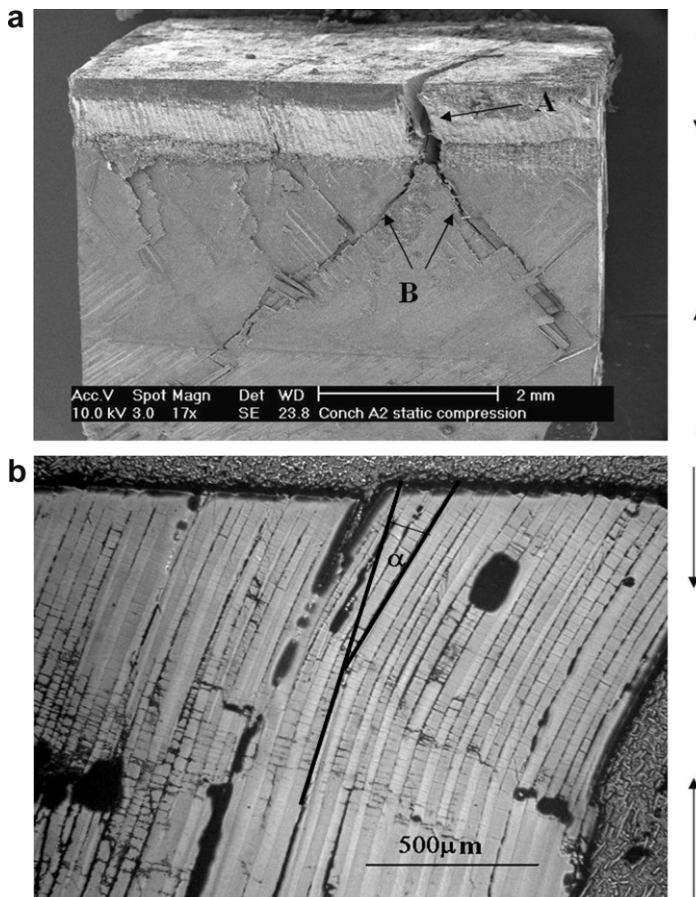

Fig. 105. (a) Crack deflection by middle macrolayer in conch (SEM taken after quasi-static compression testing) (loading direction indicated). (b) Multiple channel cracking and extensive microcracking in outer macrolayer of conch (from Menig [195]).

bone has nanoscale deformation events described by Fratzl et al. [171]. However, it also has events which occur at a considerably larger length scale: the crack bridging phenomenon, so effective in contributing to its toughness (see Section 7.3) operates at the micrometer scale. Nalla et al. [188] measured the dimensions of the bridging zone in dentin; it was on the order of 50–300 μm. In the fracture of crab exoskeleton, the vent holes and tubules play a key role. Their spacing is ∼2 μm.

The failure of shells is a classic example of multiscale strengthening. In the case of *S. gigas*, the macrolayers are powerful crack deflectors. Indeed, Fig. 105a shows a crack that started in the inside and is deflected by the interface between the inner and middle macrolayer. This was pointed out by Ballarini et al. [194], who showed that the toughness of bone and *S. gigas* was accomplished by the hierarchy of barriers, the most important being the arrest of cracks at macrolayer interfaces. The first-order lamellae (see Fig. 105a) act as bridges, closing the cracks. This crack-bridging mechanism operates at the millimeter scale.

The same effect contributes to the toughness of abalone shells. The mesolayers, 0.3 mm apart, are separated by organic layers, as discussed in Section 6.1. The cracks are arrested and deflected at these interfaces. Ballarini et al. [194] argue that the Aveston–Cooper–Kelly limit [196] estimates the length of the bridging zone and the amount of crack growth required to reach the ACK limit.

In conclusion, it can be said that the hierarchical structure of biological materials, starting at the nanometer level and continuing up to the structural dimensions, is key to the determination of the mechanical response. In this context, statistical models akin to the one developed by Bazant and Pang [197,198] for quasi-brittle materials have to be developed. They propose a cumulative density function of strength of a representative volume element (RVE) which obeys a Maxwell–Boltzmann relationship, then connect these volumes in series and parallel, constructing new distribution functions at a larger space scale. These couplings between RVEs lead to a macroscopic Weibull distribution such as that one that is observed in abalone and conch (Section 6.2).

7. Biological polymers and polymer composites

The term used by Ashby and Wegst [17], biological polymers, describes the soft tissues found in biological systems. Biological polymers can be unidirectional, such as in tendons, two-dimensional, such as in membranes (arteries, heart pericardium, skin), or tri-dimensional.

Fibers are strong in tension but cannot resist compression without buckling and kinking. Thus, these fibers are most often used in tension. According to Jeronimidis [199], nature provides compressive strength by

(a) Inserting mineral elements and in this manner creating ceramic composites.
(b) Increasing the cross-linking between the fibers and between fiber and matrix to generate stiffness.
(c) Pre-stressing fibers in tension via an internal pressure. This is the case for skids, where rigidity of the wall is provided by an internal water pressure that is higher than the external one.
(d) Pre-stressing parts of the structure so that some parts are in tension while others are in compression. For example in trees the periphery of the trunk is in tension while the core is under compression.

7.1. Ligaments

The function of a ligament is to connect bone to another bone. Tendon connects bone to muscle. The hierarchical structure of ligament is similar to that of tendon and is based on collagen fibers. The mechanical behavior of tendon and ligament are similar. *Ligamentum nuchae* is almost pure elastin and has remarkable elastic properties [27] as will be shown in Section 8.1. Fig. 106a shows the stress–strain curve of *ligamentum flavum* (ligament between lumbar vertebrae) from pig [200]. The ligament has a high ductility and is able to transmit the stress until maximum stress. Sikoryn and Hukins [200] obtained a maximum stress of 2.6 MPa at a low strain rate and of 3.0 MPa at a high strain rate. The ligament strength seems to be independent of the strain rate. A small strain rate effect has been observed at
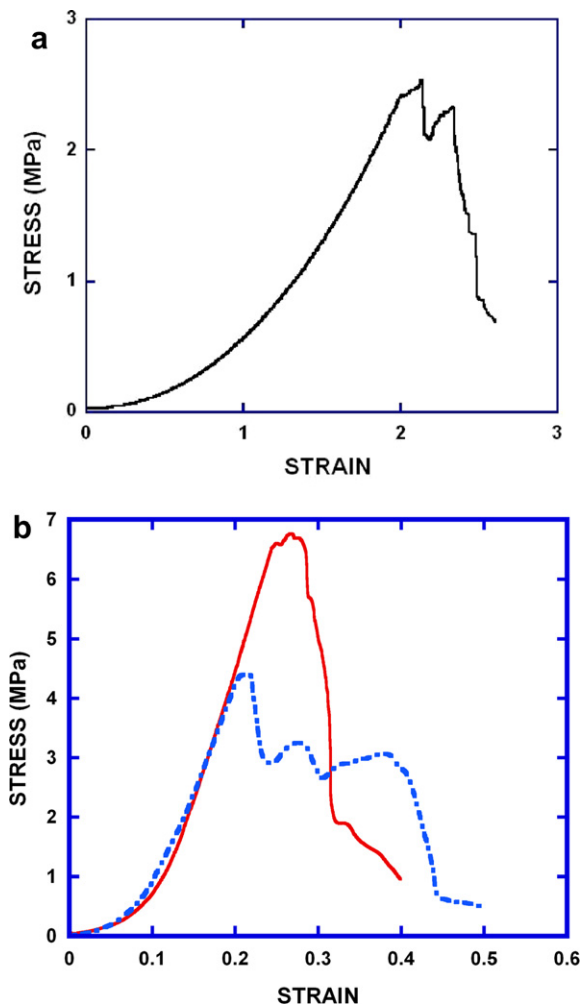

Fig. 106. Stress–strain curve of ligament from (a) pig (*Ligamentum Flavum*) (reproduced from Sikoryn and Hukins [200]), (b) human (Inferior *Glenohumeral* ligament) (reproduced from Bigliana et al. [204]).

the tendon of horse [201]. Nachemson and Evans [202] reported that the maximum stress for human *ligamentum flavum* had a value 4.4 ± 3.6 MPa. Although the maximum stress for *ligamentum flavum* in pigs and humans is on the same order, the strain at maximum stress is not. The maximum stress and strain decreases significantly with age for humans. For young subjects (13 years old), the maximum stress was 10 MPa, decreasing to 2 MPa for old subjects (79 years old). The strain at maximum stress is about 2 for pig *ligamentum flavum*, as shown in Fig. 106a. For human *ligamentum flavum*, the strain values are lower (0.5 ± 0.2). It should be mentioned that Chazal et al. [203] reported a much higher maximum stress of 15 ± 5 MPa and much lower strain at maximum stress of 0.21 ± 0.04.

Fig. 106b shows the stress–strain curves for the inferior glenohumeral ligament (from shoulders) from human [204]. Two different failure mechanisms were observed: the abrupt failure which occurs at the bone-ligament interface (solid line), and the step-like failure which occurs within ligaments (dashed line) [204–206]. Fig. 107 shows the fracture surface of *ligamentum flavum* [200]. The ligament failed at the bone-ligament interface due to the difficulty of connecting flexible ligament to the stiffer bone. B corresponds to the bone, while L is the *ligamentum flavum*. The arrows indicate interface between tissues.

7.2. Silk

Silk is composed of two proteins: fibroin (tough strands) and sericin (gummy glue). Fig. 108 shows silk (a) with and (b) without the sericin layer. The mechanical properties (strength and maximum elongation) can vary widely, depending of the application intended by the animal. For instance, spiders produce two types of silk. The first is the dragline, used in the radial components of the web. This is the structural component, and has high tensile strength (0.6–1.1 GPa) and a strain at failure of about 6%. The tangential components, called spiral, are intended to capture prey, and are "soft" and "sticky." The strain at failure can exceed 16 (or 1600%).
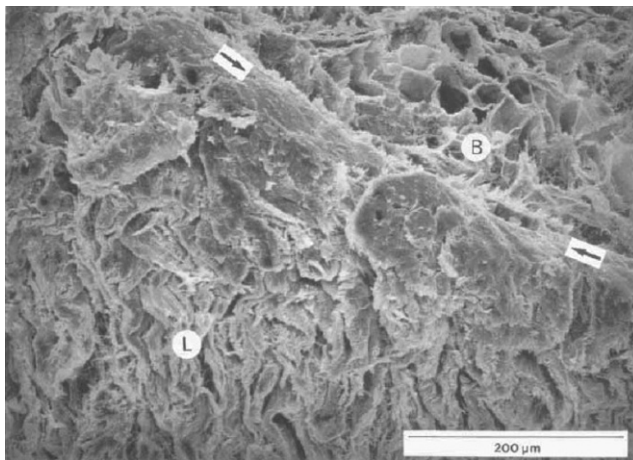

Fig. 107. Fracture surface of ligamentum flavum after tension; B: Bone, L: ligamentum flavum (from Sikoryn and Huskins [200]).
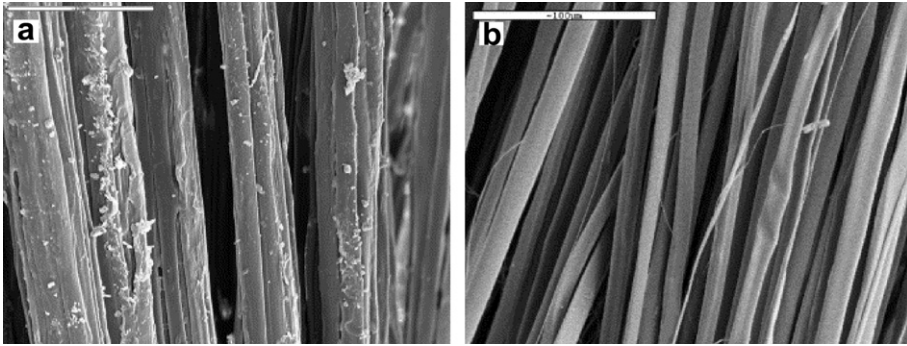
Fig. 108. SEM micrograph of *B. mori* silk fibers (a) with and (b) without the gum-like sericin proteins (from Altman et al. [217]).

The silks produced by orb-web-spinning spiders exhibit mechanical properties that are superior to almost all natural and man-made materials. Although orb-webs evolved over 180 million years ago [207,208] the investigation of the physical structure and properties of spider's silk only began in the late 1970s, starting with Denny et al. [209]. Since then the mechanical properties of various spider silks have been well described by Kaplan et al.

Table 14
Tensile mechanical properties of spider silks and other materials

Material	Stiffness (GPa)	Strength (GPa)	Extensibility	Toughness (MJ m^{-3})	Hysteresis (%)	Source
Nature fibers						
Araneus MA silk	10	1.1	0.27	160	65	[213]
Araneus viscid silk	0.003	0.5	2.7	150	65	[213]
Nephila clavipes silk	11–13	0.88–0.97	0.17–0.18			[214]
Bombyx mori cocoon silk	7	0.6	0.18	70		[213]
B. mori silk (w/ sericin)	5–12	0.5	0.19			[215]
B. mori silk (w/o sericin)	15–17	0.61–0.69	0.4–0.16			[215]
B. mori silk	10	0.74	0.2			[214]
Rat-tail collagen	0.002–0.05	0.0009–0.0074	0.24–0.68			[216]
Rat-tail collagen X-linked	0.4–0.8	0.047–0.072	0.12–0.16			[216]
Tendon collagen	1.5	0.15	0.12	7.5	7	[213]
Bone	20	0.16	0.03	4		[213]
Wool, 100%RH	0.5	0.2	0.5	60		[213]
Elastin	0.001	0.002	1.5	2	10	[213]
Resilin	0.002	0.003	1.9	4	6	[213]
Synthetic materials						
Synthetic rubber	0.001	0.05	8.5	100		[213]
Nylon fiber	5	0.95	0.18	80		[213]
Kevlar 49 fiber	130	3.6	0.027	50		[213]
Carbon fiber	300	4	0.013	25		[213]
High-tensile steel	200	1.5	0.008	6		[213]

[210], Gosline et al. [211], Vollrath et al. [212], and others. The properties of *Araneus diadematus* and *Bombyx mori* silk in comparison to various other materials are listed in Table 14 [213–216]. The removal of sericin increases the strength of the silk.

Spiders are capable of producing a variety of silks, each with distinct functions and mechanical characteristics. The two most studied are

(a) the support, or safety dragline silks, which create the spokes and frame of a web as well as the lines from which a spider hangs, and
(b) the viscid silks which are used as the prey catching spirals of a web.

Support and dragline silk is spun from the major ampullate (MA) gland of the spider and is often referred to as the MA silk. Because of its function, MA silk is much stiffer and stronger then the viscid silk fibers which compose the spirals of the web. It can have an elastic modulus on the order of 10 GPa, and a maximum strength of over 1 GPa [210–212]. On the other hand, viscid silk exhibits remarkable extensibility, withstanding up to 500% strain before failure in some species [212]. Its elastic modulus is over three orders of magnitude lower then MA silk yet both have surprisingly similar and incredible toughness. The stress–strain curves of both silks are presented in Fig. 109 [213]; a dramatic difference in properties can be seen.

It seems intuitive that the function of the web is to absorb the kinetic energy of a flying insect then relax without an elastic recoil that could reject a prey from its entanglement [218]. The microstructure of the MA silk provides a support framework which is able to produce the required viscoelastic response. It can be thought of as a semi-crystalline material, with an amorphous region composed of disordered protein chains connected to protein crystals [20,213,219]. These crystals form from layers of anti-parallel amino acid sequences which are known as β-pleated sheets. Fig. 110 provides an illustration of the microstructure consisting of amorphous proteins crosslinked through crystalline blocks. The silk is spun from multiple fibers of this semi-crystalline material.

The combination of a hard crystalline region and an elastic amorphous region results in a viscoelastic material with a notable strain-rate sensitivity. As shown in Fig. 111,
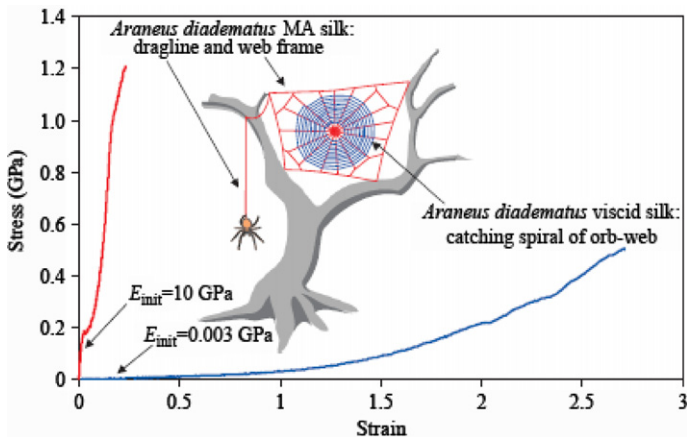

Fig. 109. Stress–strain curves for MA glad silk and viscid silks from the spider *A. diadematus* (from Gosline et al. [213]).
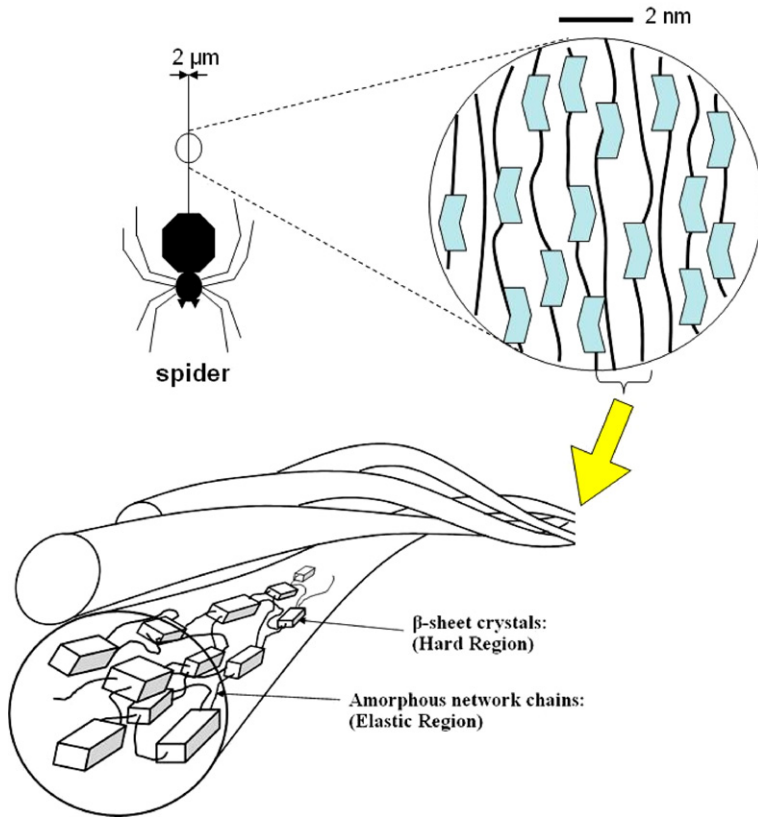
Fig. 110. Schematic representation of the hierarchical microstructure of spider silk (adapted from Elices [30]).
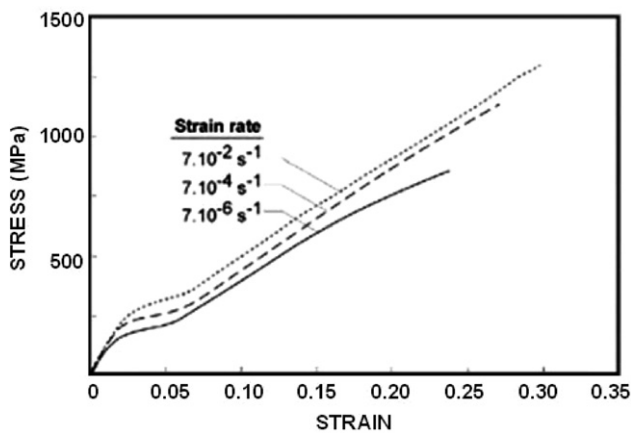

Fig. 111. Strain rate dependence of MA dragline silk (from Elices et al. [220]).

increased strain rates result in increased yield stress, tensile strength, and breaking strain [220]. High strain rates reflect the natural condition under which the material is loaded, i.e.
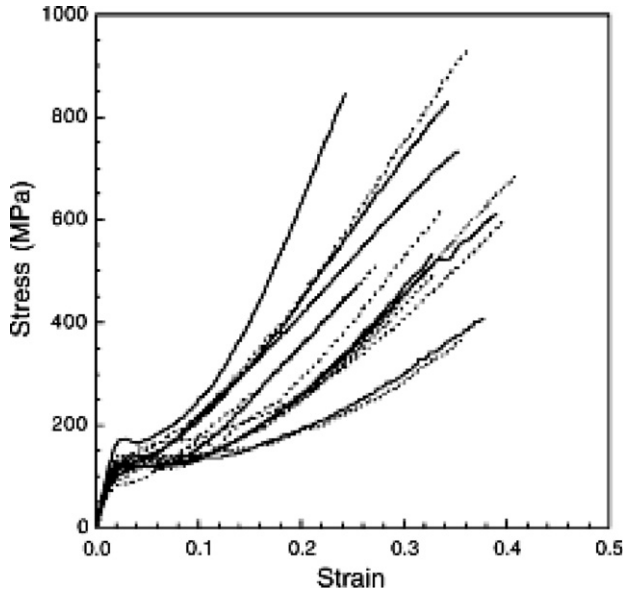
Fig. 112. Strain hardening in MA dragline spider silk (from Garrido et al. [221]).

the impact of a fast moving insect. When the material is loaded past its yield stress a region of strain hardening is observed [221]. The plot in Fig. 112 shows this strain hardening region under which most of the energy absorption occurs. This may be due to the rearrangement of the β-pleated sheet blocks in the amorphous network. The different curves represent different specimens; the figure also illustrates the variability between different specimens, a characteristic of biological materials.

7.3. Arthropod exoskeletons

Arthropods are the largest phylum of animals including the trilobites, chelicerates (spiders, mites, and scorpions), mariapods (millipedes and centipedes), hexapods (insects), and crustaceans (crabs, shrimps, lobsters, and others). All arthropods are covered by a rigid exoskeleton, which is periodically shed as the animal grows. The arthropod exoskeleton is multifunctional: it not only supports the body, resists mechanical loads, but also provides environmental protection and resistance to desiccation [3,222–224].

The three main components of exoskeleton are chitin, a polysaccharide, structural proteins, and inorganic minerals, typically calcium carbonate. In the crustacean species, the exoskeleton shows a high degree of mineralization. However, calcium carbonate is absent in the exoskeletons of insects.

The exoskeleton is a multi-layered structure that can be observed under optical microscope, sometimes even by naked eye. The outermost layer is the epicuticle, a thin, waxy layer which is the main waterproofing barrier. Beneath the epicuticle is the procuticle, the main structural part which is primarily designed to resist mechanical loads. The procuticle is further divided into two parts, an exocuticle and an endocuticle. The mesostructure of the lobster exoskeleton is shown in Fig. 113a. The exocuticle (outer layer) and
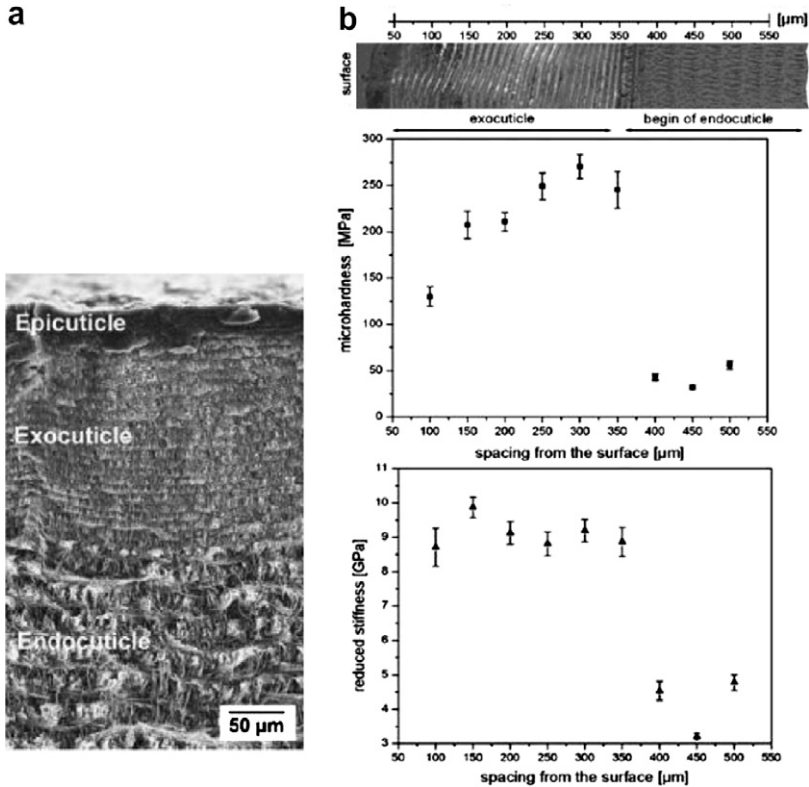
Fig. 113. (a) A through-thickness SEM micrograph showing that the exocuticle has higher stacking density than the endocuticle (from Raabe et al. [236, p. 144, Fig. 2]). (b) The hardness and the reduced stiffness through the thickness of the lobster exoskeleton (from Raabe et al. [235, p. 4284, Fig. 2]).

endocuticle (inner layer) are similar in structure and composition. The difference between exocuticle and endocuticle is that the exocuticle is stacked more densely while the endocuticle is sparsely stacked. The spacing between layers varies from species to species. Generally, the layer spacing in the endocuticle is about three times thicker than that in the exocuticle.

The most characteristic feature of arthropod exoskeletons is their well-defined hierarchical organization which reveals different structural levels as shown in Fig. 5. At the molecular level is the polysaccharide chitin. Several chitin molecules arrange in an antiparallel fashion forming α-chitin crystals. The next structure level consists of 18–25 of such molecules, wrapped by proteins, forming nanofibrils of about 2–5 nm in diameter and about 300 nm in length. These nanofibrils further assemble into bundles of fibers of about 50–300 nm in diameter. The fibers then arrange parallel to each other and form horizontal planes. These planes are stacked in a helicoid fashion, creating a twisted plywood or Bouligand structure [46,47,225–227]. A stack of layers that have completed a 180° rotation is referred to as Bouligand or twisted plywood layer, which further forms the exocuticle and endocuticle. The Bouligand (helical stacking) arrangement provides structural strength that is in-plane isotropic (plane XY) in spite of the anisotropic nature of the
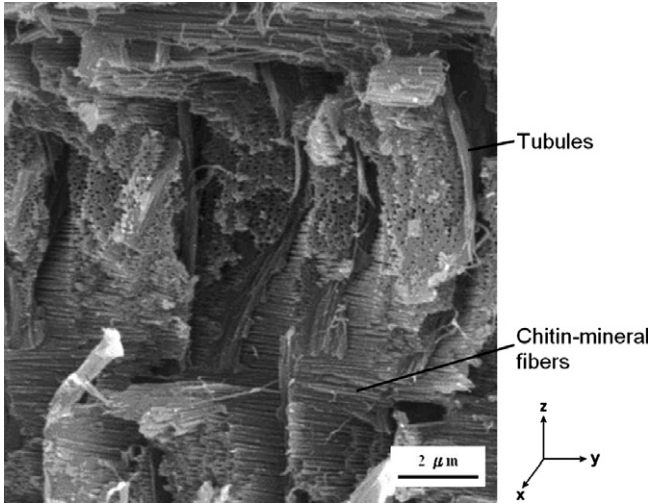
Fig. 114. SEM micrograph of fracture surface showing the twisted plywood (Bouligand) structure of crab exoskeleton (from Chen et al. [230]).

individual fiber bundles. In crustaceans, the minerals are mostly in the form of crystalline $CaCO_3$, deposited within the chitin–protein matrix [7,31,228,229]. The highly mineralized Bouligand arrangement provides strength in the in-plane (or in-surface) direction and can be considered as the hard or brittle component. The flat fracture surface in Fig. 114 shows clear evidence of the brittle structure.

In the vertical direction (Z-direction) as shown in Fig. 115, there are well-developed, high density pore canals (spacing between canals is ∼2 μm) containing tubules penetrating through the exoskeleton, as shown in Fig. 115a. These tubules are hollow and have a flattened configuration (∼2–3 μm wide) that twists in a helical fashion. They play an important role not only in the transport of ions during the mineralization of the new exoskeleton after the animals molt, but also in the enhancement of mechanical properties in the Z-direction. These tubules are organic materials and can be considered as soft or ductile component which stitch the fibrous layers together and provide the toughness to the structure. A region where separation was initiated by tensile tractions is shown in Fig. 115a. The tubules are stretched and fail in a ductile mode. The neck cross-section is reduced to a small fraction of the original thickness. Fig. 115b shows the top view of the fracture surface (XY plane); the tubules are the lighter segments protruding. Many of them are curled, evidence of their softness and ductility. It is thought that this ductile component helps to 'stitch' together the brittle bundles arranged in the Bouligand pattern and provides the toughness to the structure. It also plays undoubtedly a role in keeping the exoskeleton in place even when it is fractured, allowing for self-healing. These aspects were investigated by Chen et al. [230].

The mechanical properties of crustacean exoskeletons (mud crab, *Scylla serrata* and the prawn, *Penaeus mondon*) were first investigated by Hepburn and Joffe [231,232], followed by Raabe and coworkers (American lobster, *Homarus americanus*) [233–239] and Chen et al. [230] (sheep crab, *Loxorhynchun grandis* and Dungeness crab, *Cancer magister*).
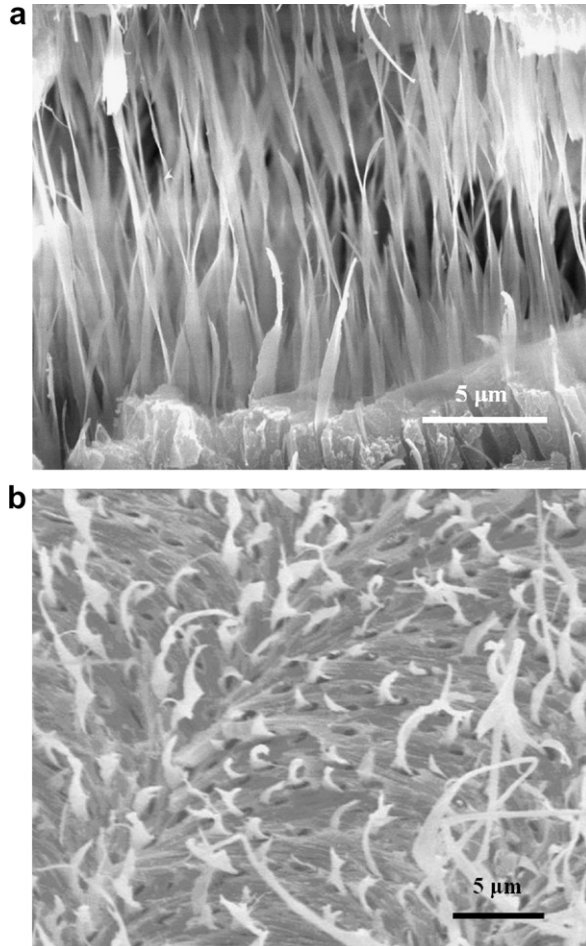
Fig. 115. SEM micrographs of ductile fracture surface show the tubules in the *Z*-direction in crab exoskeleton; (a) side view showing the necked tubules; (b) top view showing fractured tubules in tensile extension (from Chen et al. [230]).

The tensile stress–strain curves for various exoskeletons are shown in Fig. 116. The results from Hepburn and Joffe [231] show a unique discontinuity (load drop) in the low strain region. They suggested that this discontinuity is associated with the brittle failure of the mineral phase. When exoskeleton specimens are stretched, brittle failure of the mineral phase occurs at a low strain, leaving the chitin and protein phases to bear the load. Table 15 shows the mechanical properties of crustacean exoskeletons [230–232]. The presence of water plays an important role in mechanical properties as shown in Fig. 116. The dried exoskeleton material is rigid and brittle compared to that in the hydrated state.

Melnick et al. [240] studied the hardness and toughness of exoskeleton of the stone crab, *Menippe mercenaria*, which exhibits a dark color (ranging from amber to black) on tips of chelae and walking legs. The dark material was much harder and tougher than the light-colored material from the same crab chela (Table 16). Scanning electron
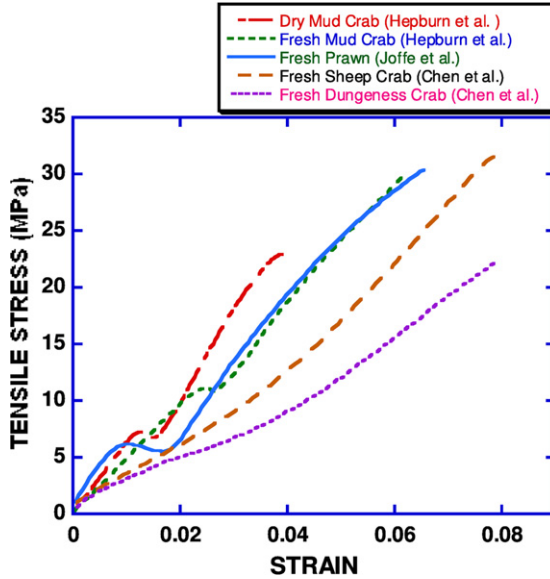
Fig. 116. Tensile stress–strain curves for crustacean exoskeletons.

Table 15
Mechanical properties of crustacean exoskeletons

		UTS (MPa)	Young's modulus (MPa)	Fracture strain (%)	Source
Sheep crab	Wet	29.8 ± 7.2	467 ± 92	6.9 ± 1.8	[230]
Loxorhynchus grandis	Dry	12.5 ± 2.3	735 ± 65	1.7 ± 0.3	
Mud crab	Wet	30.1 ± 5.0	481 ± 75	6.2	[231]
Scylla serrata	Dry	23.0 ± 3.8	640 ± 89	3.9	
Prawn	Wet	28.0 ± 3.8	549 ± 48	6.9	[232]
Penaeus mondon	Dry	29.5 ± 4.1	682 ± 110	4.9	

Table 16
Mechanical properties of stone crab, *Menippe mercenaria* [240]

	Hardness (GPa)	Fracture strength, σ_f (MPa)	Fracture toughness, K_{Ic} (MPa m$^{1/2}$)
Black	1.33	108.9	2.3
Yellow	0.48	32.4	1.0

micrographs (Fig. 117) showed that the dark exoskeleton material has lower level of porosity, and this may relate to the tanning effect. It may also be more highly mineralized.

Raabe and co-workers extensively studied the structure and mechanical properties of the exoskeleton of American lobster, *Homarus americanus* [233–239]. They observed the unique honeycomb-type arrangement of the chitin–protein fibers surrounding pore canals, as shown in the Fig. 118. The honeycomb structure of lobster is quite stable after chemical and heat treatments, and could be made suitable for medical applications, for example, tissue engineering [239]. The through-thickness mechanical properties of American lobster
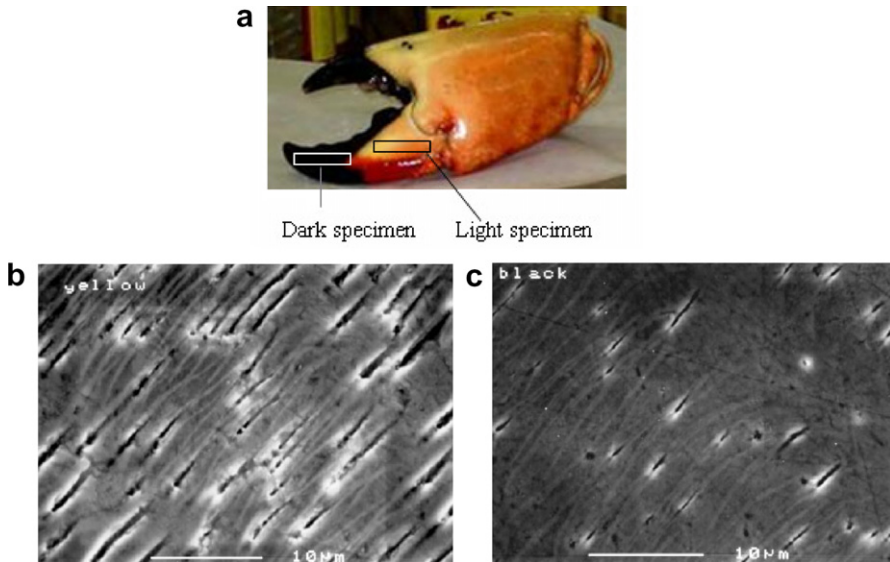
Fig. 117. (a) Stone crab, *Menippe mercenaria*, chelae showing dark and light-colored region. (b) SEM photograph showing high level of porosity in yellow exoskeleton material. (c) SEM photograph showing high level of porosity in black exoskeleton material (from Melnick et al. [240, p. 2901, Figs. 4–5]).

exoskeleton were studied using both micro- and nanoindentation techniques [235,237]. The hardness and stiffness of the exocuticle (outer layer) are higher than those of endocuticle (inner layer) as shown in Fig. 113 (b). This is due to the dense twisted plywood structure in exocuticle compared to the coarse twisted plywood structure in endocuticle (Fig. 113a).

7.4. Keratin-based materials: hoof and horn

Keratin consists of dead cells that are produced by biological systems. The most common examples are hairs, nails, hooves, and horns. We briefly describe the later two.

The complex design of equine hoof wall consists of two structural elements: tubules and intertubular material [241–244]. Fig. 119a shows the schematic of the equine hoof wall. Hollow tubules occupy half of the wall and are parallel to the surfaces. The intermediate filament, a fibrous structure of keratin, is embedded in the keratin matrix and is composed of α-helical protein bundles with a diameter of 8 nm. In the innermost wall, the intermediate filament is mainly oriented along the tubule axis and placed horizontally in the intertubular material, shown in Fig. 119b. In the mid wall region, the intermediate filament in intertubular material is arranged in helical fashion with angles from 0° to 33°. This complex design of the hoof wall provides a wide range of mechanical properties in 0–100% of humidity condition. As the water content increases, the Young's modulus decreases. This effect can be dramatic. Fig. 120 shows the initial Young's modulus plotted as a function of water content. The mechanical role of the tubules and orientation of the intermediate filaments are to control the crack propagation process and enhance fracture toughness of the wall. Fig. 121 shows that the *J*-integral of the hoof wall is not very sensitive to the rate of load application. The average *J*-integral is $12 \pm 3 \, \text{kJ/m}^2$; the hoof wall prevents brittle
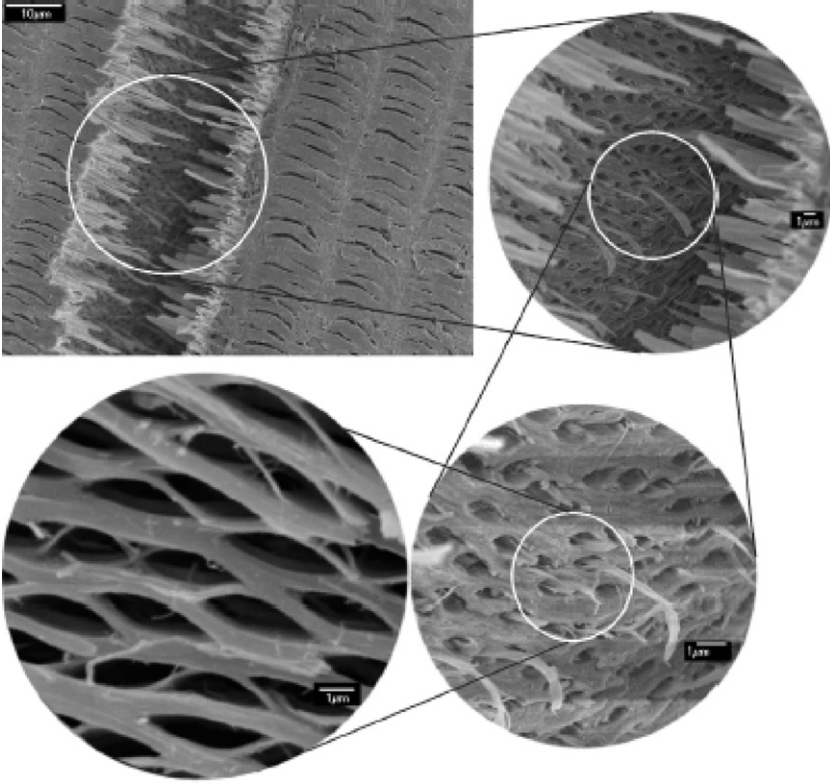
Fig. 118. Scanning electron micrographs (SEM) taken from fractured specimens of lobster *Homarus americanus* showing the hierarchical structure. The honeycomb-type arrangement of the chitin–protein fibers is visible at higher magnifications (from Raabe et al. [234, p. 6, Fig. 5]).

failure in the entire strain rate range investigated: $1.6 \times 10^{-3} \rightarrow 70 \text{ s}^{-1}$. This covers most situations encountered by ungulates.

The structure of the rhinoceros horn is similar to the hoof; it has a laminated structure of tubules shown in Fig. 122 [245]. Horn tubules are more closely placed to each other than hoof tubules. The mechanical properties of the oryx horn have been studied and composite theory has been applied to predict the stiffness [246]. Viscoelastic behavior of the gemsbok horn has been investigated at different water contents [247]. Fig. 123 shows stress–strain curves of horn along transverse and longitudinal directions [248]. There is a great degree of anisotropy with the strength in the longitudinal direction (parallel to the tubules) being approximately 10 times that in the transverse direction (perpendicular to tubules).

8. Biological elastomers

8.1. Skin

The skin has multifunctionalities such as temperature regulation, barrier between organism and environment, and even camouflage from predators. Basically, the layered
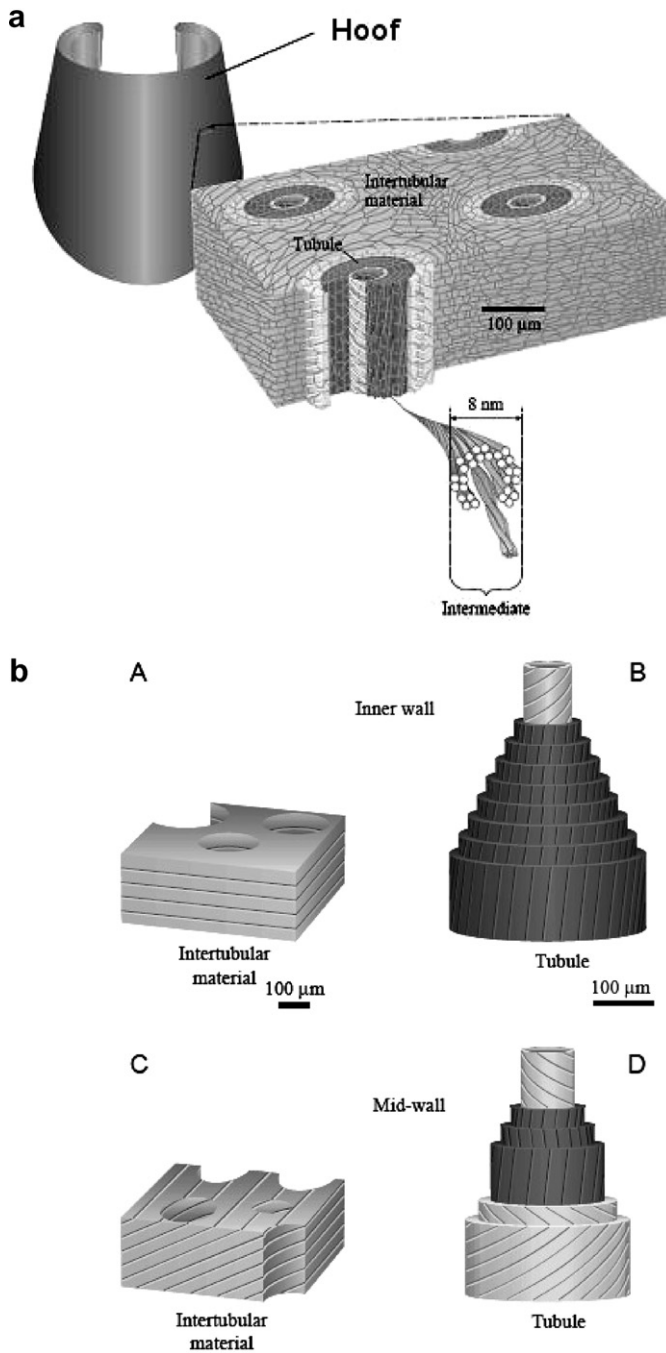
Fig. 119. (a) Schematic of hoof wall; (b) the orientation of intermediate filament in inner wall and mid-wall (from Kaspi and Gosline [244, p. 373, Fig. 1 and p. 374, Fig. 2]).
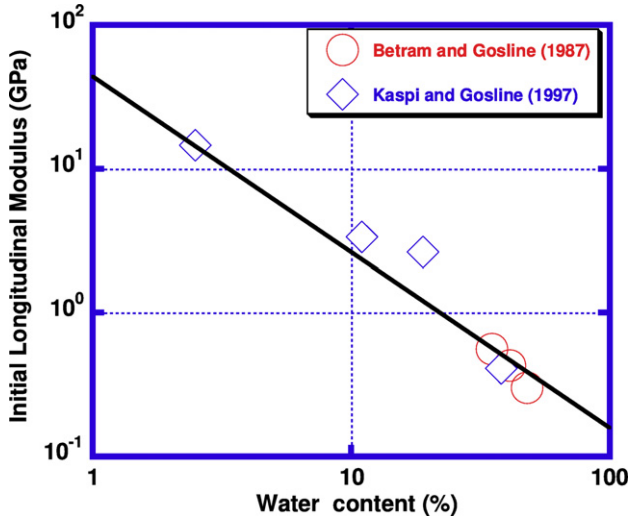
Fig. 120. Initial Young's modulus as a function of water content (from Betram and Gosline [241, p. 130] and Kaspi and Gosline [243, p. 1646, Fig. 8]).
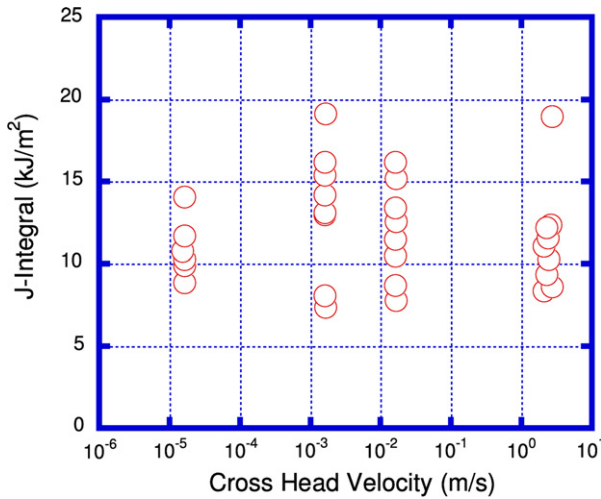

Fig. 121. *J*-integral of hoof wall at different strain rate (from Kaspi and Gosline [243, p. 1132, Fig. 9]).

structure of the skin is composed of the epidermis and dermis layers. The epidermis is a protective layer of the skin and consists of several layers shown in Fig. 124 [79]. The outermost layer of the mammalian skin is *stratum corneum* made from thin soft keratin. *Stratum corneum* plays a role as a barrier between environment and organism [249,250]. Dermis is a connective tissue between epidermis and organism. Primary proteins of the dermis are elastin and collagen. Elastin has an outstanding elastic property and Fig. 125 shows the stress–strain curve. Collagen is the main source of the mechanical
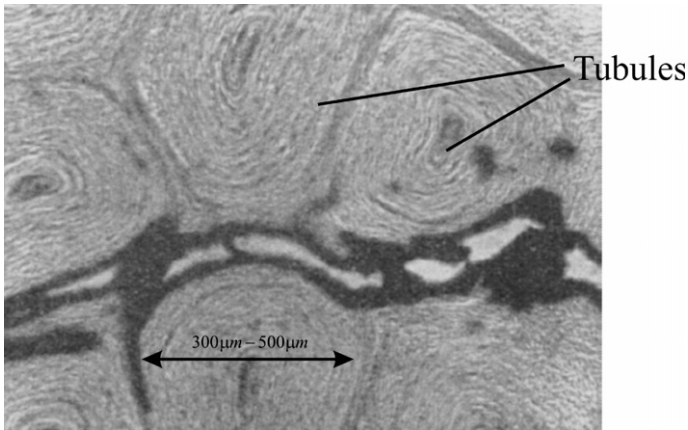
Fig. 122. Transverse section of rhinoceros horn showing six tubules (magnification 220×) (from Ryder [245, p. 1195, Fig. 1]).
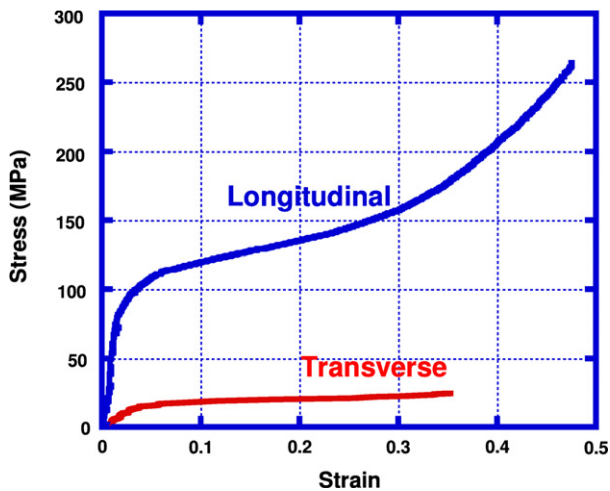

Fig. 123. Stress–strain curves of horn (adapted from Druhala and Feughelman [248, p. 381 Fig. 8]).

properties of skins and elastin is not significant. Elastin is responsible for the small deformation of the skin and helps it to recover to the original position [251].

Wu et al. studied mechanical properties of *stratum corneum* as a function of temperature and under different environmental conditions (humidity) as shown in Figs. 126a and b [252]. The strength is decreased with an increase of humidity and temperature. They also studied the role of lipids in the *stratum corneum* and found that delipidized samples provide higher mechanical strength as shown in Fig. 126c and d. The maximum delamination energy of untreated *stratum corneum* is 8 J/m^2 and that of delipidized *stratum corneum* is 13 J/m^2 at low temperature. The mechanical properties of skin vary with age [253]. Fig. 127 shows the ratio of the recovered deformation, U_R, and initial deformation of skin,
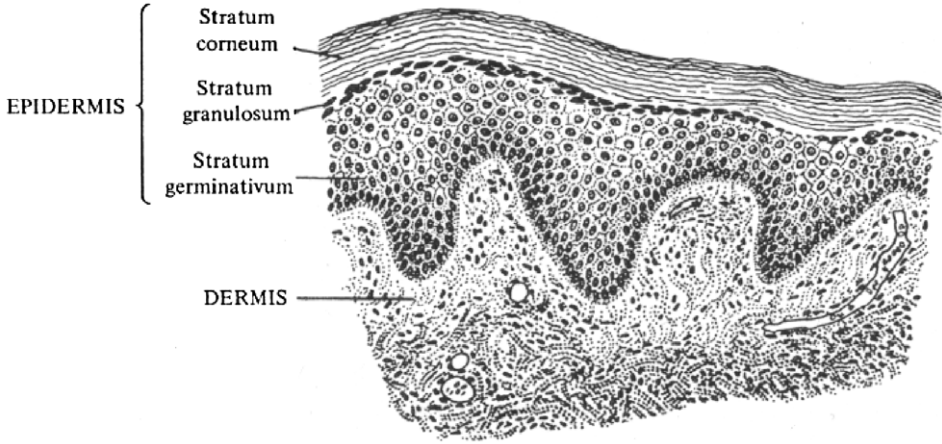
Fig. 124. Structure of mammalian skin (from Fraser and Macre [79, p. 208, Fig. 1]).
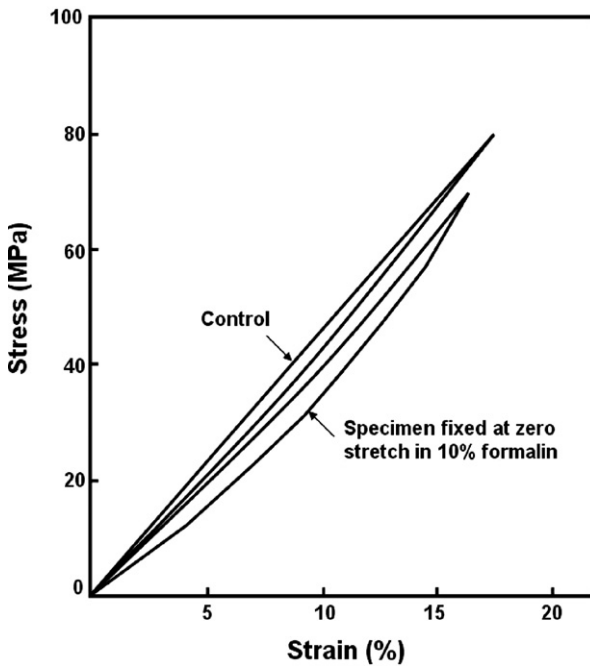

Fig. 125. Stress–strain curves of elastin (reproduced from Fung [24, p. 240, Fig. 7.2:1]).

U_E as a function of age; this represents elastic recovery of skin after deformation. The elasticity of skin continuously decreases with age [253]. The skin strength is also strain-rate sensitive [254]. Fig. 128 shows Young's modulus plotted as a function of strain rate. As the strain rate increases, the elastic modulus also increases. This is typical of viscoelastic materials.
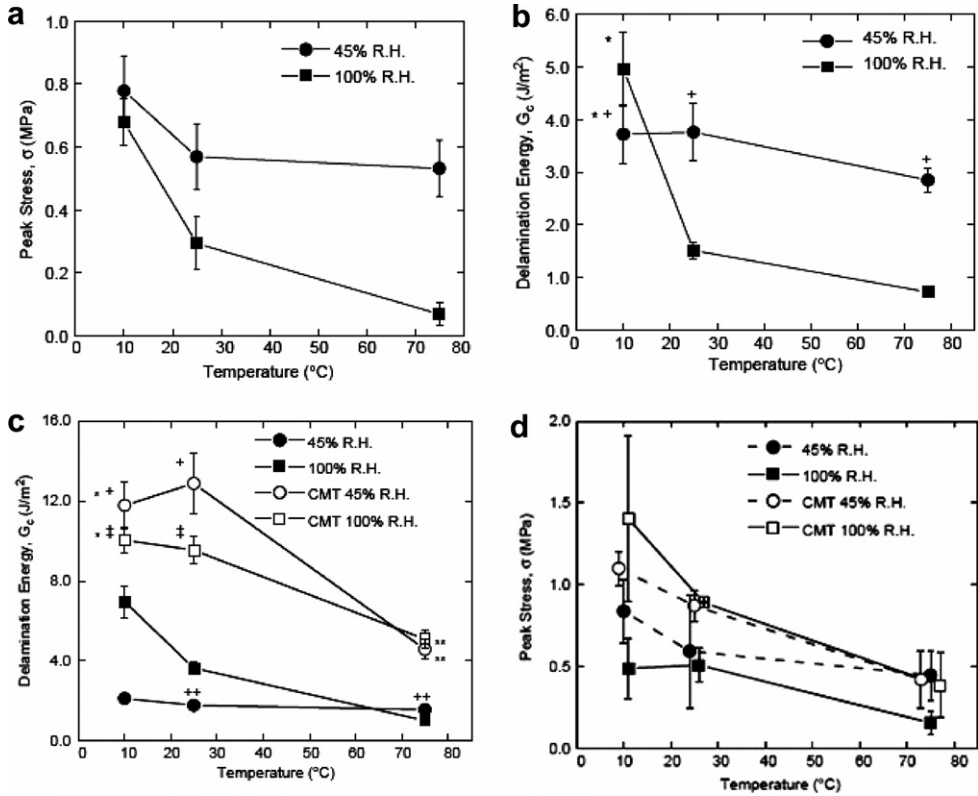
Fig. 126. Mechanical properties of *stratum corneum*; (a,b) peak stress and delamination energy of *stratum corneum* with variation of temperature and humidity ;(c,d) peak stress and delamination energy of delipidized and untreated stratum corneum with variation of temperature and humidity (from Wu et al. [252, p. 783, Fig. 3 and p. 784, Fig. 4]).
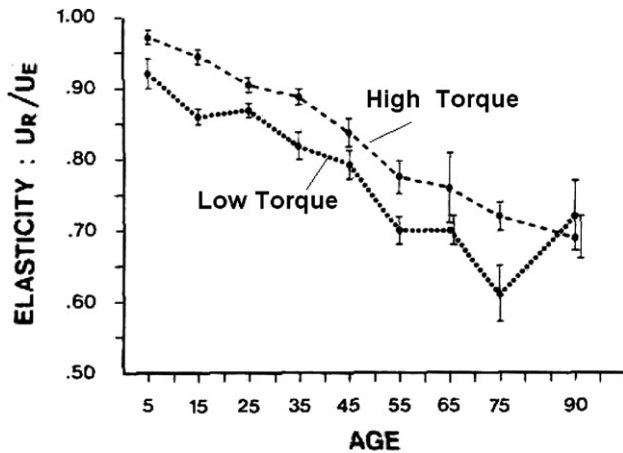

Fig. 127. Skin elasticity recovery /extensibility ratio (U_R/U_E) as a function of age for high torque and low torque (from Escoffier et al. [253, p. 351, Fig. 7]).
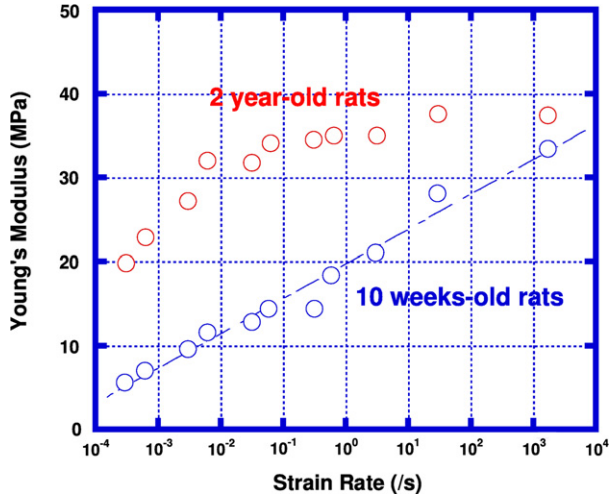
Fig. 128. Young's modulus of rat skin plotted as a function of strain rate (adapted from Vogel [254, p. 82, Fig. 3]).

Both structure and mechanical property differences exist over the body and in all mammalian animals [249]. For example, the rhinoceros has an amazingly thick and tough skin for protection. Figs. 129a and b show collagenous rhinoceros skin of flank and belly; the thickness is 25 mm and 15 mm, respectively [255]. The tensile strength of the dorsolateral (flank) skin is 30.5 MPa and, compressive strength is 170 MPa. This is much higher than other mammalian skin. The average toughness of dorsolateral skin of rhinoceros is 77 kJ/m^2, which is higher than the maximum toughness of rat skin, 30 kJ/m^2 [256]. Fig. 130 shows stress–strain curves of three collagenous materials; the schematic in the Fig. 130 shows the orientation of the collagen fibers. The highly aligned collagen fibers in the tendon provide the highest strength and stiffness ($\sim$80 MPa). Cat skin, on the other hand, exhibits a large elastic strain of ($\sim$1), due to the loose arrangement of fibers. Rhinoceros skin has the same strength as cat skin, but much less elasticity because the collagen molecules are extended.

8.2. Muscle

The maximum force that a muscle fiber can generate depends on the velocity at which it is activated. Fig. 131 shows the stress that can be generated as a function of strain rate for "slow-twitch" and "fast-twitch" muscles. We use slow-twitch muscles for long-range events (e.g., distance running) and fast-twitch muscles for explosive activities, such as sprinting or throwing a punch. Both muscles show a decreasing ability to generate stress as the strain rate is increased. However, the fast-twitch muscles show a lower decay.

The plot shown in Fig. 131 is only schematic and represents the rat *soleus* (slow-twitch) and extensor *digitorum longus* (fast-twitch). The equation that describes the response in Fig. 131 is called the Hill equation [257]. It has the form

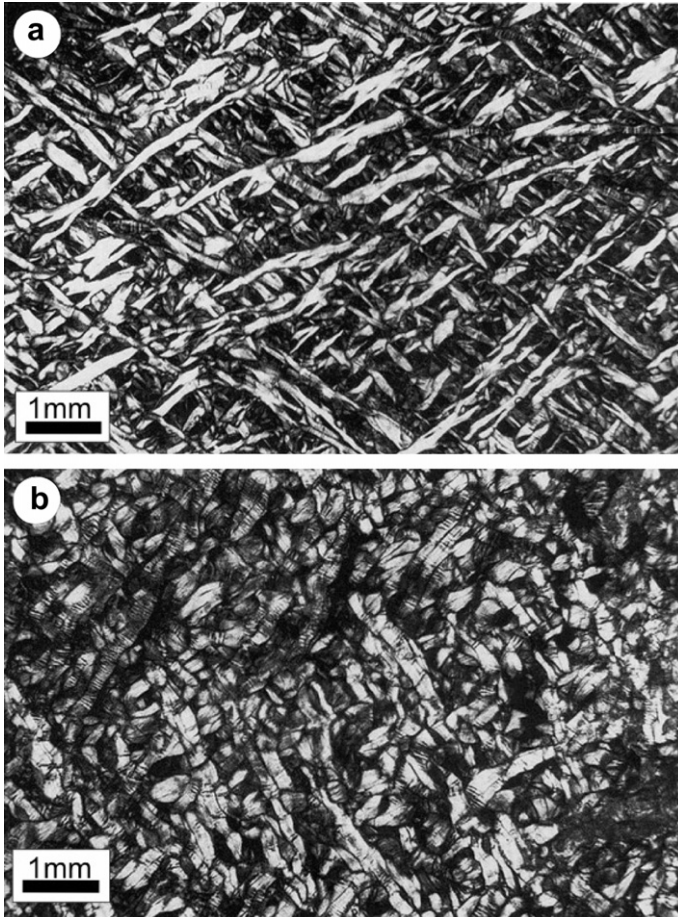$$(\sigma + a)(\dot{\varepsilon} + b) = (\sigma_0 + a)b \tag{43}$$

Fig. 129. Skin of the rhinoceros; (a) the skin of flank; (b) the skin of belly (from Shadwick et al. [255, p. 417, Fig. 4]).

where σ_0 is the stress at zero velocity (equal to 200 kPa in Fig. 131). The range of σ_0 is usually between 100 and 300 kPa. a and b are parameters and $\dot{\varepsilon}$ is the strain rate (obtained from the velocity).

8.3. Blood vessels

The vascular system provides the transport of nutrients, oxygen, and other chemical signals to the various parts of the body. It is divided into two subsystems: pulmonary and circulatory system. We will not go into any details of the pathology of these two sub-systems. Rather, we will concentrate on their mechanical properties. Arteries (which carry blood from the heart to the various parts of the body) and veins (that collect blood back to the heart) exhibit some significant differences in structure. Arteries are exposed to higher pressures and fluctuations associated with the diastolic and systolic portions of the cardiac cycle. Fig. 132 shows the longitudinal and normal sections of an artery. The structure is
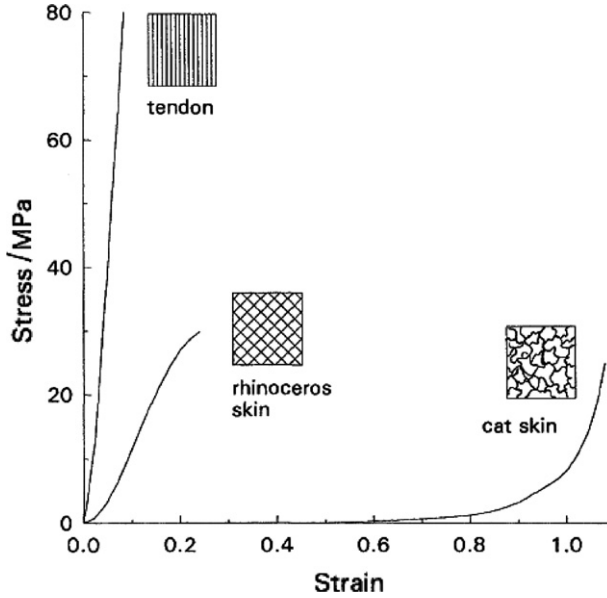
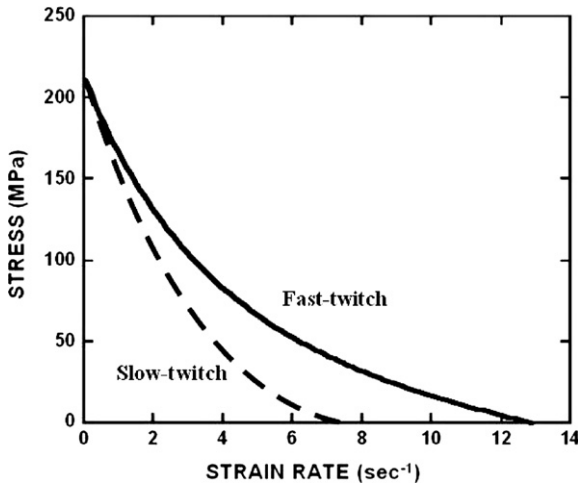Fig. 130. Stress strain curves of collagenous materials (from Shadwick et al. [255, p. 417, Fig. 11]).

Fig. 131. Stress vs. strain rate for slow-twitch and fast-twitch muscles.

layered with three distinct regions: tunica intima (innermost), tunica media (middle), and tunica adventitia (outermost).

Bursting (longitudinal splitting) of blood vessels or aneurysm (tensile instability forming a local bulge) are highly undesirable but all too frequent events in humans. There are two unique aspects of the mechanical response of arteries and veins that are instrumental
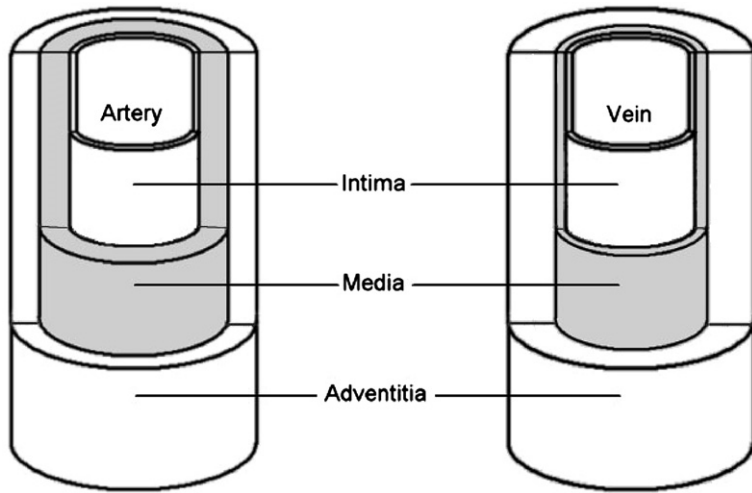
Fig. 132. Cross-section of an artery and vein, composed of the endothelium, tunica intima, tunica media, and tunics adventitia.

Table 17
Dimensions and composition of blood vessels

	Vessel	Dimensions (mm)		Composition
Artery	Aorta	Diameter	25	
		Thickness	2	
	Medium-sized artery	Diameter	1	
		Thickness	4	
Vein		Diameter	20	
		Thickness	1	

in minimizing the chance of the aforementioned problems: non-linear elasticity and resid-ual stresses.

8.3.1. Non-linear elasticity

The three layers comprising blood vessels have different functions and compositions. Table 17 summarizes the similarities and differences between arteries and veins, including main vessels such as the aorta. The composition of arteries is made up primarily of elastic fibers (elastin), collagen, and smooth muscle. Compared to veins, arteries contain much more elastic material. Thicker arteries, such as the aorta, contain less smooth muscle than both smaller arteries and also veins. These differences account for the ability of arteries to resist large pressure fluctuations during the cardiac cycle.

The mechanical response of blood vessels is shown in Fig. 133a. This is the longitudinal stress–strain response of human *vena cava*. The response is non-linear elastic. We know that it is elastic because on unloading the artery returns to its original dimension. However, there is a slight hysteresis on loading and unloading, due to viscoelastic processes. The slope approaches infinity as the strain approaches 0.3. This increase in slope is due to the extension of the collagen and elastin fibers. If they are stretched beyond this point, failure takes place. Instead of the strain, ε, the stretch ratio ($\lambda = \varepsilon + 1$) is used in the plot.

It is instructive to plot the slope, $d\sigma/d\varepsilon = E$, as a function of stress. This is done in Fig. 133b for the aorta of a dog (circumferential strip). The slope first increases by a relationship that can be described by a power function. Then, it reaches a linear range, in which the increase is more gradual. This non-linear elastic behavior is a characteristic feature of many soft tissues in the human body. It serves as an important function: as the pressure in the blood vessels is increased, the vessels become stiffer.

This response, typical of arteries, has been successfully represented by the equation:

$$\sigma = (\sigma^* + \beta)e^{\alpha(\varepsilon - \varepsilon^*)} - \beta \tag{44}$$

where α and β are parameters defined in Fig. 133b. α is the slope of the linear portion and β is related to the intercept. σ^* and ε^* correspond to the onset of the linear portion. This equation is known as the Fung equation. This equation can also be expressed in terms of λ, the stretch ratios.

8.3.2. Residual stresses

Biological materials such as arteries contain residual stress. In the case of a segment of artery that is not under internal blood pressure, the walls of the artery are under strain and therefore, have residual stress. Fung [25] has shown that if one makes an axial cut in the wall of an artery, the artery will spontaneously open. This geometry is known as the zero-stress state. The angle by which the artery springs open is defined as the opening angle. As this opening angle increases the stress distribution in the wall under pressure becomes more uniform. This makes sense since under normal blood pressure arteries inflate, causing higher strain on the inner wall of the artery (compared to the outer wall). In arteries, stress is an exponential function of strain, so the observed increase in strain at the inner wall will be accompanied by an increase in stress at the inner wall.

Four different arteries, with different zero-stress angles, are shown in Fig. 134: $\alpha = 0°$, 10°, 70°, and 155°. For the same arteries, the wall under pressure stresses at two values of the applied internal pressure are shown. For zero pressure, there is a detrimental effect on the stress distribution. However, this is not the critical condition. For 100 mm internal pressure (in the range of pressure of blood inside our body), the artery with the highest value of α has the lowest stress in the wall. Thus, the residual stress reduces the maximum stress in the artery walls.
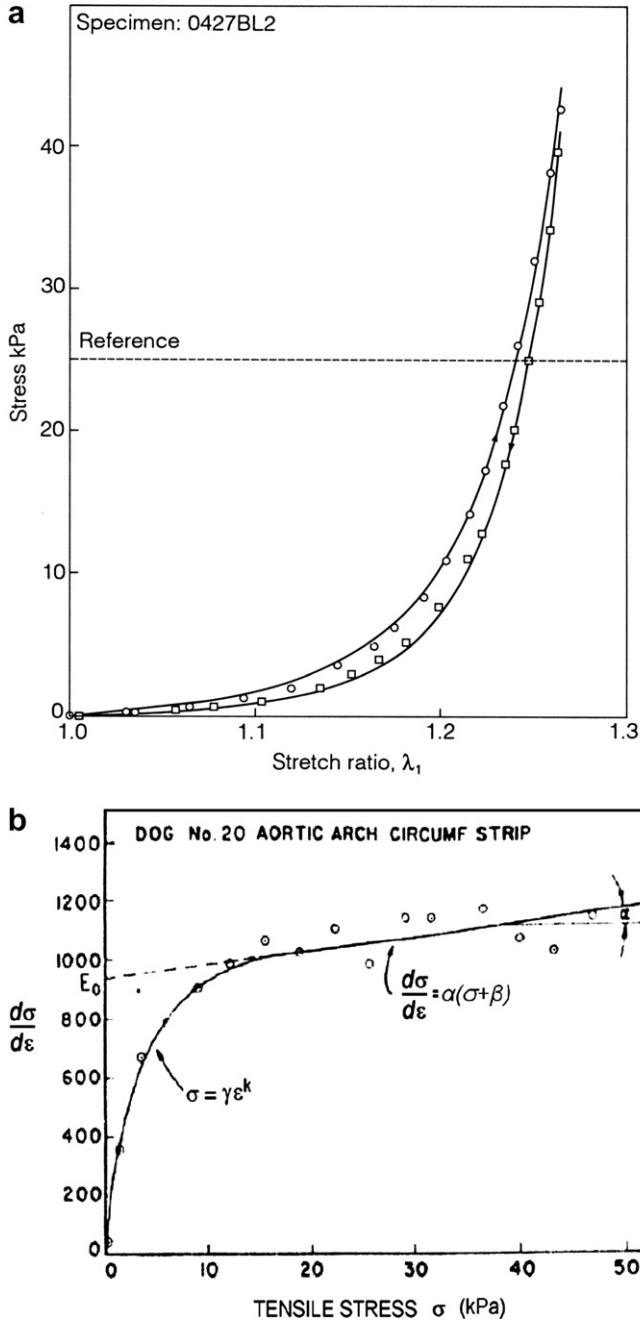
Fig. 133. (a) Stress–strain response of human vena cava: circles-loading; squares-unloading; (b) representation of mechanical response in terms of tangent modulus (slope of stress–strain curve) vs. stress (adapted from Fung [24, p. 325]).
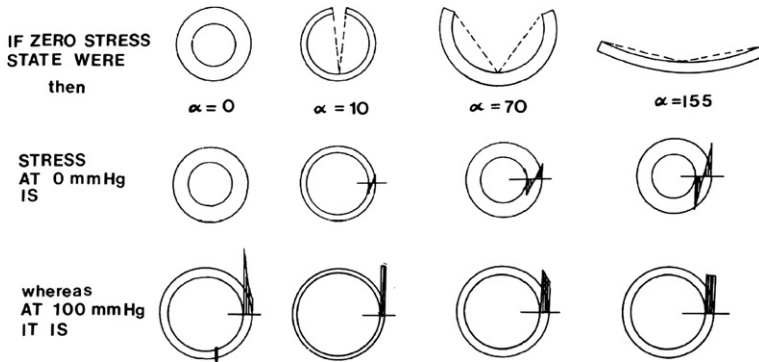
Fig. 134. Residual stresses in arteries; the artery is sliced longitudinally and the angle α is measured (from Fung [25, p. 384, Fig. 11.3.2]).

8.4. Mussel byssus

The byssal threads of marine mussels act as the only anchor lines which attach the animals to reefs, rocks, and other fixtures. These thin hair-like fibers undergo repeated shock from pounding waves and changing currents and must survive without failure to prevent the animal from being swept out to sea. Thus, the toughness the byssal thread material
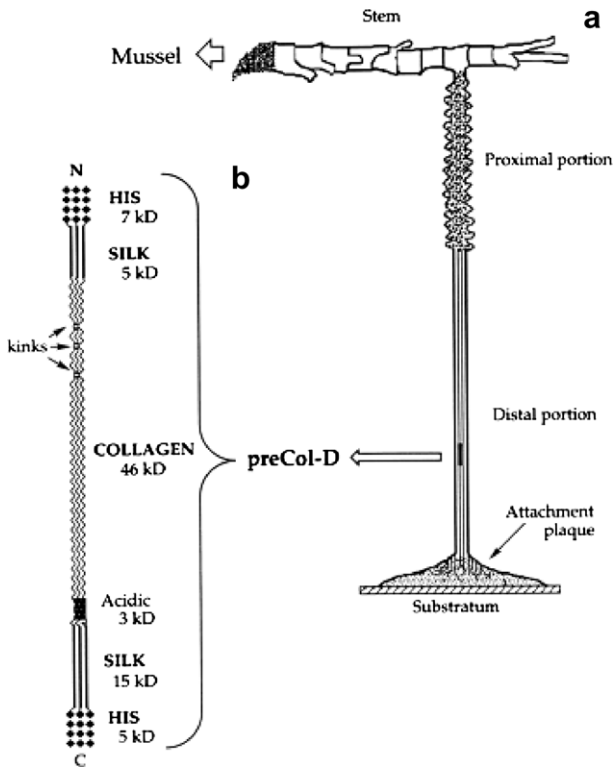

Fig. 135. Schematic representation of mussel byssal threads (from Qin et al. [260]).
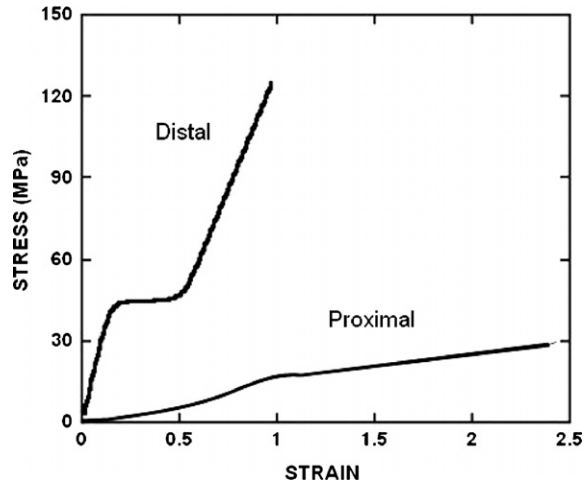
Fig. 136. Stress strain curve of the Distal and Proximal region of the mussel byssal thread (reproduced from Bell and Gasoline [262]).

is of the utmost importance. On the macro scale the threads are composed of both a stiff tether region (the distal thread) which is attaches to rock, and an elastic region (the proximal thread) which acts as a shock absorber for the animal [258]. The microstructure of byssal threads is roughly similar to that of tendons. The distal region consists of many bundles of collagen fibrils separated by fibrion-like domains and histidine-rich blocks, including possible β-sheet regions [259–261]. An illustration of the byssal thread micro and macrostructure is presented in Fig. 135 [261]. Although these threads are similar to tendons in tensile strength, the distal region is remarkably more extensible and much tougher [258].

The two regions of the thread serve different functions and thus have very different mechanical properties. The elastic modulus of the proximal thread is approximately an order of magnitude lower than that of the distal region [258]. However, failure almost exclusively occurs in the proximal region [262]. This implies the distal region is considerably tougher, as can be seen from the area under the curves in Fig. 136 [262].

The mismatch in elastic modulus of the two regions presents an interesting Materials Science problem. Failure often occurs at the interface of joined materials with high modulus mismatches [263,264]. This does not occur in the case of the byssal threads and is likely the result of modulus management in which the distal region softens and the proximal portion stiffens close to the interface.

8.5. Cells

Cells constitute the basic structural building blocks of living organisms and perform a variety of functions: self-replication, protection from the environment, acquisition of nutrients, movement, communication, catabolism of extrinsic molecules, degradation and renewal of aged intrinsic molecules, and energy generation.

8.5.1. Structure and mechanical properties

Most of the biological cells are 1–100 μm in size, and they comprise many constituents (Fig. 137a) [265]. The interior of the cell includes a liquid phase (cytosol), a nucleus, the
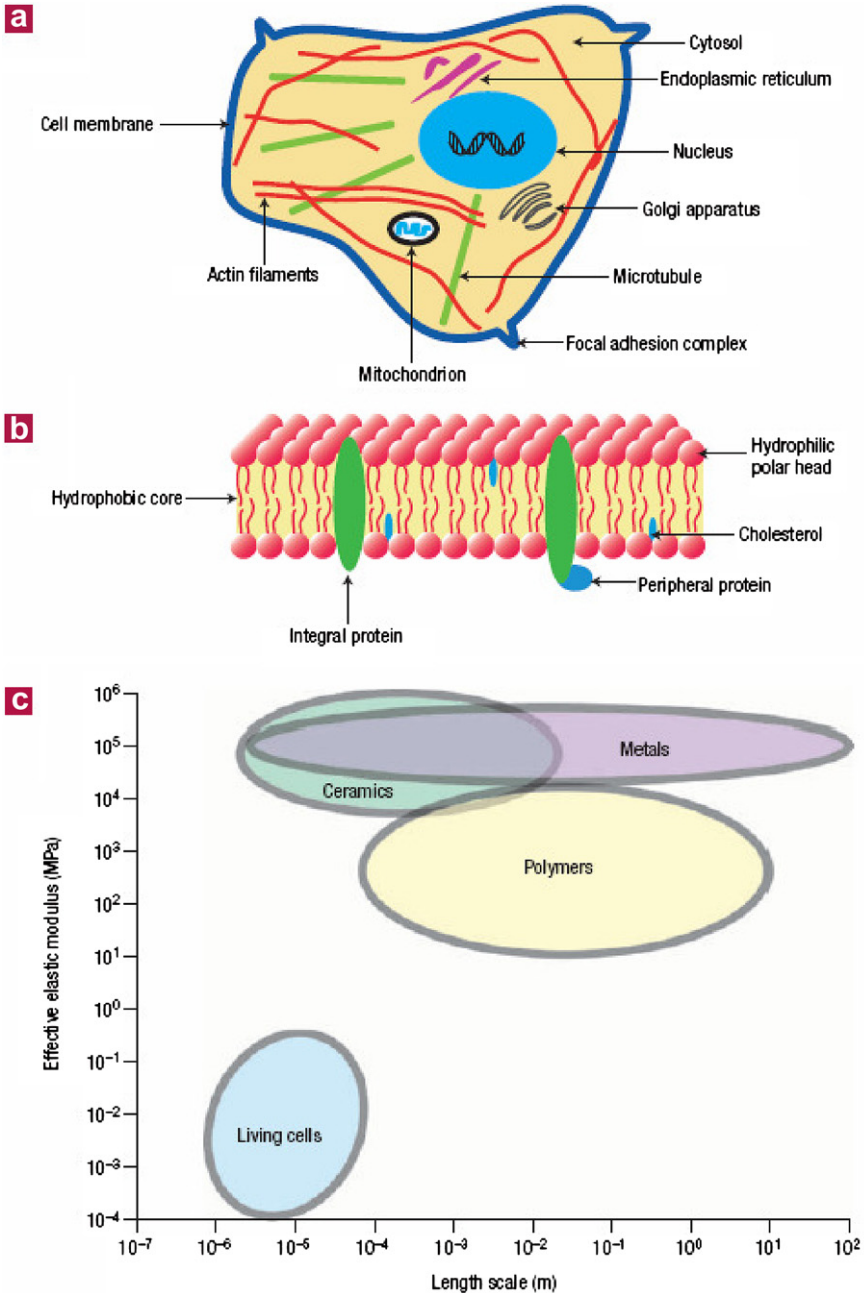
Fig. 137. Eukariotic cell structure and elastic properties (from Bao and Suresh [265, Fig. 1]).

cytoskeleton consisting of networks of microtubules, actin and intermediate filaments, organelles of different sizes and shapes, and other proteins. The exterior of the cell is covered by a phospholipid bilayer membrane reinforced with protein molecules (Fig. 137b).

The resistance of single cells to elastic deformation, as quantified by an effective elastic modulus, ranges from 10^2 to 10^5 Pa (Fig. 137c), orders of magnitude smaller than that of metals, ceramics and polymers. The deformability of cells is determined largely by the cytoskeleton, whose rigidity is influenced by the mechanical and chemical environments including cell–cell and cell–extracellular matrix (ECM) interactions.

Living cells are constantly subjected to mechanical stimulations throughout life. These stresses and strains can arise from both the external environmental and internal physiological conditions. Depending on the magnitude, direction and distribution of these mechanical stimuli, cells can respond in a variety of ways. For example, within the body, fluid shear of endothelial cells activates hormone release and intracellular calcium signaling as well as stiffening the cells by inducing rearrangement of the cytoskeleton. The mechanical compression of cells, such as chondrocytes, is known to modulate proteoglycan synthesis. Furthermore, the tensile stretching of cell substrate can alter both cell motility and orientation. As a result, to understand how cells mechanically respond to physical loads is an important first step to further investigate how the transmission and distribution of these mechanical signals are eventually converted to biological and chemical responses.

8.5.2. Mechanical testing

With the recent advances in molecular and cell biology, biophysics, nanotechnology, and materials science, several innovative experimental techniques and equipments have been developed to probe the structural mechanical properties of biostructures from the micro down to the nanoscale. These techniques can not only perform direct mechanical probing and manipulation of single cells and biomolecules, but also allow such tests to be conducted under physiological conditions. Lim et al. [266] summarized biomechanical testing and imaging instruments/techniques employed to study biological structures ranging from single biomolecules, cells to tissues, as shown in Fig. 138. Fig. 138a shows some of the experimental techniques used for conducting biomechanical tests in single cells and single molecules while Fig. 138b shows the imaging techniques available for use in such tests. Bao and Suresh [265] further classified the experimental techniques into three types (Fig. 139):

Type A: local probes in which a portion of the cell is deformed.
Type B: mechanical loading of an entire cell.
Type C: simultaneous mechanical stressing of a population of cells.

Atomic force microscopy (AFM) and magnetic twisting cytometry (MTC) belong to type A. AFM has become a powerful technique for both imaging surface morphology and sensing force. A sharp tip mounted at the end of a flexible cantilever directly contacts the sample surface and generates a local deformation (Fig. 139a). The interaction between the tip and sample surface induces deflection of the cantilever, which can be calibrated to estimate the applied force. Fig. 140 represents the deformation and unfolding of protein by AFM. Magnetic twisting cytometry (MTC) involves magnetic beads with functionalized surfaces. Magnetic beads are attached to a cell and a magnetic field imposes a twisting moment on the beads, deforming a portion of the cell (Fig. 139b). Deformation generated by magnetic beads is analyzed and the mechanical properties of the cell can be obtained.

Micropipette aspiration (MA) and optical tweezers are common methods of type B. A suction pressure was applied through a micropipette to deform a single cell (Fig. 139c).
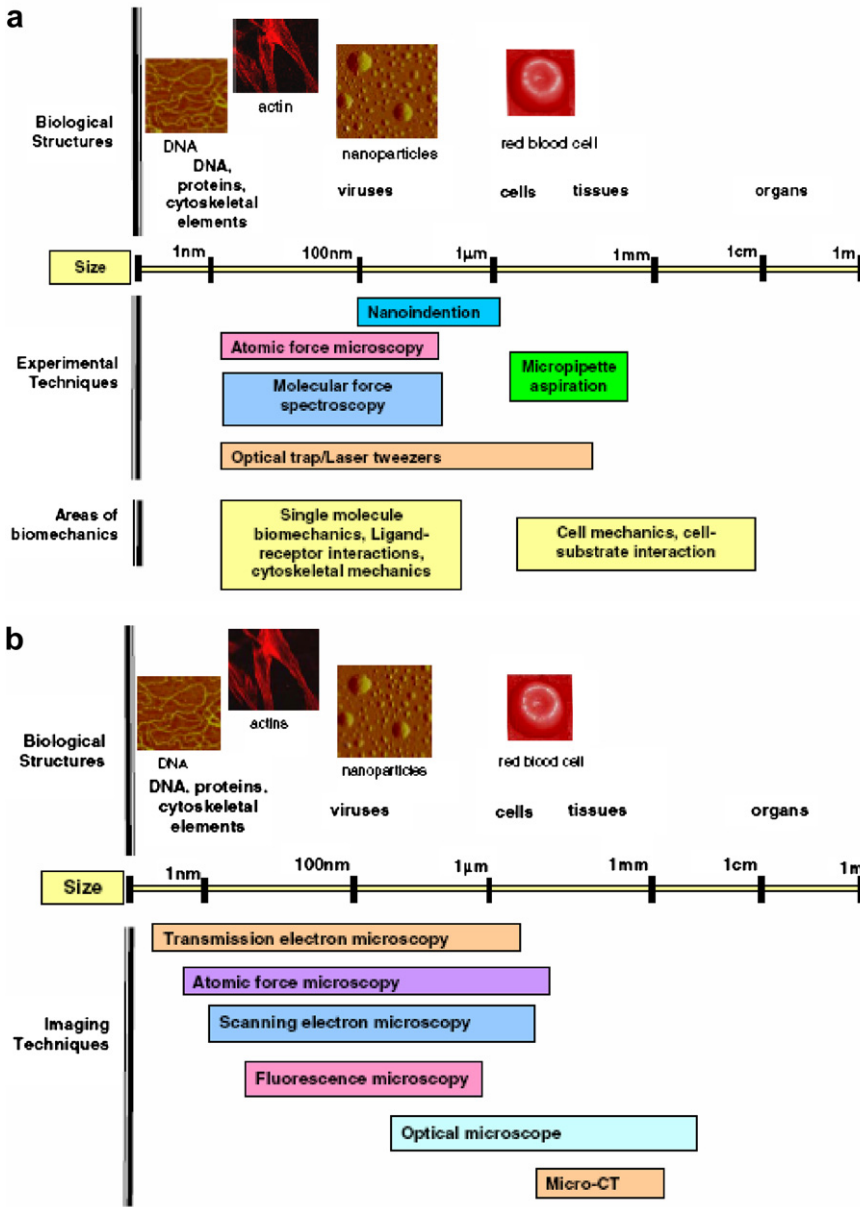
Fig. 138. (a) Experimental techniques for conducting mechanical tests in single cell and single molecule biomechanics. (b) Imaging techniques that can be used to observe physical, biological and biochemical changes occurring in biological structures during biomechanical tests of cells and biomolecules (from Lim et al. [266]).

The shape change of the cell is recorded by video microscopy. By measuring the elongation into the pipette as a result of the suction pressure, the mechanical properties can be evaluated. Micropipette aspiration is widely used to study the mechanical response of blood
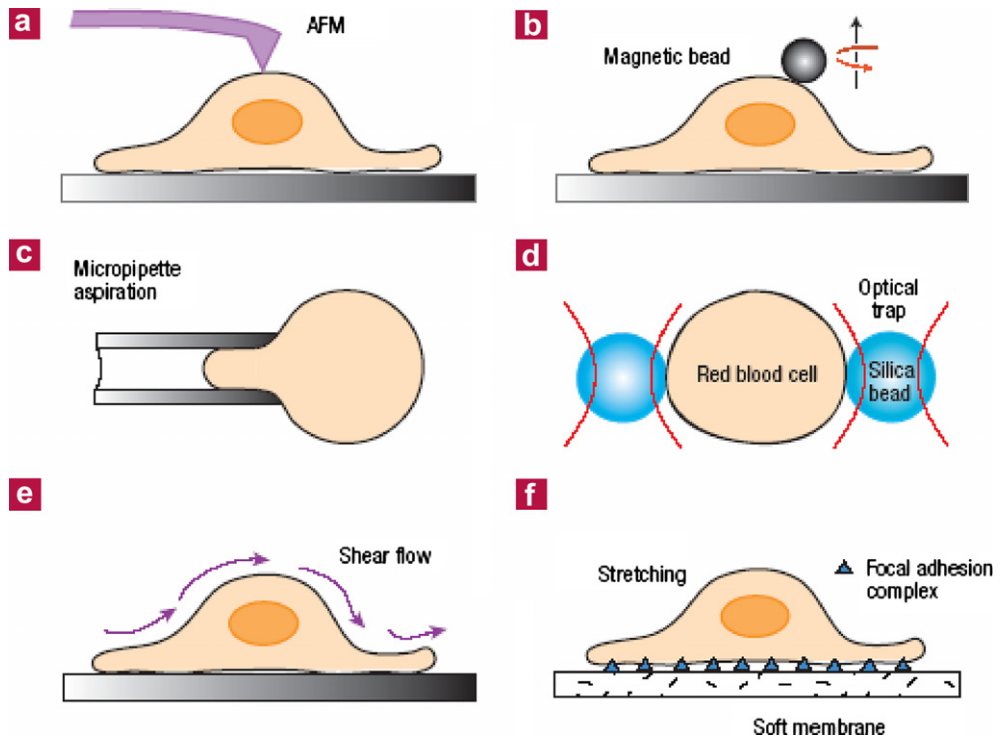
Fig. 139. Schematic representation of different types of experimental techniques used to probe living cells (from Bao and Suresh [265, Fig. 2]).

cells. Optical tweezers or laser traps use laser to control particles in a medium. When a laser beam shines on a dielectric particle with higher refractive index than the medium, the gradient force is higher than the scattering force. As a result, a net force pushes the particle towards the focal point of the laser. In order to deform a single cell, a laser trap is used with two microbeads attached to the opposite ends of a cell (Fig. 139d).

Shear-flow methods (Fig. 139e) and stretching devices (Fig. 139(f)) are type C methods used to study the mechanical response of an entire population of 10^2–10^4 cells. Shear-flow experiments are conducted with either a cone-and-plate viscometer or a parallel-plate flow chamber. The shear stress applied to cells for both cases can be quantified. Different stretching devices (uniaxial, biaxial, and pressure-controlled) have been developed to deform cells. Cells are cultured on a thin polymer substrate, which is coated with extracellular matrix (ECM) molecules for cell adhesion. The substrate is then mechanically deformed while maintaining the cell's viability *in vitro*. The effects of mechanical loading on cell morphology, phenotype and injury can be examined.

The developments and advances in nanotechnology and biophysical techniques enable a better understanding of the pathophysiology and pathogenesis of human diseases that manifest structural and mechanical properties changes. Recent works by Lim [267] and Lee and Lim [268] highlighted some of the biomechanics research carried out on several types of diseases, such as malaria, sickle cell anemia, and cancer.
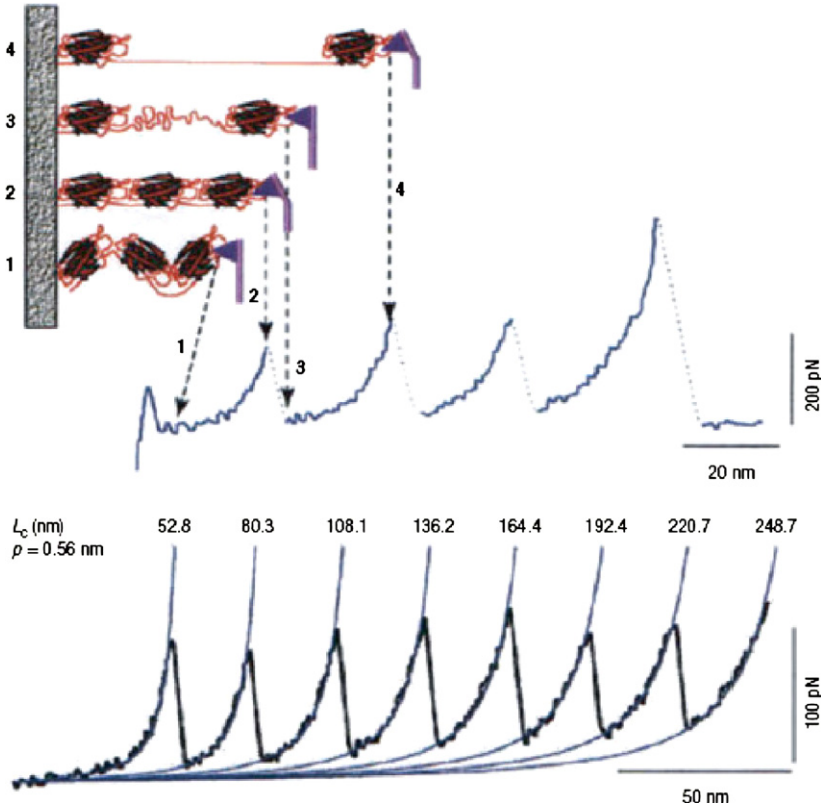
Fig. 140. Domain deformation and unfolding of a multidomain protein under stretching with AFM (from Fisher et al. [274]).

The human red blood cell, which has a biconcave shape with an average diameter of about 8 μm is highly deformable. During the circulation in the narrow capillaries (about 3 μm in diameter), it undergoes severe deformation and transforms the biconcave shape to bullet shape by folding. The cell fully recovers its original shape after it flows through small capillaries. Blood cells can harden and lose their elasticity through disease, such as malaria and sickle cell anemia. The change in mechanical properties causes serious impairment of blood flow and results in severe anemia, coma, or even death. Suresh and coworkers [269–272] studied the mechanical response of living cells. Ingenious experimental techniques developed in collaboration with Lim enabled establishing the load extension response of a single cell. From this, the researchers extracted the elastic response of the cell and how it is altered by disease. Figs. 141a and b show the conceptual experiment [271]. Two glass beads (diameter of approximately 5 μm) attach themselves to the ends of the cell by capillary forces. A laser beam is used to trap one of the beads. This is an optical (laser tweezer) trapping device. The glass slide under the cell is moved and the load is measured. The displacement of the cell is recorded. The actual photographs of the cells as they are being stretched are shown in Fig. 140c and d. This information thus obtained is compared with computational simulations using both a finite element mesh and a new approach based on actual spectrin fibrous molecules, developed by the MIT
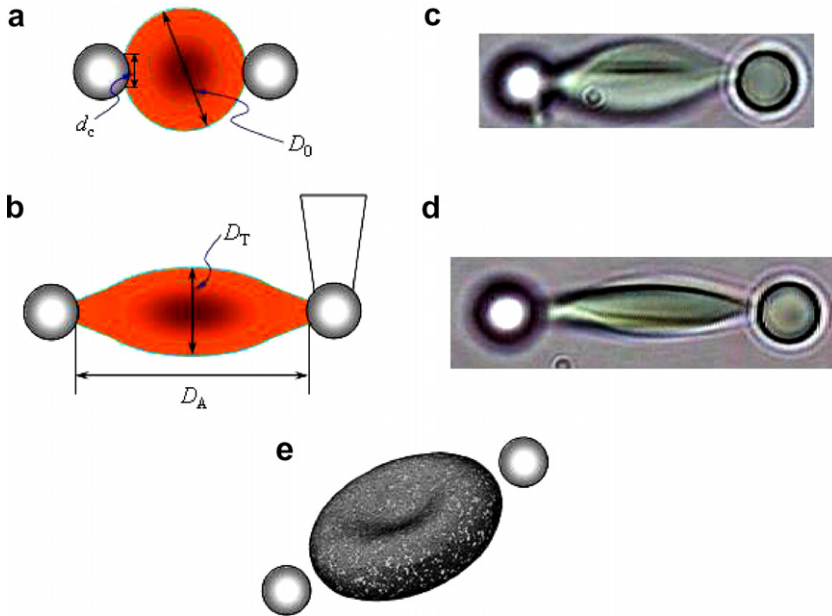
Fig. 141. (a,b) Schematic representation of single cell extension apparatus; (c,d) photomicrographs of red blood cells in extended configuration; (e) spectrin fiber simulation of process; initial unstretched configuration shown (from Dao et al. [271]).

group (Fig. 140e). Fig. 142 shows the molecular based and continuum models of red blood cell membrane [271]. Lim et al. [273] have a comprehensive review on mechanical models for living cell.

8.5.3. Cell motility, locomotion, and adhesion

Most cells have the ability to move. Some cells are specialized for locomotion, such as amoebae and spermatozoids. In most cells, locomotion is usually repressed. However, this ability can be activated in wounds and oncogenesis. The mechanism of amoeboid cell motility (crawling, or gliding) involves the actin cytoskeleton. Actin filaments themselves are likely to be involved in the force-generating mechanisms. The major components of cell motility are shown in Fig. 143 [275]. Protrusion is the forward motility of the membrane at the front of the cell. Adhesion of the advancing portion of cell is required for protrusion to be converted into movement along the substrate. The last step in locomotion is comprised of two mechanistically distinct processes: de-adhesion and tail retraction.

The protrusion at the front of motile cells requires dense arrays of actin filaments. It seems that these filaments are organized with their barbed ends oriented preferentially in the direction of protrusion. The web of actin filaments is organized as an orthogonal cross-weave between two sets of filaments oriented at approximately 45° to the direction of protrusion Two mechanisms for generating protrusive force have been proposed:

(a) The action of motor proteins to drive protrusion: Myosin I molecules contribute to this, just as in the case of muscles (Section 8.2); myosin I moves toward the actin filament barbed ends.
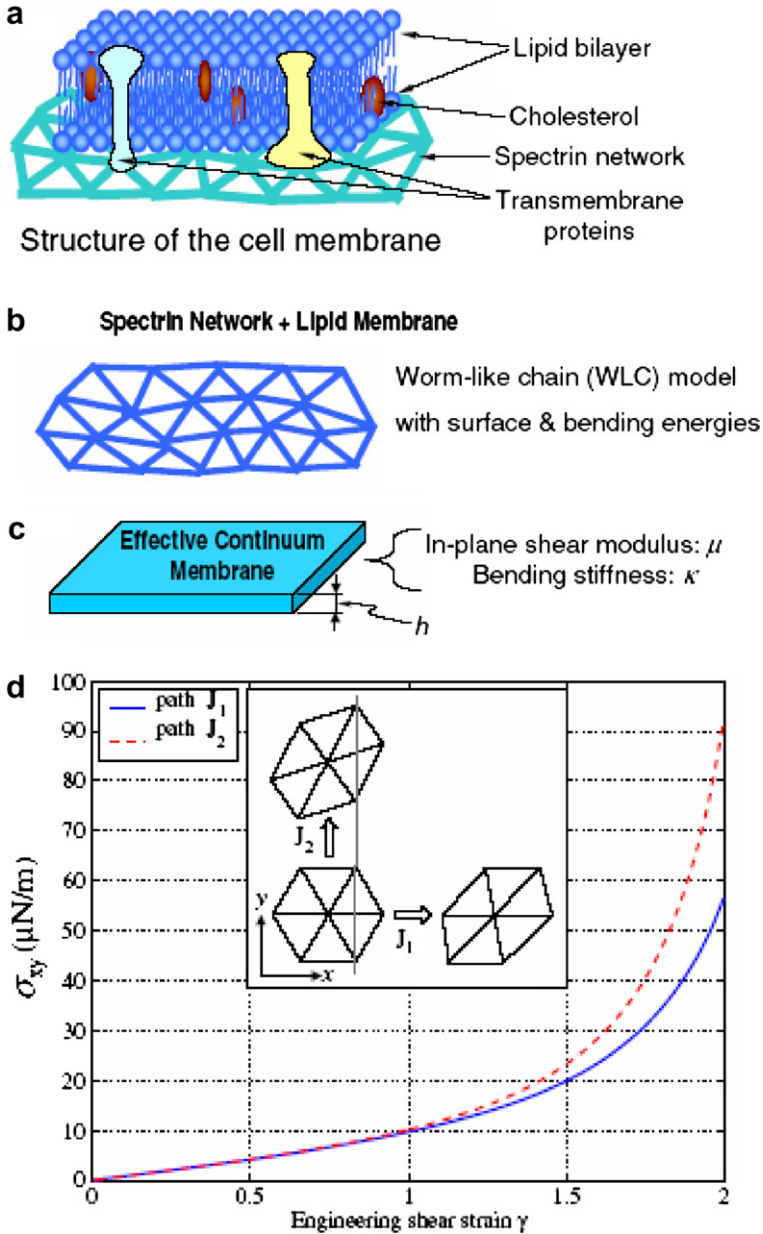
Fig. 142. Molecular based and continuum models of red blood cell membrane. (a) Schematic drawing of the red blood cell membrane structure (not to scale). (b) Molecular based model. (c) Effective continuum membrane. (d) Large-strain response of "single-crystal" worm-like chain membrane ($p = 8.5$ nm, $L_0 = 87$ nm, $L_{max} = 238$ nm) for two area-preserving shear paths J_1 and J_2 (from Dao et al. [271]).

(b) Actin polymerization itself produces force. Polymerization of pure actin inside a lipid vesicle can deform the cell membrane; polymerization of other proteins also produces membrane-deforming force.
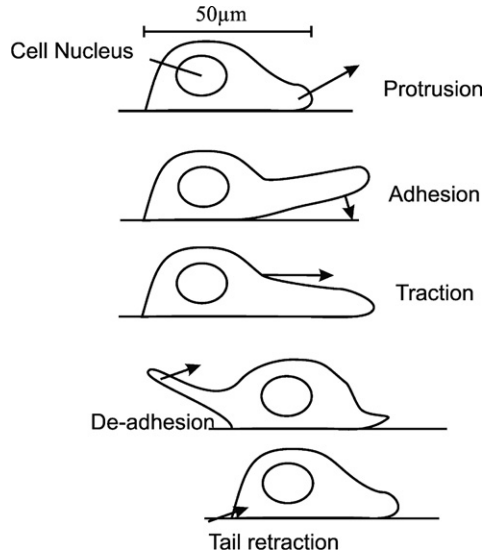
Fig. 143. Sequence motility showing elements involved in the locomotion of cell; protrusion–adhesion–traction–de-adhesion and tail retraction (reproduced from Mitchison and Cramer [275, Fig. 1]).

Force production requires an energy source and this derives from the chemical energy of nucleotide hydrolysis in the ATPase motor. In the polymer model, thermally driven movements create the movement.

Cell motility is an important property, especially since it is involved in diseases such as cancer metastasis. The cancer cells separate themselves from the primary tumour, pass through the extracellular matrix in the body and enter the circulatory system. Then, after being arrested, they penetrate through the blood vessel walls (extravasation) at a secondary location. This sequence is shown in Fig. 144. Indeed, the application of Mechanics and Materials Science to the study of cancer cells will hopefully help in elucidating the basic mechanism. Suresh [276] reviews the subject and presents a framework for this new field of investigation, which will incorporate cancer cell mechanics, motility, deformability, differentiation, and neoplastic transformation.

In the adhesion of cells to the extracellular matrix (ECM) or to other cells the protein integrin plays a key role. Integrin-mediated adhesion is a complex process. Integrins play an important role by providing anchorage that ensures cell survival, and migration (motility). Integrins are important in how cells react to implants, in tissue engineering, and in how cells behave in cell arrays and biotechnology cell culture. Fig. 145 [277] shows schematics of cells attaching themselves to synthetic biomaterials whose surfaces were modified by different means:

(a) proteins adsorbed from solution, such as blood, plasma, or serum;
(b) ligands engineered at the surface, such as RGDs (arginine–glycine–aspartic acid);
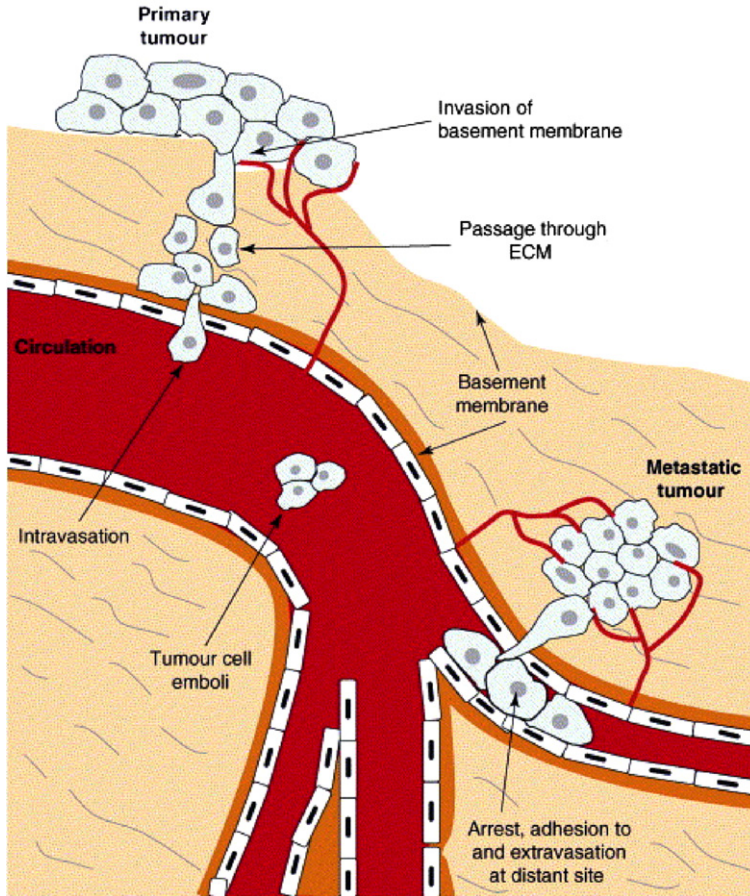(c) ligands deposited by cells, e.g., collagen deposition.

Fig. 144. Schematic diagram showing different stages of cancer metastasis; cancer cells penetrate through ECM and into the blood stream, then extravasate into secondary site, where metastasis takes place (from Lee and Lim [268, Fig. 5]).
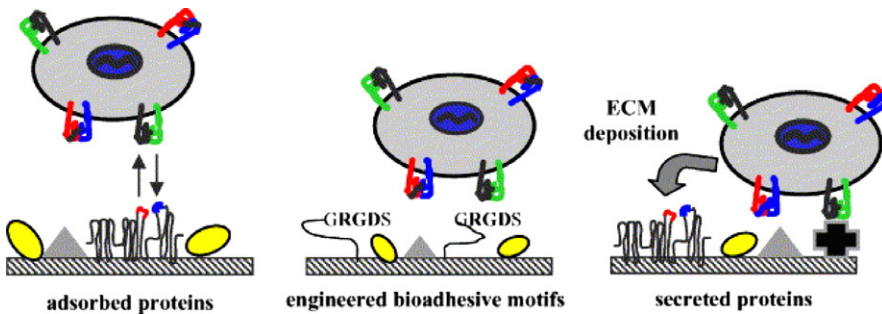

Fig. 145. Mechanisms controlling cell adhesion to biomaterials (from Garcia [277, Fig. 1]).
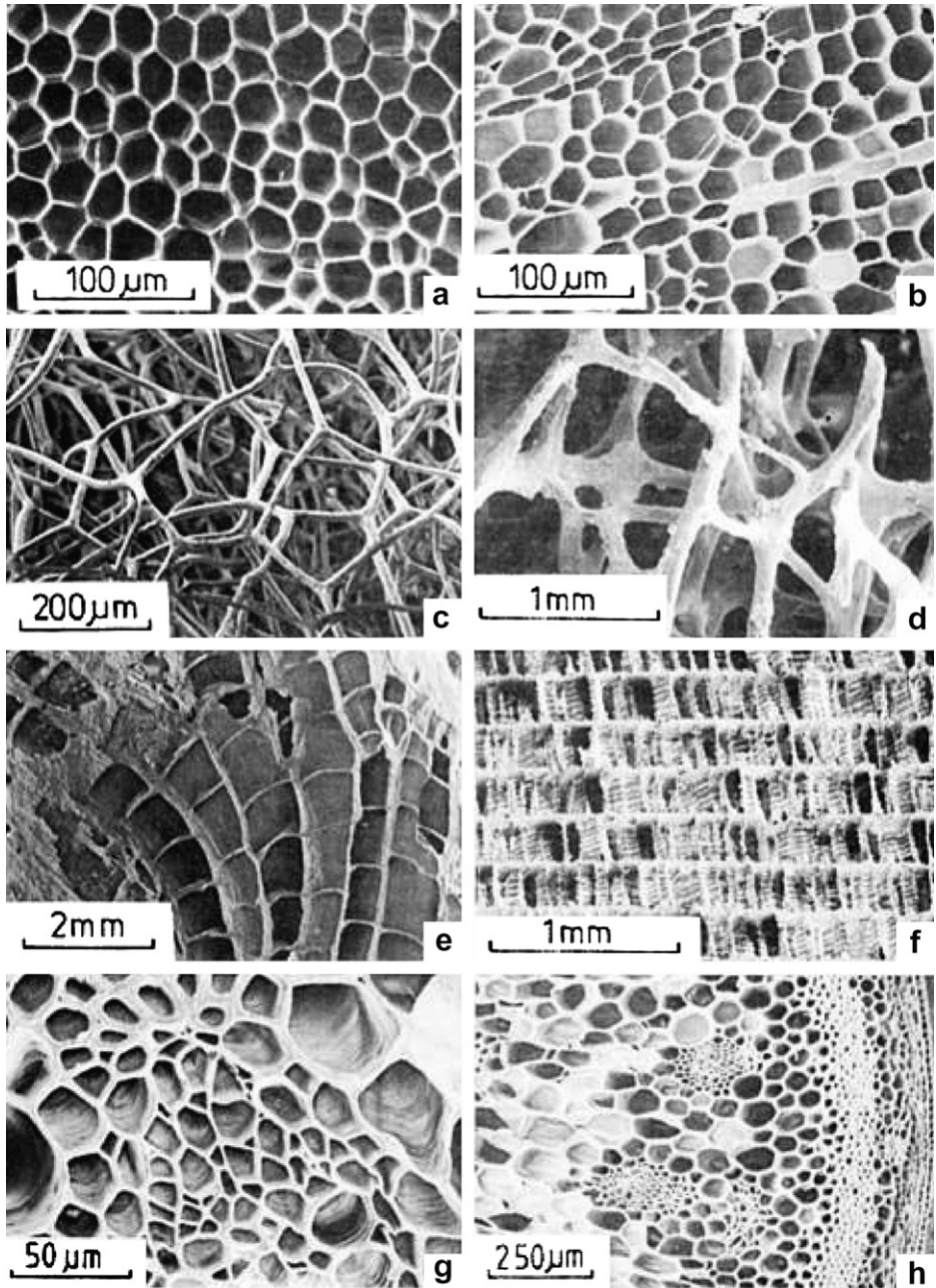
Fig. 146. Examples of cellular materials (a – cork; b – balsa; c – sponge; d – cancellous bone; e – coral; f – cuttlefish bone; g – iris leaf; h – stalk of plant) (from Gibson and Ashby [28, p. 17, Fig. 2.5]).

9. Biological cellular materials

Many naturally occurring materials are not fully dense, i.e. they possess internal cavities. This type of design is intentional, since it reduces the density. Examples are cork, bones, wood, sponge, and plant stalks and they are shown in Fig. 146 [28].

Modern synthetic materials have also adopted this form, and we have metallic, ceramic, and polymeric foams. Some are of common and every day usage, such as Styrofoam. Others are quite esoteric, such as the Space Shuttle tiles, which have a density of 0.141 g/cm^3 and a maximum temperature capability of 1260 °C.

An example of a biological cellular material is cancellous bone. Bone is designed to have a variable density. Regions subjected to higher stress are denser. The outside surface is made of high density material and is called compact bone. The inside of bone tends to have a lower density and is termed cancellous bone. Figs. 81a and 147 show the longitudinal section of a tibia. The same occurs in antlers. Fig. 81b shows the cross-section of an elk antler. The surface region is compact, whereas the center is cellular. This is also justified by the resistance to flexure: the inside is not subjected to such high stresses as the outside ($\sigma \alpha r$, where r is radial distance). Thus, the strength requirement increases linearly from the neutral axis to the surface. This corresponds approximately to the porosity distribution.

There are numerous other examples of cellular materials. These cellular materials are used either by themselves or in sandwich arrangements. Sandwich structures range from common cardboard used in packaging to important uses in the aircraft industry. The basic idea is to have a dense skin and a light-weight interior. Fig. 148 shows a cross-section of a horseshoe crab, where we can see that a cellular network provides the rigidity [278]. Two other examples, wood and beak interior, are described in Sections 9.2 and 9.3, respectively.

9.1. Basic equations

The compressive stress–strain curves of cellular materials have three characteristic regions: (a) an elastic region, (b) a collapse plateau, and (c) a densification region. These
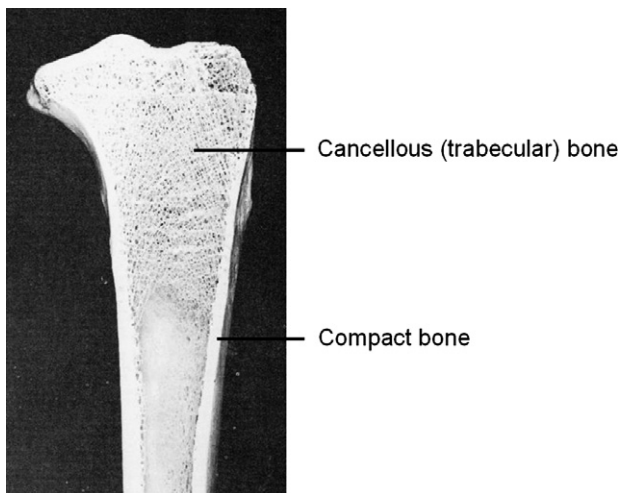

Fig. 147. Longitudinal section of tibia (from Gibson and Ashby [28, p. 430, Fig. 11.1]).
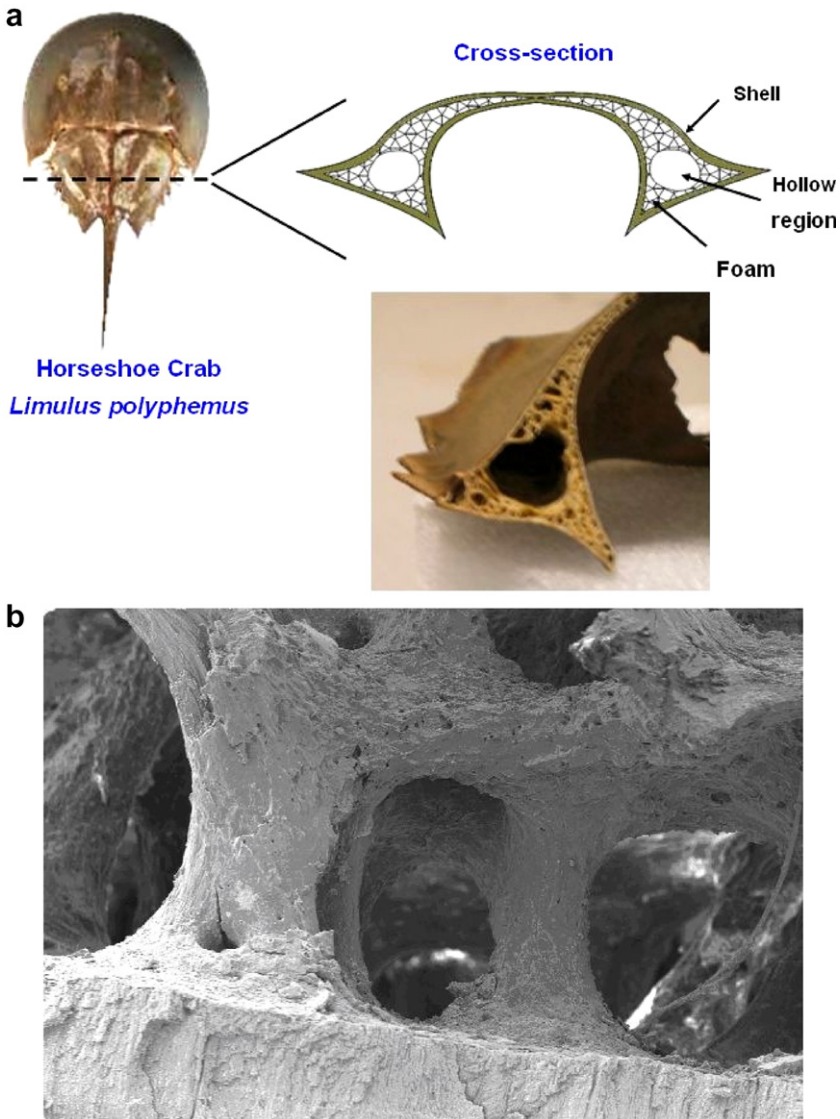
Fig. 148. (a) Cross-section image of horseshoe crab exoskeleton showing the foam structure. (b) SEM micrograph shows the detail of the foam structure in horseshoe crab exoskeleton (from Chen et al. [278]).

are shown in Fig. 149 [28]. The higher the initial density, expressed in Fig. 149 by ρ^*/ρ_s, the smaller the collapse plateau region. It also occurs at a higher stress.

We will develop expressions that predict this behavior. These are the Gibson–Ashby equations. They are developed here for an open cell geometry that represents well cellular materials with a low relative density. Section 9.3.2 will present the equivalent equations for a closed cell geometry. Fig. 150 represents this open-cell structure. It consists of straight beams with a square cross-section [28]. The model is very simple but captures the essential physics. There are two characteristic dimensions: the cell size, l, and the beam thickness, t.
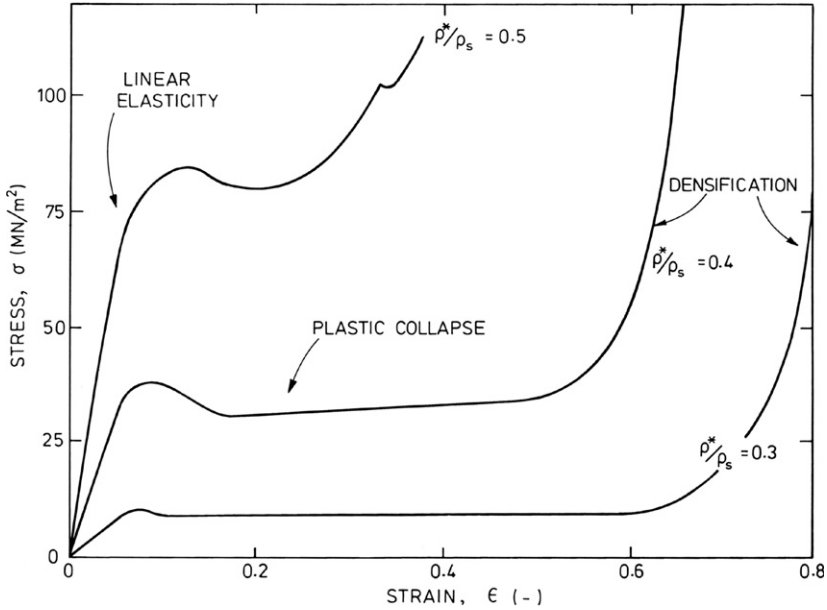
Fig. 149. Stress–strain curves for cancellous bone at three different relative densities: 0.3, 0.4, and 0.5 (from Gibson and Ashby [28, p. 317, Fig. 11.5]).
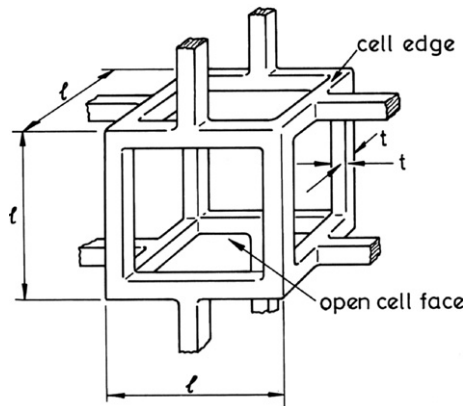
Fig. 150. Open-cell structure for cellular materials with low relative density. This is the structure upon which the Gibson–Ashby equations are based (from Gibson and Ashby [28, p. 185, Fig. 5.6]).

(a) Elastic region

Three elastic constants are defined for an isotropic foam: E^*, G^*, and v^*. The density of the cellular material is ρ^*, and that of the solid material is ρ. From Fig. 150 we can obtain an expression for the density in terms of l and t

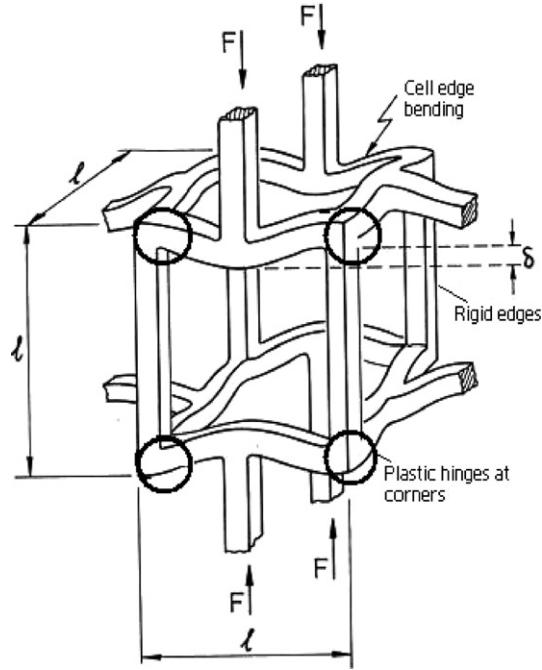Fig. 151. The open cell configuration under compressive loading. Note the deflection δ observed (from Gibson and Ashby [28, p. 185, Fig. 5.6]).

$$\frac{\rho^*}{\rho_s} = C_1 \left(\frac{t}{l}\right)^2 \tag{45}$$

C_1 is a proportionality constant. When the cell is subjected to compressive loading, it will deflect as shown in Fig. 151 [28]. The vertical columns push on the horizontal beams and cause them to bend. A force F on each column produces a deflection δ in the beam. The moment of inertia of a beam with a rectangular section (sides of b and h) is

$$I = \frac{bh^3}{12} \tag{46}$$

For the square cross-section with side t

$$I = \frac{t^4}{12} \tag{47}$$

Beam theory states that the deflection, δ, is given by

$$\delta = C_2 \frac{Fl^3}{E_s I} \tag{48}$$

C_2 is a constant. The stress acting on the cell is related to the force, F, by (each force F is shared by two neighboring cells)

$$\sigma = \frac{F}{l^2} \tag{49}$$

The strain, ε, is related to the deflection by

$$\varepsilon = \frac{2\delta}{l} \tag{50}$$

Thus, the Young's modulus, E^*, is

$$E^* = \frac{E_s I}{2C_2 l^4} = \frac{E_s t^4}{24C_2 l^4}$$

This can be expressed as a function of density (Eq. (45))

$$\frac{E^*}{E_s} = \frac{C_1}{24C_2} \left(\frac{\rho^*}{\rho_s}\right)^2 \tag{51}$$

Experimental measurements indicate that $C_1/24C_2$ should be approximately equal to one. Thus

$$\frac{E^*}{E_s} \sim \left(\frac{\rho^*}{\rho_s}\right)^2 \tag{52}$$

Similarly, an expression for the shear modulus can be obtained

$$\frac{G^*}{E_s} = \frac{3}{8} \left(\frac{\rho^*}{\rho_s}\right)^2 \tag{53}$$

(b) Plastic plateau

At a certain level of deformation, elastic behavior gives way to plastic deformation. The Gibson–Ashby equations are based on the formation of plastic hinges at the regions where the beams terminate. Four of these plastic hinges are circled in Fig. 151.

For the elastic case, the stresses increase linearly from the neutral axis. For the case of a plastic hinge, $\sigma = \sigma_{ys}$, the stresses acting on the cross-section are uniform and tensile above the neutral axis and uniform and compressive below the neutral axis. Fig. 151 shows the configuration.

The plastic moment, M_p, about the neutral axis is

$$M_p = F\frac{t}{2} \tag{54}$$

The yield stress is related to F by

$$\sigma_{ys} = \frac{F}{t\dfrac{t}{2}} \tag{55}$$

Thus, substituting Eq. (54) into Eq. (55)

$$M_p = \frac{1}{4}\sigma_{ys} t^3 \tag{56}$$

But, taking the beam with length $l/2$ and considering the force $F/2$ applied to each of the two hinges

$$M_p = \frac{F}{2}\frac{l}{2} = \frac{1}{4}Fl \tag{57}$$

The global stress acting on the foam is the force F divided by the area upon which it acts, l^2

$$\sigma_{pl}^* = \frac{F}{l^2} \tag{58}$$

Equating Eqs. (56) and (57) and applying Eq. (58)

$$\frac{\sigma_{pl}^*}{\sigma_{ys}} = \left(\frac{t}{l}\right)^3 \tag{59}$$

Substituting Eq. (45) into Eq. (59)

$$\frac{\sigma_{pl}^*}{\sigma_{ys}} = C_1^{-3/2} \left(\frac{\rho^*}{\rho_s}\right)^{3/2} \tag{60}$$

There are other expressions for the closed-walled cell, for cells that do not undergo plastic deformation, and for other cases.

(c) Densification

Densification starts when the plastic plateau comes to an end. This region is characterized by a complex deformation pattern. The stresses required for the densification rise rapidly as the open spaces between the collapsed cell structure close up. The analytical treatment for the collapse of pores and voids will not be presented here. There are theories that address this problem. One of the best known, the Carroll–Holt–Torre theory [279,280], assumes a spherical hole inside a solid sphere. By applying an external pressure it is possible to collapse the internal hole. The smaller the hole is, the higher the stress is. The Helle et al. model [281] addresses the same problem. A third formulation is the Fischmeister–Arzt theory [282].

9.2. Wood

Wood is one of the most ancient structural materials in the world and has played an important role in civilization. It is still widely used in buildings, furniture, ships, musical instruments, paper and so on. Wood has high specific stiffness (stiffness per unit weight) and specific strength that is comparable with steel [17]. The outstanding mechanical properties are mainly due to the hierarchical structure and optimized reinforcement orientation of cellulose fibrils.

Wood is a cellular composite with four levels of hierarchical structure: molecular, fibrillar, cellular, and macroscopic structure [283]. Fig. 152 shows the hierarchical structure of wood [284]. The main structural constituent of wood is cellulose, a high molecular weight polysaccharide (see Section 5.4, 2) which contributes the stiffness and strength. The cellulose is organized into microfibrils of about 10–20 nm in diameter. The microfibrils consist of both crystalline and amorphous regions. Bundles of cellulose microfibrils further form macrofibrils which are embedded in an amorphous matrix of lignin, hemicellulose, and other compounds.

The most characteristic structural level is the cellular structure, or the wood tracheid. Mark and Preston [285,286] carried out comprehensive studies on the structure of wood tracheids. Fig. 153a shows a simplified and generalized model of a wood tracheid [287]. Cotton fibers, which consist mainly of cellulose, have a similar multilayer structure
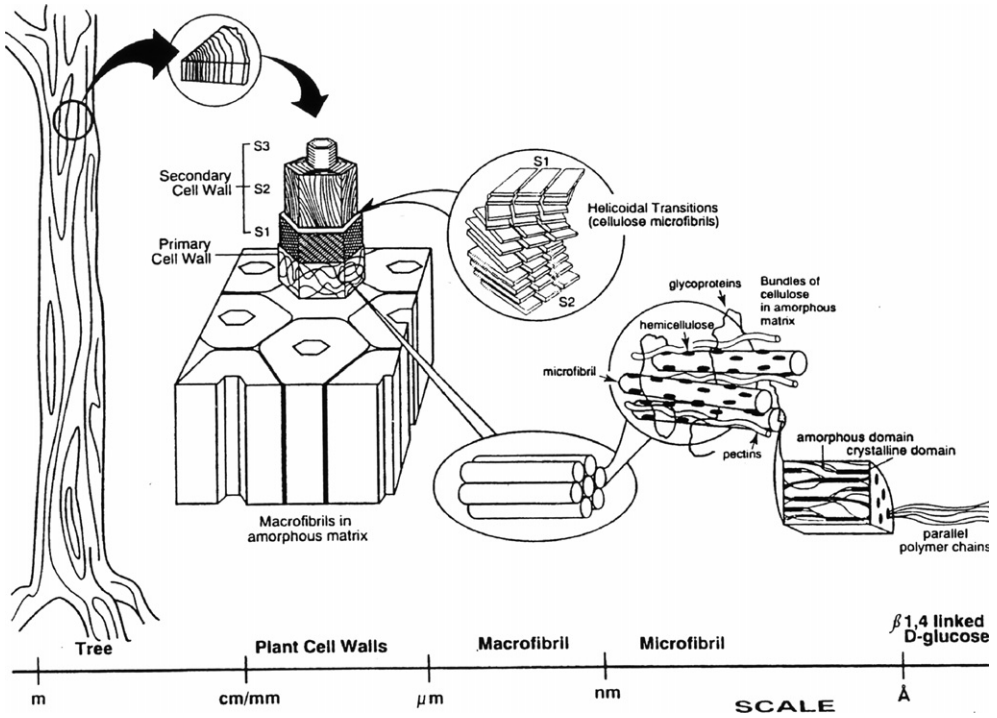
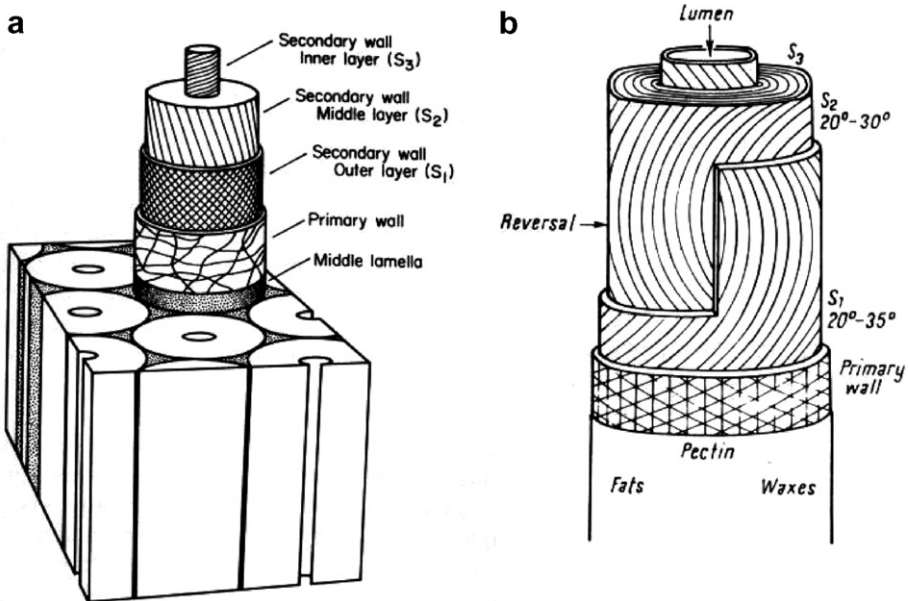Fig. 152. Hierarchical structure of cellulose in wood (courtesy of Kaplan [284]).

Fig. 153. Structure of (a) wood tracheid and (b) cotton fibers showing microfibril orientation and relative size of different layers of the cell wall (courtesy of J.O. Warwicker, the Shirley Institute, Manchester, England. [287]).

(Fig. 153b). From the outer surface to the center, the fiber has a cuticle, a primary wall, a secondary wall, a lumen wall, and a lumen. The cuticle is a waxy layer less than 0.25 μm thick. The primary wall is the original cell wall and consists of cellular fibrils in a randomly oriented network. The primary wall can restrict swelling of fibers. The secondary wall is composed of an outer layer (S_1), middle layer (S_2), and inner layer (S_3). The three layers of the secondary wall are built up by lamellae formed by almost parallel microfibrils and stack in a helicoidal pattern. The S_1 layer is roughly 0.2–0.3 μm and has an angle of 20–35° with respect to the fiber axis (parallel to the trunk). The S_3 layer, also know as lumen wall, is not always detected. It is 0.1 μm thin and has an angle of 60–90°. The S_2 layer constitutes about 95% by weight of the wood tracheid and can be 4 to 5 μm thick. The microfibrils in the S_2 layer have an angle of 20–30° [288]. The relative cross-sectional area (roughly 80% of the total cell wall area) and the low microfibrillar angle make the S_2 layer the major load bearing component [283]. The macroscopic structure of wood can be seen through naked eyes. Growing rings and rays can be observed in most species.

The mechanical properties of wood are highly anisotropic due to the preferred orientation of cellulose fibrils (parallel to the trunk). Gibson and Ashby [28] have a comprehensive review on the mechanical properties of wood. Fig. 154 shows three orthogonal planes of symmetry of wood: the radial, the tangential, and the axial directions. The stiffness and strength are greatest in the axial direction by a factor of 2–20 than that in the radial and tangential directions, depending on the species.

The general compressive stress–strain curves for wood (balsa wood) in three directions are shown in Fig. 155a. This curve has the same three stages discussed in Section 9.1 and is similar to the one for cancellous bone (Fig. 146a). At small strains (less than 0.02), the behavior is elastic in all three directions. The Young's modulus in the axial direction is much larger than that in the tangential and radial directions. Beyond the elastic regime, the loading curves in the three directions show extensive stress plateaus. The yield stress in the axial direction is much higher than that in the tangential and radial directions and is followed by a sharply serrated plateau. The plateaus in the tangential and radial directions are relatively flat and smooth. Compression in the tangential direction causes
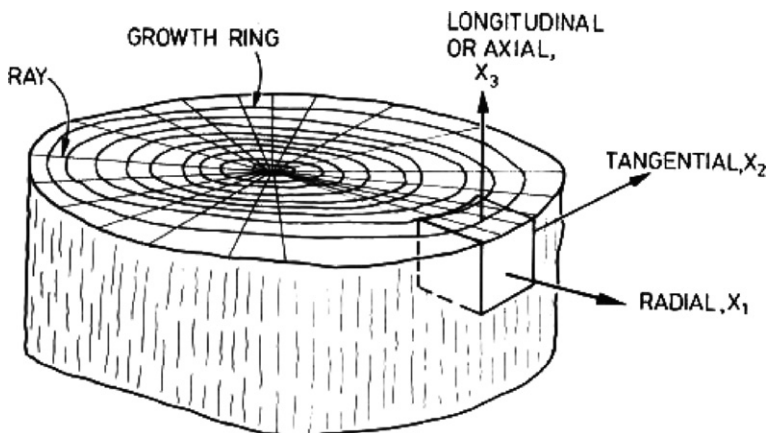

Fig. 154. A cross-section through the trunk of a tree showing the radial, tangential, and axial (longitudinal) directions (from Gibson and Ashby [28, p. 390, Fig. 10.1]).
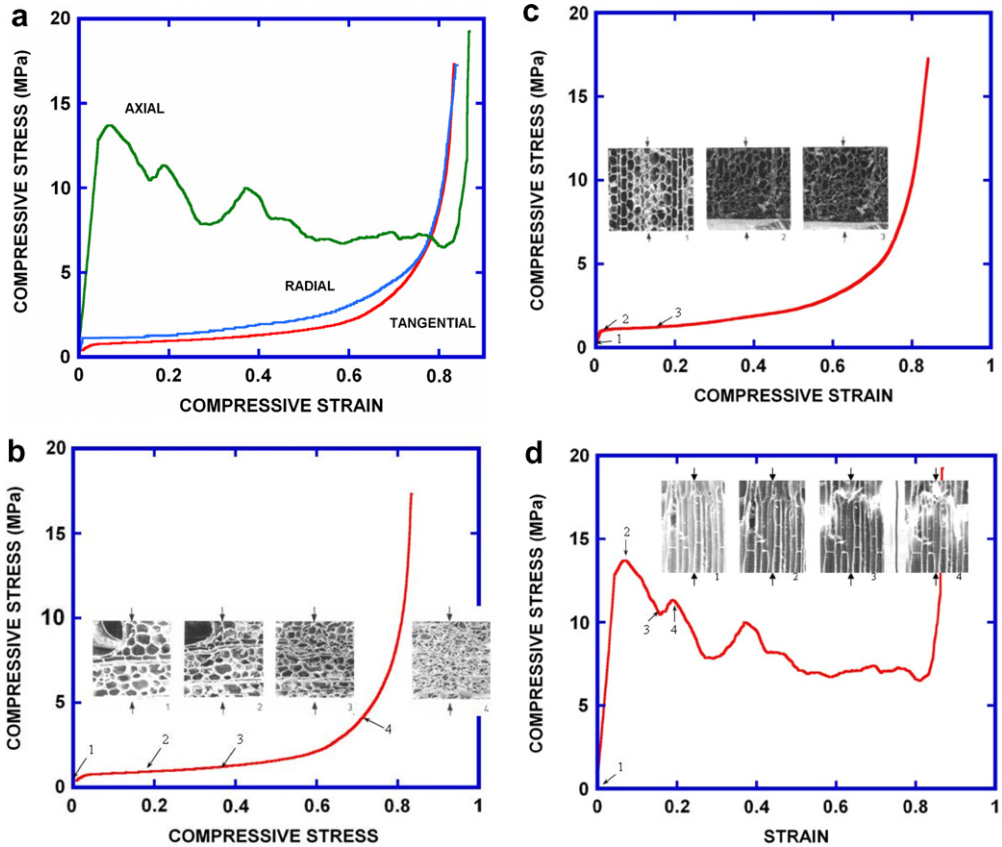
Fig. 155. (a) Compressive stress–strain curves for balsa tree. (b) Tangential compression, with scanning electron micrographs showing the deformation of the cells. (c) Radial compression and (d) axial compression with scanning electron micrographs showing the deformation of the cells (reproduced from Gibson and Ashby [28, p. 397–398, Figs. 10.4(a)–(d)]).

uniform bending and uniform collapse by plastic yielding of the cell walls (Fig. 155b) [289]. Compression in the radial direction causes uniform bending and uniform plastic collapse (Fig. 155c). A schematic drawing of the deformation under compressive loading in the radial direction is shown in Fig. 156. This is the mechanism modeled in Section 9.1 (Fig. 150). The deformation in the tangential direction is the same.

The mechanism of compressive deformation in the axial direction is quite different (Fig. 155d). In woods of low density, the cell walls collapse by end cap fracture (Fig. 157b). The stress drops until the next layer of end cap is intercepted; then, the stress increases until the second end cap breaks. The repeated deformation process gives the sharply serrated plateau. In woods of high density, the cell walls collapse by local buckling of the cell walls (Fig. 157c). As the density of the wood increases, both the Young's modulus and strength increase.

A most remarkable property of wood is highly anisotropic fracture toughness. Its highest value is 10 times greater than that of a fibrous composite with the same volume fraction of fibers and matrix. Jeronimidis [290] proposed that the creation of new surface area by
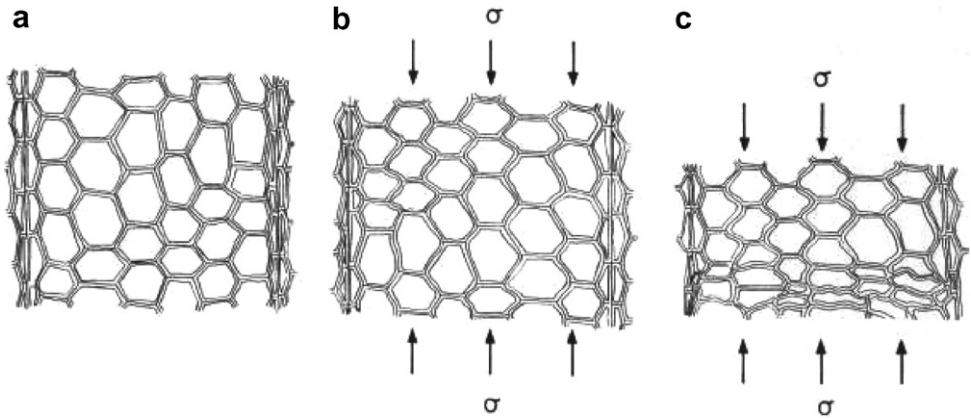
Fig. 156. Schematic drawing of the deformation of wood cells under loading in the radial direction: (a) no applied load; (b) cell-wall bending in the linear-elastic range; (c) non-uniform cell collapse by plastic yielding (from Gibson and Ashby [28, p. 401, Fig. 10.9]).
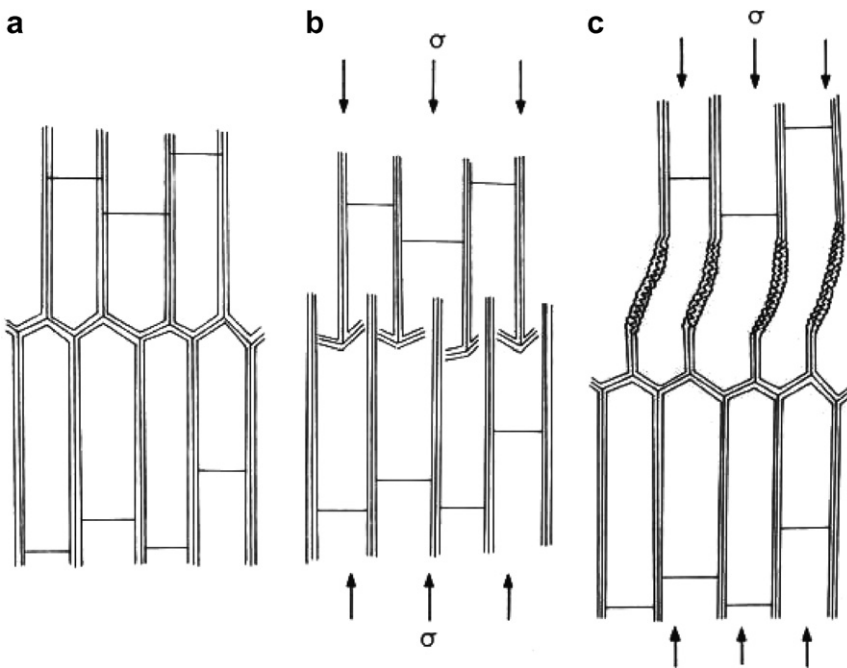

Fig. 157. Schematic drawing of the deformation of wood cells under loading in the axial direction: (a) no applied load; (b) cell collapse by end cap fracture; (c) cell collapse by local buckling of the cell walls (from Gibson and Ashby [28, p. 403, Fig. 10.11]).

fiber pull-out is responsible for fracture toughness. The cracks due to shearing will open and propagate longitudinally, which allows each cell wall to be pulled apart without being broken through. Simulation of the S_2 cell walls [291] has shown that when the helical angle of the fibrils is 15–20°, there is an optimum compromise between energy absorption and
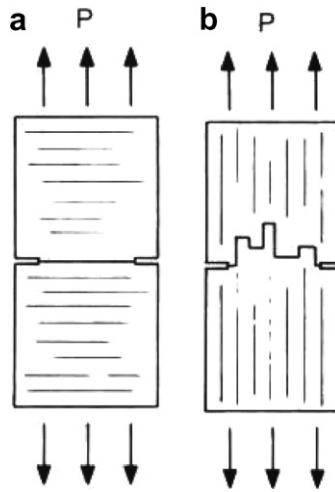
Fig. 158. Crack propagation in wood: (a) initial crack parallel to the grains; (b) initial crack perpendicular to the grains (from Gibson and Ashby [28, p. 424, Fig. 10.23]).

reduction in axial stiffness. Fig. 158 shows the crack propagation in wood along directions (a) parallel and (b) perpendicular to the grain. Whereas it is easy for a crack to propagate parallel, perpendicular propagation to the grain is very difficult. This fracture mode is analogous to that of the nacre when the shell is loaded along the direction of its surface; the individual platelets are pulled out and this provides the high toughness. The sap channels can stop cracks from propagating as shown in Fig. 159. When the crack propagates towards a sap channel, it can either enter it or run around its wall and then stop.

9.3. Beak interior

9.3.1. Toucan and hornbill beaks

Bird beaks usually fall into two categories: short/thick, and long/thin. The toucan is an exception. It has a long beak that is also thick, a necessity for food gathering in tall trees. This is accomplished by an ingenious solution, enabling a low density and high stiffness: a composite structure consisting of an external solid keratin shell and a cellular core. Fig. 160 shows the toucan and hornbill beaks in a schematic fashion. The toucan beak has a density of approximately 0.1 g/cm^3, which enables the bird to fly while maintaining a center of mass at the line of the wings. Indeed, the beak comprises 1/3 the length of the bird, yet only makes up about 1/20 of its mass. The hornbill beak, consisting of 1/4 of the total length, has a density of approximately 0.3 g/cm^3. A distinctive feature of the hornbill is its casque formed from cornified keratin layer. The mesostructure and microstructure of toucan and hornbill beaks reveal a material which is reminiscent of sandwich structures of functionally graded materials, with components made of foam covered by a hard surface layer. Therefore, this biological material serves as a useful source for research and as an inspiration for structural design in engineering.

Figs. 161a and b show optical and scanning electron micrographs of the toucan and hornbill beaks. The structure is similar to cancellous bone and the foams consist of
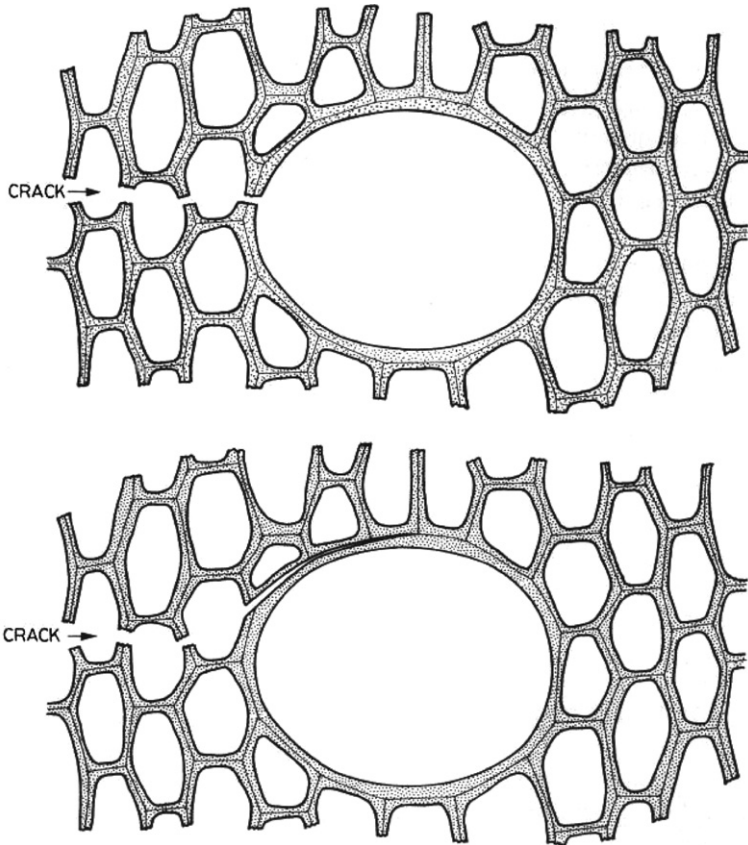
Fig. 159. Crack is arrested by a sap channel: (a) a schematic drawing of a crack breaking into a sap channel, (b) a schematic drawing of a crack splitting the wall of a sap channel (from Gibson and Ashby [28, p. 413, Fig. 10.21]).

asymmetric rod-like structure. Most of the cells in the toucan and hornbill are sealed off by thin membranes. Thus, it can be considered a closed-cell system. The cell sizes vary with location and the closed-cell network is comprised of struts with a connectivity of normally three or four.

Energy disperse X-ray analysis (Fig. 162a and b) shows that toucan and hornbill keratins contain principally carbon and oxygen, which are the main components of the protein. A relatively low content of sulfur in the chemical component of keratin seems to point out to a low content of cystine, a sulfur-containing amino acid. The beak keratin also contains minerals as indicated by the presence of calcium, potassium, sodium, and chlorine. The presence of calcium indicates a degree of mineralization that provides the hardness of the keratin. However, the content of calcium is low and is less than 1% in the keratin of the beak. Fig. 162c and d are in stark contrast with Fig. 162a and b. The trabeculae of the foam contain more minerals than the shell of the beak. Distinctively, the trabeculae contain a great amount of calcium, giving rise to the increased hardness. The EDX results can be compared with chromatographic compositional studies from several bird beaks by Frenkel et al. [292]. It is confirmed here that the keratins of the Toco
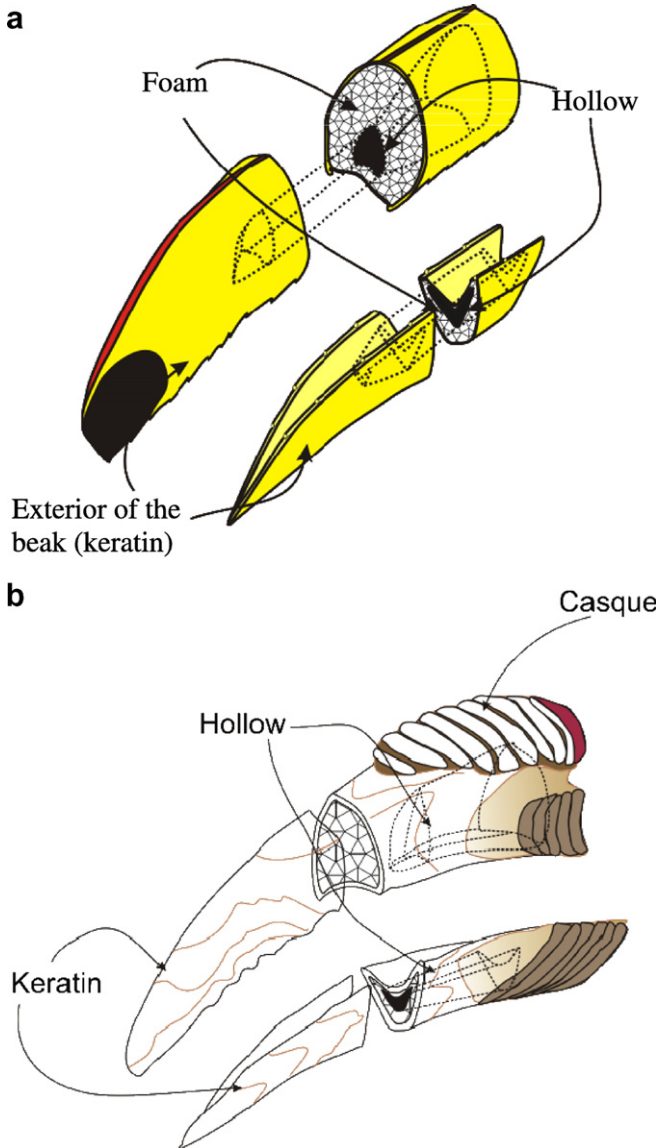
Fig. 160. Schematic of the beaks; (a) toucan beak; (b) hornbill beak.

toucan and hornbill beaks appear to be similar to other bird species with a low sulfur and mineral content. Pautard [80] reported that 0.28% of the pigeon beak is comprised of calcium.

9.3.2. Modeling of interior foam (Gibson–Ashby constitutive equations)

The most significant feature of the cellular solid is the relative density, ρ^*/ρ_S (the density of the cellular material, ρ^*, divided by the density of the solid material, ρ_S). Gibson and
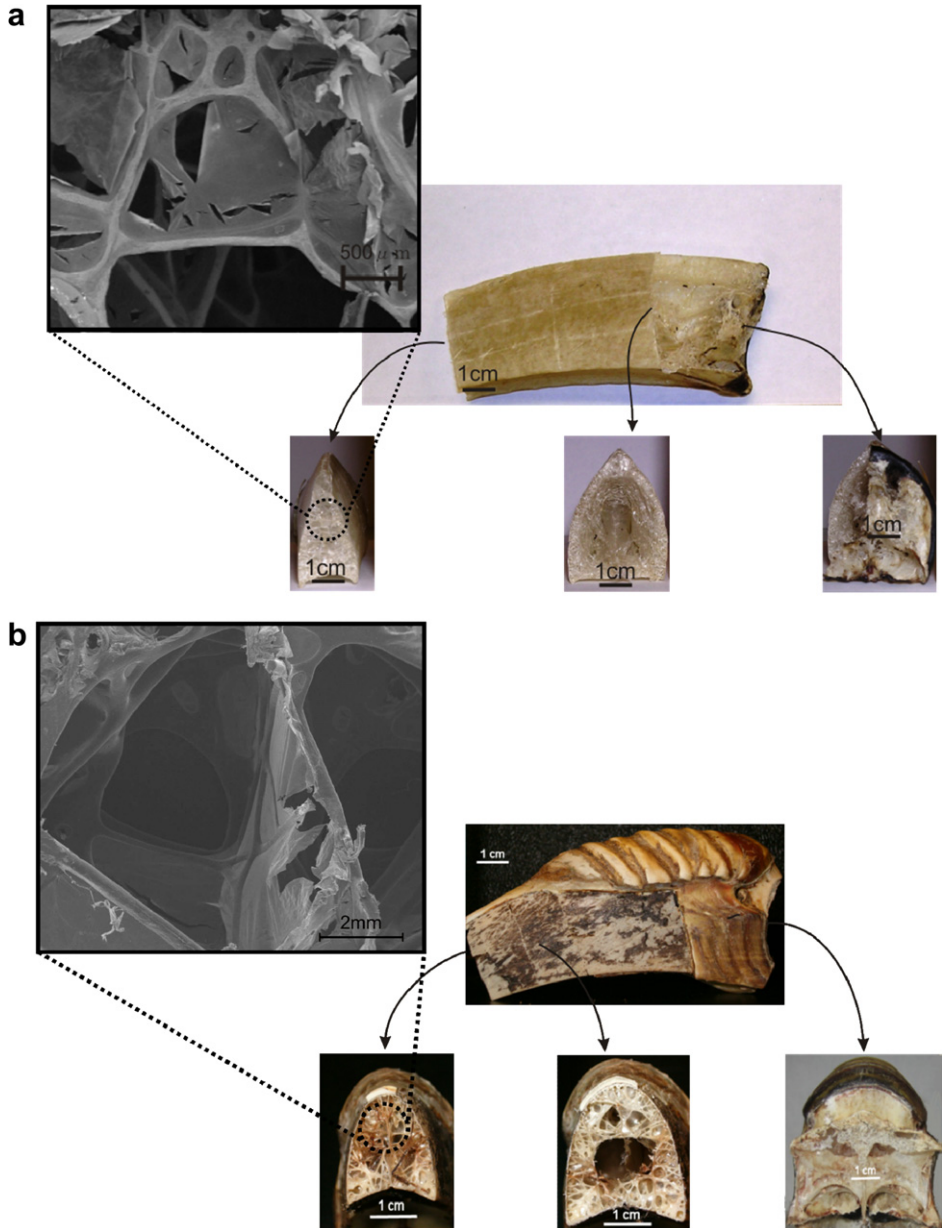
Fig. 161. Images of internal foam structure with three cross-sections and scanning electron micrographs of foams; (a) toucan foam; (b) hornbill foam.

Ashby [28] provide an analytical treatment for the mechanical behavior of a broad range of cellular materials.

The toucan beak foam can be considered as a closed-cell system. Deformation of the closed cells is more complicated than that of open cells. When open-cell foams are

Fig. 162. Energy disperse X-ray results, (a) toucan keratin; (b) hornbill keratin; (c) toucan trabecula; (d) hornbill trabecula.

deformed, cell wall bending occurs. Deformation of closed-cell foam involves not only rotation of cell walls, but also stretching of the membranes and internal gas pressure.
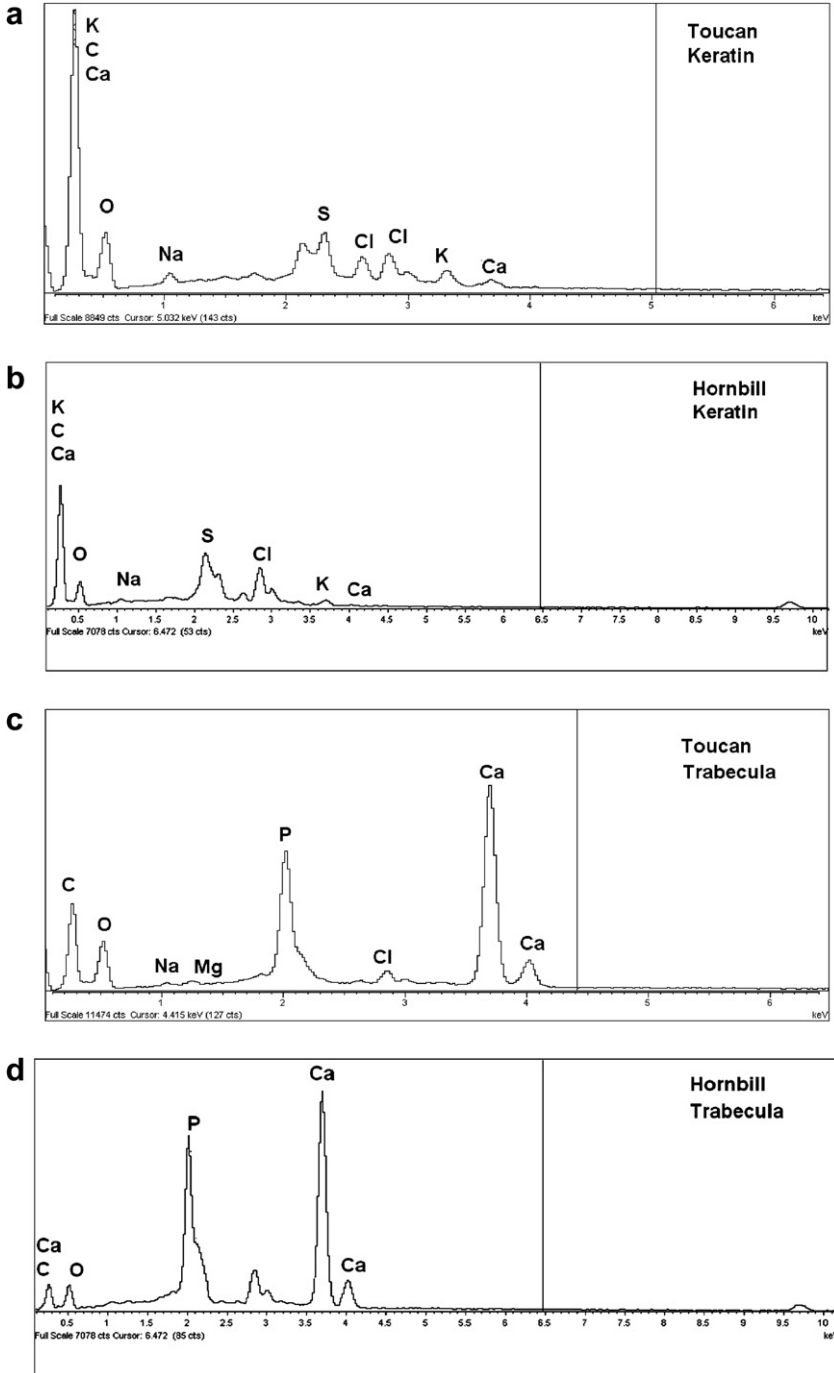
The simplest closed-cell cubic model was introduced to describe the deformation of the foam. Fig. 163 shows (a) undeformed and (b) deformed cubic closed cells envisaged by Gibson and Ashby [28]. The linear elastic region is limited to small strain. The foams made from material possessing a plastic yield stress are subjected to plastic collapse when the load is beyond the linear elastic regime. When plastic collapse occurs, there is a long horizontal plateau in the stress–strain curve. Eq. (61) represents the response of a closed-cell foam schematically shown in Fig. 163:

$$\frac{\sigma_{pl}^*}{\sigma_{ys}} = C_5 \left(\phi \frac{\rho^*}{\rho_S} \right)^{3/2} + (1 - \phi) \frac{\rho^*}{\rho_S} + \frac{p_0 - p_{at}}{\sigma_{ys}} \tag{61}$$

where σ_{pl}^* is the plastic collapse stress of foam, σ_{ys} is the yield stress of the solid portion, C_5 is a parameter, ϕ is the ratio of volume of face to volume of edge, p_0 is the initial fluid pressure, and p_{at} is the atmospheric pressure.

For the open-cell geometry, the parameter ϕ in Eq. (61) is equal to 1. Additionally, the pressure is unchanged, i.e., $p_0 - p_{at} = 0$. Thus, Eq. (61) reduces to

$$\frac{\sigma_{pl}^*}{\sigma_{ys}} = C_5 \left(\frac{\rho^*}{\rho_S} \right)^{3/2} \tag{62}$$

This is the open-cell equation from Gibson and Ashby [28] (Eq. 60, Section 9.1). The parameter C_5 has an experimentally obtained value of 0.3 for plastic collapse and 0.2 for brittle crushing (where $\sigma_{pl}^*/\sigma_{ys}$ in Eqs. (61) and (62) is replaced by the normalized crushing stress $\sigma_{cr}^*/\sigma_{fs}$).

The cell shape of toucan and hornbill foams are highly complex and consist of the combination of triangle, quadrilateral, and even higher number of edges of polygons. There are circular cells at the nodes, which are shared by several cells. To avoid the complexity
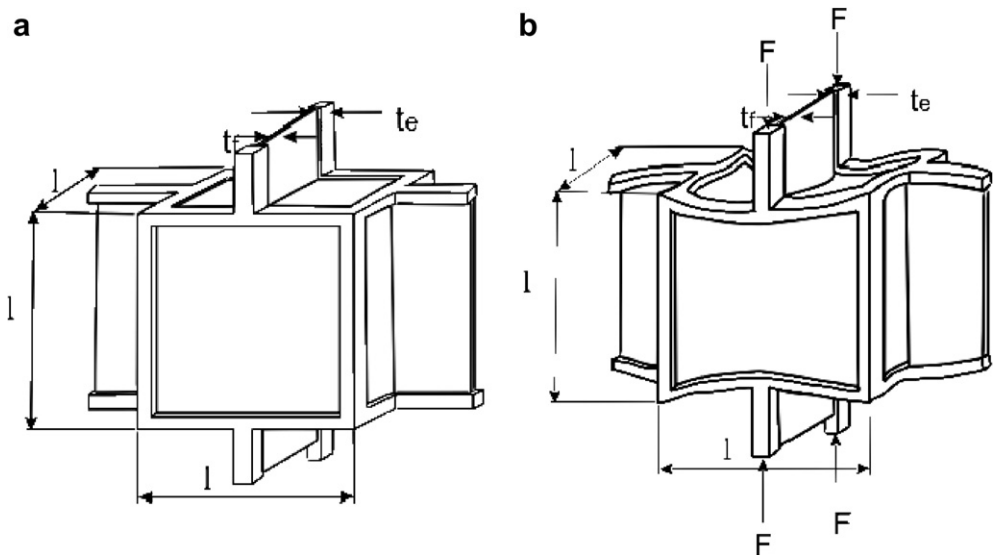

Fig. 163. (a) Gibson–Ashby model for closed-cell foam; (b) deformation of closed-cell foam.

of characterizing cell geometry of toucan and hornbill foams, we measured the relative density. The mean value of the density of the toucan foam and that of solids were measured and found to be: $\rho^* = 0.05$ and $\rho = 0.56$. Thus, the relative density of the toucan foam is approximately 0.09 and that of the hornbill foam is found to be 0.1. This value is obtained from the foam density, $\rho^* = 0.139$, and the density of the solid, $\rho = 1.4$. The yield stresses of the toucan and hornbill trabeculae, σ_{ys}, are estimated from microindentation values ($H \approx 3\sigma_y$), which seem to be more accurate than the nanoindentation values due to the size effect. This gives values of $\sigma_{ys} = 91$ MPa for toucan and $\sigma_{ys} = 128$ MPa for hornbill.

Fig. 164a shows the predictions from Eqs. (61) and (62) as well as experimental results for a number of materials [293–298]. These equations bracket the experimental results quite well. A more detailed plot of the compressive strength for the toucan foam as a function of relative density is shown in Fig. 164b. Although the relative density of toucan and hornbill foams show a small difference, the relative yield strength of the hornbill trabeculae is more than fourfold higher due to the high degree of mineralization. It should be noted that the membranes are not expected to contribute significantly to the mechanical response
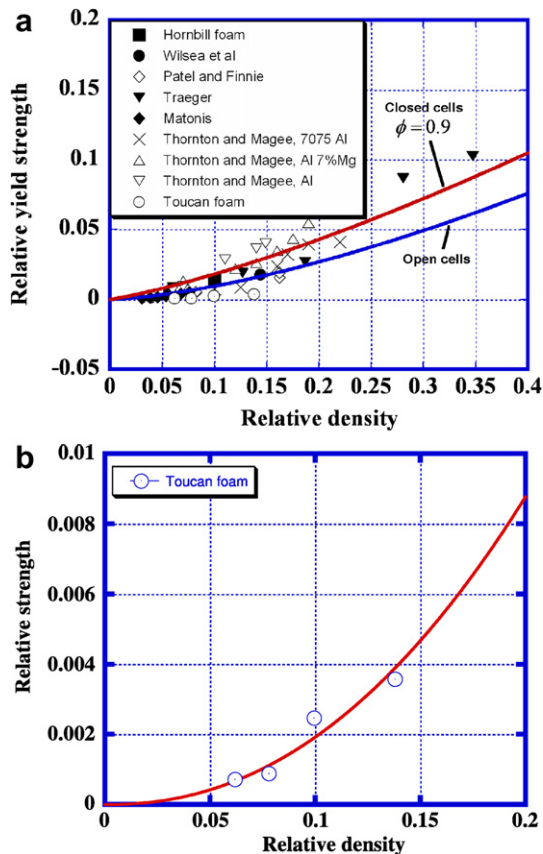

Fig. 164. (a) Experimental results (hollow circles) and Gibson–Ashby prediction for open-cell and closed cell foams (continuous lines); (b) detailed plot.
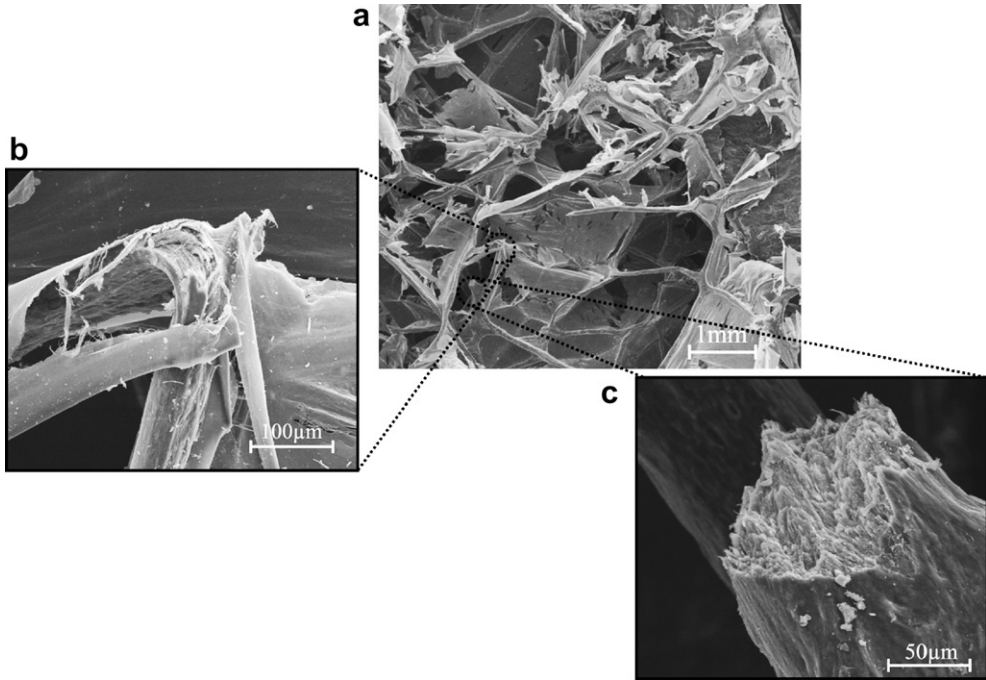
Fig. 165. Fracture morphology of closed-cell foam showing profuse trabecula bending; (a) overall view; (b) "green twig" fracture; (c) total fracture of trabecula.

of the foam since many of them contain tears due to desiccation. However, one would not expect this to be the case for the live animal. Gibson and Ashby [28] give values of $C_5 = 0.3$ and $C_5 = 0.2$ for plastic buckling and brittle crushing, respectively. The response of the toucan foam is intermediate between the two.

Fig. 165a shows the fracture pattern in the foam. It is composed of a mixture of plastic deformation, partial, and total fracture of the trabeculae. The trabeculae have a fibrous structure similar to wood and can fracture partially when they are subjected to bending (Fig. 165b). In other locations, the trabeculae undergo total fracture. Fig. 165c shows an example. The "green twig" appearance of the trabecula is evident in Fig. 165b. Hence, the cellular material does not crumble when compressed to its maximum strain. Rather, it collapses in a semi-plastic manner.

9.4. Feather

Feathers are very light and sometimes stiff epidermal structures that distinguish the class of Aves. The basic structure of bird feather is composed of the main shaft, or 'rachis' and side branches called barbs or 'rami'. Fig. 166a shows a schematic of feather matched with scanning electron micrographs of feather belonging to Blue-and-Gold Macaw (*Ara ararauna*). Closed-cell foam can be observed within both the rachis and barb structures [299]. The tertiary structures extending from the barb are called barbules or 'radii'. They are tied together by 'hooklets.' Barbs, barbules, and hooklets extending from the rachis comprise the vane or vexillum of feather. The rachis consists of a hollow cylinder called
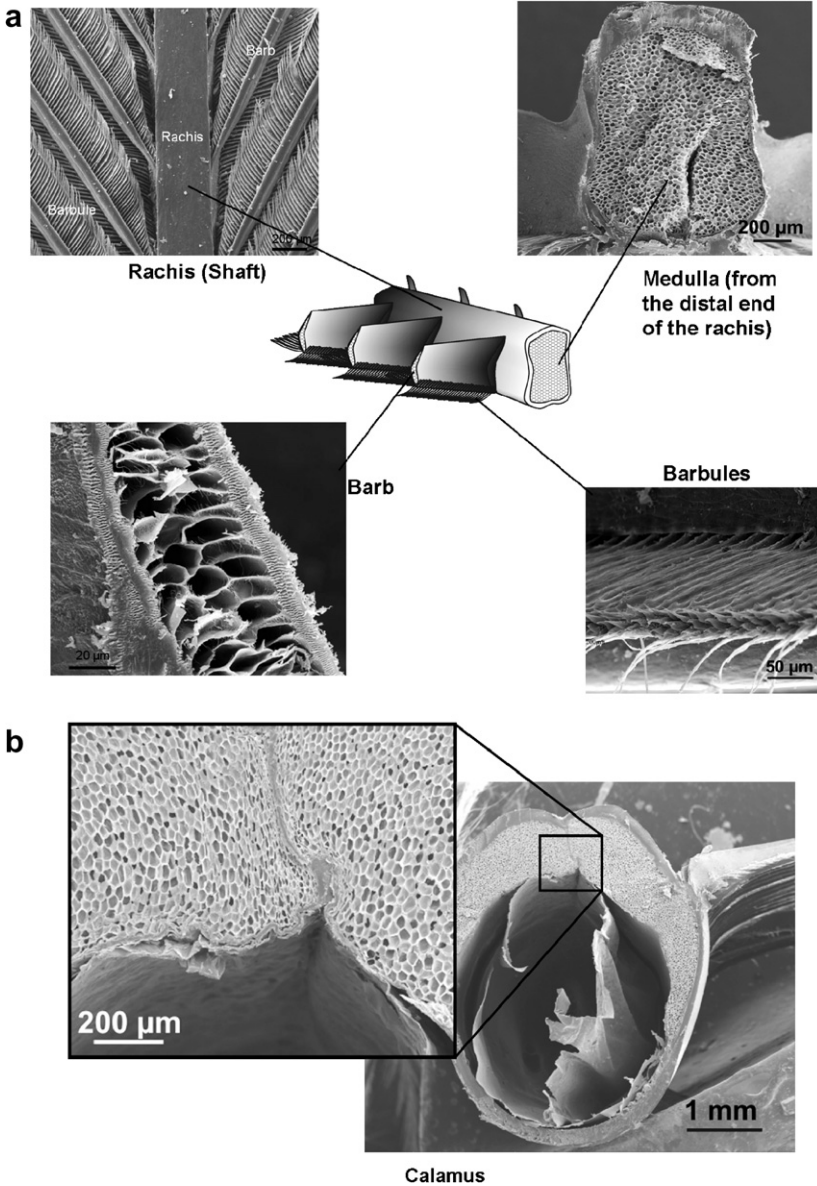
Fig. 166. (a) Schematics of feather structure with scanning electron micrographs of macaw feather. (b) Scanning electron micrographs of a hollow section of macaw rachis (courtesy of S.G. Bodde [299]).

'cortex' and supporting foam core called 'medulla'. The rachis is completely filled with medullary foam at the distal end and has a hollow at the root section or 'calamus,' shown in Fig. 166b [299]. X-ray diffraction studies report that the crystallinity and the diffraction pattern of feather keratin are very similar to that of other avian keratins such as claw and beak [79]. However, there are differences in composition between feather and other avian

keratins [300,301]. Brush [300] measured the molecular weight of avian keratins and found 10,500 g/mol for feather, which is lower than claw and beak keratins which range from 13,000 g/mol to 14,500 g/mol.

The bending behavior of foam-reinforced feather rachis is of great importance. The feather must have stiffness and flexibility in order to withstand some degree of bending caused by flight activity. The bending behavior of the rachis (feather shaft) has been studied by Purslow and Vincent [302]. They demonstrated that the bending behavior of the rachis depends on the size and geometry of the cortex. The calamus of the feather has a circular or square cross-section, which becomes elliptical toward the distal end. Bonser and Purslow found an average Young's modulus of 2.5 GPa in tension [303]. Young's modulus of volant bird feather varies with the orientation of the rachis, while that of flightless bird is almost same at any position along the length of rachis [304]. Corning et al. investigated the uniaxial oscillatory strain pattern of feather during the flight and the peak compressive strain was found to be just over twice the peak tensile strain [305].

Mechanical properties of feather keratin demonstrate humidity sensitivity. Stiffness of feather rachis decreases with an increased moisture content, which is similar to behavior of other keratinous tissue [306]. Fig. 167 shows stress–strain curves of feather rachis and claw keratin for three different humidity levels. The feather rachis is stiffer than claw keratin due to molecular orientation differences. The compressive behavior of the medullary foam was studied and the Young's modulus was found to increase with relative density [307]. Fig. 168 shows Young's modulus revised from Bonser's results [307] plotted as a function of relative density.

The relationship between melanin and mechanical properties of the avian keratin has also drawn attention after Bonser and Witter described increased hardness of Starling (*Sturnis vulgaris*) bill associated with seasonal melanization [308]. Butler and Johnson have studied melanized and non-melanized barbs of feather [309]. They considered not only color but also the location along the rachis of the feather. Fig. 169 shows the breaking
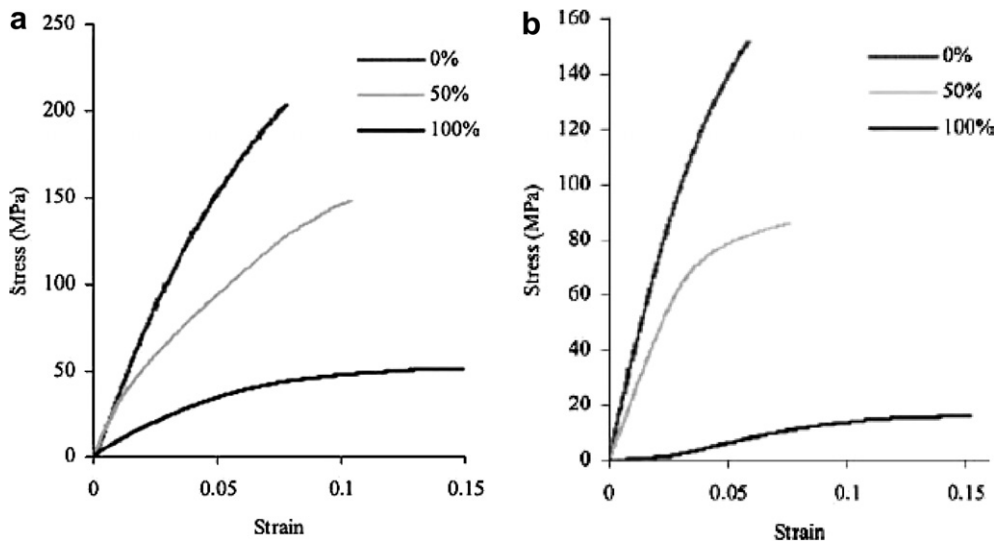

Fig. 167. (a) Stress–strain curve of feather at three different humidity conditions; (b) stress–strain curves of claw keratin at three different humidity conditions (from Taylor et al. [306, p. 935, Figs. 1 and 2]).
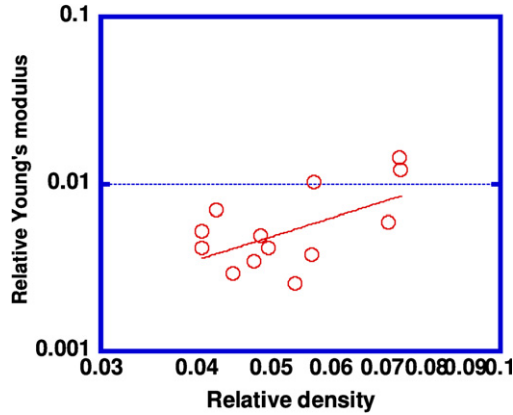
Fig. 168. Relative Young's modulus vs. relative density of medulla (reproduced from Bonser [307, p. 936, Fig. 2]).

stress as a function of positional distance of the barb along the length of the rachis. Black dots represent melanic and white dots represent non-melanic regions. In this case, the individual barb morphology, especially cross-sectional area (which however may not be absolutely independent of melanin-induced effects). Variation in barb strength was observed along the rachis from the proximal end, enduring higher stresses during flight, to the distal end. Therefore, mechanical effects of melanin were found to insignificant relative to geometric variation in feather barb and position along the rachis.

10. Functional biological materials

10.1. Gecko feet and other biological attachment devices

The gecko feet present a fascinating problem of adhesion [310]. This attachment system has first recognized by Ruibal and Ernst [311]. Indeed, there are several biological systems
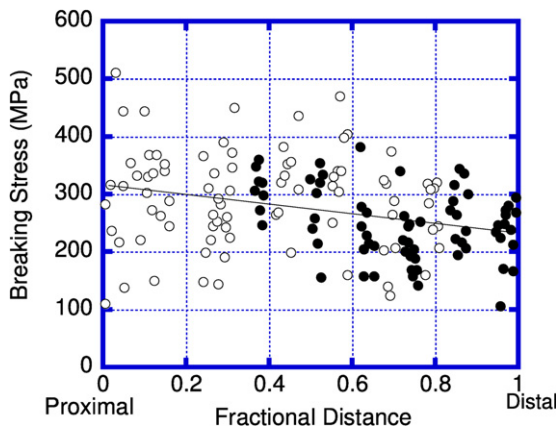

Fig. 169. Breaking stress as a function of fractional distance (reproduced from Butler and Johnson [309, p. 284, Fig. 4]).
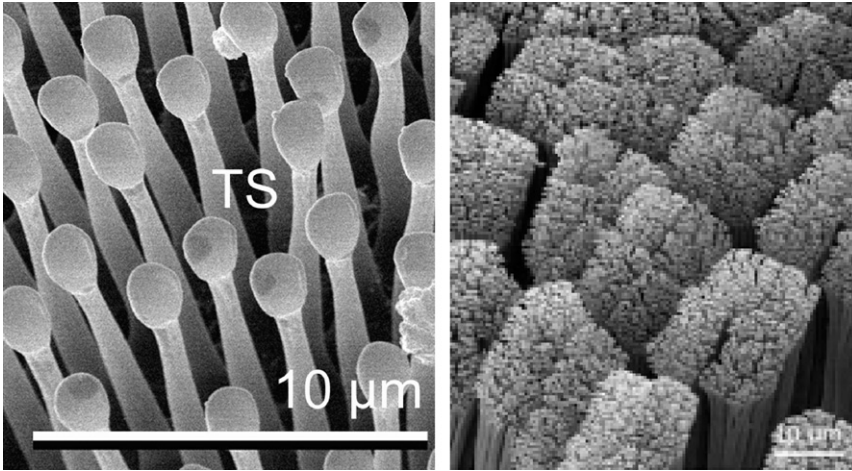
Fig. 170. Setae and distal spatulae fly *Callifora vicina*. Van der Waals forces at spatula-surface interface generate attachment forces that in the gecko can be as high as 20 N (from E. Arzt, MPI, Stuttgart, Germany [5]).

in which the attachment to surfaces uses similar principles: flies, beetles, and spiders. Preliminary results show that the tree frog might be included in this category [315]. Again, novel experimental techniques coupled with analysis are revealing these mechanisms. The fly and gecko feet are made of a myriad of thin rods, called setae, terminated by spatulae, with submicron diameters. These are shown for the fly *Calliphora vicina* in Fig. 170. Fig. 171a shows a cross-section of the gecko foot with setae marked (st). Each seta has, at its tip, a number of spatulae, marked (sp) in Fig. 171b. Arzt et al. [5,312] and Spolenak et al. [313] calculated the stress required to pull off a contact. This calculation is based on the van der Waals forces combined with Hertzian contact stresses. For simplicity, spherical spatulas are assumed, as shown in Fig. 172.

The Hertzian stress is given by

$$d^3 = \frac{12RF}{E^*} \tag{63}$$

where R is the radius of the spatula, d is the contact area, F is the adhesion force, and E^* is a biaxial elastic modulus. The attractive interfacial adhesion energy per unit area, γ, was added to the calculation (Johnson, Kendall, and Roberts) leading to the pull-off force F

$$F = \frac{3}{2}\pi R\gamma \tag{64}$$

where γ is the adhesion energy per area. The stress required to pull off a spatula is the force F divided by the apparent area (see Fig. 172) A_{app}

$$\sigma_{app} = \frac{3}{2}\frac{f\gamma}{R} \tag{65}$$

where f is the fraction of the area covered by setae

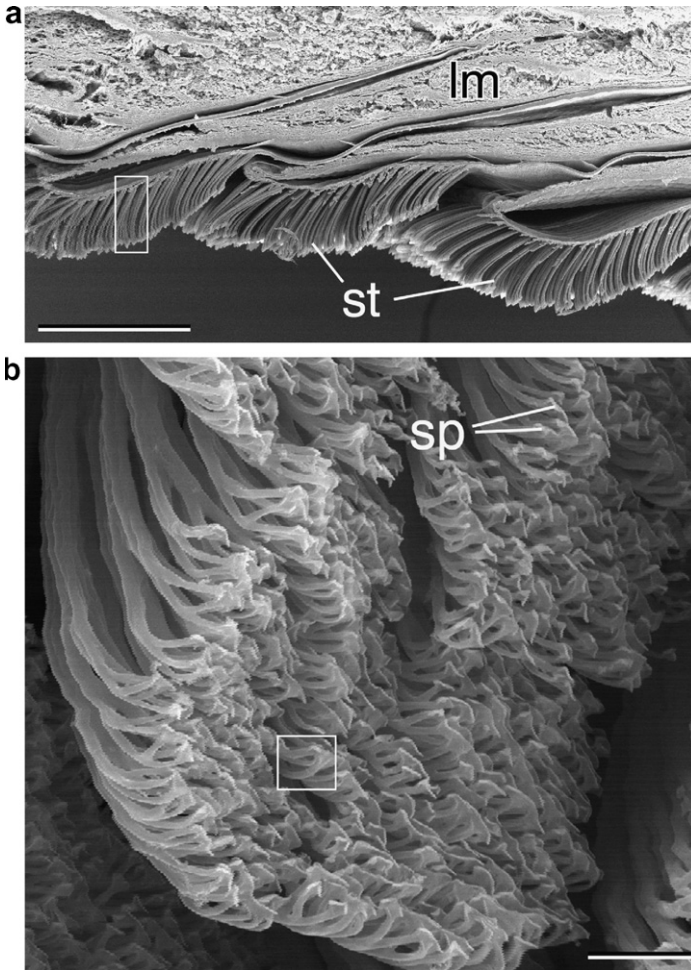$$f = \frac{\pi R^2}{A_{app}} \tag{66}$$

Fig. 171. SEM micrographs showing the detail of (a) setae; and (b) spatulae (courtesy from E. Artz and G. Huber).

It can be seen that the pull-off stress is inversely proportional to R. Thus, the larger the mass of the biological system, the smaller R has to be. This is confirmed by the experimental plot of Fig. 173. The number density of attachments, proportional to R^{-2}, increases with the mass. For geckos, that have a mass of approximately 100 g, it is equal to 1000 setae per 100 μm^2, or 10 setae per μm^2. This is in full agreement with Fig. 170, which shows spatulae having an approximate diameter of 0.2 μm.

Spolinek et al. [313] developed a design map that incorporates both the tensile strength of setae and the ideal contact strength. This plot is shown in Fig. 174. It represents the fiber radius in the ordinate plotted against the Young's modulus in the abscissa. Two major lines define an inverted cone in which the system should be. The line with negative slope represents the failure of setae by tension and is obtained from the application of the theoretical strength ($\sigma_{th} = E/10$) to Eq. (65). This results in
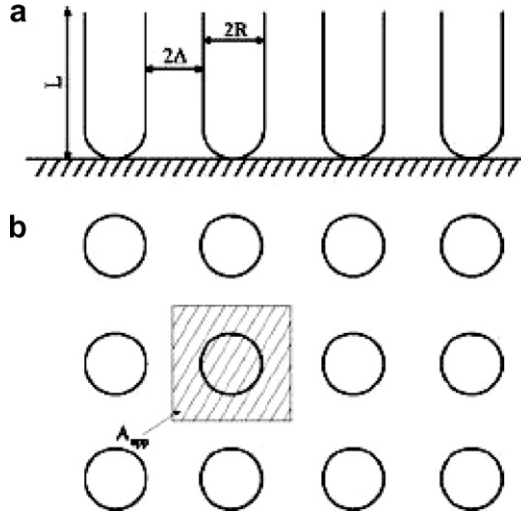
Fig. 172. Idealized arrangement of attachment system with spherical tip shape (radius R and spacing 2Λ) (from Spolenak et al. [313, Fig. 2]).
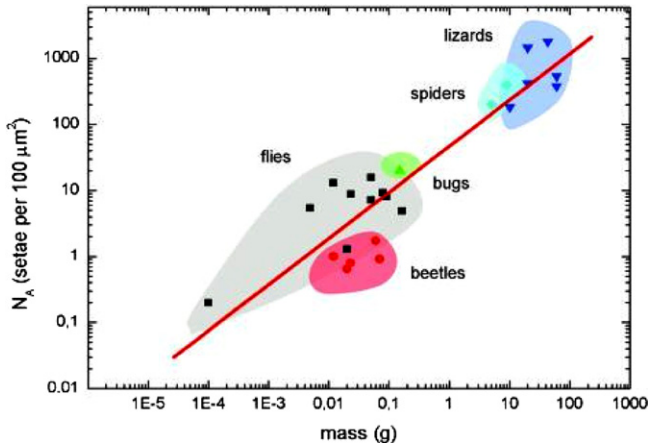
Fig. 173. Idealized arrangement of attachment system with spherical tip shape (radius R and spacing 2Λ) (from Artz et al. [312]).

$$R \geqslant \frac{3\gamma}{2\sigma_{\text{th}}} = \frac{15\gamma}{E} \tag{67}$$

The second line, on the right side, represents the ideal contact strength and is given by

$$R \geqslant kE^2 \tag{68}$$

k is a parameter incorporating several dimensions. Indeed, the biological systems fall within the V region of the plot, showing that the calculations bracket the requirements well.
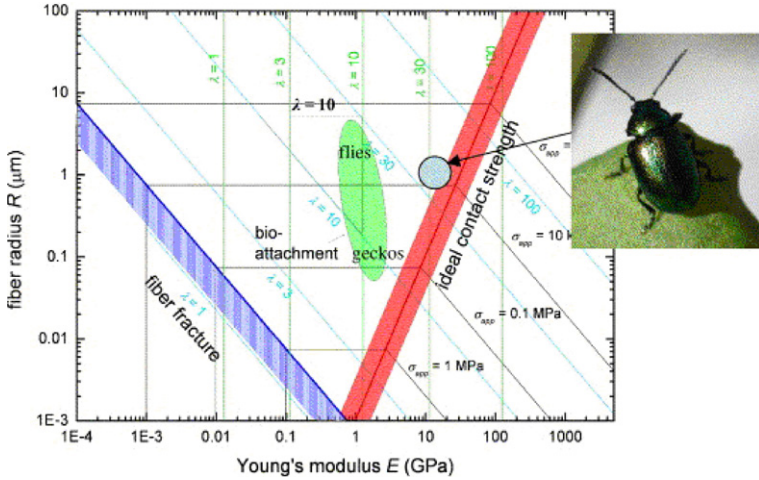
Fig. 174. Partial adhesion map for a spherical tip shape; thin lines are contours of equal apparent contact strength; oval section represents the regime of bioattachments (from Spolenak et al. [313, Fig. 10]).

The biomimicking of this attachment principle is being implemented in synthetic systems. Whereas the paws of a gecko can generate adhesion forces of tens of N, much greater forces will be hopefully achieved in synthetic systems, and Spiderman is in the realm of reality.

However, van der Waals forces are not complete story, and capillarity plays a role. The adhesion force of exerted by a single gecko spatula was measured by Huber et al. [314]

Fig. 175. Force of single seta pulled parallel to surface (preload of 15 μN) (from Autumn et al. [310]).

after modifying the substrates. The seta of a gecko was glued to an AFM cantilever. Although work by Autumn et al. [310] indicated that the pull-off force did not increase with humidity, this is clearly evident in Fig. 175. The results are expressed analytically as

$$F = F_{drag}\left(1 + 1.22Hg\sqrt{\frac{A_W}{A_S}}\right) \tag{69}$$

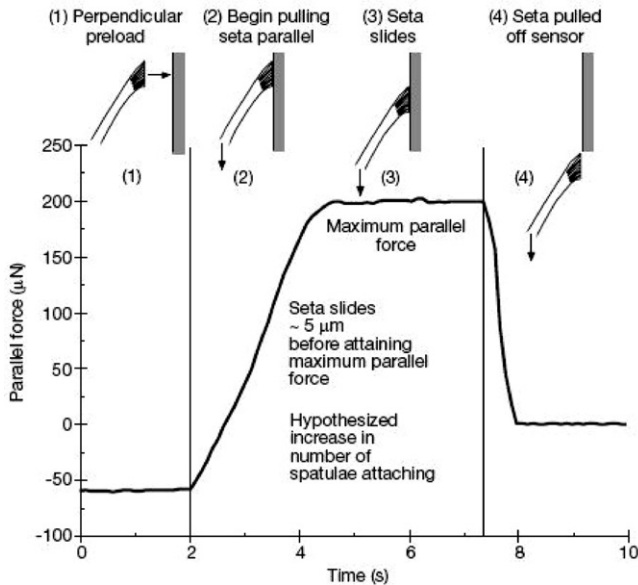where H is the humidity, g is a geometrical parameter ($\sim$1.2), A_W (3.7×10^{-20} J) and A_S (6.5×10^{-20} J) are the Hamaker constants for water and the substrate, respectively.

10.2. Structural colors

Structural color is a phenomenon of wave properties of light. Biological systems are able to produce structural color using highly precise and sophisticated nanometer-scale architectures [316]. The coloration of birds has attracted many scientists and is related to sexual signaling as is obvious in the case of nuptial plumage change, camouflage, and aggression. The mechanisms of coloration to be discussed are chemical or pigmentary and physical or structural. And among structural colors, scattering by photonic crystal arrays and interference in thin films will be addressed.

Pigment is greatly responsible for coloration of birds [317]. Melanin and its types are pigments responsible for black, grey or brown color. Melanin is secreted by melanocytes embedded in the epidermis. Melanin also serves to increase hardness of bill keratin, as Bonser and Witter presented in the case of the seasonal change of bill color in the European Starling (*Sturnis vulgaris*) [308]. Bonser and Witter, among other scenarios, proposed that
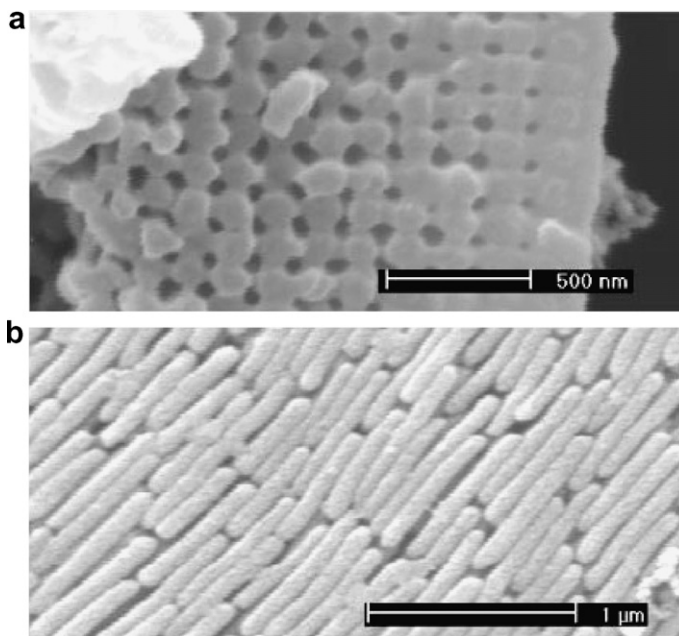

Fig. 176. (a) SEM of burbles of peacock; (b) SEM of melanin rods embedded in keratin layer (from Zi et al. [318, Fig. 1]).

the harder melanic bill keratin may resist increased abrasion and wear experienced during foraging in winter months. Carotenoids are diffuse organic pigments of which there are two classes: xanthophylls, or oxygen-containing carotenoids, responsible for yellow coloration and carotenes, or oxygen-free, producing red coloration. In avian coloration, however, there is no blue pigment. Blue and generally green coloration is possible by structural color or the interaction between carotenoid pigments and structurally produced color.

10.2.1. Photonic crystal arrays

Photonic structures are widely distributed in nature, such as in feathers, scales, or insect cuticles. In birds, blue color is produced when light is scattered coherently from an array of melanin granules suspended in a matrix of keratin and air vacuoles in the feather parts, for example. Iridescence such as that observable in the peacock's (*Pavo muticus*) feather is produced by interference. Fig. 176a shows scanning electron micrographs of peacock barbules [318]. The barbules are composed of medullary core bound by a melanin-containing cortex and encased by a thin keratinous cuticle. In this case, a periodic array of melanin rods is observable in the cortex, shown in Fig. 176b. By varying the lattice constants in simulation of the 2-D photonic-crystal-like structure, Zi et al. were able to vary the wavelength of the scattered light.

Structural coloration is not limited to the class of Aves; it is observed in fish and in insects such as butterflies (lepidoptera), discussed in Section 10.2, or beetles (celeoptera). One of the most striking examples of color-producing structures is that present in the *Lepidoptera* (butterflies and moths) species, including the tropical *Morpho* family [319–322]. The *Morpho* butterflies are among the largest in the world with a wingspread of 7.5–20 cm. The males of *Morpho menelaus* have brilliant blue coloration on the dorsal side wings and camouflaged brown color on the ventral side of the wings. Such designs help them to elude potential predators, birds, for example. When they fly, the top surfaces of wings continuously change from metallic blue to dull brown as the angle of the light striking the wing changes. They seem to disappear and then reappear a distance away during flight. Coupled with the unpredictable pattern of flight, the ability to change color makes them difficult for predators to pursue. When the *Morpho* butterflies land, they close their wings completely, showing the camouflaged brown underside of wings that matches the surrounding and protects them from being found.

The blue color of *Morpho* butterfly comes from the well-defined structure of the wings. This is another example of hierarchical structure from nanometer, micrometer, to millimeter found in nature (Fig. 177 [316]). The wings of butterflies and moths consist of a translucent membrane covered by a layer of scales. Butterfly scales are comprised of chitin,
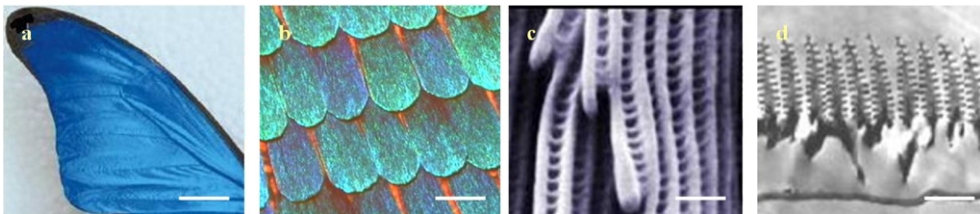

Fig. 177. Hierarchical structure of the butterfly, *Morpho rhetenor* wing: (a) wing; (b) scales; (c) ridges (top view); (d) ridges (cross-section). Scale bars (a) 1 cm; (b) 50 μm; (c) 1.8 μm; (d) 1.8 μm (from Vukusic and Sambles [316]).
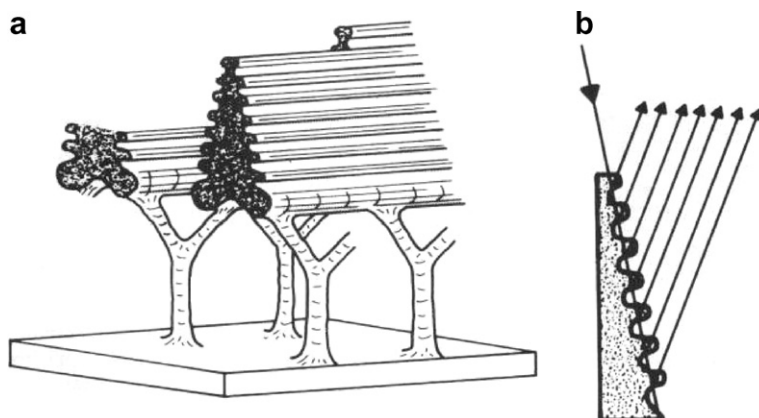
Fig. 178. Schematic drawing showing (a) the structure of the vanes on the surface of scales of *M. rhetenor* and (b) constructive interference in the ridges (from Nassau [319]).

which is a white colored polysaccharide widely found in arthropod cuticles [321] (see Section 5.4). Each scale is a flattened outgrowth of a single cell that fits into a socket on the wing and is about 100 μm long and 50 μm wide. The scales overlap like roof tiles and completely cover the membrane, appearing as dust to the naked eye. Each scale is covered by longitudinal ridges joined at intervals by cross-ribs, as shown in Fig. 178a [319]. Ridges and cross-ribs frame a series of windows that open into the interior of the scale, where the pigment granules are located. For more radiant color observed in other species, the ridges are much higher and have very precise nano-structure. The cross-sectional view of ridges reveals the discretely configured multiple slits, which are spaced 200 nm apart. Interference occurs when light waves striking the wing interact with light waves reflected by the wing. Though sunlight contains a full range of light wavelengths, only high-energy waves survive scattering events. The periodicity of the nano-structure defines a reflected wavelength of blue light, ranging from 400 nm to 480 nm [319,320]. Fig. 178b [319] shows the detailed grating responsible for interference. There is frequently a background layer of a dark pigment such as melanin which absorbs low-energy waves, perhaps serving to intensify the reflected blue color.

10.2.2. Thin film interference

As another example of structural coloration, the feather of Hadeda Ibis, *Bostrychia hagedash*, has been studied [323]. At first glance, the plumage of this species appears dull brown in color. However, the color appears to "change" from blue to green to reddish. Interestingly, the Hadeda Ibis plumage also reflects ultraviolet and infrared while it is known that only one animal, the Common Goldfish can detect both. Fig. 179a shows a scanning electron micrograph of iridescent feather of Hadeda Ibis and Fig. 179b is a transmission electron micrograph of cross-section of a single barbule. The barbules are rotated by 90° so that the flattened surface reflects light normal to the contour of the Hadeda Ibis's body. The thickness of single barbule is 0.8 μm. Hollow melanosomes are visible in barbules by TEM. Unlike in other bird species, in Hadeda Ibis melanosomes only play a minor role, only to define the thick keratinous cortex in the production of structural color. Interference at the boundaries of the unusually thick keratinous cortex is responsible for the iridescence of the feather [323].
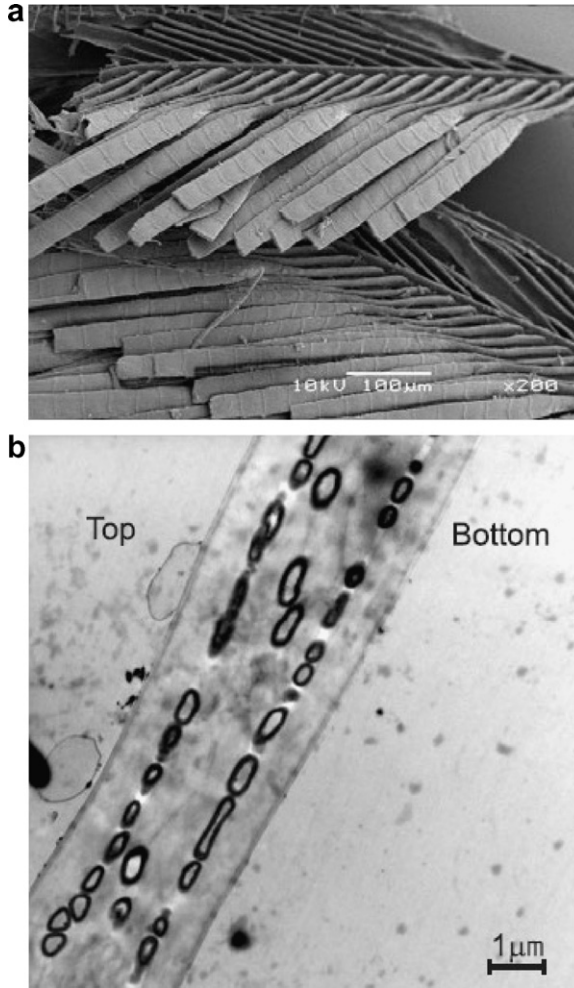
Fig. 179. (a) Scanning electron micrograph of Hadeda Ibis feather; (b) transmission electron micrograph of cross-section of barbules (from Brink and van der Berg [323, p. 809, Fig. 1]).

Structural colors in biological systems are due to thin film interference involving well-defined multilayer structure or else coherent scattering from photonic arrays. The layers may be composed of chitin as in wings of butterfly or keratin as in avian plumage coloration as discussed. Other examples of structural coloration in nature include calcium carbonate films in mother of pearl, chitin films in iridescent cuticle of beetles, and melanosome platelets in hummingbird [320].

10.3. Chameleon

We have seen earlier that α-keratin is mammalian, whereas β-keratin is avian; the epidermis of the reptilian is unique, consisting of both α-and β-keratin. Metachrosis (changing color) in lizard is the most famous and complex feature in reptile family [324]. The

Fig. 180. Cross-Section of epidermis of American Chameleon. O: oberhautchen layer, B: beta layer, M: mesos layer, A: alpha layer (from Alexander and Parakkal [325, Fig. 1]).

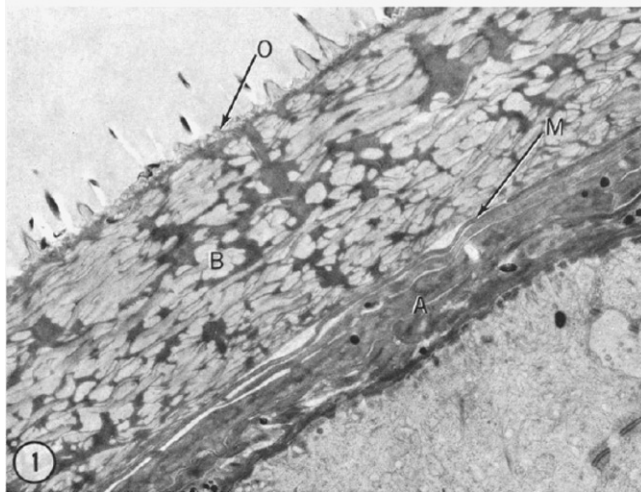structure of the chameleon skin consists of several layers. The thin outermost layer of *oberhautchen* consists of cornified cells with spinules throughout its surface. This covers a thicker β layer which decreases in thickness along its hinges [325,326]. Fig. 180 shows the cross-section of epidermis of the American chameleon (*Anolis carlinensis*) and the meso-layer between the α-layer and β-layer [325]. Below the α-layer, the structure is similar to a mammalian epidermis. The chameleon has pigment-containing cells called chromatophores, embedded in the dermal layers. The chromatophores allow the chameleon to change its skin color. Two or three kinds of pigments have been detected in the body of the American chameleon [328] while the African chameleon has five pigments. Fig. 181 shows vertically sectioned back scale of American chameleon [327]. The hexagonal scale of epidermis varies with position from 250 μm to 400 μm. There are two types of chromatophores containing yellow pigment (xanthophore) and red pigments (erythrophore). The xanthophore (cells containing yellow pigment) layer lies under the stratum germinativum layer, providing 10 μm of the dermal layer [327]. There is a 10–20 μm in thickness of iridophore layer below the xanthophore layer. This contains inorganic crystalline pellets that reflect blue or white light. Erythrophores (cells containing red pigment) have been found in the basal zone of the iridophore layer of American chameleon [327]. Fig. 182 shows iridophore platelets in the iridophore layers. The crystalline structure of iridophore platelets yields blue-green light [329]. The melanophores, which contain melanin, are the largest of the chromatophores. These produce black or brown colors. This layer is followed by the iridophore layer which reaches the xanthophore layer [327]. The collagenous basement lamella lies at the bottom of dermal layer. The skin color is controlled by the expansion or contraction of the chromatophores producing a variety of colors from the different combination of chromatophore. The light modulation of color is provided by the melanophores. Although the chameleon does contain any green pigmentation, the yellow pigment and the reflecting blue light at iridophore layer produce the green color of the skin.
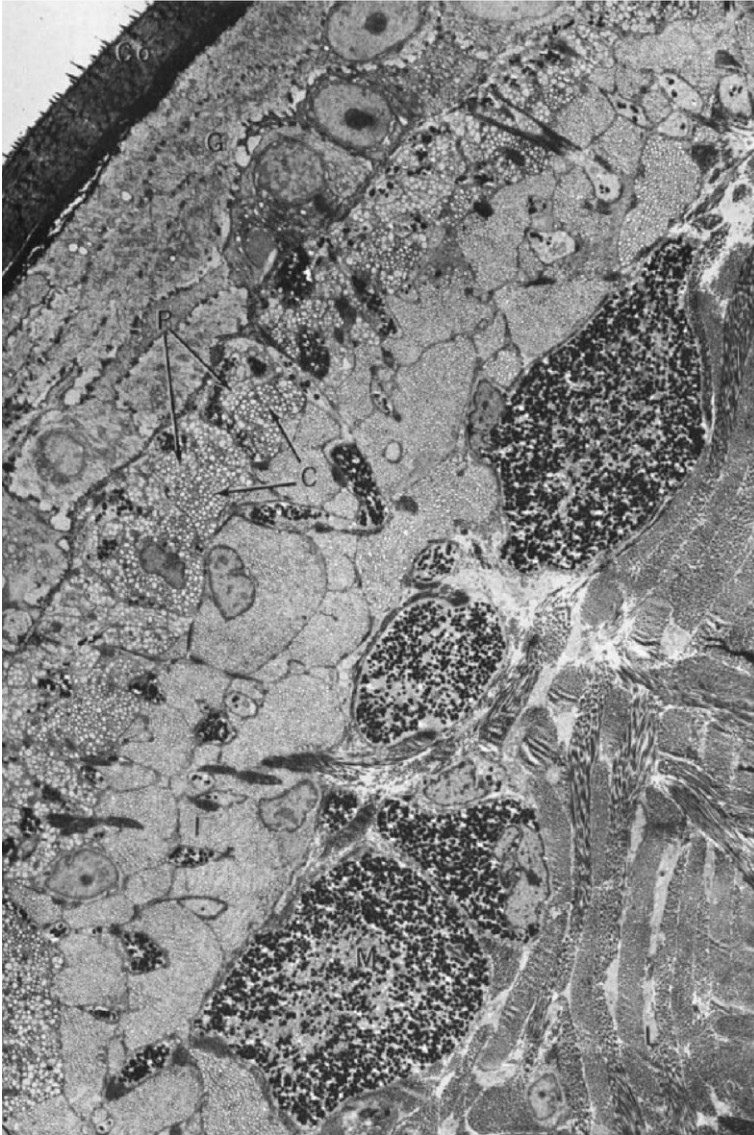
Fig. 181. Cross-section of integument of American chameleon. Co: stratum corneum, G: stratum germinativum, P: xanthophore layer, C: carotenoid containing cell, I: iridophore, M: melanophore layer, L: collagenous basement lamella (from Alexander and Fahrenbach [327, p. 47, Fig. 2]).

11. Bioinspired materials

Natural selection provides a tool with which nature has processed, improved, and refined biologically-based elements over millions of years. As scientists we can learn from these evolutionary refinements and use them with the intention of creating novel improvements in technology. Materials Science is beginning to explore the resources presented by

Fig. 182. Light micrograph of iridophore crystals (marked I) from American chameleon skin (from Rohrlich and Rubin [329, p. 632, Fig. 1]).

nature and use them to create novel advances in technology [330–333]. This interdisciplinary synergy between is the field of *Biomimetics* [4,6].

The production of inorganic materials in nature generally occurs at ambient temperature and pressure under isothermal and isobaric conditions. Yet the simple organisms through which t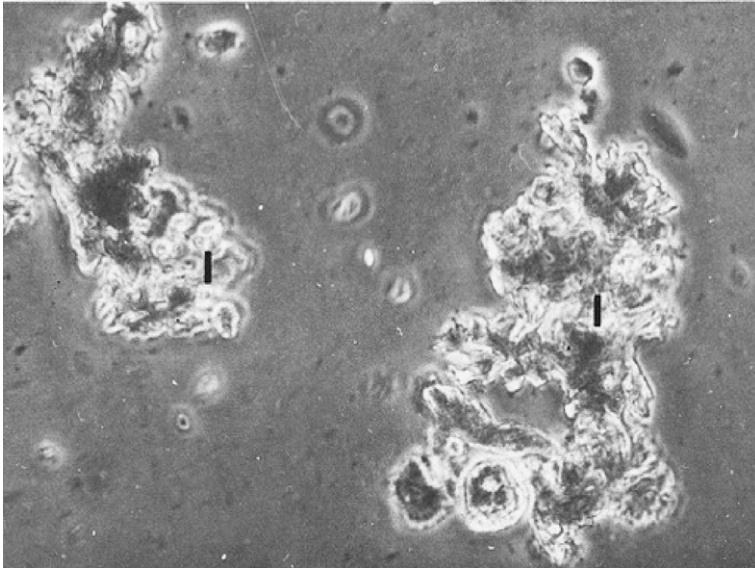hese inorganic materials are formed create extremely precise and complex structures with advanced functionality [228]. Furthermore, the constituent materials provided in nature are often brittle and weak. Thus, the strength of hard tissues such as shells or bones is derived from the structure rather than through materials selection. As material selection reaches its limitations, engineers look toward nature's example of structural optimization for the next generation of technology.

There have been two approaches in generating bioinspired materials and structures. It can be hardly argued that all early attempts at flying were inspired most rather probably by birds. The Greek legend of Icarus comes to mind. This traditional approach has utilized synthetic materials to produce performance that mimicks biological materials. Many of the early biomaterials (Vitallium, gold, etc.) are based on this approach. This will be discussed in Section 11.1. The current frontier in bioinspired materials goes further and uses bioinspired processes at the molecular level to generate new materials and structures. Such is the case of tissue engineering and other molecular-based approaches. Some of these efforts are presented in Section 11.2.

11.1. Traditional biomimetics

11.1.1. Aerospace materials

The effect of gravity applies to both technology and nature as can be seen in the design characteristics of biological avian materials such as bird beaks and bones. There is an
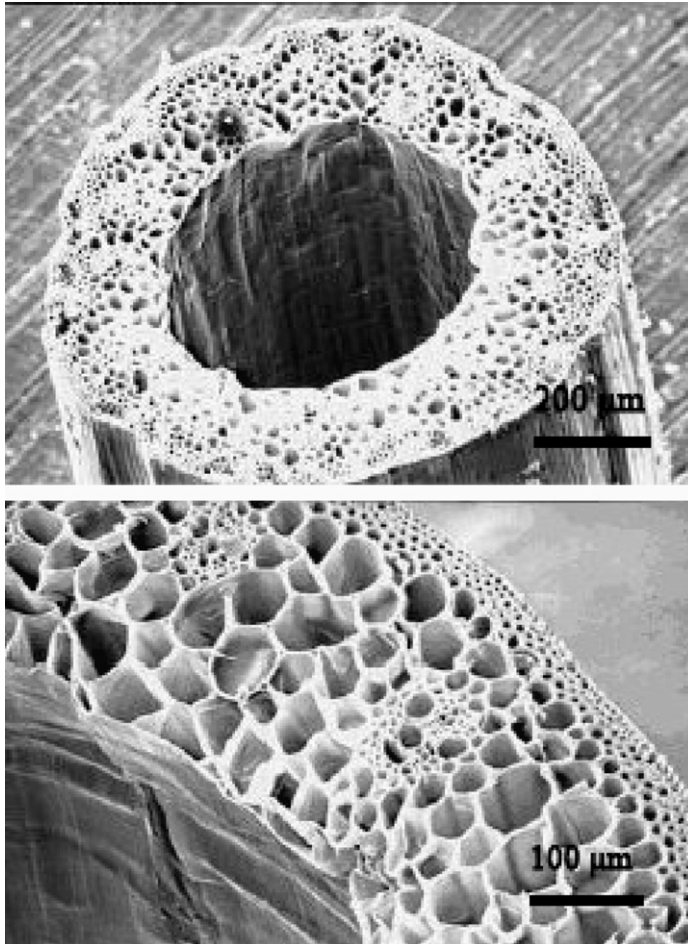
Fig. 183. Cross-section of grass stem (*Elytrigia repens*) showing a shell structure with a foam-like core (from Karam and Gibson [337]).

apparent optimization of weight to strength through sandwich structures consisting of solid shells filled with compliant cellular cores [12,13]. The core significantly increases the buckling capabilities of the entire system while maintaining the light weight required for flight. This synergism between a hard shell and a compliant core is also exhibited in other biological structures which require resistance against axial buckling. Plant stems are an example of this, often consisting of thin-walled cylindrical structures filled with a cellular core [334,335]. Their large aspect ratio creates an interesting engineering problem which has been posed both in nature and technology. Fig. 183 provides an examples of this structure in nature: a grass stem.

Birds have structures that are optimized for weight, and Fig. 184a shows the metacarpal bone in a vulture wing. This bone has a unique structure composed of two layers connected by a tridimensional array of inclined struts. This structure provides the stiffness required by minimizing weight, since most of the mass is displaced away from the neutral plane. Interestingly, researchers are developing structures that are very similar (Fig. 184b).
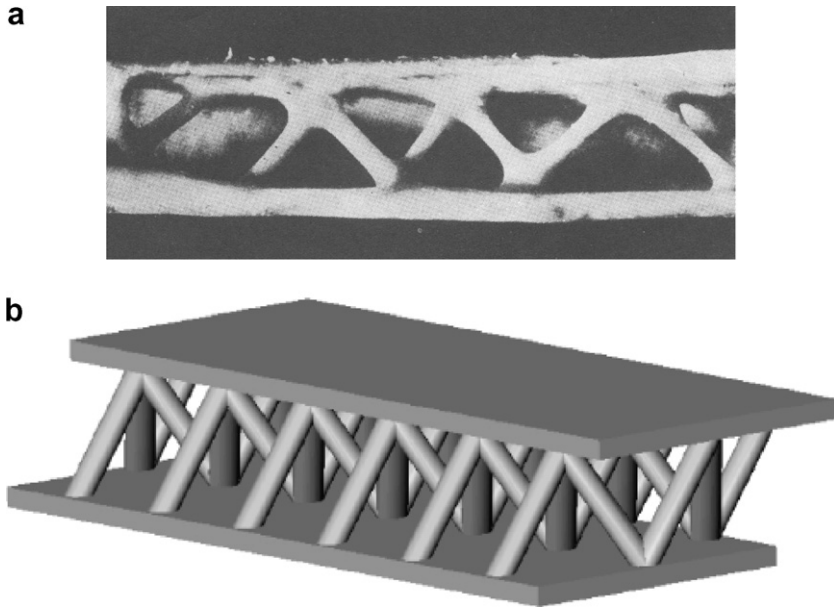
Fig. 184. (a) Metacarpal bone from a vulture's wing. The structure is stiffened by V-shaped struts in a 3-D configuration (from Thompson [1, p. 976, Fig. 460]). (b) A CAD image of the truss core structure. The multifunctional cellular metals has a similar structure to the metacarpal bone of vulture (from Evans et al. [348, p. 319, Fig. 11a]).

The example shown in Fig. 184b was developed for an experimental multifunctional material. This is a clear example of modern research finding solutions that have been applied by biological systems for millions of years.

Karam and Gibson examined the elastic buckling of thin cylindrical shells filled with compliant elastic cores [335–337]. Their results confirmed the benefit of the hard shell – elastic core synergy. Again, nature's design stood up to the test, showing significant mechanical improvement with limited weight gain. Furthermore, the problem of axial buckling in structures with high aspect ratios is approached as such materials and structures are commonly found in both nature and technology.

11.1.2. Building designs

Other examples of buckling resistance can be found throughout the natural world; even the deepest parts of the ocean can accommodate organisms with interesting biomimetic potential. The skeleton of a sea sponge, for example, exhibits amazing hierarchical levels of complexity, each providing the essential components of structural design necessary for the conversion of the otherwise brittle constituent material (silica) into a sophisticated masterpiece of architectural evolution. This structure has been studied to expose some of the engineering lessons which have stood the test of time over millions of years [40,94]. Fig. 185 shows a section of the skeleton of the sponge *Euplectella* [94]. Fig. 34 shows the sea sponge in its entirety. The cylindrical cage extends 20–25 cm in length and 2–4 cm in diameter. The frame of the cage consists of long vertical struts running the entire length of the structure. Horizontal struts form a regular square lattice with
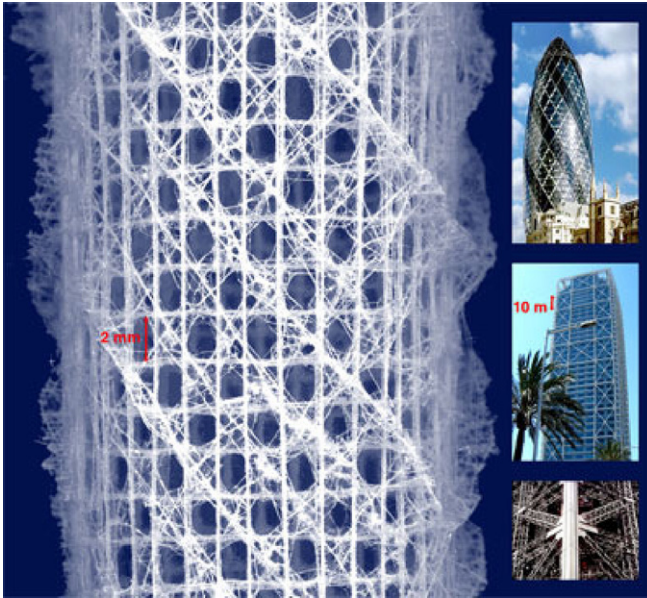
Fig. 185. Skeleton of the deep sea sponge *Euplectella* (from Aizenberg et al. [94]).

the vertical struts. This structure is reinforced by external ridges that extend off of the surface of the cylinder and spiral the cage at an angle of 45° to the cross-sectional plane. A brittle material loaded in torsion will fail along the surface where tensile stresses are the maximum. This occurs 45° to the cross-sectional plane resulting in helical fractures [161]. The helical reinforcement of the cage is no accident of nature; the spiraling struts offer important strengthening mechanisms to combat the destructive forces applied through the ocean's currents. Many similar reinforcements can be seen in advanced structural engineering masterpieces including the Swiss Re Tower in London, Hotel De Las Artes in Barcelona, Spain and the Eiffel Tower in Paris as can be seen in the inserts of Fig. 185 (taken from Bell Labs).

11.1.3. Fiber optics and micro-lenses

Structural reinforcement of this deep sea sponge is not limited to its macro-level design described earlier. Each strut of the cage is composed of bundles of silica spicules. These spicules, that were discussed in detail in Section 6.1, consisting almost entirely silica, exhibit remarkable flexibility and toughness. Unlike their commercial counterparts, they can be bent and tied into knots without fracture. This is attributed to the concentric lamellar structure. Cylindrical layers, 0.2–1.5 μm thick are separated by extremely thin organic inter-layers shown in Fig. 186 [94]. This style of interplay between hard and soft materials can be seen throughout the natural world. In almost all cases the laminate design of brittle inorganic layers separated by thin elastic regions of organic material leads to a dramatic increase in toughness of otherwise weak materials. These organic regions are usually very small percent of entire composite. The optimization of composition and microstructure in this natural material may inspire some novel improvements for its man made equivalent.
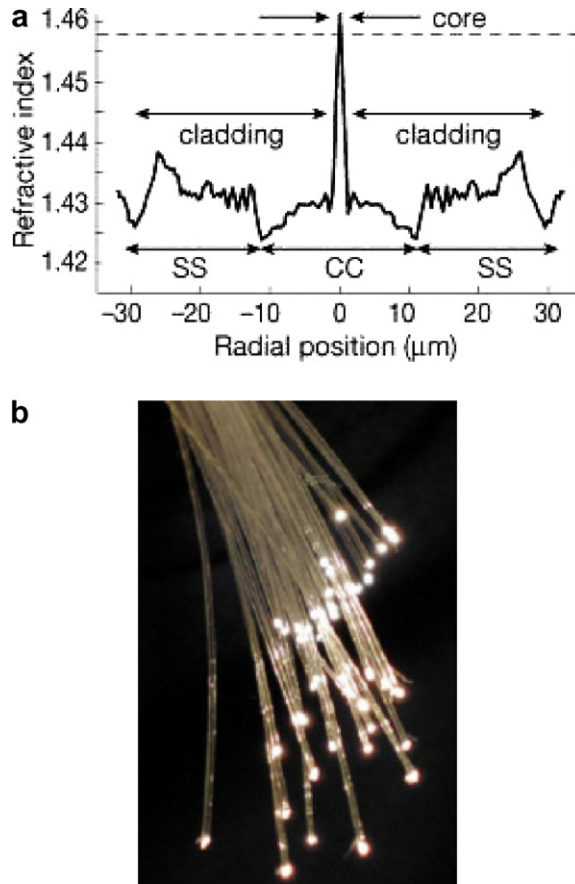
Fig. 186. Sponge spicule with (a) 'core-cladding' profile showing wave guiding properties, (b) commercial fiber optics (from Sundar et al. [95]).

However the similarities between these two materials is not only limited to composition. The variation of reflective index of the various sections of the spicule results in wave-guiding properties similar to those found in modern fiber optics [95]. Described by Aizenberg et al. [94], the cross-section in Fig. 186a shows three distinct regions: a core of pure silica surrounding an organic filament, a central cylinder of high organic content, and the laminate layers with decreasing organic content. Interferometric refractive index profiling revealed a high reflective index at the core surrounded by a low reflective index in the central cylinder. The 'core-cladding' profile in Fig. 186b shows how light can be confined within the core and guided through the spicule. It is not clear whether the organism uses the optical properties of the spicule, however in comparison to manmade counterparts the technical advantages are impressive.

The brittlestar is a marine animal that has great sensitivity to light. It was discovered by Aizenberg and Hendler [338] that this organism, that does not have specialized eyes, has a set of lenses that channel light. These lenses focus the light 4–7 μm below the array, into the neural bundles that exist in the animal. Fig. 187a shows these lenses. They have many features that are superior to synthetic microlenses. They minimize spherical aberration,
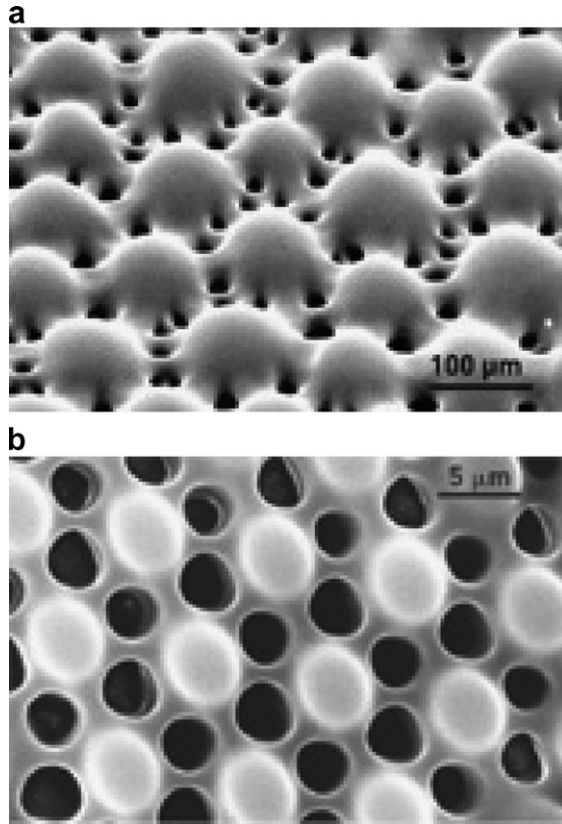
Fig. 187. (a) Brittlestar lenses; (b) synthetically produced microlens array (from Aizenberg and Hendler [338]).

have a crystallographic orientation that eliminates birefringence, and contain an organic–inorganic composite that prevents the brittle calcium carbonate from fracturing easily. This brittlestar lens design was used at Bell laboratories to produce synthetic lenses mimicking the properties. These synthetically produced microlens arrays have sub-10-μm pores and controlled crystallographic orientation. They are shown in Fig. 187b.

11.1.4. Manufacturing

The incredible control of nanoscaled material design in nature is unparalleled in current technology [7,60,64]. As mentioned earlier, the sophisticated structures and materials are created in nature under ambient temperature and pressure. The man-made counterparts of these materials are typically produced under extreme conditions resulting in a myriad of engineering obstacles which often times drive up the cost of production. Biomimetically inspired manufacturing techniques may result in the technical evolution of the way in which we think of manufacturing. Morse and coworkers [339] developed a manufacturing method for semiconductor thin films using inspiration from spicule formation. They found that by putting enzymes, similar to those of marine sponges, onto gold surfaces they could create templates on which semiconductor films could grow. Using concepts of biomimetics catalysts they were able to grow films at room temperature [340].
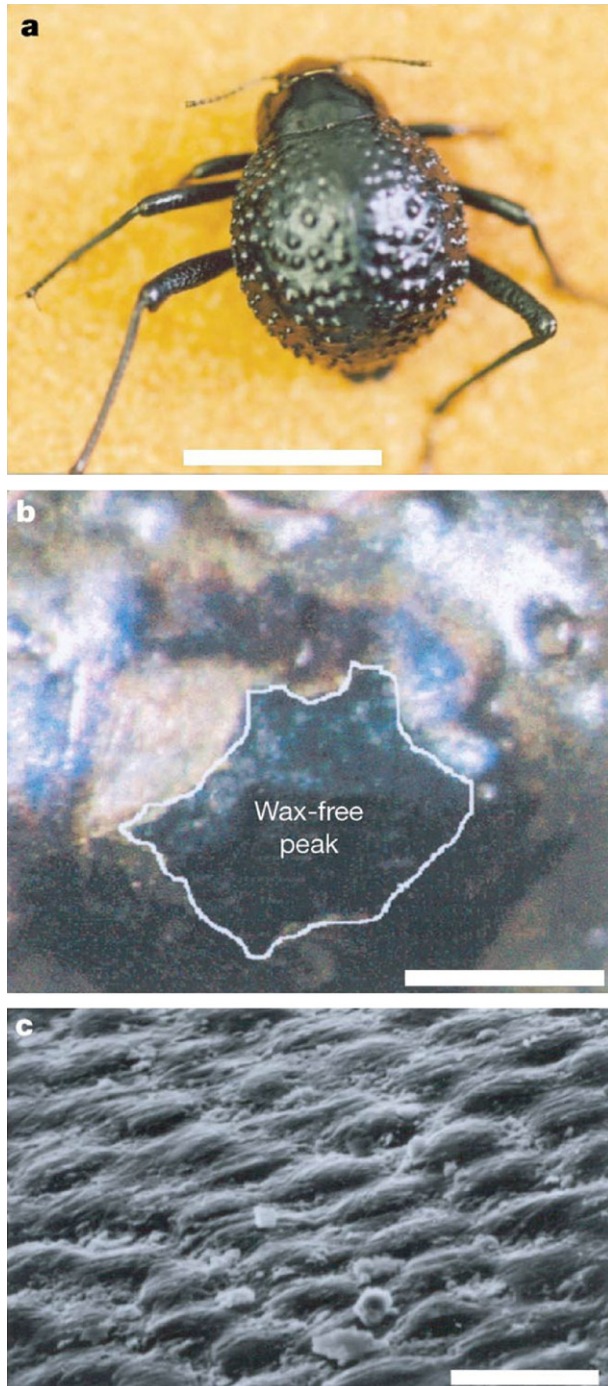
Fig. 188. (a) Adult female, dorsal view; peaks and troughs are evident on the surface. (b) A 'bump' showing hydrophilic wax free region. (c) Scanning electron micrograph of the textured surface of the depressed areas. Scale bars, (a) 10 mm; (b) 0.2 mm; (c) 10 μm (from Parker and Lawrence [342]).

11.1.5. Water collection

Even the most extreme climates in the world can host animal life. The desert beetle, for example, survives in one of the driest environments known to man. Extreme daytime temperatures, howling winds, and almost nonexistent rainfall leave desert areas almost entirely uninhabited. Yet every morning the tenebrionid bettle *Stenocara* sp. walks through a transitory fog, collecting essential drinking water on its back [341]. The bumpy back of beetle is designed to pull moisture from the air along alternating regions of hydrophobic and hydrophilic surfaces [342]. Macro scaled bumps of approximately 0.5 mm diameter pepper the back of the beetle as shown in Fig. 188a [342]. At the peak of each bump a hydrophilic region protrudes into the surrounding atmosphere (Fig. 188b) [342]. The troughs between bumps and the sloping sides which descend from each peak are covered in wax. This area is equipped with a microstructure of tightly packed flattened hemispheres 10 μm in diameter (Fig. 188c) [342]. As a result the surface of the back, with exception to the peak of each bump, is superhydrophobic. The hydrophilic peaks act as nucleation points for droplets to form from the surrounding moisture of the fog. As droplets grow to a critical size they slide off of their unstable position at the peak of each bump and into the hydrophobic troughs where they can roll down towards the mouth of the beetle.

As a biomimetic material this type of functionality could be easily reproduced for commercial use [342]. Sheets of a similar structure could provide the essential drinking water to the inhabitants of the extreme corners of the world.

11.1.6. Velcro

One of the most successfully commercialized biomimetic materials literally stuck itself to its inventor's pants. In the summer of 1948, the electrical engineer George de Mestral was walking with his dog when he realized his pants had become covered in a plethora of seed-bearing burrs. As he sat in frustration, tediously pulling burr after burr from the fabric of his clothes, curiosity grew in George's mind. When he investigated the structure of the burr under his microscope Mestral realized the secret to the seeds ability to
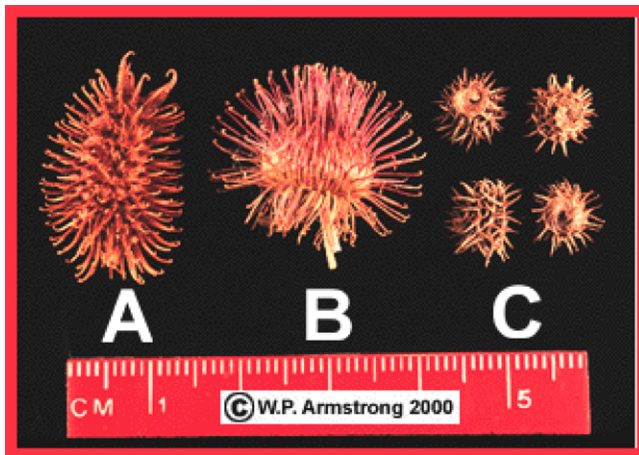

Fig. 189. Burs of a seed similar to the seed which gave birth to Velcro (from Armstrong [343]).

fasten themselves to many surfaces. It was tiny little hooks which covered the seed as shown in Fig. 189 [343]. From this Velours and Crochet 'Velcro' was born, giving rise to a multi-billion dollar industry.

11.1.7. Gecko feet

As seen in Section 10.1, tiny nanoscaled hairs known as spatulae line the bottom of a gecko's foot. They are used to create an electric bond with any surface they touch [312,344]. A Van der Waals attraction between individual atoms on the tip of each hair and the atoms on a surface is created. When millions of these hairs are all creating an attraction the combined force is great enough to keep the gecko tightly secured a wall. In fact the combined force theoretically could hold much more then just the weight of a gecko. The unique attachment devices of geckos (Section 10.1) are being used as inspiration for synthetic devices. Artificial hair covered tapes made by engineers attempting to mimic the gecko's foot promise to holds as much as 3 kilograms per cubic centimeter of surface area [345]. However these tapes, seen in Fig. 190, still lack the ability to truly recreate the ingenious design of nature. The artificial tapes tend to quickly become laden with water or dust particles rendering them useless while the individual spatulae of the gecko are able to remain clean and reusable. This self-cleaning ability has yet to be successfully mimicked by man.

This work was first carried out by Sitti and Fearing [162], who produced synthetic polyethylene bristles by casting them from ceramic with nanoholes that had some of the properties. However, they were marred with problems. The dashed line in Fig. 191 represents the theoretical pull-off strength obtained from Johnson–Kendall–Roberts equation [163]. This gives the $R^{-1/2}$ dependence of pullout strength. The experimental data (continuous lines) apply to synthetic pillar arrays manufactured by the Arzt group [312,357]. These arrays are shown in the photomicrographs at the corners of plot. Arrays with different diameters were produced, as shown in photographs. This is only a first effort, but the Kendall relationship between the pillar radius and the pull-out strength is obeyed.
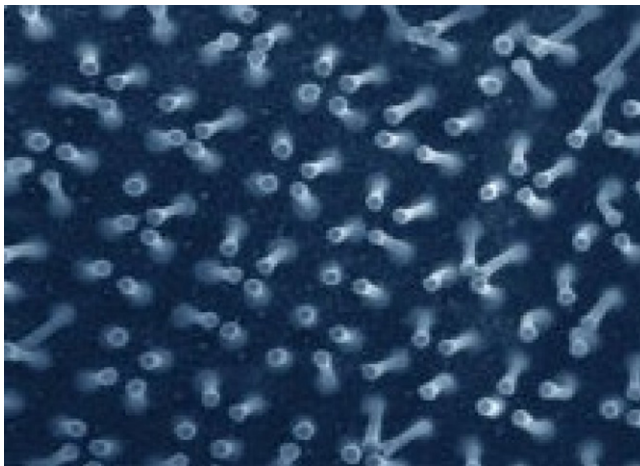

Fig. 190. Biomimetic man made tape using gecko feet as inspiration (from Geim et al. [345]).
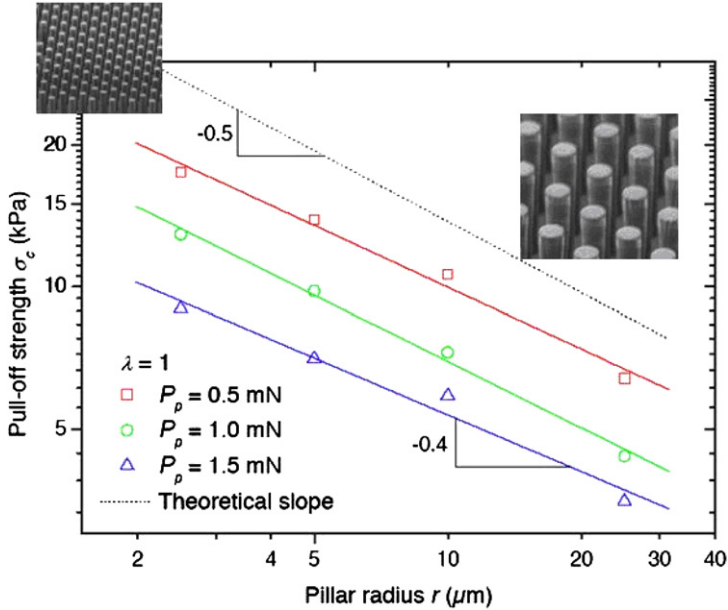
Fig. 191. Pull-off strength as a function of pillar radius (from Huber et al. [314]).

11.1.8. Abalone

The first attempt at biomimicking dates back to the 1980s. A laminated structure of Al-B₄C was produced by Sarikaya and Aksay [140]. They demonstrated significant increases in toughness. In Fig. 192, an increase in the fracture toughness of B_4C ($K_{Ic} \sim 3$ MPa m$^{1/2}$) to about 16 MPa m$^{1/2}$ was shown for the B₄C-Al laminate. However, severe problems occurred because of the reaction of Al with B₄C forming Al_4C_3, a very brittle material. Although improvements were achieved in the mechanical properties of synthetic laminated composites [164,166,349] based on biological architecture, these have not been as extraordinary as the one nacre provides in comparison with monolithic $CaCO_3$. This may be due to limited laminate thickness in synthetic composites and the still not yet clearly identified composition and structure, especially of the complex nanolaminated structure in the organic layer. Thus, the potential benefits of complex architectures have not been explored fully yet. Nevertheless, research into bioinspired (specifically, abalone) armor continues.

Almqvist et al. [165] tried to reproduce the structure of the abalone by using tile with the addition of a synthetic polymer as bonding. Tile has composition $Mg_3(Si_4O_{10})(OH)_2$ These particles have dimensions on the order of the $CaCO_3$ tiles in abalone: a thickness of a few hundred nanometer and diameter of 3–10 μm.

There is considerable industrial application of tile-polymer composites, with the polymer being more than 60 wt%. During extrusion, the particles orient themselves along the polymer flow direction. Almqvist et al. [165] attempted to reduce the polymer content to less than 10% by aligning the tile particles though several techniques including sedimentation, centrifugation, shearing, and spinning. They encountered significant problems in wetting the tile particles with the polymer. They were not able to reproduce the high degree
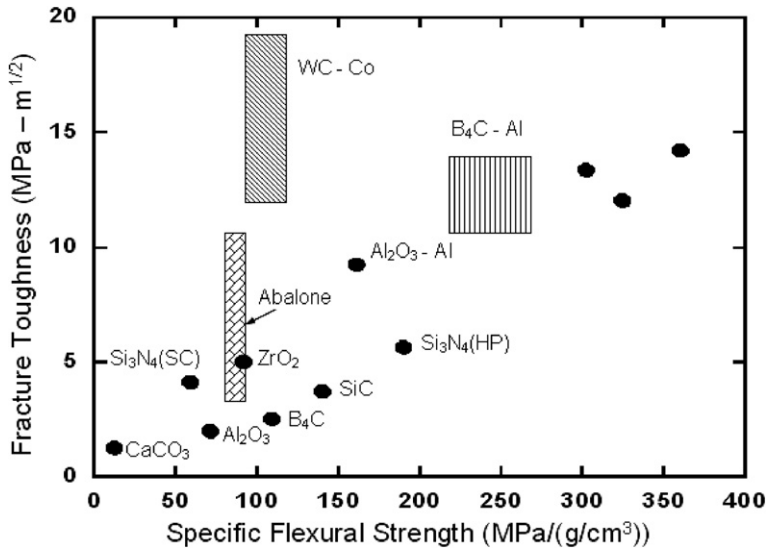
Fig. 192. Fracture toughness versus fracture strength of the nacre section of an Abalone shell compared to some high technology ceramic material (reproduced from Sarikaya et al. [134]).

of order existing in nacre, although significant alignment of the tablets was achieved. They concluded that the poor flexure strength achieved (in comparison with nacre) could be increased by using a polymer with greater similarity to the viscoelastic organic component in nacre.

There have been many other attempts at making microlaminates. Tang et al. [350,351] used electrical potential to sequentially deposit clay (montmorillomite) platelets and polymer chains and in this manner produced thin layers of a glue with the tiles arranged much more regularly than the ones produced by Almqvist et al. [165]. However, the sequential deposition on a silicon wafer substrate created layers that were only a few μm thick, since the individual Montmorillomite bricks had thicknesses of only 0.9 nm. This is seen in Fig. 193a and b. There have also been macro scale attempts at biomimictry of abalone nacre. An example of this is provided in Fig. 193c. LAST® armor tiles, built by Foster–Miller (foster-miller.com), consist of SiC or B_4C hexagonal tiles covered in a Kevlar® thermoset laminate which are held together with a Velcro®-type adhesive. This nacre-like structure provides energy absorption and toughening through many of the same mechanisms as its natural counterpart. The armor has been implemented onto various ground and air vehicles including over 1000 Humvees for the US Marines.

Manne and Aksay [352,353] considered other approaches to synthesize microlaminates:

(a) Langmuir–Blodgett (LB) deposition.The particles are floated on a water surface after being coated with a hydrophobic layer.
(b) Covalent self-assembly.
(c) Alternating sequential absorption.
(d) Intercalation of organics into layered inorganic structures.
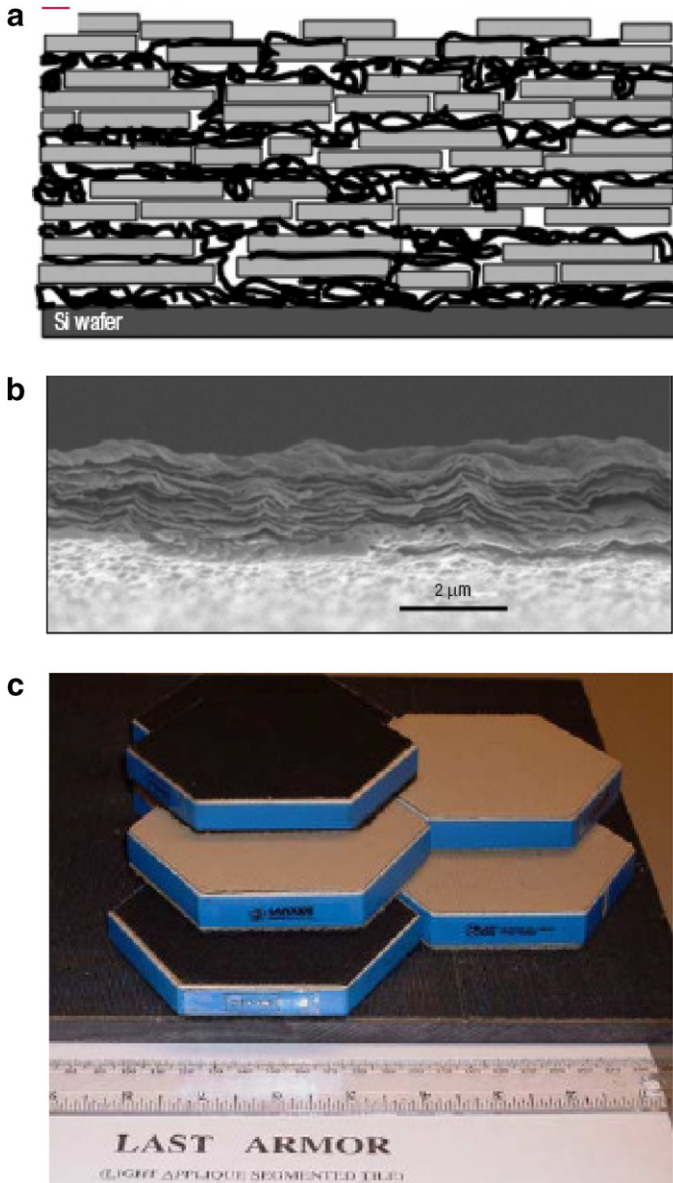
Fig. 193. (a) Schematic illustration of the $(P/C)_n$ film structure. The thickness of each clay platelet is 0.9 nm. (b) Scanning electron microscopy of an edge of a $(P/C)_{100}$ film. (adapted from Tang et al. [350]). (c) LAST® armor built by Foster–Miller (Foster-miller.com).

A very innovative approach was recently demonstrated by Deville et al. [354,355]. They used the directional growth of ice crystals (dendrites) from a surface as the basis of their synthesis technique. As the ceramic slurry is frozen, the ice crystals expel the ceramic particles. Fig. 194 shows the ice crystals forming columns or lamellae. The layers are as thin as

Fig. 194. Schematic illustration of the LBL synthesis of laminates through the growth of ice crystals (ice template, IT).

1 μm. The porous ceramic scaffolds formed by sublimation of the ice are then filled with either a polymeric or metallic phase. Deville et al. [354,355] used hydroxyapatite as the ceramic phase and were able to ach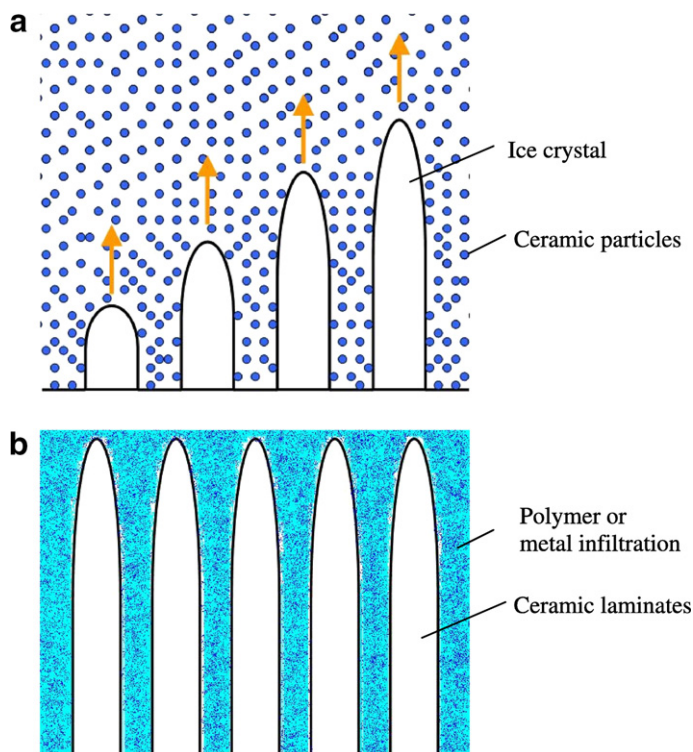ieve a controlled porosity. The mechanical strength of the porous skeleton (without infiltration of metal or ceramic) was significantly superior to that of porous hydroxyapatite produced by other techniques (Fig. 195).

As seen in Section 6.1, marine sponges and other organisms produce silica via aqueous bio-mediated methods. This approach inspired Schwanzer et al. [356] to grow ZnO thin films. These ZnO films are conventionally grown by MOCVD, PLD, or MBE; they have a unique combination of optoelectronic, piezoelectronic properties, and are transparent. Schwanzer et al. [356] successively grow ZnO and $Zn_5(OH)_8(NO_3)_3 2H_2O$ thin films (including ITO coated glass) on different substrates using an aqueous approach that mimics the biosilicification of marine sponges.

11.1.9. Marine adhesives

When developing an anchoring system for marine vessels, why not look at the systems which have truly stood the test of time? The tides of the oceans have provided a tumultuous environment of marine life since the beginning of life on this earth. Organisms such as the common mussel have been forced to develop remarkable methods of attaching themselves onto structures in order to avoid being swept out to an inevitable and gruesome death. The mussel byssus threads seen in Fig. 196 are 5 times tougher and 16 times more
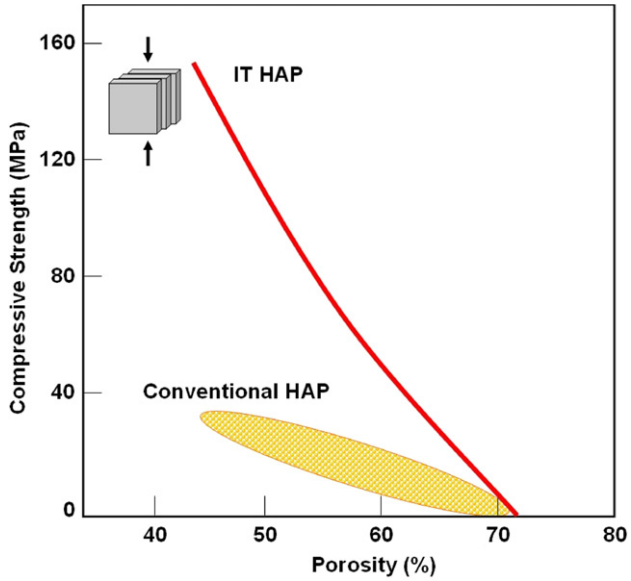
Fig. 195. Comparison of conventional porous hydroxyapatite and material produced by ice template (IT) method (reproduced from Deville et al. [354,355]).

Fig. 196. Mussel Byssus threads which provide the anchoring system for this marine organism (from Holl et al. [346]).

extensible then the human tendon [346,347], furthermore the natural glue which attaches each thread to a surface is stronger then any man-made marine adhesive [258]. They are described in greater detail in Section 8.4. The creation of commercial materials with these properties could be possible after first understanding the mechanisms with which nature produces them.
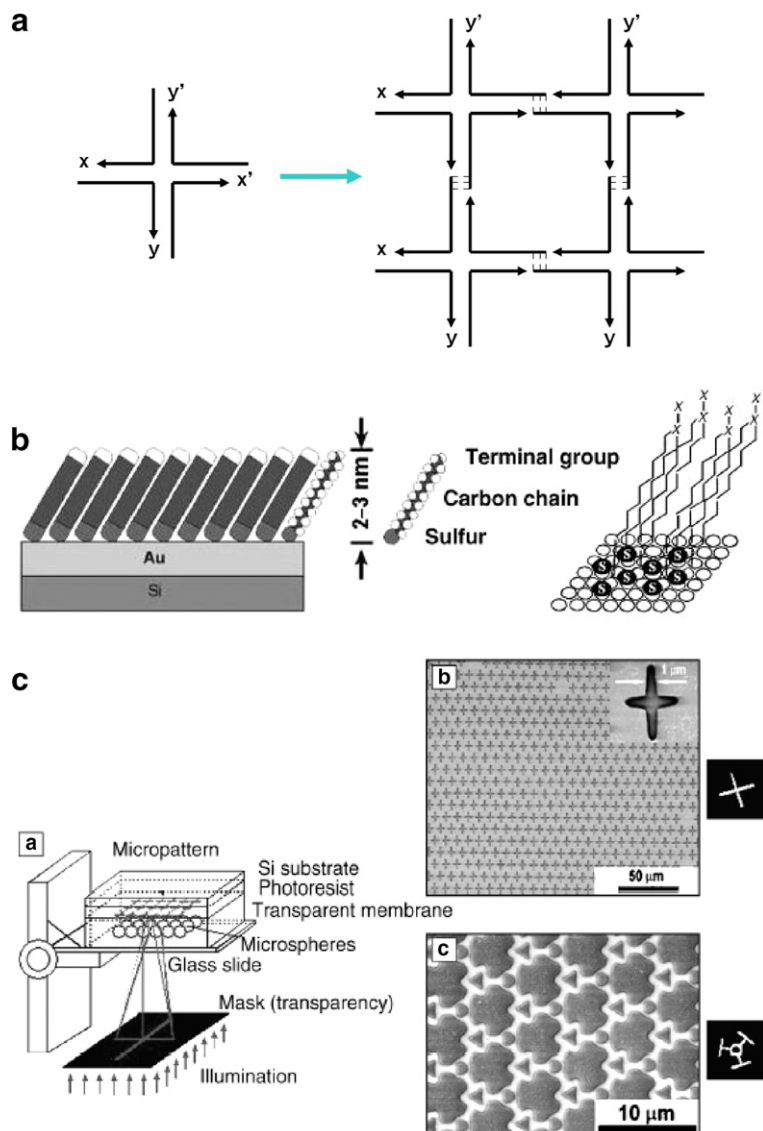
Fig. 197. (a) Formation of a 2-D lattice from a junction with sticky ends. X and Y are sticky ends and X′ and Y′ are their complements. Four of the monomers assemble the structure on the right (reproduced from Seeman and Belcher [358]). (b) Self-assembled monolayers (SAMs) of alkanethiols can be formed on gold evaporated onto a solid flat substrate such as silicon or glass. The sulfur groups interact covalently with the gold, the poylmethylene chains pack tightly to form the monolayer, and the head groups are exposed (from Whitesides [37, p. 61, Fig. 3]). (c) Near-field phototlithography with self-assembled microlenses (from Whitesides [37, p. 61, Fig. 8]).

11.2. Molecular-based biomimetics

Aragonite and hydroxyapatite growth are, as seen in Section 6, complex processes including proteins and self-assembly. The current frontier in bio-inspired materials goes beyond copying the structural elements. It starts at the nanometer level, with genetically engineered proteins; it also seeks to form the structures by self-assembly of its components. This field of research is still in its infancy but has enormous potential.

An example of the effect that genetic modification is the work by Snead et al. [185]. They demonstrated in dental enamel that the self-assembly of proteins called amelogenin into nanospheres provides the environment from which hydroxyapatite crystals grow in the woven pattern shown in Fig. 95b. By changing the amelogenin, transgenic mice were produced that had teeth where the enamel was less hard and exhibited a different structure. This was accomplished by genetic engineering, which consisted of altering or deleting amino acids in the two highly conserved domains of mouse amelogenin.

The process of self-assembly is the essential component of the bottom-up approach though which biological systems are formed. This process can be one-, two-, or three-dimensional. Fig. 197a illustrates how a two-dimensional network of branched DNA molecules, in the form of a cross with "sticky" ends (left-hand side), can self-assemble to form a reticulated network (right hand side) [358]. This is just an illustration, and many more complex arrays are possible, depending on the functionality of the bonds. The possible applications of the DNA lattice shown in Fig. 197a are

- Scaffolding to crystallize biological macromolecules.
- Organization of compounds in nanoelectronics.
- Bio-inspired nano-component chips (quantum dots).

Whitesides and coworkers have pioneered self-assembled structures and used a number of approaches. The early experiments on self-assembled monolayers (SAMs) by Nuzzo and Allara [51] inspired Bain and Whitesides [37,359] to use molecules with sulfur terminations. The sulfur atoms bond to the gold substrate and the molecules therefore form a monolayer. This is shown in Fig. 197b. The end of the molecule opposite to sulfur can have a functional termination that changes the properties of the gold surface. For instance, if the end is a methyl group, the surface is hydrophobic. It the end is a carboxylic acid group, the surface is highly hydrophilic.

The Whitesides group [37,359,360] has also used 5 mm diameter balls (octahedrons with the corners cut off) with solder connections and shown that they can be self-assembled. After self-assembly, the solder of the junctions can be made to fuse them together. This is accomplished by placing the balls in a warm solution and tumbling them. If the solder dots, placed at specific facets, encounter one another, they fuse. If they encounter a surface with a LED, they do not fuse. After the assembly was completed, a current was passed through and the LEDs were lit. This approach illustrates the potential of using self-assembly to create electrical networks and represents a prototype for possible future. A photolithographic technique where the lenses are self-assembled is shown in Fig. 197c.

The bacteriophage (nicknamed 'phage') is a microbe that has nanoscale dimensions. Phages, like viruses, do not have reproductive organs. The T4 phage injects DNA into E. coli bacteria. Fig. 198a shows the schematic representation of a phage that has an icosahedral head (capsid), a cylindrical tail sheath, and six legs. The scale of a T4 phage is
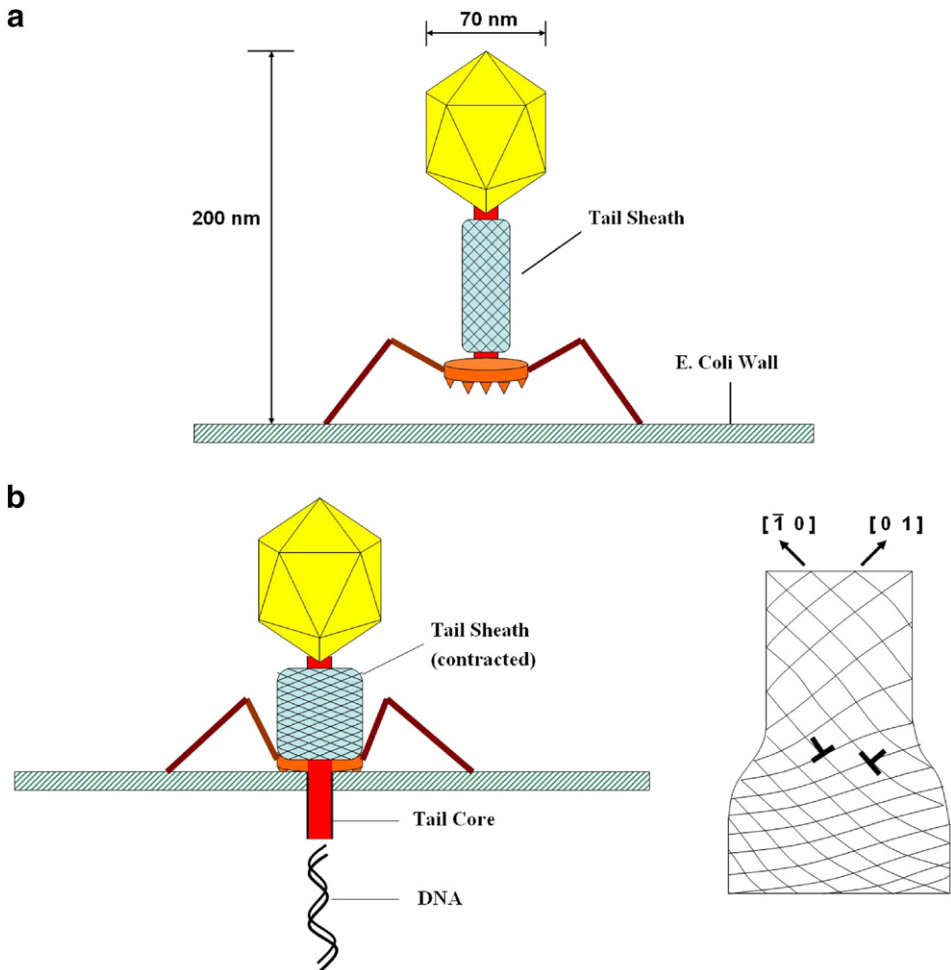
Fig. 198. (a) A T4 Phage attaches to E. coli cell wall; (b) Insertion of the genetic material by a T4 phage. (c) Cylindrical crystal structure of virus tail-sheath during contraction by martensitic transformation. Interface is described by coherency dislocations which spiral up helical close-packed crystal rows (reproduced from Olson and Cohen [362]).

approximately 70 nm in diameter and 200 nm in length. It has unique properties which we briefly discuss below. The T4 phage, resembling a Mars Lander, connects to the membrane of a bacterium through the six legs. At that point, the tail sheath contracts and penetrates the wall (Fig. 198b). This contraction is accomplished by a martensitic-like transformation in the tail sheath, as shown in Fig. 198c and as identified by Olson and Hartman [361,362]. The contraction of the tail sheath propels a needle (tail core) through the bacterium wall. This enables the release of the DNA into the interior, where it uses the genetic machinery of the bacterium to reproduce itself.

The phages very simple: they consist of geometrical assemblies of DNA and a few proteins. There is no fatty tissue, no blood, no reproductive system. These components, once manufactured inside the bacterium, self-assemble. As the bacterium dies, the phages spew
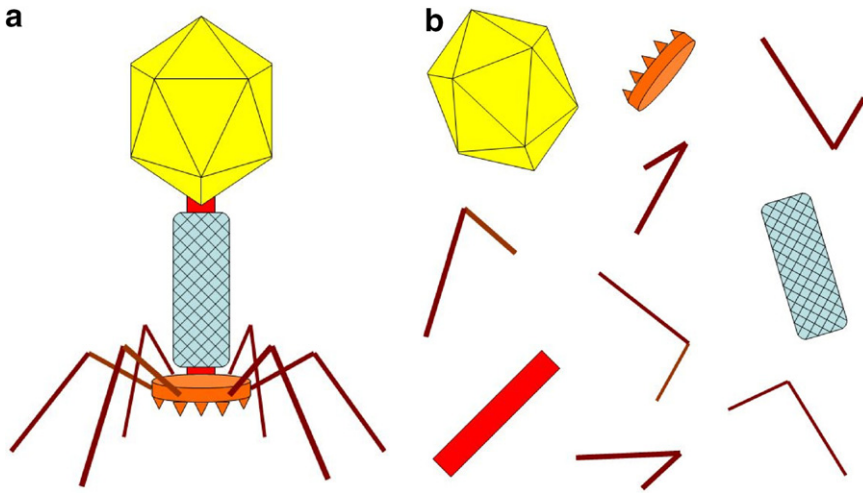
Fig. 199. (a) The structure of the T4 bacteriophage; (b) Phage broken into parts can reassemble spontaneously.

out and continue the cycle [34]. Phages can reassemble in a test tube after being broken up in a blender. This is shown in Fig. 199. This ability of phages to self-assemble in a quasi-mechanical way without any DNA templating or using proteins is inspiring scientists. Could this be used in the future?

Sarikaya and coworkers [53,332] used phages to find the proteins required for specific surface interactions. Of special interest to materials scientists are protein interactions with inorganic substrates, such as silicon or gold. They used a technique from the molecular biology field called phage display (PD) [53,332] to select proteins that bind to selected inorganic surfaces. This was based on earlier work by Brown [363], who found that some proteins selectively bind to specific inorganic surfaces. Sarikaya and coworkers [53,332] engineered new polypeptides that selectively bond to different inorganic substrates:

Noble metals (Pt, Au, Ag, Pd).
Metal oxides (ZnO, Al_2O_3, SiO_2).
Semiconductors (GaN, Cu_2O, TiO_2, ITO, Sulfides, Serenades).
Other functional materials.

This method, that they call GEPI (Genetically Engineered Polypeptides for Inorganics) is represented in Fig. 200. The first step consists of obtaining random sequences of amino acids by breaking up DNA. These are then incorporated into phages. These coated phages are shown as step 2, Fig. 200. These phages are then exposed to the selected surface (step 3) and washed away (step 4). Several washes are required. The polypeptides that bind to the selected surface can not be removed by the washes, and are eluted (step 5). These polypeptides are then replicated by having the phage inject the DNA into a bacterium. An attractive methodology to PD is cell-surface display. There, the polypeptides are incorporated into cell surfaces. These genetically engineered polypeptides can potentially be used for generating a variety of nanoscale arrays on the surfaces of inorganics. These arrays have a range of applications; connected with the anchoring, coupling, branching, displaying,
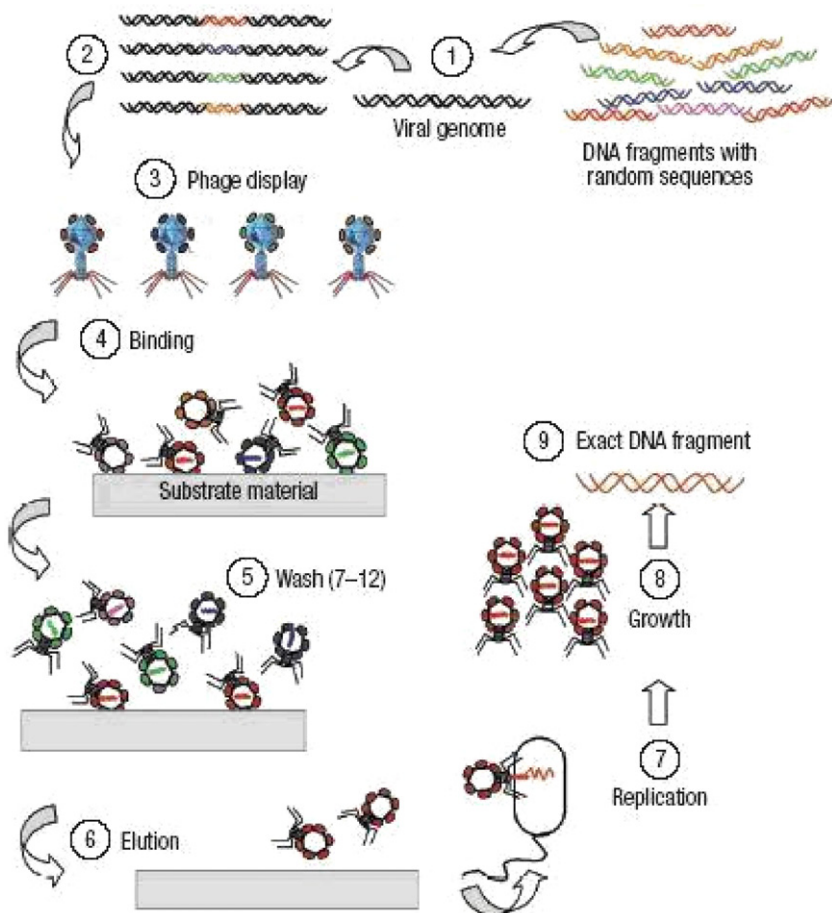
Fig. 200. Method for obtaining genetically engineered polypeptides for inorganics (GEPIs) by phage display; (1) DNA is broken up into random sequences; (3) sequences are incorporated into phages; (4), (5) phages are put into contact with inorganic surface and washed sequentially; (6) phages that stick to surface are eluted and have their DNA injected into bacterium for expression replication (7); (9) exact DNA fragments (polypeptides) that stick to surface are thus obtained; these are the famous GEPIs (adapted from Sarikaya et al. [332]).

and assembling of functional molecules, nanoparticles, and structures. The basic methodology is illustrated in Fig. 201. Two different GEPIs are used: GEPI-A and GEPI-B. They are assembled on a patterned substrate. Each GEPI is connected to an inorganic. These inorganics serve, on their turn, to attach functionalized monomers. These functionalized monomers can serve a variety of functions, such as conductors, photonic devices, or other functions. Thus, the GEPIs can hypothetically serve as nanoscale platforms for nanoarrays.

Belcher [364] took the process one step further by using the phages directly to bind to ZnS particles. The phages held the ZnS particles into position. Nanoscale ZnS particles can, by this stratagem, produce regular arrays. Belcher's [364] intended application for this approach is to create quantum dot devices.
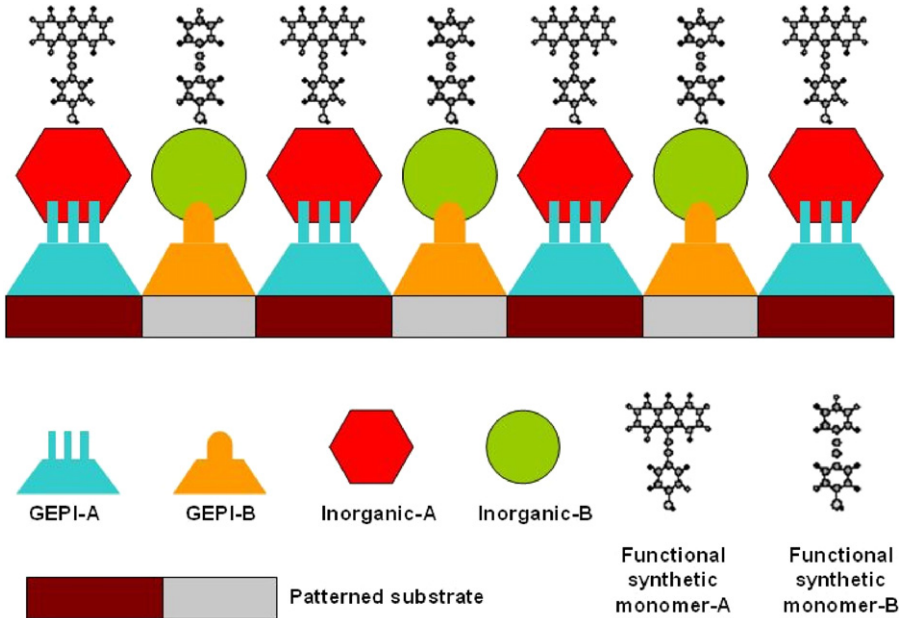
Fig. 201. The potential of using GEPI as 'molecular erector' sets. Two different GEPI proteins (A and B) are assembled on ordered molecular or nanoscale substrates. The inorganic particles A and B are immobilized selectively on GEPI-A and GEPI-B, respectively. Synthetic molecules are assembled using functionalized side-groups on the nanoparticles (reproduced from Sarikaya et al. [332]).

In summary, the range of Biomimetic materials has barely been exposed. The development of novel technological advances could greatly benefit from the lessons taught by nature. Millions of years of trial and error have resulted in designs which are incomparably refined.

12. Summary and conclusions

The field of biological materials represents a growing component in Materials Science and Engineering. It is indeed one of its frontiers, since the first fifty years since MSE's inception have been devoted to metals, ceramics, polymers, and their composites in a unified way. The expansion into biological materials adds a level of complexity that is indeed a challenge that will stimulate an entire generation of researchers. The increased availability of nanoscale testing, characterization, and modeling methods has been and will continue provide the tools required to advance our understanding of the behavior of structural biological materials. The principal experimental and analytical tools are given below:

Nanoscale testing: nanoindentation, optical tweezers.
Nanoscale characterization: TEM, AFM, Field Emission SEM.
Nanoscale modeling: Molecular dynamics (MD).
The unique and defining features of biological materials are:

(a) *Self-assembly*: They are first assembled at the molecular level; the structures are constructed form the bottom up.

(b) *Hierarchical structure*: The structure varies in architecture with scale. The different hierarchical levels operate in a synergistic fashion. In this monograph, we present the examples of tendon, nacreous layer of shells, arthropod exoskeleton, silk, dentin, and bone.

(c) Biological materials are, for the most, produced in an *aqueous environment* and at *ambient temperature*.

(d) *Multi-functionality*: Many components in biological systems must have more than one function, whereas synthetic systems often separate structural from functional component.

(e) *Self healing*: Most biological materials have built-in capacity to self-heal. This seems to be a direct result of self-assembly, because the growth is not dictated from an overarching scheme but occurs locally, from the bottom up, each molecule sensing its direct environment and responding to it.

Materials and design are intimately connected and inseparable in biological materials. This has traditionally not the case in man-made structures, where the process of design calls for standard, off-the-shelf, materials, and where the development of materials and evolution in design has often followed different courses. A further defining characteristic of biological systems is that they are ''grown'', rather than ''made'' [365]. This is a direct result of self-assembly and is in contrast to many synthetic manufacturing processing in which the assembly of the component is dictated from a global plan. This has a profound effect on their structure, since they can undergo structural adjustments as the loads change. For example, a bone will undergo deposition in regions where the stresses are highest. The same happens in the growth of trees. The trunk and branches will thicken where the stresses are highest. This feature is called ''adaptive mechanical design''.

Nature accomplishes these functions of having a broad range of mechanical properties with a rather limited number of materials. The availability of materials in biological systems is dictated by the two overarching constraints: ambient temperature and aqueous environment. Thus, it is the ingenious design of materials systems that produces the wide range of mechanical properties available to them.

The basic building blocks of soft biological materials are the 20 amino acids which produce chains, called polypeptides. These polypeptide chains are the base for proteins. The name protein comes from the Greek Proteios, which means ''primary'' or ''first''. Structural proteins are the long molecular chains that, through their hierarchical organization, produce a range of elastic stiffness and strength: collagen, keratin, elastin, resilin, chitin, actin, myosin, and abductin are the most important structural proteins. There are also proteins in tri-dimensional networks: hemoglobin and myoglobin are examples. In addition to polypeptides, polysacchrides are the building blocks for chitin and cellulose.

Many hard biological materials (shells, bone, teeth, and crustacean exoskeleton) contain a mineral phase. This mineral phase is embedded in an organic (collagen) matrix in bone and dentin. In gastropod and bivalve shells (e.g. abalone), the mineral aragonite forms tiles with dimensions of $\sim 10\,\mu m \times 0.5\,\mu m$ and these are separated by thin ($\sim 50\,nm$) layers of organic. Some of the larger shells, the *S. gigas*, exhibit a greater degree of mineralization with a more extensive growth of aragonite, while others (the conus family) exhibits a tessellated organization of the shells.

The mechanical strength of mineralized biological materials is connected to its nanostructure and to the scale, which limits the sizes of existing flaws to the level close to

the theoretical strength of the mineral. This was recently demonstrated by Gao et al. [149]. However, this is only part of the story, and hierarchical aspects play a key role. In bone, crack bridging, which occurs on the scale of ~20 μm, is utmost importance in determining the toughness, as pointed out by Nalla et al. [180]. In conch, the scale is even larger, on the order of millimeters [194].

An important class of biological materials is cellular, i.e. they have a structure akin to foam. Such is the case of trabecular bone, the inside of bird beaks, wood, hedgehog spikes, and plant stems. The presence of a cellular core is for the most part of a structure containing a solid shell. These structures are designed to minimize the weight while maximizing the stiffness.

Two goals of Materials Scientists to study biological materials:

(a) The 'materials' approach of connecting the (nano-, micro-, meso-) structure to the mechanical properties is different from the viewpoint of biologists and chemists, since it analyses them as mechanical systems. This has yielded novel results and is helping to elucidate many aspects of the structure here to fore not understood.
(b) The ultimate goal of synthesizing bioinspired structures is a novel approach within the design and manufacture. This approach has yielded some early successes such as Velcro (the well known hook-loop attachment device) in which the material components were conventional and their performance was biomimicked.

A new direction consists of starting at the atomic/molecular level (bottom-up approach) through self-assembly and to proceeds up in the dimensional scale, incorporating the hierarchical complexity of biological materials. This approach is at the confluence of biology and nanotechnology and is already yielding new architectures that have potential applications in a number of areas, including quantum dots, photonic materials, drug delivery, tissue engineering, and genetically engineered biomaterials.

Acknowledgements

References

[1] Thompson DW. On growth and form. 2nd ed., reprinted. Cambridge: Cambridge University Press; 1968.
[2] Currey JD. Bones: structure and mechanics. New Jersey: Princeton University Press; 2002.
[3] Vincent JFV. Structural biomaterials. revised ed. New Jersey: Princeton University Press; 1991.
[4] Srinivasan AV, Haritos G. Hedberg Appl Mech Rev 1991;44:463–82.
[5] Arzt E. Mater Sci Eng C 2006;26:1245–50.
[6] Sarikaya M. Micro Res Tech 1994;27:360–75.
[7] Mann S. Biomineralization: principles and concepts in bioinorganic materials chemistry. New York: Oxford University Press; 2001.
[8] Menig R, Meyers MH, Meyers MA, Vecchio KS. Acta Mater 2000;45:2383–98.
[9] Lin A, Meyers MA. Mater Sci Eng A 2005;390:27–41.
[10] Lin AYM, Meyers MA, Vecchio KS. Mater Sci Eng C 2006;26:1380–9.
[11] Menig R, Meyers MH, Meyers MA, Vecchio KS. Mater Sci Eng A 2001;297:203–11.
[12] Seki Y, Schneider MS, Meyers MA. Acta Mater 2005;53:5281–96.
[13] Seki Y, Kad B, Benson D, Meyers MA. Mater Sci Eng C 2006;26:1412–20.
[14] Chen PY, Lin AYM, Meyers MA. Unpublished results.
[15] Ashby MF. Materials selection in mechanical design. Oxford: Butterworth-Heinemann; 1992.
[16] Weertman J, Weertman JR. In: Cahn RW, editor. Physical metallurgy. North Holland; 1970.
[17] Wegst UGK, Ashby MF. Philos Mag 2004;84:2167–86.
[18] Fraser RDB, MacRae TP, Rogers GE. Keratins: their composition, structure, and biosynthesis. Springfield: Thomas; 1972.
[19] Brown CH. Structural materials in animals. London: Pitman; 1975.
[20] Wainwright SA, Biggs WD, Currey JD, Gosline JW. Mechanical design in organism. Princeton: Princeton University Press; 1976.
[21] Vincent JFV, Currey JD, editors. Mechanical properties of biological materials. Cambridge: Cambridge University Press; 1980.
[22] Simkiss K, Wilbur KM. Biomineralization: cell biology and mineral deposition. San Diego: Academic Press; 1989.
[23] Byrom D. Biomaterials: novel materials from biological sources. New York: Macmillan; 1991.
[24] Fung YC. Biomechanics: mechanical properties of living tissues. 2nd ed. New York: Springer-Verlag; 1993.
[25] Fung YC. Biomechanics: motion, flow, stress, and growth. New York: Springer-Verlag; 1990.
[26] Fung YC. Biomechanics: circulation. 2nd ed. New York: Springer-Verlag; 1997.
[27] Feughhelman M. Mechanical properties and structure of alpha-keratin fibers. Sydney: UNSW Press; 1997.
[28] Gibson LJ, Ashby MF. Cellular solids: structure and properties. 2nd ed. Cambridge: Cambridge University Press; 1997.
[29] McGrath KP, Kaplan DL. Protein-based materials. Boston: Birkhäuser; 1997.
[30] Elices M, editor. Structural biological materials. New York: Pergamon; 2001.
[31] Lowenstam HA, Weiner S. On biomineralization. New York: Oxford University Press; 1989.
[32] Currey JD. The mechanical adaptations of bones. Princeton: Princeton University Press; 1984.
[33] Ratner BD, Hoffman AS, Schoen FJ, Lemons JE. Biomaterials science: an introduction to materials in medicine. New York: Academic Press; 2005.
[34] Forbes P. The gecko's foot. London: Fourth Estate; 2007.
[35] Mann S, Archibals DD, Didymus JM, Douglas T, Heywood BR, Meldrum FC, et al. Science 1993;261:1286–92.
[36] Kamat S, Su X, Ballarini R, Heuer AH. Nature 2000;405:1038–40.
[37] Whitesides GM. Mater Res Soc Bull 2002;27:56–65.
[38] Mayer G, Sarikaya M. Exp Mech 2002;42:395–403.
[39] Altman GH, Diaz F, Jakuba C, Calabro T, Horan RL, Chen J, et al. Biomaterials 2003;24:401–16.
[40] Mayer G. Science 2005;310:1144–7.
[41] Sanchez C, Arribart H, Giraud-Guille MM. Nat Mater 2005;4:277–88.
[42] Wilt FW. Dev Biol 2005;280:15–25.
[43] Meyers MA, Lin AYM, Seki Y, Chen PY, Kad BK, Bodde S. JOM 2006;58:35–41.
[44] Mayer G. Mater Eng Sci C 2006;26:1261–8.
[45] Lee GYH, Lim CT. Trends Biotechnol 2007;25:111–8.

[46] Bouligand Y. 7ème Congrès, int., Microsc, Électr, vol. 3, Grenoble, France 1970:105–6.
[47] Bouligand Y. Tissue Cell 1972;4:189.
[48] Prigogine I. Non-equilibrium statistical mechanics. New York: Wiley-Interscience; 1962.
[49] Nicolis G, Prigogine I. Exploring complexity. New York: W.H. Freeman; 1989.
[50] Teilhard de Chardin P. Le phénomène humain. Paris: Seuil; 1970.
[51] Nuzzo RG, Allara DL. J Am Chem Soc 1983;105:4481.
[52] Wu H, Thalladi VR, Whitesides S, Whitesides GM. J Am Ceram Soc 2002;124:14495.
[53] Tamarler C, Sarikaya M. Acta Biomater 2007;3:289–99.
[54] Hildebrand M. J Nanosci Nanotech 2005;5:146–57.
[55] Hildebrand M. Prog Org Coatings 2003;47:256–66.
[56] Lodish HF, Baltimore D, Berk A, Zipursky SL, Matsudaira P, Darnell J. Molecular cell biology. 4th ed. New York: W.H. Freeman; 1999.
[57] Vander A, Sherman J, Luciano D. Human physiology. 8th ed. New York: McGraw-Hill; 2001.
[58] Weiner S, Addadi L. Science 2002;298:375–6.
[59] Weissbuch I, Addadi L, Leiserowitz L. Science 1991;253:637–45.
[60] Mann S, Archibald DA, Didymus JM, Douglas T, Heywood BR, Meldrum FC, et al. Science 1993;261:1286–92.
[61] Addadi L, Weiner S. Proc Natl Acad Sci USA 1985;82:4110.
[62] Addadi L, Moradian J, Shay E, Maroudas NG, Weiner S. Proc Natl Acad Sci USA 1987;84:2732.
[63] Addadi L, Raz S, Weiner S. Adv Mater 2003;15:959–70.
[64] Belcher AM, Wu XH, Christensen RJ, Hansma PK, Stucky GD, Morse DE. Nature 1996;381:56–8.
[65] Hansma PK. Biophys J 2000;79:3307–12.
[66] Orme CA, Noy A, Wierzbickl A, McBride MT, Grantham M, Teng HH, et al. Nature 2001;411:775–8.
[67] Teng HH, Dove PM, Orme CA, DeYoreo JJ. Science 1988;282:724–7.
[68] Ehrlich H, Worch H. Collagen, a huge matrix in glass sponge flexible spicules of the meter-long *Hyalonema sieboldi*. In: Baüerlein E, Behrens P, Epple M, editors. Hand book of biomineralization. Weinheim: Wiley-VCH; 2007.
[69] Traub W, Arad T, Weiner S. Proc Natl Acad Sci USA 1989;86:9822–6.
[70] Baer E, Hiltner A, Morgan RJ. Phys Today 1992;45:60–7.
[71] Liao J, Yang L, Grashow J, Sacks M. Acta Biomater 2005;1:45.
[72] Fratzl P, Misof K, Zizak I, Rapp G, Amenitsch H, Bernstorff S. J Struct Biol 1997;122:119.
[73] Sacks M. Trans ASME 2003;125:280.
[74] Mooney M. J Appl Phys 1940;11:582.
[75] Rivlin RS, Saunders DW. Philos Trans Roy Soc London 1951;243:251–88.
[76] Mercer EH. Keratin and keratinization: an essay in molecular biology. New York: Pergamon Press; 1961.
[77] Fraser RDB, Parry DAD. Int J Biol Macro 1996;19:207–11.
[78] Cao J. J Mole Struct 2002;607:69–75.
[79] Fraser RDB, Macrae TP. Molecular structure and mechanical properties of keratins. In: Vincent JFV, Currey JD, editors. The mechanical properties of biological materials. Symp Soc Exp Biol, vol. XXXIV. New York: Cambridge Press; 1980. p. 211–46.
[80] Pautard FGE. Nature 1963;199:531–5.
[81] Gray WR, Sandberg LB, Foster JA. Nature 1973;246:461–6.
[82] Shen X, Belcher AM, Hansma PK, Stucky GD, Morse DE. J Biol Chem 1997;272:32472–81.
[83] Cha JN, Shimizu K, Zhou Y, Christiansen SC, Chmelka BF, Stucky GD, et al. Proc Natl Acad Sci USA 1999;96:361.
[84] Kohr E. Chitin: fulfilling a biomaterials promise. Oxford: Elsevier; 2001.
[85] Levi-Kalisman Y, Falini G, Addadi L, Weiner S. J Struct Biol 2001;135:8–17.
[87] Weiss IM, Schönitzer V. J Struct Biol 2006;153:264–77.
[88] Krajewska B. Enzyme Microbial Tech 2004;35:129.
[89] Rinaudo M. Prog Polym Sci 2006;31:603–32.
[90] Nelson DL, Cox MM. Lehninger principles of biochemistry. 4th ed. New York: W.H. Freeman; 2005.
[91] Bledzki AK, Gassan J. Prog Polym Sci 1999;24:221–74.
[92] Nevell TP, Zeronian SH. Cellulose chemistry and its applications. New York: Wiley; 1985.
[93] Levi C, Barton JL, Guillemet C, Le Bras E, Jehuede PJ. Mater Sci Lett 1989;8:337.
[94] Aizenberg J, Weaver JC, Thanawala MS, Sundar VC, Morse DE, Fratzl P. Science 2005;309:275–8.
[95] Sundar VC, Yablon AD, Grazul JL, Ilan M, Aizenberg J. Nature 2003;427:899–900.

[96] Sarikaya M, Fong H, Sunderland N, Flinn BD, Mayer G, Mescher A, et al. J Mater Res 2001;16:1420–8.
[97] Ehrlich H, Maldonado M, Spindler KD, Eckert C, Hanke T, Born R, et al. J Exp Zool, in press.
[98] Ehrlich H, Krautter M, Hanke T, Simon P, Knieb C, Heinemann S, et al. J Exp Zool, in press.
[99] Cazorla O, Freiburg A, Helmes M, Centner T, McNabb M, Wu Y, et al. Circulation Res 2000;86:59.
[100] Skalak R, Farrow DA, Hoger A. J Math Biol 1997;35:869–907.
[101] Nakahara H, Bevelander G, Kakei M. Venus Jpn J Malac 1982;41:33–46.
[102] Sarikaya M. Microsc Res Tech 1994;27:360.
[103] Vecchio KS. Unpublished results.
[104] Wada K. Bull Jpn Soc Sci Fish 1958;24:421–7.
[105] Wada K. Bull Jpn Soc Sci Fish 1959;25:342–5.
[106] Watabe N, Wilbur KM. Nature 1960;188:334.
[107] Bevelander G, Nakahara H. Calc Tiss Res 1960;7:84–92.
[108] Zaremba CM, Belcher AM, Fritz M, Li Y, Mann S, Hansma PK, et al. Chem Mater 1996;8:679–90.
[109] Belcher AM. PhD thesis, University of California, Santa Barbara, 1996.
[110] Belcher AM, Hansma PK, Stucky GD, Morse DE. Acta Mater 1997;46:733.
[111] Belcher AM, Gooch EE. In: Bauerlein E, editor. Biomineralization. Weinheim: Wiley-VCH. Fritz M, Morse DE, Col Int Sci 1998;3:55.
[112] Su X, Belcher AM, Zaremba CM, Morse DE, Stucky GD, Heuer AH. Chem Mater 2002;14:3106.
[113] Fritz M, Belcher AM, Radmacher M, Walters DA, Hansma PK, Strucky GD, et al. Nature 1994;371:49.
[114] Fritz M, Morse DE. Col Int Sci 1998;3:55.
[115] Lin AYM, Chen PY, Meyers MA. Acta Biomater 2007; in press.
[116] Wada K. Bull Natl Pearl Res Lab 1964;9:1087–98.
[117] Wada K. Bull Jap Soc Sci Fish 1966;32:304–11.
[118] Bevelander G, Nakahara H. In: Omori M, Watabe N, editors. The mechanisms of biomineralization in animals and plants. Tokyo: Tokai University Press; 1980. p. 19–27.
[119] Simkiss K, Wilbur KM. Biomineralization. Academic Press; 1989.
[120] Nakahara H. Calcification of gastropod nacre. In: Westbroek P, De Jong EW, editors. Biomineralization and biological metal accumulation. Dordrecht, Holland: D. Reidel Publishing Company; 1982. p. 225.
[121] Nakahara H. Nacre formation in bivalve and gastropod molluscs. In: Suga S, Nakahara H, editors. Mechanisms and phylogeny of mineralizaion in biological systems. New York: Springer-Verlag; 1991. p. 343.
[122] Sarikaya M. Personal Communication, 1997.
[123] Song F, Zhang XH, Bai YL. J Mater Res 2002;17:1567–70.
[124] Song F, Soh AK, Bai YL. Biomaterials 2003;24:3623.
[125] Schäffer TE, Ionescu-Zanetti C, Proksch R, Fritz M, Walters DE, Almqvist N, et al. Chem Mater 1997;9:1731–40.
[126] Wang RZ, Suo Z, Evans AG, Yao N, Aksay IA. J Mater Res Soc 2001;16:2485.
[127] Cartwright JHE, Checa AG. J R Soc Interface 2007;4:491–504.
[128] Laraia VJ, Heuer AH. J Am Ceram Soc 1989;72:2177–9.
[129] Jackson AP, Vincent JFV, Turner RM. Comp Sci Tech 1989;36:255–66.
[130] Gregoire C. Arch Int Phys Bioch 1961;69:374.
[131] Heuer AH, Fink DJ, Laraia VJ, Arias JL, Calvert PD, Kendall K, et al. Science 1992;255:1098.
[132] Currey JD. Proc Roy Soc Lond 1977;196:443–63.
[133] Jackson AP, Vincent JFV, Turner RM. Proc Roy Soc London B 1988;B234:415.
[134] Sarikaya M, Gunnison KE, Yasrebi M, Aksay JA. Mater Res Soc 1990;174:109.
[135] Weibull W. J Appl Mech 1951;18:293.
[136] Argon AS. Fracture of composites. New York: Treatise of Materials Science and Technology, Academic Press; 1972. p. 1.
[137] Budiansky B. Comp Struct 1983;16:3.
[138] Fleck NA, Deng L, Budiansky B. J Appl Mech 1995;62:329.
[139] Jelf PM, Fleck NA. J Comp Mater 1992;26:18.
[140] Sarikaya M, Aksay JA. In: Case S, editor. Results and problems in cell differentiation in biopolymers. Amsterdam: Springer-Verlag; 1992. p. 1.
[141] Meyers MA, Lin AYM, Chen PY, Muyco J. J Mech Behav Biomed Mater, in press.
[142] Mathur AB, Collinsworth AM, Reichert WM, Kraus WE, Truskey GA. J Biomech 2001;34:1545–53.

[143] Belcher AM, Gooch EE. In: Bauerlein E, editor. Biomineralization: from biology to biotechnology and medical application. Germany: Wiley-Interscience; 2000. p. 221.
[144] Weiner S. Am Zool 1984;24:945–52.
[145] Weiner S, Traub W. FEBS Lett 1982;111:311.
[146] Weiner S. Cal Tissue Int 1979;29:163.
[147] Evans AG, Suo Z, Wang RZ, Aksay IA, He MY, Hutchinson JW. J Mater Res Soc 2001;16:2475.
[148] Bruet BJF, Qi HJ, Boyce MC, Panas R, Tai K, Frick L, et al. Nanoscale morphology and indentation of individual nacre tablets from the gastropod mollusc *Trochus niloticus*. J Mater Res 2005;20:2400–19.
[149] Gao HJ, Ji BH, Jäger IL, Arzt E, Fratzl P. Proc Natl Acad Sci USA 2003;100:5597–600.
[150] Ji BH, Gao HJ. J Mech Phys Solid 2004;52:1963–90.
[151] Ji BH, Gao HJ, Hsia KJ. Phil Mag Lett 2004;84:631–41.
[152] Barthelat F, Li CM, Comi C, Espinosa HD. J Mater Res 2006;21:1977–86.
[153] Hou DF, Zhou GS, Zheng M. Biomaterials 2004;25:751–6.
[154] Kamat S, Su X, Ballarini R, Heuer AH. Nature 2000;405:1036–40.
[155] Kuhn-Spearing LF, Kessler H, Chateau E, Ballarini R, Heuer AH. J Mater Sci 1996;31:6583–94.
[156] Currey JD, Kohn AJ. J Mater Sci 1976;11:1614.
[157] Kamat S, Kessler H, Ballarini R, Nassirou M, Heuer AH. Acta Mater 2004;52:2395–406.
[158] Rosewater JR. Indo-Pacific Mollusca 1965;1:347–96.
[159] Moir BG. J Archaeol Sci 1990;17:329–45.
[160] Kobayashim I. Am Zool 1969;9:633–72.
[161] Meyers MA, Chawla KK. Mechanical behavior of materials. New Jersey: Prentice Hall Inc.; 1999.
[162] Sitti M, Fearing RS. J Adhes Sci Tech 2003;17:1055–74.
[163] Johnson KL, Kendall K, Roberts AD. Proc Roy Soc London 1971;324:301–13.
[164] Khanuja S. Processing of laminated B4C-polymer laminated composites. MS Thesis, University of Washington, 1991.
[165] Almqvist N, Thomson NH, Smith BL, Stucky GD, Morse DE, Hansma PK. Mater Sci Eng C 1999;7:37–43.
[166] Chen B, Peng X, Wang JG, Wu X. Ceram Int 2004;30:2011–4.
[167] Currey JD, Nash A, Bonfield W. J Mater Sci 1982;17:1939.
[168] Lowenstam HA. Bull Geol Soc Am 1962;73:435.
[169] Lichtenegger HC, Schöberl T, Bartl MH, Waite H, Stucky GD. Science 2002;298:389.
[170] Katz JL. J Biomech 1971;4:455–73.
[171] Jäger I, Fratzl P. Biophys J 2000;79:1737–46.
[172] Lucas GL, Cooke FW, Friis EA. A primer on biomechanics. New York: Springer; 1999. Fig. 17.7, p. 268.
[173] Evans AG, Charles EA. J Am Ceram Soc 1976;59:371.
[174] McElhaney JH. J Appl Physiol 1966;21:1231.
[175] Adharapurapu RR, Jiang F, Vecchio KS. Mater Sci Eng C 2006;26:1325–32.
[176] Treloar LGR. Trans Far Soc 1944;40:59.
[177] Arruda E, Boyce MC. JMPS 1993;41:389–412.
[178] Melvin JW, Evans FG. ASME biomaterials symposium. Detroit, MI, 1973.
[179] Behiri JC, Bonfield W. J Mater Sci 1980;15:1841–9.
[180] Nalla RK, Kinney JH, Ritchie RO. Nat Mater 2003;2:164.
[181] Hall SJ. Basic biomechanics. 4th ed. Boston: McGraw-Hill; 2003. Fig. 4–6, p. 102.
[182] Malik CL, Gibeling JC, Martin RB, Stover SM. J Biomech 2003;36:194.
[183] Yang QD, Cox BN, Nalla RK, Ritchie RO. Biomaterials 2006;27:2095.
[184] Nalla RK, Kruzic JJ, Kinney JH, Balooch M, Ager JW, Ritchie RO. Mater Sci Eng C 2006;26:1251–60.
[185] Snead ML, Zhu D, Lei Y, White SN, Snead CM, Luo Wen, et al. Mater Sci Eng C 2006;26:1296–300.
[186] Imbeni V, Nalla RK, Bosi C, Kinney JH, Ritchie RO. J Biomed Mater Res A 2003;66:1–9.
[187] Imbeni V, Kruzic JJ, Marshall GW, Marshall SJ, Ritchie RO. Nat Mater 2005;4:229–32.
[188] Nalla RK, Kinney JH, Ritchie RO. Biomaterials 2003;24:3955–68.
[189] Monteiro SN, Rangel JJA. Proc 62nd Congress ABM, Victoria, Brazil; 2007. p. 24.
[190] Deymier A, Stock S, Dunand DC. Unpublished result.
[191] Kruzic JJ, Nalla RK, Kinney JH, Ritchie RO. Biomaterials 2003;24:5209–21.
[192] Nalla RK, Kinney JH, Tomsia AP, Ritchie RO. J Dent Res 2006;85:1022–6.
[193] Gao H, Klein PA. J Mech Phys Solids 1998;46:187–218.
[194] Ballarini R, Kaycan R, Ulm F-J, Belytschko T, Heuer AH. Int J Fract 2005;135:187.

[195] Menig R. MS Thesis, University of California, San Diego, 1998.
[196] Aveston J, Cooper GA, Kelly A. Proc conf 15, National Phys lab. IPC AScience and Tech press; 1971.
[197] Bazant Z, Pang S-D. J Mech Phys Solids 2007;55:91.
[198] Bazant Z, Pang S-D. Proc Natl Acad Sci USA 2006;103:9434.
[199] Jeronimidis G. Structure–property relationships in biological materials. In: Elices M, editor. Structural biological materials. New York: Pergamon; 2001.
[200] Sikoryn TA, Hukins DWL. J Orthop Res 1990;8:586.
[201] Herrick WC, Kingsbury HB, Lou DYS. J Biom Mat Res 1978;12:877.
[202] Nachemson A, Evans JH. J Biomech 1968;1:211–20.
[203] Chazal J, Tangguy A, Bourges M, Gaurel G, Escande G, Guillot M, et al. J Biomech 1985;18:167–79.
[204] Bigliana LU, Pollock RG, Soslowsky LJ, Flatow EL, Pawluk RJ, Mow VC. J Orthop Res 1992;10:187–97.
[205] Bulter DL, Grood ES, Noyes FR. J Biomach 1984;17:579–96.
[206] Pollock RG, Soslowsky LJ, Bigliani LU, Flatow EL, Mow VC. Trans Orthop Res Soc 1990;15:510.
[207] Selden PA. Nature 1989;340:711–2.
[208] Shear WA, Palmer JA, Coddington JA, Bonamo PM. Science 1989;246:479–81.
[209] Denny M. J Exp Biol 1976;65:483–506.
[210] Kaplan DL, Lombardi SJ, Muller WS, Fossey SA. Silk. In: Byrom D, editor. Biomaterials. Novel materials from biological sources. New York: Stockton Press; 1991.
[211] Gosline JM, DeMont ME, Denny MW. Endeavour 1986;10:37–43.
[212] Vollrath F. Rev Mol Biotechnol 2000;74:67–83.
[213] Gosline JM, Guerette PA, Ortlepp CS, Savage KN. J Exp Biol 1999;202:3295–303.
[214] Cunniff PM, Fossey SA, Auerbach MA, Song JW, Kaplan DL, Adams WW, et al. Polym Adv Technol 1944;5:401–10.
[215] Perez-Rigueiro J, Viney C, Llorca J, Elices M. J Appl Polym Sci 2000;75:1270–7.
[216] Pins GD, Christiansen DL, Patel R, Silver FH. Biophys J 1977;73:2164–72.
[217] Altman GH, Diaz F, Jakuba C, Calabro T, Rebecca LH, et al. Biomaterials 2003;24:401–16.
[218] Gosline JM, Denny MW, DeMont ME. Nature 1984;3009:551–2.
[219] Kaplan D, Adams WW, Viney C, Farmen B. Am Chem Soc Symp 1994:S544.
[220] Elices M, Perez-Rigueiro J, Plaza GR, Guinea GV. J Metals 2005:60–6.
[221] Garrido MA, Elices M, Viney C, Perez-Riguerio J. Polymer 2002;43:4495–502.
[222] Neville AC. Biology of the arthropod cuticle. New York: Springer-Verlag; 1975.
[223] Vincent JFV. Composites 2002;A33:1311–5.
[224] Vincent JFV, Wegst UGK. Arthropod Struc Dev 2004;33:187–99.
[225] Giraud-Guille MM. Tissue Cell 1984;16:75–92.
[226] Giraud-Guille MM. J Struct Biol 1990;103:232–40.
[227] Giraud-Guille MM. Curr Opin Solid State Mater Sci 1998;3:221–8.
[228] Lowenstam HA. Science 1981;211:1126–31.
[229] Giraud-Guille MM, Bouligand Y. Crystal growth in a chitin matrix: the study of calcite development in the crab cuticle. In: Karnicki ZS, editor. Chitin world. Wirtschaftsverlag NW: Bremerhaven; 1995. p. 136–44.
[230] Chen PY, Lin AYM, Meyers MA, McKittrick JM. Acta Biomater, submitted for publication.
[231] Hepburn HR, Joffe I, Green N, Nelson KJ. Comp Biochem Physiol 1975;50:551.
[232] Joffe I, Hepburn HR, Nelson KJ, Green N. Comp Biochem Physiol 1975;50:545.
[233] Raabe D, Al-Sawalmih A, Romano P, Sachs C, Brokmeier HG, Yi SB, et al. Mater Sci Forum 2005;495–497:1665–74.
[234] Raabe D, Romano P, Sachs C, Al-Sawalmih A, Brokmeier HG, Yi SB, et al. J Crystal Growth 2005;283:1–7.
[235] Raabe D, Sachs C, Romano P. Acta Mater 2005;53:4281–92.
[236] Raabe D, Romano P, Sachs C, Fabritius H, Al-Sawalmih A, Yi SB, et al. Mater Sci Eng A 2006;421:143–53.
[237] Sachs C, Fabritius H, Raabe D. J Mater Res 2006;21:1987–95.
[238] Sachs C, Fabritius H, Raabe D. J Struct Biol 2006;155:409–25.
[239] Romano P, Fabritius H, Raabe D. Acta Biomater 2007;3:301–9.
[240] Melnick CA, Chen S, Mecholsky JJ. J Mater Res 1996;11:2903–7.
[241] Bertram JEA, Gosline JM. J Exp Biol 1987;130:121–36.
[242] Kaspi MA, Gosline JM. J Exp Biol 1996;199:1133–46.
[243] Kaspi MA, Gosline JM. J Exp Biol 1997;200:1639–59.

[244] Kaspi MA, Gosline JM. J Exp Biol 1999;202:377–91.
[245] Ryder ML. Nature 1962;193:1199–201.
[246] Kitchener A, Vincent JFV. J Mater Sci 1987;22:1385–9.
[247] Kitchener A. J Mat Sci Lett 1987;6:321–2.
[248] Druhala M, Feughelman M. Colloid Poly Sci 1974;252:381–91.
[249] Montagna W, Parakkal PF. The structure and function of skin. 3rd ed. New York: Academic press; 1974.
[250] Marks R, Plewig G. Stratum corneum. New York: Springer-Verlag; 1983.
[251] Oxlund H, Manschot J, Viidik A. J Biomech 1988;3:213–8.
[252] Wu KS, van Osdol WW, Dauskardt RH. Biomaterials 2006;27:785–95.
[253] Escoffier C et al. J Invest Dermatol 1989;93:353–7.
[254] Vogel HG. Biochim Biophys Acta 1972;286:79–83.
[255] Shadwick RE, Russell AP, Lauff RF. Philos Trans Roy Soc London B 1992;337:419–28.
[256] Purslow PP. J Mater Sci 1983;18:3591–8.
[257] Hill AV. Proc Roy Soc London B 1938;126:136–95.
[258] Smeathers JE, Vincent JFV. J Molluscan Stud 1979;49:219–30.
[259] Gathercole LJ, Keller A. Struct Fibrous Biopolym 1975:153–75.
[260] Qin X, Colyne K, Waite JH. J Exp Biol 1996;199:1005–17.
[261] Rudall KM. Symp Soc Exp Biol 1955;9:49–69.
[262] Bell EC, Gasoline JM. J Exp Biol 1996;199:1005–17.
[263] Rabin BH, Williamson RL, Suresh S. Mat Res Soc Bull 1995;20:37–9.
[264] Vaccaro E, Waite JH. Biomacromolecules 2001;2:906–11.
[265] Bao G, Suresh S. Nature Mater 2003;2:715–25.
[266] Lim CT, Zhou EH, Li A, Vedula SRK, Fu Hx. Mater Sci Eng C 2006;26:1278–88.
[267] Lim CT. J Biomech Sci Eng 2006;1:82–92.
[268] Lee GYH, Lim CT. Trends Biotech 2007;25:111–8.
[269] Suresh S, Spatz J, Mills JP, Micoulet A, Dao M, Lim CT, et al. Acta Biomater 2005;1:15–30.
[270] Lim CT, Dao M, Suresh S, Sow CH, Chew KT. Acta Mater 2004;52:1837–45.
[271] Dao M, Li J, Suresh S. Mater Sci Eng C 2006;26:1232–44.
[272] Dao M, Lim CT, Suresh S. J Mech Phys Solid 2003;51:2259–80.
[273] Lim CT, Zhou EH, Quek ST. J Biomech 2006;39:195–216.
[274] Fisher TE, Marszalek PE, Fernandez JM. Trends Biochem Sci 1999;24:379–84.
[275] Mitchison TJ, Cramer LP. Cell 1996;84:371–9.
[276] Suresh S. Acta Biomater 2007;3:413–38.
[277] Garcia A. Biomaterials 2005;26:7525.
[278] Chen PY, Lin AYM, Meyers MA, McKittrick JM. J Mech Behav Biol Mater, submitted for publication.
[279] Carrol M, Holt AC. J Appl Phys 1972;43:759.
[280] Torre C. Huttenmonats. Hochschule leoben 1948;93:62.
[281] Helle AS, Easterling KE, Ashby MF. Acta Met 1985;33:2163.
[282] Fischmeister H, Arzt E. Power Met 1982;26:82.
[283] Jeronimidis G. Symp Soc Exp Biol 1980;34:169–82.
[284] Tirrell DA. Hierarchical structures in biology as a guide for new materials technology. Washington, DC: National Academy Press; 1994.
[285] Mark RE. Cell wall mechanics of wood tracheids. New Haven: Yale University Press; 1967.
[286] Preston RD. The physical biology of plant cell walls. London: Chapman and Hall; 1974.
[287] Young RA, Rowell RM. Cellulose: structure, modification, and hydrolysis. New York: John Wiley and Sons; 1986.
[288] Nevell TP, Zeronian SH. Cellulose chemistry and its applications. New York: John Wiley and Sons; 1985.
[289] Easterling KE, Harrysson R, Gibson LJ, Ashby MF. Proc Roy Soc A 1982;383:31.
[290] Jeronimidis G. In: Baas P, Bolton AJ, Catling DM, editors. Wood structure in biological and technological research. Leiden: The University Press; 1976.
[291] Gordon JE, Jeronimidis G. Philos Trans Roy Soc London A 1980;297:545–50.
[292] Frenkel MJ, Gillespie JM. Aust J Biol Sci 1976;29:467–79.
[293] Traeger RK. J Cell Plact 1967;3:405–18.
[294] Matonis VA. Soc Plast Eng J 1964(September):1024–30.
[295] Thornton PH, Magee CL. Met Trans 1975;6A:1253–63.
[296] Thornton PH, Magee CL. Met Trans 1975;6A:1801–7.

[297] Wilsea M, Johnson KL, Ashby MF. Int J Mech Sci 1975;17:457–60.
[298] Patel MR, Finnie I. J Mat 1970;5:909–32.
[299] Bodde SG, Seki Y, Meyers MA. Unpublished result, 2007.
[300] Brush AH, Wyld JA. Comp Biochem Physiol B 1982;73:313–25.
[301] Brush AH. Biochem Syst Ecol 1986;14:547–51.
[302] Purslow PP, Vincent JFV. J Exp Biol 1978;72:251–60.
[303] Bonser RHC, Purslow PP. J Exp Biol 1995;198:1029–33.
[304] Cameron GJ, Wess TJ, Bonser RHC. J Struct Biol 2003;143:118–23.
[305] Corning WR, Biewener AA. J Exp Biol 1998;201:3057–65.
[306] Taylor AM, Bonser RHC, Farrent JW. J Mater Sci 2004;39:939–42.
[307] Bonser RHC. J Mater Sci Lett 2001;20:941–2.
[308] Bonser RHC, Witter MS. The Condor 1993;95:736–8.
[309] Butler M, Johnson AS. J Exp Biol 2004;207:285–93.
[310] Autumn K, Liang Y, Hsieh ST, Zesch W, Chan WP, Kenny TW, et al. Nature 2000;405:681.
[311] Ruibal R, Ernst V. J Morphol 1965;117:271–93.
[312] Arzt E, Gorg S, Spolenak R. Proc Natl Acad Sci USA 2003;100:10603–6.
[313] Spolenak R, Gorb S, Arzt E. Acta Biom 2005;1:5.
[314] Huber G, Mantz H, Spoolenak R, Mecke K, Jocobs K, Gorb SN, et al. Proc Natl Acad Sci USA 2005;102:16293–6.
[315] Meyers MA, Lin AYM, Chen P-Y. Unpublished result, 2007.
[316] Vukusic P, Sambles JR. Nature 2003;424:852–5.
[317] Bereiter-Hahn J, Matoltsy AG, Richards KS. Biology of the integument, vol. 2. Vertebrate.
[318] Zi J, Yu X, Li Y, Hu X, Xu C, Wang X, et al. Proc Natl Acad Sci USA 2003;100:12576–8.
[319] Nassau K. The physics and chemistry of color. 2nd ed. New York: Wiley; 2001.
[320] Nassau K. Color for science, art, and technology. New York: Elsevier; 1998.
[321] Ghiradella H. Appl Opt 1991;30:3492–500.
[322] Lawrence C, Vukusic P, Sambles JR. Appl Opt 2002;41:437–41.
[323] Brink DJ, van der Berg NG. J Phys D: Appl Phys 2004;37:813–8.
[324] Zoond A, Eyre J. Philos Trans Roy Soc London B 1934;223:27–55.
[325] Alexander NJ, Parakkal PF. Z Zellforsch 1969;101:72–87.
[326] Alexander NJ. Z Zellforsch 1970;110:153–65.
[327] Alexander NJ, Fahrenbach WF. AM J Anat 1969;126:41–56.
[328] Carlton FC. Proc Am Acad Arts Sci 1903;39:259–77.
[329] Rohrlich ST, Rubin RW. The J Cell Biol 1975;66:635–45.
[330] Vincent JFV, Mann DL. Philos Trans Roy Soc London A 2002;360:159–73.
[331] Weiner S, Addadi L, Wagner HD. Mater Sci Eng C 2000;11:1–8.
[332] Sarikaya M, Tamerler C, Jen AKY, Schulten K, Baneyx F. Nat Mater 2003;2:577–85.
[333] Zhou BL. Mater Chem Phys 1996;45:114–9.
[334] Dawson MA, Gibson LJ. Int J Solids Struct, in press.
[335] Karam GN, Gibson LJ. Mater Sci Eng C 1994;2:113–32.
[336] Karam GN, Gibson LJ. Int J Solids Struct 1995;32:1259–83.
[337] Karam GN, Gibson LJ. Int J Solids Struct 1995;32:1285–306.
[338] Aizenberg J, Hendler G. J Mater Chem 2004;14:2066.
[339] Kisailus D, Truong Q, Amemiya Y, Weaver JC, Morse DE. Proc Natl Acad Sci 2006;103:5652–7.
[340] Schwenzer B, Gomm JR, Morse DE. Langmuir 2006;22:9829–31.
[341] Hamilton WJ, Selly MK. Nature 1976;262:284–5.
[342] Parker AR, Lawrence CR. Nature 2001;414:33–4.
[343] Armstrong WP. Environment Southwest Number 1979;486:20–3.
[344] Autumn K, Sitti M, Liang Y. Proc Natl Acad Sci USA 2000;19:12252–6.
[345] Geim AK, Dubonos SV, Nvoselov KS, Ahukov AA, Shapoval SY. Nat Mater 2003;2:461–3.
[346] Holl SM, Hansen D, Waite JH, Shaefer J. Arch Biochem Biophys 1993;302:255–8.
[347] Waite JH, Lichtenegger HC, Stucky GD, Hansma P. Biochemistry 2004;43:7653–62.
[348] Evans AG, Hutchinson JW, Fleck NA, Ashby MF, Wadley HNG. Prog Mater Sci 2001;3–4:309–27.
[349] Yasrebi M, Kim GH, Gunnison KE, Milius DL, Sarikaya M, Aksay IA. Mater Res Soc 1990:625–35.
[350] Tang Z, Kotov NA, Magonov S, Ozturk B. Nat Mater 2003;2:413.
[351] Rubner M. Nature 2003;423:925.

[352] Manne S, Aksay IA. Curr Opin Solid State Mater Sci 1997;2:358.
[353] Aksay IA, Trau M, Manne S, Honma I, Yao N, Zhou L, et al. Science 1996;273:892–8.
[354] Deville S, Saiz E, Nalla RK, Tomsia AP. Science 2006;311:515–8.
[355] Deville S, Saiz E, Tomsia AP. Biomaterials 2006;27:5480–9.
[356] Schwenzer B, Roth KM, Gomm JR, Murr M, Morse DE. Langmuir 2006;22:9829–31.
[357] Greiner C, del Campo A, Artz E. Langmuir, in press.
[358] Seeman NC, Belcher AM. Proc Natl Acad Sci USA 2002;99:6451–5.
[359] Bain CD, Whitesides GM. Science 1988;256:62.
[360] Bowden N, Tamerler C, Carbech J, Whitesides GM. Science 1997;276:233.
[361] Olson GB, Hartman H. Proc intl con mart transf ICOMAT-82, Leuven, Belgium. J Phys 1982;43:C4-855.
[362] Olson GB, Cohen M. In: Meyers MA, Inal OT, editors. Frontiers in materials technology. Elsevier; 1985. p. 43.
[363] Brown S. Nat Biotechnol 1997;15:272–96.
[364] Lee SW, Mao CB, Flynn CE, Belcher AM. Science 2002;296:892–5.
[365] Jeronimidis G. Design and function of structural biological materials. In: Elices M, editor. Structural biological materials. New York: Pergamon; 2001.